Large Scale Structure Cosmology on the Light Cone

Dan Pryer

Department of Physics and Astronomy
University of Sussex

This dissertation is submitted for the degree of
Doctor of Philosophy

Supervisors: Dr. Jon Loveday & Dr. Robert Smith

September 2021

Declaration

I hereby declare that this thesis has not been and will not be submitted in whole or in part to another University for the award of any other degree. Parts of this thesis have been undertaken in collaboration with other researchers. Where this is the case, I identify my personal contributions at the end of each chapter.

The work in Chapter §2 has been written up into a paper: Pryer, Smith, Booth, Blake, Eggemeier, Loveday (JCAP submitted).

Dan Pryer
September 2021

Acknowledgements

Firstly, I'd like to start of by thanking my supervisors: Robert, for always pushing me forward and keeping me positive, and without whom this work would not have been possible, and Jon, for always being available when I needed help, and for the useful discussions regarding the clustering pipeline and all things 4MOST. I also really appreciated you both spending the time to give me helpful comments and corrections on the thesis: thank you! Additionally, a special thanks to Chris Blake, my supervisor while on a four-month attachment in Melbourne, Australia. I'm grateful to you and your team for welcoming me in when so far from home, and for teaching me useful techniques that were invaluable to this work. I hope to be able to come back and visit one day!

A big thanks goes to the wonderful Astronomy Department at Sussex, and in particular my office buddies over the past few years, for the interesting conversations, trips to the pub and games of squash! A special thanks to Lucas, for being on the PhD journey with me since day one and keeping me sane and entertained, Alex and Ridwan for being our initial mentors the welcoming faces into the department and team, and Robin, Cameron and Stephen for keeping me company in 4C15! Thanks to the wider department: Laura, Dan, Trist, Tyler, Lennart, Aziza, Pippa, Sunayana, Chris, Aswin, David, Andy, Jussi, Steve, Raph, Kareem, Maria, Reese, Will, Luke, Ian, Itzi and all the rest! My time at Sussex wouldn't have been the same without you. I'd also like to acknowledge the various members of staff around MPS, including Chris, Kathy, David, Steve, Winni, Xavier, Antony, Seb, Mark, Fab, Antonella, Iacopo, Philip and Peter, for making the department the welcoming and friendly place that it is.

The last few years has had some ups and downs, but a huge thanks goes to my partner Z, for always being there for me with support and encouragement, taking me away to interesting places whenever we had the chance, and keeping me well fed with yummy food, particularly on the occasions I've been so absorbed in work I've forgotten to eat. I also count myself extremely lucky to be able to rely on a large group of friends in Brighton, with whom I have shared many special occasions and celebrations over the years, and who make it so easy to unwind from work.

Last but not least, thank you to my family and in particular my parents, without whom I would never have been able to go back to university and start on this path. Their endless love, support and encouragement has always helped to push me forward and keep me on track. This work is dedicated to them.

Abstract

The power spectrum is a very successful statistic for extracting cosmological information from the large-scale structure of the universe. When applied to data provided by galaxy redshift surveys, one of the key strengths of the power spectrum is its ability to determine the growth rate of structure and the expansion history of the universe, two important probes of cosmological models. Upcoming and future surveys will provide a higher number density of targets over a much greater volume than previously attainable, enabling the power spectrum to test cosmological models with more precision. Consequently, these large-volume surveys will require modelling of the power spectrum to a high degree of accuracy over a wider range of scales, and any previous modelling assumptions should be tested to assess their validity in this new regime.

The main task of this work is to address some of these challenges posed when modelling the galaxy power spectrum for very deep and wide-angle redshift surveys. Working with these conditions presents two problems that many previous smaller surveys did not necessarily have to address. Firstly, the distant observer approximation is no longer valid, and so working in spherical coordinates is required to properly model the survey window function that becomes convolved with the power spectrum in any volume or magnitude-limited sample. This choice of coordinate system introduces spherical Bessel functions into the integrals of the model equations, which can be notoriously difficult to evaluate. Secondly, when working with very deep surveys, the pair counting of objects that exist at significantly different redshifts from one another requires the use of unequal-time correlators for a full treatment of the modelling, otherwise this may introduce systematic errors when trying to recover cosmological parameters.

We start off by reviewing the existing model for the power spectrum on the past lightcone, working in the simple case of unbiased tracers on the full sky, and extend this model further into the non-linear regime. We develop numerical code in C++ that is able to compute the model in an accurate and timely manner, and test the validity of the standard mean-redshift approximation to the unequal-time correlator. We find this to cause a significant bias in the expected power spectrum amplitude, particularly for deep surveys. Following from this, we show that an effective fixed-time redshift can be easily determined that gives a good approximation to the unequal-time case, over a wide range of scales and redshifts. We then test the model against mock lightcone catalogues, created from large-volume N-body simulations, and find excellent agreement between our measurements and the theory, to within $\pm 5\%$, over a range of magnitude-limited samples, and for the scales $4 \times 10^{-3} \leq k \leq 0.5$ [h Mpc^{-1}]. We also tested how well the commonly used

FKP weights effected the measurements, for various values of fiducial power P_0 and over the range of magnitude cuts, finding they could boost the signal-to-noise by factors of a few. Using the mock lightcone catalogues, we then forecast the probability of upcoming and future galaxy redshift surveys being able to robustly detect the turnover-scale in the power spectrum. We found that a turnover was detectable with a probability of $P \geq 95\%$ in an all-sky catalogue, limited to an apparent magnitude of $m_{\rm lim} \sim 21$, with this probability remaining high for surveys with $m_{\rm lim} \sim 22$ at 20% sky coverage.

We then extend the model of the power spectrum on the past lightcone to make it more applicable to realistic surveys, by including terms for galaxy bias and a survey mask that is not necessarily isotropic. As accounting for these effects produces a more mathematically complicated model, we look for new methods to make numerical evaluation more feasible. We find that as long as time-separability of the unequal-time correlator holds, an approximation that was employed for the previous full-sky case can still be used to make the calculation of the model at small-scales a trivial task. For evaluation of the model at large scales, we apply the FFTLog method in conjunction with analytic transforms of Bessel integrals, deriving expressions for our specific case and listing an example of a step-by-step algorithm for implementing this numerically.

Finally, we give an overview of the 4MOST Cosmology Redshift Survey, an upcoming spectroscopic survey in the southern hemisphere which aims to synergize with weak lensing and CMB surveys to better constrain the late-time universe. We detail the clustering pipeline that we have developed in Python for this survey, which utilises existing libraries to compute two-point statistics in both configuration and Fourier space. This can be used for for assessing the quality of the mock catalogues being generated in advance of the survey going live, as well as for survey design optimisation. We end by briefly reviewing some of the results produced by the pipeline when being run on the most up-to-date mocks from the 4MOST simulation team.

Contents

List of Figures

List of Tables

Chapter 1

Introduction

Modern cosmology, the scientific study of the origin and evolution of the Universe, emerged just after the turn of the 20th century, and is grounded on Einstein's theory of General Relativity as well as the cosmological principle. While the former describes gravity as a geometric property of space-time, the latter states that we as observers hold no special place in the universe: it should look statistically the same no matter which direction we look out into the sky (isotropic) and be independent of where it is observed (homogeneous). Initial cosmological models favoured a static universe, in which space is deemed as flat, infinite in expanse and neither expanding or contracting. To counteract the force of gravity that would eventually cause everything to collapse in on itself, Einstein introduced the cosmological constant Λ into his field equations, which acts as an outwards pressure, counteracting the force of gravity and thus producing a static universe.

However, observations of galaxies by Hubble in 1929 [1] showed that a galaxy's recession velocity from us is roughly proportional to its separation distance, now known as Hubble's Law, forming the basis for the theory that the universe is not static, but instead is expanding. Shortly after this, measurements of galaxies in the nearby Coma Cluster by Zwicky [2] showed orbital velocities for galaxies far in excess of what would be expected if the cluster consisted of ordinary baryonic matter alone. This was the first strong evidence that the universe must contain what is referred to as Dark Matter - a hypothetical form of matter that does not interact with the electromagnetic force, and only acts gravitationally. Independent studies of clusters in the latter half of the century would confirm this result [3], and the 1983 work by Rubin [4] suggested that galaxies are embedded in a halo of dark matter to account for their higher-than-expected rotation velocities.

In the latter half of the 20th century, the accidental discovery of the cosmic microwave background (CMB) in 1965 by Penzias and Wilson [5] was a major milestone, supporting the idea of an expanding universe and providing strong evidence for the Big Bang theory: that the universe originated from a very hot and dense state. In addition to this, before the turn of the millennium, measurements by Reiss, Schmidt and Perlmutter [6, 7] of Type Ia Supernova, which act as standard candles, revealed that more distant galaxies are receding from us at rates faster than expected for a matter dominated Universe, implying that the Universe's expansion is accelerating. This development rekindled interest in the cosmological constant Λ, which Einstein had introduced for his static

universe, and subsequently called his biggest blunder after the discovery of the expanding universe by Hubble. The unknown substance which provides the driving force behind this acceleration, hereafter referred to as Dark Energy, showed remarkably similar properties to the effects of having a positive value of Λ in the field equations. Understanding Dark Energy is one of the most active areas of research in astronomy at the present time.

All of these ingredients have contributed to the current most widely accepted model of cosmology, called ΛCDM (Λ - dark energy, CDM - cold dark matter) or concordance cosmology. This model assumes that gravity is accurately described by General Relativity on cosmological scales, and is able to explain many observed phenomena, such as the CMB and large-scale structure of the universe today, the chemical abundances of light atoms, and the accelerated expansion of the universe [8].

More recent technological advances, such as the advent of modern high performance computers, high resolution, low readout noise CCDs, as well as the ability to construct larger and more accurate telescopes, have lead to a wealth of observational data for cosmologists. From ever increasingly precise measurements of the CMB and its temperature anisotropies by the Cosmic Background Explorer (COBE [9]), Wilkinson Microwave Anisotropy Probe (WMAP [10]) and Planck [11, 12, 13] missions, to late-time large-scale structure measurements by galaxy surveys such as the Two-degree-Field Galaxy Survey (2dF [14]), Sloan Digital Sky Survey (SDSS [15]) and Dark Energy Survey (DES [16]), we now have a much clearer understanding of the universe 100 years on from from the inception of Physical cosmology. Despite this, there are still fundamental outstanding issues in the field, not least being that Dark Matter and Dark Energy combined make up for around 94% of the energy density of the universe today, and we have yet to properly discern the true nature of either of these quantities. Additionally, significant tensions remain between late-time and early-time measurements of the inferred Hubble constant today, H_0, governing how fast we think the universe is expanding. These are currently two of the main driving issues for cosmologists: can improved understanding of the data resolve the tensions in ΛCDM, or is it just a model we have fitted to the data, that does not truly encapsulate the underlying physics? In the next section, we will review the model in more detail, highlighting some of its successes, as well as its flaws.

1.1 The standard model of Cosmology

We now review some of the important aspects underpinning the current standard model of cosmology, highlighting key developments and observations that influenced its shaping, as well as detailing some of the unresolved challenges it faces.

1.1.1 The field equations and density

The general solution to Einstein's field equations that satisfy the cosmological principle was discovered independently in the 1920's and 30's and is named after its discoverers: the *Friedmann-Lemaitre-Robertson-Walker* (FLRW) metric. The corresponding line element of this metric de-

scribes how to measure distances in an expanding space, and in spherical coordinates can be written as

$$ds^2 = c^2dt^2 - R^2(t)\Big[\frac{dr^2}{1-kr^2} + r^2(d\theta^2 + \sin^2\theta\ d\phi^2)\Big]\ , \tag{1.1}$$

where r represents a re-scaled (but dimensionless) radial coordinate and $R(t)$ is a quantity called the *scale factor*, which parameterises the expansion of space and has units of length. The dimensionless parameter k determines the spatial curvature and can have the values $\{-1, 0, 1\}$, corresponding to a negatively curved or closed space, a flat space, and positively curved or open space, respectively. The Hubble rate, which defines the rate of expansion of the universe, is defined as[1]

$$H(t) \equiv \frac{\dot{a}(t)}{a(t)}\ , \tag{1.2}$$

where the dot denotes a derivative with respect to coordinate time t. It is often parameterised by its value today as $H(t_0) = H_0 = 100h\text{km/s/Mpc}$, with h quantifying the uncertainty in the measured value. The observational form of Hubble's law relates the recession velocity v of a galaxy to its proper distance d (see next section) from us:

$$v \approx H_0 d \qquad \text{(for small distances)}\ , \tag{1.3}$$

and was established by Hubble in 1929. While his original observations measured a value of $H_0 \approx 500\text{km/s/Mpc}$[2], more recent observations from various sources put the figure at around $H_0 \approx 70\text{km/s/Mpc}$ (see Fig. 1.1), although the exact value remains a key point of contention in the field today.

To solve the FLRW metric of Eq. (1.1), we require some understanding of the matter content of the universe. From the gravitational field equations of GR, we have that

$$G_{\mu\nu} = R_{\mu\nu} - \frac{1}{2}g_{\mu\nu}R + \Lambda g_{\mu\nu} = -\frac{8\pi G}{c^4}T_{\mu\nu}\ , \tag{1.4}$$

with $G_{\mu\nu}$ the Einstein tensor, describing the geometry of spacetime, Λ the cosmological constant, and $R_{\mu\nu}$ and R the Ricci tensor and Ricci scalar respectively, both of which consist of derivatives of the metric tensor $g_{\mu\nu}$. On the right hand side of the equation, we have Newton's gravitational constant G, the speed of light c, and the energy-momentum tensor $T_{\mu\nu}$, describing the density and flux of energy and momentum in spacetime. Thus, we see that this theory of gravity is one in which the energy density of spacetime is intrinsically linked to its geometry. When applying these equations in the cosmological context, the universe is approximated as a perfect fluid, which is characterised at each point by its proper density ρ and pressure p in the instantaneous rest frame.

[1] Here, $a(t)$ is a dimensionless scale factor, given by $a(t) \equiv R(t)/R(t_0)$ where t_0 is the current age of the universe and therefore by definition we have $a(t_0) = 1$.

[2] This high value was the result of errors in distance calibration.

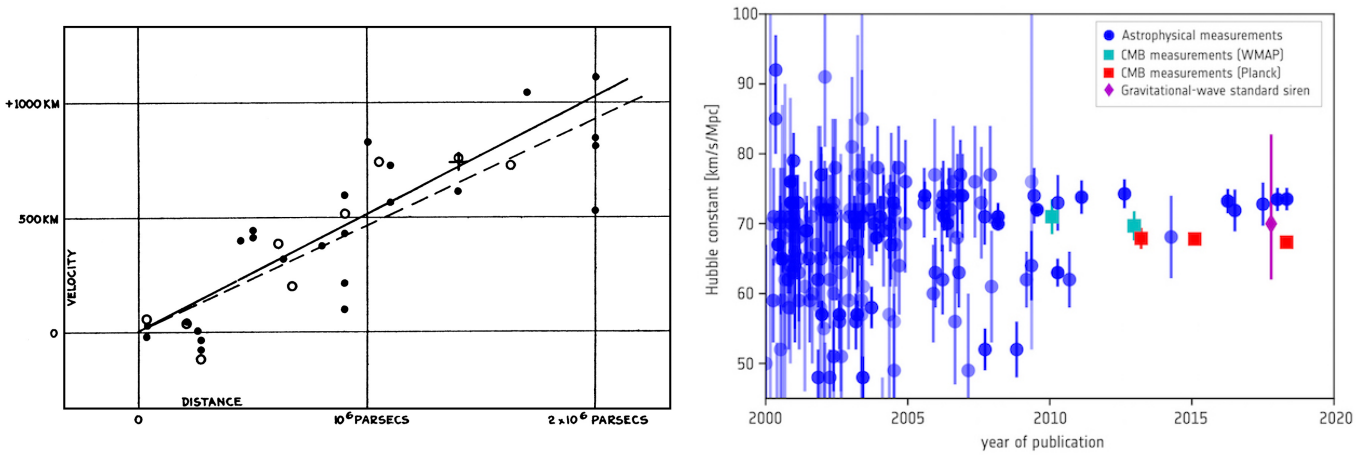

Figure 1.1: Left: Measurements of the recession velocities of extra-galactic nebulae by Hubble [1], as a function of their distance from us, with overlaid lines from an inferred linear relationship (now known as Hubble's Law). Right: Measurements of the Hubble constant H_0 from various works, as a function of publication year (image provided by the European Space Agency). These measurements rely on an assumption being made about the model of cosmology (in this case ΛCDM), as well as the cosmic distance ladder - a succession of techniques used to measure distance in the universe, with each rung of the ladder providing information for measuring a distance at the next rung up . We see the accuracy improvements of the more recent measurements, as well as the discrepancy in the value inferred from astrophysical and CMB probes.

The resulting energy momentum tensor is therefore

$$T_{\mu\nu} = \begin{pmatrix} \rho c^2 & 0 & 0 & 0 \\ 0 & p & 0 & 0 \\ 0 & 0 & p & 0 \\ 0 & 0 & 0 & p \end{pmatrix} , \tag{1.5}$$

where we see our simple model is devoid of any shear-viscous, bulk-viscous or heat-conductive properties, apparent by the lack of off-diagonal elements. In keeping with the requirements of our model that the universe must be homogeneous and isotropic, ρ and p can depend only on time, and combining the line element of Eq. (1.1) with the field equations (1.4) and our energy-momentum tensor (1.5), the cosmological field equations can be derived:

$$\frac{\ddot{R}}{R} = -\frac{4\pi G}{3}\left(\rho + \frac{3p}{c^2}\right) + \frac{\Lambda c^2}{3} , \tag{1.6}$$

$$\left(\frac{\dot{R}}{R}\right)^2 = \frac{8\pi G + \Lambda c^2}{3}\rho - \frac{c^2 k}{R^2} . \tag{1.7}$$

These two differential equations are known as the Friedmann-Lemaitre equations, and determine the time evolution of the scale factor $R(t)$. For cosmological calculations, it is often useful to derive a third equation, known as the cosmic fluid equation, which can be used to tell us how the energy

density ρ evolves with time:

$$\dot{\rho} + \left(\rho + \frac{p}{c^2}\right)3H = 0 \ . \tag{1.8}$$

This follows from the conservation of energy of the energy-momentum tensor, $\nabla_\mu T^{\mu\nu} = 0$, and has a solution

$$\rho \propto a^{-3(1+w)} \ , \tag{1.9}$$

where w is the equation of state parameter, defined as $w \equiv p/\rho c^2$. As our cosmological fluid consists of multiple components, we can write the density and pressure parameters as the sum of their constituents parts,

$$\rho = \sum_i \rho_i \qquad \text{and} \qquad p = \sum_i p_i \ , \tag{1.10}$$

and look for solutions to equation Eq. (1.8) on an individual basis. For the ΛCDM model, our cosmological fluid consists of matter ρ_m, radiation ρ_r, curvature ρ_k, and the vacuum energy ρ_Λ (neglecting any contribution from neutrinos which is thought to be very small). In this model, the equations of state are constant, and the density parameters evolve as

$$\rho_m(z) = \rho_{m,0}(1+z)^3 \ , \tag{1.11}$$

$$\rho_r(z) = \rho_{r,0}(1+z)^4 \ , \tag{1.12}$$

$$\rho_\Lambda(z) = \rho_{\Lambda,0} \ , \tag{1.13}$$

$$\rho_k(z) = \rho_{k,0}(1+z)^2 \ . \tag{1.14}$$

These solutions are often given in terms of the critical density, defined as the density of the universe in the case where there is zero overall curvature (see Fig. 1.2). We can derive an expression for this density by setting $k = 0$ in our second Friedmann-Lemaitre equation, giving

$$\rho_{\rm crit}(t) = \frac{3H^2(t)}{8\pi G} \ , \tag{1.15}$$

and following from this, define the density parameters of our individual constituents of the cosmological fluid as

$$\Omega_i(t) \equiv \frac{\rho_i(t)}{\rho_{\rm crit}(t)} \ . \tag{1.16}$$

By substituting Eq. (1.10) into our second cosmological field equation (1.7), and then rewriting the individual densities in terms of their density parameters of Eq. (1.16), we obtain

$$1 = \Omega_m + \Omega_r + \Omega_\Lambda - \frac{c^2 k}{H^2 R^2} \ , \tag{1.17}$$

where the last term on the right hand side is then defined as the curvature density parameter $\Omega_k \equiv -c^2k/H^2R^2$. This equation holds true at all times, and at late times of the universe, where

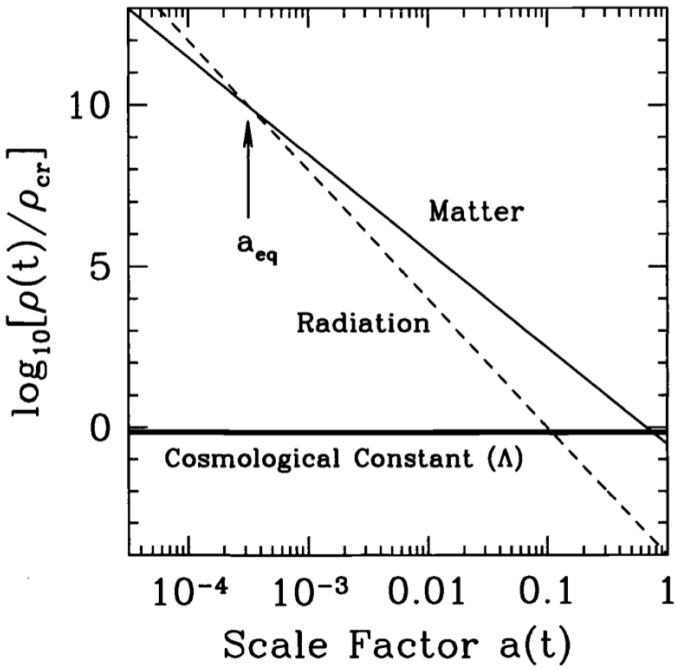

Figure 1.2: Plot showing the evolution of the density parameters, relative to the critical density, as a function of scale factor, in a flat universe. We see that the very early universe was dominated by radiation and matter. The point at which these two components are equal is labelled $a_{\rm eq}$. Plot from [8].

the contribution from radiation is small, we have the relationship

$$\Omega_m + \Omega_\Lambda \simeq 1 - \Omega_k \ . \tag{1.18}$$

Thus, we only need to measure the matter and vacuum energy density parameters to determine the curvature of the universe, with recent measurements of the CMB [17][12] showing this to be consistent with zero ($\Omega_k = -0.005^{+0.016}_{-0.017}$ from Planck combined probes).

1.1.2 Distance measures in cosmology

Being able to accurately measure distances in the universe is an essential part of cosmology. In an expanding universe, the traditional notion of a Cartesian separation between two points is often not the most useful measure of distance, as objects are constantly drifting away from each other. In addition to this, due to the finite travel speed of light, whenever an observer looks out into the universe, they are observing objects on their past lightcone, and so are also looking back in time. Consequently, there are several ways that we can measure distances, which we briefly review now.

The *redshift* relates the observed wavelength of light, $\lambda_{\rm o}$, to the emitted wavelength $\lambda_{\rm e}$ for a distant galaxy. It is defined as

$$1 + z \equiv \frac{\lambda_o}{\lambda_e} = \frac{\nu_e}{\nu_o} \ , \tag{1.19}$$

where ν is the frequency of light. As redshift is an observable quantity, it is of great importance for both theory and measurements. While the redshift will predominantly be dictated by the recession velocities of objects due to the expansion of the universe, there is also a small component due to radial peculiar motions of both the observer and the galaxy around their local neighbourhood. We can therefore define both observed $z_{\rm obs}$ and cosmological $z_{\rm cos}$ redshifts, with the latter defining the redshift purely from the expansion rate only (the *Hubble flow*). These are related to peculiar velocities along the line of sight as

$$v_{\rm pec} = c\frac{(z_{\rm obs} - z_{\rm cos})}{1 + z_{\rm cos}} \ . \tag{1.20}$$

For small radial velocities (or distances), the redshift can be approximated as

$$z \approx \frac{v}{c} = \frac{d}{D_{\rm H}} \ , \tag{1.21}$$

where d is the *proper distance*, which corresponds to the distance an object would be at a specific cosmological time, and $D_{\rm H}$ is the *Hubble distance*:

$$D_{\rm H} = \frac{c}{H_0} \ , \tag{1.22}$$

measuring the distance to an object based on the Hubble flow. The redshift can also easily be related to the scale factor $a(t)$ as

$$a(t) = \frac{1}{1 + z} \ . \tag{1.23}$$

The *comoving distance* χ, between two objects moving with the Hubble flow, remains constant in time, as this distance accounts for the expansion of the universe. It is related to the proper distance at cosmic time t_0 via $d = a(t_0)\chi$ and can be derived from the FLRW metric:

$$\chi = \int_{t_1}^{t_2} \frac{c\, dt'}{a(t')} \ . \tag{1.24}$$

In this sense, the comoving distance can be thought of as the distance travelled by a photon in an expanding universe, also known as geodesic distance. Subsequently, the time taken for a photon to travel this distance, the *conformal time* η, is simply

$$\eta = \frac{\chi}{c} = \int_{t_1}^{t_2} \frac{dt'}{a(t')} \ . \tag{1.25}$$

The comoving distance is thus a useful measure for calculating the clustering of matter (or large-scale structure) that is moving with the expansion of the universe.

The *angular diameter distance* is defined as the ratio of an object's physical transverse size to

its angular size. It is related to the comoving distance by

$$D_{\rm A} = a(t) S_k(\chi) \ , \tag{1.26}$$

where $S_k(\chi)$ is a quantity relating distances with the spatial curvature:

$$S_k(\chi) = \begin{cases} \frac{c}{H_0\sqrt{|\Omega_k|}} \sin(\chi H_0 \sqrt{|\Omega_k|}/c) & \text{if } \Omega_k < 0, \\ \chi & \text{if } \Omega_k = 0, \\ \frac{c}{H_0\sqrt{\Omega_k}} \sinh(\chi H_0 \sqrt{\Omega_k}/c) & \text{if } \Omega_k > 0. \end{cases} \tag{1.27}$$

It can be used to convert angular separations measured via a telescope to actual physical distances at source, and has the interesting property that it does not increase indefinitely as $z \to \infty$, but actually turns over at around $z \sim 1$, meaning that more distant objects actually start to appear larger in angular size.

The *luminosity distance*, $D_{\rm L}$ is a distance we can calculate for an object if its luminosity is known:

$$D_{\rm L} = \sqrt{\frac{L}{4\pi S}} \ , \tag{1.28}$$

where S is the flux received by the observing telescope. This unit of measurement is important when measuring the distance to standard candles such as Type Ia supernova and Cepheid variables, which can be used to probe the expansion rate of the universe. It can be related to the comoving and angular distances via

$$D_{\rm L} = (1+z)^2 D_{\rm A} = (1+z) S_k(\chi) \ . \tag{1.29}$$

One final quantity that is useful to define is the particle horizon $H_{\rm P}(t)$, also known as the cosmological horizon or comoving horizon. This is defined as the longest distance from which an observer at time t_2 can retrieve information from its past lightcone, and can be related to the comoving distance:

$$H_{\rm P}(t_2) = \lim_{t_1 \to 0} \chi = \int_0^{t_2} \frac{c\, dt'}{a(t')} \ . \tag{1.30}$$

The particle horizon is therefore the radius of the observable universe for a given observer, with anything lying outside this horizon unable to have causal contact with the observer.

1.1.3 The successes of and challenges facing the ΛCDM model

The ΛCDM model of cosmology rose to prominence in the latter half of the last century, primarily driven by two key issues: the growing evidence that the universe is expanding, and that observations of various phenomena suggested the presence of a large amount of cold dark matter. The model can

Parameter	Symbol	Value
Physical dark matter density	$\Omega_c h^2$	0.1198 ± 0.0012
Physical baryon density	$\Omega_b h^2$	0.02233 ± 0.00015
Hubble constant (in units [km/s/Mpc])	H_0	67.37 ± 0.54
Amplitude of fluctuations	$\ln(10^{10} A_s)$	3.043 ± 0.014
Scalar spectra index	n_s	0.9652 ± 0.0042
Photon optical depth	τ	0.0540 ± 0.0074

Table 1.1: The best fit parameters with 68% confidence levels on the six free parameters of the ΛCDM model, constrained using measurements of the CMB by Planck [13].

be described by six free parameters that can be constrained through observation, three of which we have covered in the previous section: the physical dark matter $\Omega_c h^2$ and baryon density $\Omega_b h^2$ parameters (with $\Omega_m = \Omega_c + \Omega_b$) and the Hubble constant H_0. Two of the remaining parameters relate to the energy density fluctuations in the early universe, with A_s dictating the amplitude of the fluctuations, and the scalar spectral index n_s describing how these fluctuations vary as a function of scale. The final parameter τ describes the optical depth of photons at the time of reionization - a major phase transition in the early universe, where the ignition of the first stars began to reionize the abundant neutral hydrogen. This reionized gas interacts with the CMB in several ways, with one of the dominant effects being a peak suppression in the CMB power spectra, caused by some of the photons being scattered by interaction with the gas and therefore suppressing anisotropies in the distribution that have already formed. We list current best fits to these parameters with their 68% confidence levels in Table 1.1, taken from measurements of the CMB by the Plank mission. We see the remarkable precision of this instrument enables constraints on the parameters to $\lesssim 1\%$ errors.

One of the strengths of the ΛCDM is its ability to accurately model real world observations with such a small number of parameters. A striking example of this comes from measurements of the temperature fluctuations in the CMB, visualised in the left hand plot of Fig. 1.3. While this temperature has been measured to be near uniform across the sky, to incredible accuracy ($T_0 = 2.72548 \pm 0.00057K$ [18]), small-scale fluctuations in the temperature field can be quantified by their angular power spectrum D_ℓ^{TT}, which measures the strength of fluctuation as a function of angular scale ℓ. The right hand side of Fig. 1.3 shows the measurements of this power spectrum from the Planck 2018 results [13], with the solid line showing the theoretical prediction of ΛCDM fitted to this data. Remarkably, measurements of the clustering of matter in the late-time universe closely match the theoretical models when using the fitted parameters of the early universe CMB measurements, showing that the ΛCDM model is able to account well for the evolution of the universe over large stretches of time. An example of this is the measurement of the amplitude of galaxy clustering and growth rate, given by the parameter $f\sigma_8$, shown in Fig. 1.4. We see that the measurements from various galaxy surveys (markers with error bars), over a range of redshifts, agree well the prediction of ΛCDM using best fit parameters from Planck measurements (solid line).

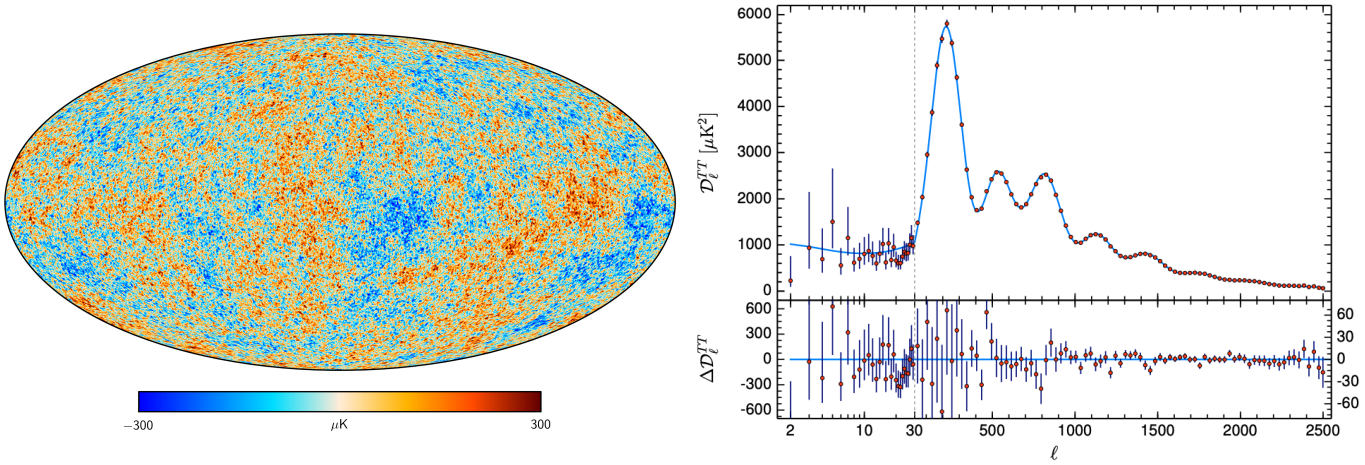

Figure 1.3: Left: The CMB temperature anisotropies as measured by Planck: while the CMB has a spectrum of a near perfect black body, subtle fluctuations exist at the sub mili-Kelvin scale, pointing to over and under dense regions of the universe. Right: The red markers with error bars show measurements of the angular temperature power spectrum of the CMB from the 2018 data release [13], with the blue line showing the best fitting ΛCDM model to the data. The lower section of this plot shows the residuals between the measurements and model.

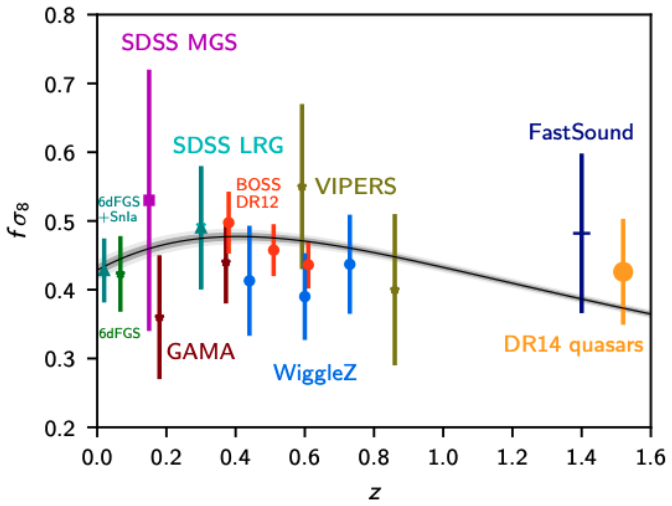

Figure 1.4: Constraints on the growth rate of fluctuations $f\sigma_8$ from various galaxy surveys (coloured markers with error bars) when compared with the prediction from ΛCDM using best fit parameters from Planck (black line with shaded grey regions showing the 68% and 95% CLs). Plot from [13].

There are however several challenges outstanding for the ΛCDM model. One of the most obvious being that, while including dark energy and matter into the model has helped explain various observed phenomena, it does not provide us with an intuition into what either of these dark components are. Dark matter has still yet to be directly detected, with searches ongoing at both particle [19, 20] and astronomical [21, 22] scales, while the measured value of the vacuum energy is hugely different from that predicted by theory (by up to 120 orders of magnitude [23]), known as the cosmological constant problem.

Further issues have arisen as observations have become more precise, in particular, the disparity of the value of H_0 inferred from measurements of the early-time and late-time universe, as can be seen by the difference in the blue and red markers in Fig. 1.1. This is a tension that has risen to the $\sim 4\sigma$ level, with CMB measurements giving $H_0 = 67.37 \pm 0.54$ [km/s/Mpc], while using Type-Ia supernova as standardisable candles to obtain distance measures gives $H_0 = 73.24 \pm 1.74$ [km/s/Mpc] [24]. Combining Planck data with Baryon Acoustic Oscillation (BAO) measurements from surveys like the extended Baryon Oscillation Spectroscopic Survey (eBOSS [25]) can help to alleviate the problem marginally, giving combined constraints of $H_0 = 69.6 \pm 1.8$ [km/s/Mpc] [26], however the tension still remains. While this could be down to some as yet unknown systematic in the measurements, such as how distances are calibrated in standard candle measurements, it may also indicate that extensions or modifications to the underlying model are required.

Several alternative theories have been put forward to try and resolve some of these issues, including those that make modifications to the base model by adding in or tweaking components, or those that are fundamentally different, by altering the underlying assumptions. One potential solution to the cosmological constant problem proposes that Λ could be cancelled out by some unknown physics, with the cosmic acceleration being driven by a new fifth force. Such models would have a dynamical dark energy equation of state, with a popular parameterisation, known as Chevallier-Polarski-Linder (CPL) [27, 28], given by $w(a) = w_0 + w_a(1 - a)$, where w_0 and w_a are constants. In this model, the equation of state gradually evolves from a value $w(a) = w_0 + w_a$ at early times to $w(a) = w_0$ today. However, the latest constraints from Planck [13], combined with supernova and BAO measurements, strongly constrain these additional parameters towards their default fixed ΛCDM values of $w_0 = -1$ and $w_a = 0$. One can also look to fundamental changes, such as basing a cosmological model on a theory of gravity other than GR. For example, generalising the Lagrangian of the Einstein-Hilbert action to be some function of the Ricci scalar leads to a family of models known as $f(R)$ gravity. In modifying how gravity behaves, these theories can generate an accelerated expansion of the universe, similar to that observed and generated by ΛCDM, without a cosmological constant or the need to introduce some unknown fifth force. The cost of this however, is a much more complicated model that needs to be fine tuned, and that spoils many of the successes of GR and the standard model (see e.g. [29] for a comprehensive review of modified gravity models).

Despite these issues, the future is bright for cosmology. There are several upcoming Stage IV

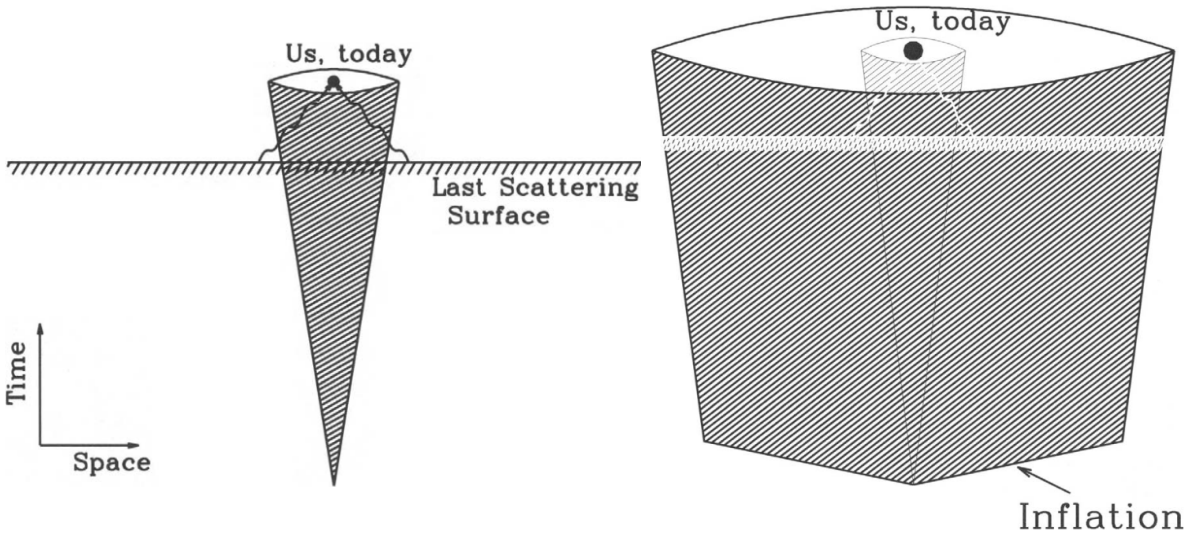

Figure 1.5: Diagram showing the Horizon problem. Left: The region inside the cone at any time is causally connected to us (at the centre). Photons emitted from the last scattering surface (at redshift ~ 1000) started outside of this region. Therefore, at the last scattering surface, they were not in causal contact with us and certainly not with each other. Yet their temperatures are almost identical. Right: By having a very rapid period of expansion in the early universe, Inflation poses a solution to the Horizon problem. In this much wider cone, all scales were causally in contact with each other, explaining how the CMB can have a near uniform temperature. Diagrams from [8].

experiments, such as CMB-S4[3], and the DESI[4], 4MOST[5], LSST[6] and EUCLID[7] galaxy surveys, which will probe the cosmos to greater precision and over larger volumes than have ever before been surveyed. In addition to this, the recent discovery of gravitational waves [30] provides a brand new window into the cosmos, granting additional ways to study the universe. Being able to reduce systematics and provide more accurate constrains on cosmological parameters will help to narrow down on the problem areas and eliminate any models that do not fit the new data, as well as give indications to where existing models may need to change.

1.2 Large-Scale Structure Cosmology

Initial fluctuations in the density field of matter in the early universe provided the seeds for the growth of structure that we see today. These fluctuations have primarily evolved under the force of gravity, and so measurements of how matter is distributed as a function of cosmological time can provide important information about our physical model of the universe.

In the following section, we provide a short review the underlying physics that govern the density field and growth of structure of the universe. We also detail some of the statistical tools

[3]https://cmb-s4.org/
[4]https://www.desi.lbl.gov/
[5]https://www.4most.eu/cms/
[6]https://www.lsst.org/about
[7]https://www.euclid-ec.org/

used to extract information from the density field, and briefly give an overview of cosmology redshift surveys, one of the primary ways to make observations of the large-scale structure in the late-time universe.

1.2.1 The seeds of structure from inflation

Precise measurements of the CMB have shown it to be near uniform and isotropic, to about 1 part in 10^5, with these tiny fluctuations evolving as the universe developed to form the late-time structure that we see today. These observations do pose some pressing questions however: firstly, where did these fluctuations come from? And how is it that distant parts of the universe at the time of last scattering appear to be in thermal equilibrium with each other, despite being outside each others causal horizons? A solution to both of these problems was proposed in the early 80s, as the theory of inflation [31, 32, 33]: the idea that at early times, the universe underwent a period of rapid exponential expansion (see Fig. 1.5). While the detailed particle physics explanation for this mechanism is still unknown, one of the most simple and well studied models of inflation is one in which we have a single scalar field $\phi(\eta)$ driving the expansion, with a slow evolution of the potential $V(\phi)$ of the field, dubbed slow-roll inflation.

To see how such inflation can turn small, primordial (quantum) fluctuations into those large enough to lead to structure formation, let us consider now a perturbation to our scalar field $\phi(t)$. This perturbation will necessarily have some spatial variation, such that

$$\phi(t) \to \phi(t) + \delta\phi(t, \mathbf{r}) \ . \tag{1.31}$$

Before proceeding, it is useful to re-define our perturbation by making a specific choice of gauge that will be physically meaningful. We require that our perturbations be gauge invariant[8], and for a single-field slow-roll inflation model, working in the spatially-flat gauge, we can define (in Fourier space)

$$\mathcal{R}_k = \frac{H\delta\phi_k}{\dot{\phi}} \ , \tag{1.32}$$

where $\mathcal{R}$ is known as the comoving curvature perturbation. Geometrically, this perturbation measures the spatial curvature of comoving hyper-surfaces, and importantly has the property that it remains constant outside the horizon. To demonstrate the advantage of this quality, let us consider a perturbation of scale $1/k$ that starts off at a sub-horizon scale ($1/k < 1/aH$). During inflation, the comoving horizon undergoes a period of shrinking (due to the relative rapid expansion of space), while the fluctuation scale remains constant. This shrinking causes the perturbations to leave the horizon as $1/k > 1/aH$, effectively becoming frozen out. Intuitively we can understand this as the perturbation being no longer able to feel its own self gravity, since it is larger than the characteristic scale over which physical processes in the universe operate. The perturbation will

[8] Our perturbations must be defined in such a way that they cannot be made to disappear by some translation of coordinates.

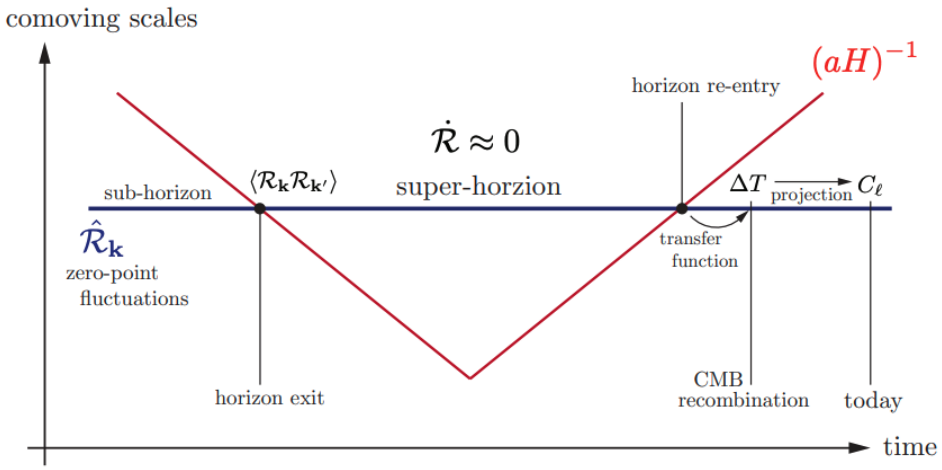

Figure 1.6: Diagram showing the creation and evolution of fluctuations from inflation. Perturbations are initially created at sub-horizon scales in the very early universe at the quantum mechanical level. As the horizon size shrinks during inflation, these fluctuations leave the horizon, becoming frozen out and remain constant. Upon horizon re-entry, the universe is now exponentially larger than it was when the fluctuations left. Plot from [34]

then remain at this fixed value until after inflation, when the horizon expands again during the Big Bang, and becomes greater than $1/k$ (see Fig. 1.6). Upon horizon re-entry, the perturbation is then free to evolve again and interact with the various constituents of the universe. The key point is that inflation enables the generation of super-horizon fluctuations in the very early universe that then go on to provide the seeds for the anisotropies we observe in the CMB today, and thus the structure of the late-time universe.

Before moving on, it is also worth quantifying the power spectrum $\mathcal{P}_{\mathcal{R}}(k)$[9] of the primordial curvature perturbations, as this will be useful in the next section. Qualitatively, this tells us the contribution to the total variance of the perturbation field per unit logarithmic interval, and is given by

$$\langle \mathcal{R}(\mathbf{r},t)\mathcal{R}^*(\mathbf{r},t)\rangle = \int_0^\infty d(\ln k)\mathcal{P}_{\mathcal{R}}(k,t) \ . \tag{1.33}$$

Taking the Fourier transform of the field to be

$$\mathcal{R}(\mathbf{r},t) = \int \frac{\mathrm{d}^3\mathbf{k}}{(2\pi)^3}\mathcal{R}(\mathbf{k},t)e^{-i\mathbf{k}\cdot\mathbf{r}} \ , \tag{1.34}$$

and remembering that for statistical isotropy and homogeneity to hold, we require that the power spectrum must depend on k and not $\mathbf{k}$, and $\langle \mathcal{R}(\mathbf{k},t)\mathcal{R}^*(\mathbf{k},t)\rangle \propto \delta^D(\mathbf{k}-\mathbf{k}')$ so that the $\mathbf{r}$ dependence

[9]There are two quantities that are often both called the power spectrum in the literature. We will denote them $\mathcal{P}(k)$ and $P(k)$, and they are related via $\mathcal{P}(k) = k^3P(k)/(2\pi^2)$. As $P(k)$ has units of volume, $\mathcal{P}(k)$ can be referred to as the dimensionless power spectrum.

cancels, we obtain:

$$\langle \mathcal{R}(\mathbf{k},t)\mathcal{R}^*(\mathbf{k}',t)\rangle = \frac{2\pi^2}{k^3} P_{\mathcal{R}}(k)\delta^D(\mathbf{k}-\mathbf{k}') \ . \tag{1.35}$$

By substituting in Eq. (1.32) and evaluating at the time when the curvature perturbations leave the horizon, it can be shown that (using slow-roll conditions) the frozen-out power spectrum is given by

$$\mathcal{P}_{\mathcal{R}}(k) = \Big(\frac{H^2}{2\pi\dot{\phi}}\Big)^2_{k=aH} \ . \tag{1.36}$$

In this slow-roll scenario, H is only slowly decreasing, while $\dot{\phi}$ is approximately constant and the scale factor is exponentially increasing. As modes with a higher k will leave the horizon at slightly later times, where H is lower, we thus see that inflation predicts a power spectrum that is slightly declining as a function of k (but almost scale invariant), something that can be tested with observations. Importantly, we can use this power spectrum to directly link to the power spectrum of the observed post-inflation structure that we see in the CMB and LSS, which we will discuss in the next section. The spectrum is often parameterised as

$$\mathcal{P}_{\mathcal{R}}(k) = A_s\Big(\frac{k}{k_s}\Big)^{n_s-1} \ , \tag{1.37}$$

where A_s is an amplitude factor, n_s is the scalar spectral index and k_s is some chosen observational scale of interest. As we covered in the previous section, A_s and n_s have both been constrained by Planck (see Table 1.1), which indeed confirmed n_s to be very close to 1, corresponding to a scale invariant spectrum.

One of the useful properties of the power spectrum is that, for Gaussian fluctuations, the power spectrum provides a complete statistical description of the field. Any amount of primordial non-Gaussianty will be encoded in the higher order correlations of the field, such as the bispectrum, $\langle \mathcal{R}_{k_1}\mathcal{R}_{k_2}\mathcal{R}_{k_3}\rangle$. In this case, single field slow-roll inflation predicts that such non-Gaussianity will be small [35]. This is often parameterised by the quantity $f_{\rm NL}$, with current constraints placing it consistent with zero but with large error bars (the most stringent constraints currently come from the CMB: $f_{\rm NL}^{\rm local} = -0.9 \pm 5.1$ [36]).

1.2.2 The growth of matter perturbations

Having covered how inflation can enlarge small-scale quantum fluctuations in the early universe to large scales at later times, acting as seeds for structure growth, we now turn our attention to the evolution of the matter field. The dynamics of this will primarily be dictated by the gravitational potential, which evolves in conjunction with the other species that constitute the universe (radiation, dark and ordinary matter). After inflation ends, the universe enters a period known as reheating, where the inflaton field decays into a hot thermal plasma of particles and thus popu-

lates the universe with the Standard Model particles that we observe today. Once this hot plasma becomes thermalised, the universe enters the radiation-dominated era, and any modes inside the horizon during this time will have their dynamics influenced by radiation pressure as well as gravity, resulting in a suppression of structure growth. These effects can be encoded in what is called the transfer function $T(k)$, which links the power spectrum of primordial fluctuations to that of which we see in the structure of the universe today:

$$P(k,z) = T^2(k)\mathcal{P}_{\mathcal{R}}(k)D^2(z) \ , \tag{1.38}$$

where $P(k,z)$ is the power spectrum of our matter fluctuations and $D(z)$ is the normalised linear growth rate which we will cover shortly. As the universe expands and cools, radiation will become subdominant, as its energy density scales inversely to the scale factor more rapidly than the matter component. At this stage the universe enters the matter-dominated era, whereby the background radiation pressure drops off, and the force of gravity can now start to generate more significant growth of structure. Under the simplifying assumption that there is no significant growth of perturbations between the time of horizon entry and matter domination, the transfer function can be very roughly approximated as

$$T \approx \begin{cases} 1 & \text{if } k \ll k_{\rm eq}, \\ (k_{\rm eq}/k)^2 & \text{if } k \gg k_{\rm eq}, \end{cases} \tag{1.39}$$

where $k_{\rm eq}$ is the turnover scale, corresponding to the horizon size at the time of matter-radiation equality. While this simplification allows for an easy and intuitive understanding of the shape of the power spectrum at these times, it is not accurate for most applications, and a more rigorous form can be found numerically from Boltzmann solvers such as CAMB [37] or CLASS [38]. Note that the transfer function now has no time dependence, as this is instead contained in what is known as the growth function, $D(z)$. This is an important term for large scale structure cosmology, as it dictates the rate at which structures grow under gravitational instability. To determine this quantity, we can model the matter content of the Universe as a continuous fluid, and look for perturbed solutions to the fluid equations. While the matter distribution is in reality discrete, this continuous approximation works perfectly well at the Megaparsec scales that the large scale structure of the Universe is modelled at[10]. Neglecting the effects of any Baryon pressure, which is negligible for non-relativistic species when compared to their energy density, we consider perturbations to the background total matter density and gravitational fields:

$$\rho(\mathbf{r},t) = \rho_0(t) + \delta\rho(\mathbf{r},t) \ , \tag{1.40}$$

$$\Phi(\mathbf{r},t) = \Phi_0(t) + \delta\Phi(\mathbf{r},t) \ . \tag{1.41}$$

[10]This approximation works well at early times but starts to break down later when compact objects start to form.

as well as taking into consideration any peculiar velocities of the matter, $\boldsymbol{v}(\boldsymbol{r}, t)$. It can be shown (see for example [39]) that the linearized fluid equations for these perturbations during matter domination, in comoving coordinates, are given by

$$\dot{\delta} + \frac{1}{a}\nabla \cdot \boldsymbol{v} = 0 \ , \tag{1.42}$$

$$\dot{\boldsymbol{v}} + H\boldsymbol{v} = -\frac{1}{a}\nabla\delta\Phi \ , \tag{1.43}$$

$$\nabla^2\delta\Phi = 4\pi G a^2 \rho_0 \delta \ , \tag{1.44}$$

where a dot denotes a derivative with respect to time t and we have defined the density contrast $\delta \equiv \delta\rho/\rho_0$. These expressions form a set of coupled differential equations for the velocity, density and gravitational fields. By taking the divergence of the Euler equation (1.43):

$$\frac{\partial}{\partial t}(\nabla \cdot \boldsymbol{v}) + H(\nabla \cdot \boldsymbol{v}) = -\frac{1}{a}\nabla^2\delta\Phi \ , \tag{1.45}$$

and combining with the continuity equation (1.42) for the relation between the velocity divergence and δ, and the Poisson equation (1.44) for relating the potential $\delta\Phi$ and δ, we thus obtain a second order differential equation for the density perturbation:

$$\ddot{\delta} + 2H\dot{\delta} = 4\pi G\rho_0\delta \ . \tag{1.46}$$

For a flat, matter-dominated universe we can use Eq. (1.15) and Eq. (1.17) to relate ρ_0 to the Hubble constant and matter density parameter, giving

$$\ddot{\delta} + 2H\dot{\delta} = \frac{3}{2}H_0^2\Omega_{m,0}\frac{1}{a^3}\delta \ . \tag{1.47}$$

One important consequence of this equation is that, if we look at the Fourier modes $\delta(\mathbf{k}, t)$, we see that all scales will grow at the same rate. Thus, we can look for linear solutions of the form

$$\delta(\mathbf{x}, t) = D^+(t)\delta(\mathbf{x}) + D^-(t)\delta(\mathbf{x}) \ , \tag{1.48}$$

where we have growing (D^+) and decaying (D^-) modes. The decaying modes will disappear, and so it is the growing modes that are important for structure formation. We can therefore write, in Fourier space,

$$\delta(\mathbf{k}, t) = D^+(t)\delta(\mathbf{k}) \ , \tag{1.49}$$

and see that our linear matter power spectrum will simply scale in time as the square of the growth factor. The precise form of the growth factor will depend on the cosmological model, specifically the matter and dark energy density parameters, and thus by measuring the power spectrum amplitude of the matter fluctuations in the CMB or the late-time structure of the universe, we are able to

constrain our cosmological parameters.

As the density perturbations $\delta(\mathbf{k}, t)$ grow over time, there will come a point where our previous linear perturbation theory treatment of the dynamics of the matter field no longer holds. At this point, we enter the regime where our fluctuations become non-linear, and need to consider higher order terms in Eqs. 1.42-1.44. Importantly, while in the linear regime, we have that all scales evolve at the same rate but remain independent of one another, however including non-linear terms in the equations of motion introduces an the effect of coupling between different Fourier modes. The impact that including these higher order terms has on the power spectrum is that it introduces corrections (see eg. [40] for a comprehensive review):

$$P(k,t) = P^{(0)}(k,t) + P^{(1)}(k,t) + \dots \ , \tag{1.50}$$

where the superscript (n) denotes the *n-loop*[11] contribution to the power spectrum, with the tree-level term (0) just being the linear spectrum[12]:

$$P^{(0)}(k,t) = D^2(t) P_L(k) \ . \tag{1.51}$$

The one-loop correction consists of two terms:

$$P^{(1)}(k,t) = P_{22}(k,t) + P_{13}(k,t) \ , \tag{1.52}$$

which in turn can be obtained by convolutions of the linear power spectrum with perturbation theory (PT) kernels, and are defined as

$$P_{22}(k,t) \equiv 2 \int \mathrm{d}^3\mathbf{q} [F_2(\mathbf{k}-\mathbf{q}, \mathbf{q})]^2 P_L(|\mathbf{k}-\mathbf{q}|, t) P_L(q,t) \ , \tag{1.53}$$

$$P_{13}(k,t) \equiv 6 P_L(k,t) \int \mathrm{d}^3\mathbf{q} F_3(\mathbf{k}, \mathbf{q}, -\mathbf{q}) P_L(q,t) \ . \tag{1.54}$$

We see that the 22 term represents mode-coupling between waves with wave-vectors $\mathbf{k}-\mathbf{q}$ and $\mathbf{q}$, whereas the 13 term can be interpreted as the first order correction to the standard linear growth. It is important to note that these equations are obtained by working in an Einstein-de Sitter cosmology, where we have $\Omega_m = 1$ and $\Omega_\Lambda = 0$ and the solutions to the equations of motion using the perturbative expansion of the density field Eq. (1.40) are relatively simple, because they are separable in k and t to all orders of expansion. For arbitrary cosmology, this in general is not the case [41], however it has been demonstrated [42, 43] that separability can be recovered in the case where[13] $f = \Omega_m^{1/2}$, which in practice is a good approximation for ΛCDM where $f(a) \approx \Omega_m^{0.55}(a)$ [44].

[11] Named after their diagrammatic representation.

[12] Note that for the rest of this work we will make the definition $D^+(t) = D(t)$ for simplicity.

[13] Here, f is the linear growth rate, defined as $f \equiv \mathrm{d}\ln(D(a))/\mathrm{d}\ln(a)$.

1.2.3 Two-point statistics as large-scale structure probes

We now turn our attention to the late-time universe, and look at statistical methods that can be used to extract cosmological information from the clustering of matter. As we covered in the previous sections, the matter fluctuation field directly ties to cosmological parameters, and so this is an important quantity for any measurement. We recall from the previous section that matter fluctuations are defined as

$$\delta(\mathbf{r},t) = \frac{\rho(\mathbf{r},t) - \bar{\rho}(t)}{\bar{\rho}(t)} \ , \tag{1.55}$$

where $\rho(\mathbf{r},t)$ is the density at a given position $\mathbf{r}$ and time t, and $\bar{\rho}(t)$ is the average background density. For statistical homogeneity to hold, we require that $\langle\rho(\mathbf{r},t)\rangle = \bar{\rho}(t)$, resulting in the ensemble average[14] of our field $\langle\delta(\mathbf{r},t)\rangle = 0$, and thus we cannot extract any interesting statistics from the first-order moment of the fluctuation field. We therefore turn our attention to correlators of pairs of the density field, and in real space this is known as the auto-correlation or two-point correlation function:

$$\xi(\mathbf{r}_1,\mathbf{r}_2) \equiv \langle\delta(\mathbf{r}_1)\delta(\mathbf{r}_2)\rangle = \int \delta(\mathbf{r}_1)\delta(\mathbf{r}_2)\mathcal{P}\big[\delta(\mathbf{r}_1),\delta(\mathbf{r}_2)\big]\mathrm{d}\delta(\mathbf{r}_1)\mathrm{d}\delta(\mathbf{r}_2) \ , \tag{1.56}$$

where $\mathcal{P}$ signifies the probability distribution of the field and for now we drop the time dependence and will return to this later. This quantity is positive if the density perturbation has the same sign at both $\mathbf{r}_1$ and $\mathbf{r}_2$, and negative if we have an over-density at one location and an under-density at the other. Thus, it probes how density perturbations at different locations are correlated to each other. Due to statistical homogeneity, this expression can only depend on the difference $\mathbf{r} \equiv \mathbf{r}_2 - \mathbf{r}_1$, and from isotropy we require that there should be no preferred direction: $r = |\mathbf{r}|$, and so we can write

$$\xi(r) \equiv \langle\delta(\mathbf{r}_1)\delta(\mathbf{r}_1+\mathbf{r})\rangle \ . \tag{1.57}$$

So far we have been discussing perturbations in the underlying matter field, however at late times what we actually measure with surveys is the positions and thus correlations of galaxies. Whereas the matter field is essentially continuous, galaxies form a discretised representation of this field. If we break up our volume of space V into δV_i small volumes (or cells), with the cells small enough that they only ever contain a maximum of one galaxy, we can write that the probability of finding a galaxy in such a cell as

$$\begin{aligned} \delta\mathcal{P}_i &= N_g\frac{\delta V_i}{V} \ , \\ &= \bar{n}_g\delta V_i \ , \end{aligned} \tag{1.58}$$

[14] See Appendix 1.A for a brief discussion on ensemble and volume averages.

with N_g the total number of galaxies over the full volume and the mean number density is $\bar{n}_g = \langle n_g(\mathbf{r})\rangle$. The probability will be proportional to the size of the volume element: doubling the volume will double the chance of finding an object within it. The mean number of objects found with a finite volume V can be found by integrating Eq. (1.58):

$$\langle N\rangle = \bar{n}_g V \ . \tag{1.59}$$

The two-point correlation function for this discrete galaxy scenario is defined by the joint probability of finding an object in both of the volume elements δV_1 and δV_2 at a separation $\mathbf{r}_{12}$:

$$\delta\mathcal{P}_{12} = \bar{n}_g^2 \delta V_1 \delta V_2 [1 + \xi_{gg}(\mathbf{r}_{12})] \ . \tag{1.60}$$

We see that the correlation function will be dimensionless, and in keeping with homogeneity and isotropy, it only depends on the separation between the points. For a uniform random Poisson process, where the probabilities of finding objects in cells δV_1 and δV_2 are independent, the joint probability is just the product of individual probabilities of Eq. (1.58):

$$\delta\mathcal{P}_{12} = \bar{n}_g^2 \delta V_1 \delta V_2 \ , \tag{1.61}$$

i.e. in this case we have $\xi_{gg} = 0$. As before, if the two positions are correlated we will have $\xi_{gg} > 0$ and if they are anti-correlated we have $-1 \leq \xi_{gg} < 0$. We immediately see from Eqs. (1.60) and (1.61) that the correlation function describes the excess in probability, relative to a Poisson, of finding two galaxies separated by a distance $\mathbf{r}_{12}$. Therefore, if we chose a galaxy at random from the ensemble, then the probability of finding a neighbour in a volume δV at some distance $\mathbf{r}$ is given by

$$\delta\mathcal{P} = \bar{n}_g \delta V [1 + \xi_{gg}(\mathbf{r})] \ . \tag{1.62}$$

To see how our discrete correlation function relates back to the continuous case of Eq. (1.57), we have from Eq. (1.58) that the probability of finding two points in volumes δV_1 and δV_2 can be written as

$$\delta\mathcal{P}_{12} = \langle N_1 N_2\rangle \equiv \langle n_g(\mathbf{r}_1) n_g(\mathbf{r}_2)\rangle \delta V_1 \delta V_2 \ . \tag{1.63}$$

Then, defining the galaxy overdensity field $\delta_g(\mathbf{r})$ as:

$$n_g(\mathbf{r}) = \bar{n}_g [1 + \delta_g(\mathbf{r})] \ , \tag{1.64}$$

and substituting this in gives

$$\begin{aligned} \delta\mathcal{P}_{12} &= \bar{n}_g^2 \delta V_1 \delta V_2 \langle [1 + \delta_g(\mathbf{r}_1)][1 + \delta_g(\mathbf{r}_2)]\rangle \ , \\ &= \bar{n}_g^2 \delta V_1 \delta V_2 [1 + \langle \delta_g(\mathbf{r}_1)\delta_g(\mathbf{r}_2)\rangle] \ , \end{aligned} \tag{1.65}$$

where we then readily see by comparing this with Eq. (1.60) that $\xi_{gg}(\mathbf{r}_{12}) = \langle \delta_g(\mathbf{r}_1)\delta_g(\mathbf{r}_2)\rangle$, analogously to the matter field.

Another useful statistical quantity to cover is the power spectrum, $P(k)$, which describes the clustering in Fourier space. We briefly covered this already in the previous sections, where we showed that inflationary theories make direct predictions of what we expect the power spectrum to be, a useful fact if we want to be able to compare our late-time measurements back to theory. The power spectrum is defined analogously to the auto-correlation function:

$$\langle \delta_g(\mathbf{k}_1)\delta_g(\mathbf{k}_2)\rangle = (2\pi)^3 P_{gg}(k)\delta^D(\mathbf{k}_1 + \mathbf{k}_2) \ . \tag{1.66}$$

We can show how this relates back to ξ_{gg}, by first taking the Fourier transform of our galaxy fluctuation field, which we define with the convention

$$\delta_g(\mathbf{k}) = \int \mathrm{d}^3\mathbf{r}\ \delta_g(\mathbf{r})e^{i\mathbf{k}\cdot\mathbf{r}} \ . \tag{1.67}$$

Looking at the ensemble of a product of fields as before, we find have

$$\langle \delta_g(\mathbf{k}_1)\delta_g(\mathbf{k}_2)\rangle = \int \mathrm{d}^3\mathbf{r}_1\mathrm{d}^3\mathbf{r}_2\ \langle \delta_g(\mathbf{r}_1)\delta_g(\mathbf{r}_2)\rangle e^{i\mathbf{k}_1\cdot\mathbf{r}_1}e^{i\mathbf{k}_2\cdot\mathbf{r}_2} \ . \tag{1.68}$$

Performing a coordinate shift of $-\mathbf{r}_1$ both density perturbations on the right hand side of this equation (which we are free to do due to homogeneity) we obtain

$$\langle \delta_g(\mathbf{k}_1)\delta_g(\mathbf{k}_2)\rangle = \int \mathrm{d}^3\mathbf{r}_1\mathrm{d}^3\mathbf{r}_2\ \langle \delta_g(0)\delta_g(\mathbf{r}_2 - \mathbf{r}_1)\rangle e^{i\mathbf{k}_1\cdot\mathbf{r}_1}e^{i\mathbf{k}_2\cdot\mathbf{r}_2} \ . \tag{1.69}$$

By defining $\mathbf{r}_{21} = \mathbf{r}_2 - \mathbf{r}_1$, we see that the correlator on the right hand side of the equation is simply the auto-correlation function defined in Eq. (1.57). Substituting this in gives

$$\begin{aligned}
\langle \delta_g(\mathbf{k}_1)\delta_g(\mathbf{k}_2)\rangle &= \int \mathrm{d}^3\mathbf{r}_1\mathrm{d}^3\mathbf{r}_{21}\ \xi(\mathbf{r}_{21})e^{i\mathbf{k}_1\cdot\mathbf{r}_1}e^{i\mathbf{k}_2\cdot(\mathbf{r}_{21}+\mathbf{r}_1)} \ , \\
&= \int \mathrm{d}^3\mathbf{r}_1 e^{i\mathbf{r}_1\cdot(\mathbf{k}_1+\mathbf{k}_2)} \int \mathrm{d}^3\mathbf{r}_{21}\ \xi(\mathbf{r}_{21})e^{i\mathbf{k}_2\cdot\mathbf{r}_{21}} \ , \\
&= (2\pi)^3\delta^D(\mathbf{k}_1 + \mathbf{k}_2) \int \mathrm{d}^3\mathbf{r}_{21}\ \xi(\mathbf{r}_{21})e^{i\mathbf{k}_2\cdot\mathbf{r}_{21}} \ ,
\end{aligned} \tag{1.70}$$

and then by matching to Eq. (1.66) we see that we arrive at another definition of the power spectrum:

$$P_{gg}(k) \equiv \int \mathrm{d}^3\mathbf{r}\ \xi_{gg}(\mathbf{r})e^{i\mathbf{k}\cdot\mathbf{r}} \ . \tag{1.71}$$

Thus, the power spectrum and auto-correlation function form a Fourier transform pair. One of the useful properties of the power spectrum is that it is necessarily positive everywhere, unlike the auto-correlation function, which can make for easy determination of unphysical results when taking measurements. In addition to this, if the underlying fluctuation field is Gaussian in nature, which

we saw from inflationary theory in the previous section is a good approximation on large scales, then all individual k modes are independent of each other, and the covariance matrix is diagonal which makes for faster calculations.

There are a few details which we have neglected so far in our calculations that can complicate matters slightly, which we will cover in more detail in Chapters 2 & 3, but will give a brief description of here. The first of these is that galaxies are what we refer to as *biased* tracers of the underlying matter field. The relationship is not one-to-one, but at linear scales is provided by a scale independent parameter b_1:

$$\delta_g = b_1 \delta \ . \tag{1.72}$$

This means that, when taking measurements of the galaxy power spectrum, we are not only measuring the amplitudes of the fluctuations at a given scale, but a combination of this with the bias parameter such that at linear order we have

$$\begin{aligned} P_{gg}(k,t) &= b_1^2(t) P(k,t) \ , \\ &= b_1^2(t) D^2(t) P(k,t_0) \ . \end{aligned} \tag{1.73}$$

We therefore require some detailed understanding of this bias parameter if we want to determine the more meaningful cosmological information contained in the growth factor $D(t)$. In addition to this, not only will this bias be different for different tracers, but it will also depend on time. At earlier times in the universe, the first galaxies to form were those that traced out the largest peaks in the underlying density field, as these were the areas with the highest gravitational potential, and therefore the bias is higher at these times than today. In the absence of any complete description of the complicated process of galaxy formation and evolution, to dictate what these bias functions should look like, the values of these bias parameters must be determined empirically through taking different statistical measures of the density field to break the degeneracy with the growth factor.

A second complication arises from the fact that, while galaxies have some recession velocity from us due to the expansion of the universe, they will also have some peculiar velocity generated by the large-scale gravitational field of their local surroundings. For any galaxies that have a non-zero component of their peculiar velocity in the radial direction to us as the observers, any distance measure we infer via redshift will be distorted. This effect is called *redshift-space distortions* (RSD) [45], and has two different effects depending on the scales considered, which we explain with the diagram in Fig. 1.7. These distortions will induce a line of sight dependence to the power spectrum, where again at linear order and working in the plane-parallel approximation, the redshift-space power spectrum is related to the real-space power spectrum via

$$P_{gg}^S(k,\mu) = P_{gg}^R(k)[1+\beta\mu^2]^2 \ . \tag{1.74}$$

Here, the superscripts S and R denote redshift-space and real-space, respectively, and the quantity

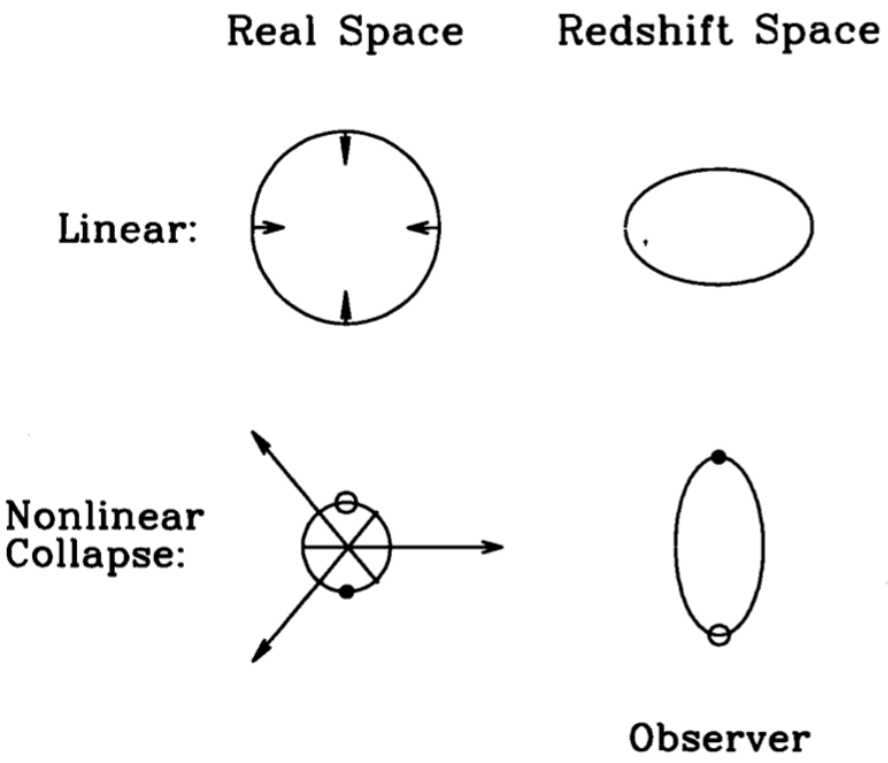

Figure 1.7: Diagram showing the effect of redshift-space distortions. The left hand side of the figure shows the real-space distribution of matter (represented by the circular shapes) falling into a central gravitational well, with the top row representing larger scales and the bottom row representing smaller scales. The right hand side shows the distribution of matter in redshift-space, as would be seen by an observer at the bottom of the diagram. On linear scales, the coherent in-fall of matter causes an apparent flattening of the distribution, known as the *Kaiser* effect, which boosts the clustering signal at these scales. At non-linear scales, the matter is deeper into the potential and has a higher velocity, appearing on the opposite side of the potential compared to its actual location. This is known as the *Fingers-of-God* effect (FoG), and causes a reduction in clustering signal at these scales. Figure from [8].

μ is the cosine of the angle to the line of sight. The parameter β describes the relationship between the galaxy bias and the linear growth rate f, defined as

$$\beta \equiv \frac{f}{b} \,, \tag{1.75}$$

RSD further complicate measurements of the power spectrum, however, as they are caused by the galaxy velocity field that is sourced by the gravitational potential of the local environment, they can be used to probe the matter-density parameter.

Finally, in our definitions so far in this section, we have chosen to neglect the time dependence of our correlation function and power spectrum, assuming that we are correlating density fields existing at the same cosmological time, known as the fixed-time regime. This however is only an approximation, as in reality we observe galaxies on our past lightcone, and so correlating any two points not at the same radial distance from the observer will be existing at different redshifts and

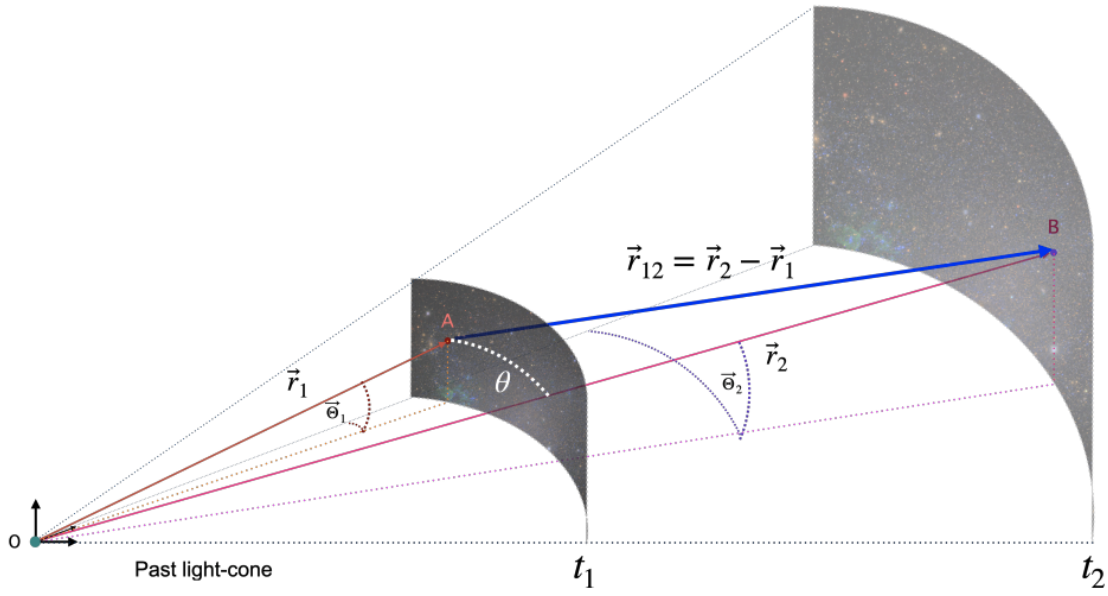

Figure 1.8: As we observe galaxies on our past lightcone, galaxies at different radial distances from us will exist at different cosmological times. If the difference in radial distance between the two galaxies $\mathbf{r}_{12}$ is small, then approximating them to be at equal times will only incur a small error in calculations (see Chapter 2). However as this distance grows lager, a full treatment of the unequal time correlator is required so as to not significantly bias any results. Diagram from [46].

therefore different cosmological times (see Fig. 1.8). While the fixed-time prescription has served as a good approximation for previous surveys that have either been shallow in depth, or have looked to break up measurement regions into thin redshift slices, for upcoming deep-redshift surveys, a proper model involving the unequal time correlator will be necessary to avoid biasing clustering statistics. In this instance, we will be interested in correlators of the form

$$\langle \delta_g(k_1, t_1)\delta_g(k_2, t_2)\rangle = (2\pi)^3 P_{gg}(k_1, t_1, t_2)\delta^D(\mathbf{k}_1 + \mathbf{k}_2) \ , \tag{1.76}$$

where $P(k_1, t_1, t_2)$ is known as the unequal time power spectrum [47]. This is one of the primary focuses of this piece of work, which we will cover in more detail in the following chapters.

1.2.4 Cosmology redshift surveys

Three-dimensional galaxy redshift surveys, which measure the redshift distance to a galaxy, and pair this with angular positional data, form a vital tool for understanding the distribution of matter in the universe. By using statistical tools like the two-point correlation function, and its Fourier counterpart the power spectrum, cosmologists can use survey data to extract information about the type of universe we live in. While the angular positions of galaxies are relatively easy to record, the redshift information is more difficult to measure due to the need for powerful telescopes and a longer observation time per target. In addition, redshifts obtained need to be accurate for robust 3D analysis, as any positional error will translate into uncertainties in the statistical

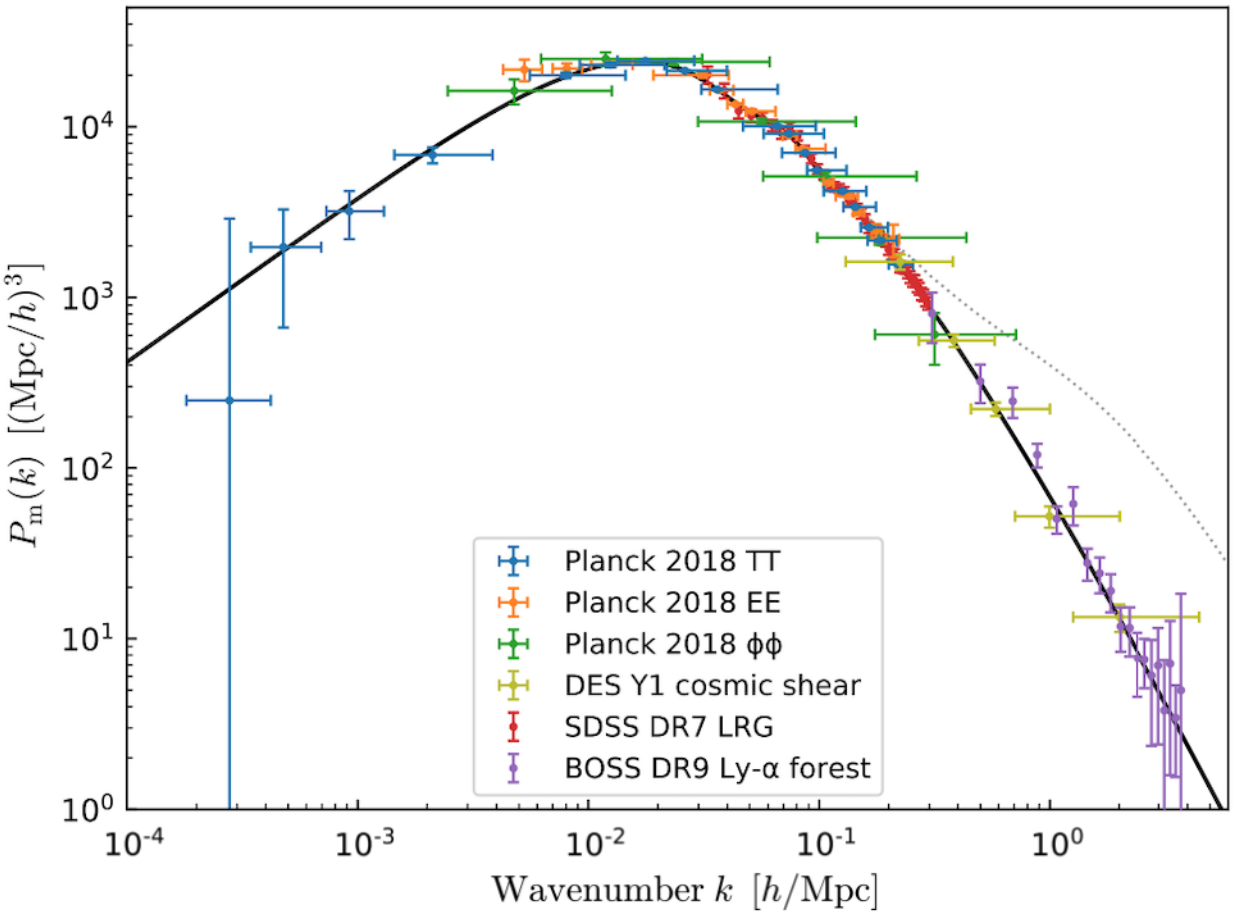

Figure 1.9: Plot of the inferred linear matter power spectrum from various probes of the large scale structure and CMB, across a variety of redshift ranges, but normalised to today. Solid line shows the theoretical linear matter power spectrum, with the dotted line indicating the non-linear spectrum, based on best-fit Planck 2018 data [13]. Figure from [48], where they describe the corrections performed to account for non-linear clustering and time evolution.

probes. Remembering that the redshift of a target is related to the wavelength of light observed, redshifts can be determined by recording where spectral features of distant galaxies appear as a function of wavelength, and see how much these features have shifted when compared with baseline values. Galaxy surveys fall into two different categories for recording redshifts: photometric and spectroscopic. While spectroscopic instruments record the full spectrum of light by passing it through a dispersive element before it reaches the detector, and recording the intensity as a function of wavelength, photometric instruments pass the light through specific colour filters, focusing on a band of wavelengths at a time. Each method has its advantages and disadvantages: spectroscopic methods will generally have a greater discriminating power of spectral features due to seeing the full spectrum, but the light is more spread out over the detector and thus it takes longer to achieve the desired signal-to-noise. Conversely, by focusing on specific wavelengths at a time, photometric instruments can reach this signal-to-noise faster, or see more distant targets, at the expense of diminished ability to identify spectral features.

The earliest wide-angle galaxy redshift surveys were the CfA survey [49] and its follow up, CfA2 [50] in the 70's and 80's, with the latter recording 18,000 spectroscopic redshifts of bright galaxies in the northern sky. These were the first surveys to robustly probe the large-scale structure of the universe, with CfA2 discovering a large filament-like feature made up of galaxies, dubbed the *CfA2 great wall*. The existence of such structures was subsequently confirmed by more modern surveys like 2dFS and SDSS, which provided orders of magnitude increase in both volume probed and number of redshifts recorded. These surveys are shown in Fig. 1.10, where we can clearly see that the large-scale distribution of galaxies in the universe consists of a web-like structure, containing large clusters of galaxies connected by filaments and separated by voids. Also shown in this figure is the results from the Millennium simulations [51], large N-body simulated galaxy catalogues, which we see can be calibrated to accurately mimic the real world data on these scales. Such simulations are useful for testing models, statistical analysis and forecasting the accuracy of potential future surveys.

As more modern surveys grow larger in scale and scope, they offer the chance to probe a wider range of scales with our clustering statistics, and enable us to test the universe in new ways. Figure 1.9 shows the measurement of the matter power spectrum from various cosmological probes, with amplitudes normalised to today. We see that galaxy redshift surveys to date (red markers from SDSS data release 7) have only been able to robustly measure the power spectrum on intermediate scales of $0.03 \lesssim k \lesssim 0.3\ h\mathrm{Mpc}^{-1}$, with the largest scales currently probed solely by the CMB. Upcoming and future surveys will enable the measurement of the power spectrum out to these larger scales, enabling joint constraints with the CMB on features such as the turnover scale, corresponding to the size of the cosmic horizon at the time of matter-radiation equality in the early universe. This is an interesting scale, as it allows us to measure the redshift of this epoch, as well as the matter density parameter. Another prospect will be the ability to more robustly constrain primordial non-Gaussianty (PNG) from the large-scale galaxy power spectrum, an area where the CMB currently holds the most accurate measurement. Being able to test the universe over a range of scales, from probes at different epochs, is key to being able to test our cosmological models.

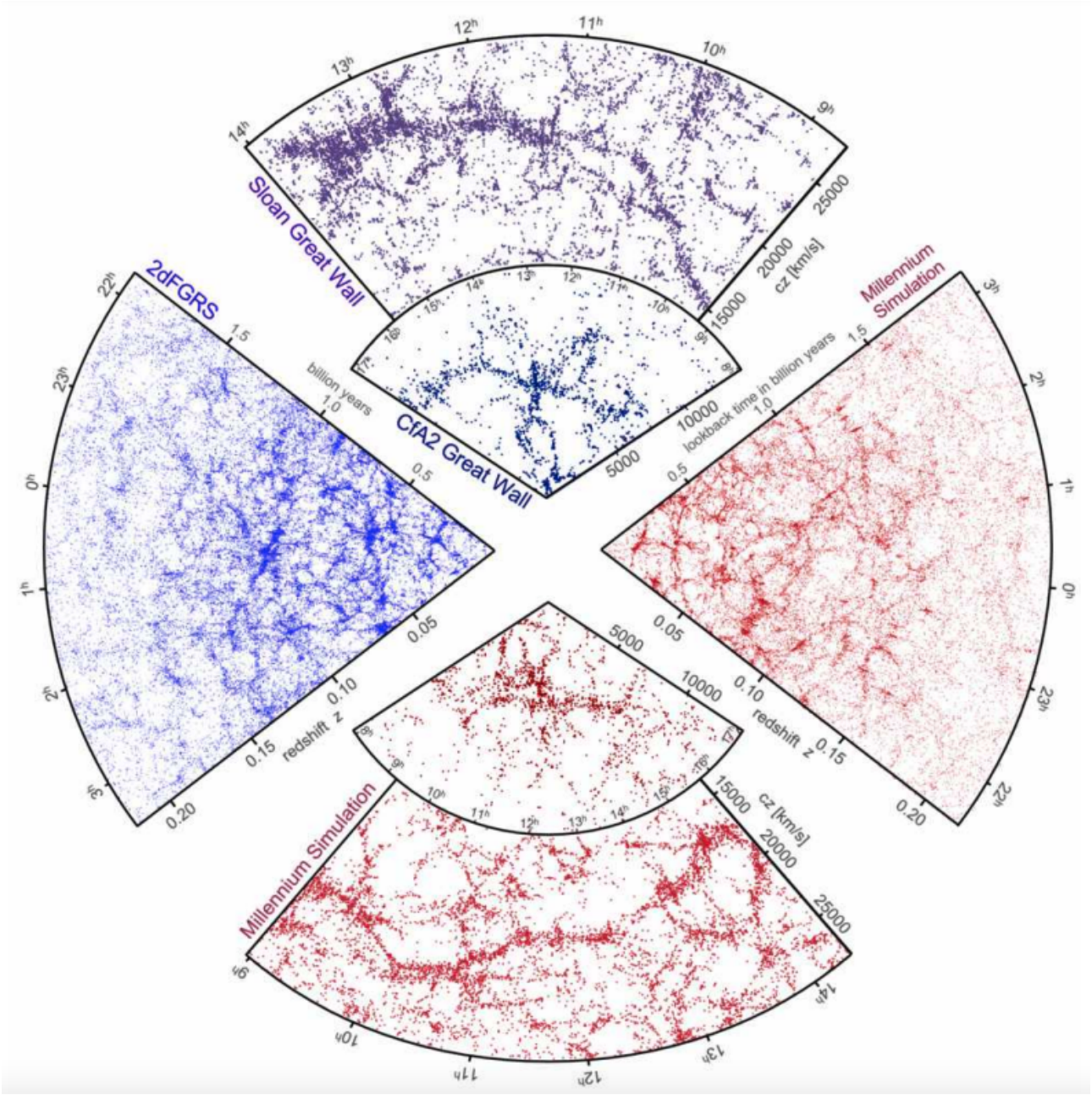

Figure 1.10: Upper and left: Slices from the CfA2, 2dF and SDSS galaxy redshift surveys, showing the large-scale structure of matter in the universe (the 'cosmic web') as viewed by us as observers at the centre of the image. Structures such as filaments and nodes consisting of large clusters of millions of galaxies, as well the spaces in between the structures, called voids, containing very little matter are easily visible. Lower and right: Slices of simulated data from the Millennium Simulations, where each slice was created with a selection function and magnitude cuts corresponding to the diametrically opposed real data. At the visual level, we can clearly see how closely the simulations are able to match the survey data. Figure from [52].

1.3 Motivation and outline of thesis

The power spectrum is one of the most useful tools for measuring the large-scale structure of the universe. One of the key quantities it enables us to constrain is the growth rate of structure, an important factor for discerning between different cosmological models. As upcoming and future galaxy surveys such as 4MOST, DESI, EUCLID and LSST will probe structure out to greater volumes and with higher number densities than previous endeavours, it is important that we review how we model the power spectrum, with a focus on large-scale effects that previously may not have been important.

One of the most commonly used approximations to date when modelling the power spectrum is the equal time approximation - that the whole galaxy sample is taken to be existing on the same constant-time hyper-surface, at some effective or mean redshift. While this approximation may be valid for shallow surveys, the main aim of this thesis it to investigate what effect it has as survey depth grows. In addition to this, as future surveys will cover large fractions of the sky, we look to perform all of our analysis in spherical coordinates, taking into consideration an angular survey mask. While this provides more accurate modelling for wide-angle surveys than simply assuming a flat-sky approximation, it does introduce numerical challenges in the form of spherical Bessel functions, which can be tricky to compute when performing integration. We therefore also investigate how existing numerical and analytic methods can be used to evaluate such expressions with accuracy and speed.

The thesis outline is as follows:

- In Chapter 2 we derive a model for the galaxy power spectrum on the past lightcone, in the simple case of a full-sky survey with no galaxy bias. We evaluate this model up to two-loop corrections in the non-linear regime, and investigate how the use of mean redshift and effective redshift approximations have on the amplitude and shape of the power spectrum, over a wide range of scales. We develop numerical code for both evaluating the model, and also for estimating the power spectrum from survey data. Our model is then put to the test by comparing it to power spectra that we estimate from lightcone mock catalogues, constructed from large N-body simulations, and review what effect using an optimum weighting scheme has on the signal-to-noise of the estimated power. Finally, we look to constrain the power spectrum turnover scale from our simulated mocks, and investigate how survey size effects the probability of being able to robustly detect if a turnover has occurred.

- In Chapter 3 we further develop the model of the previous chapter, by introducing an angular survey mask and galaxy bias. Due to the complex nature of the model, we also investigate ways in which such a model can be computed numerically, using power series expansions and analytic transforms of integrals to avoid having to compute spherical Bessel functions that a spherical decomposition of the density field introduces.

- In Chapter 4 we review the upcoming 4MOST project, with a particular focus on the Cosmology Redshift survey. We detail a clustering pipeline that we have developed for performing two-point clustering statistics to analyse multi-tracer mock catalogues from the 4MOST simulation team, to be used for analysis and planning before the launch of the survey.

Appendices

1.A A note on ensemble averages

In this work we will often encounter ensemble averages, and it is worth spending a second defining what we mean by this and how it differs from the volume average.

The volume average applies to a particular realisation (and some volume V in it). It is denoted with an over bar, and for a quantity $f(\boldsymbol{x})$ is defined as

$$\bar{f} \equiv \frac{1}{V}\int_V \mathrm{d}V(\boldsymbol{x}) f(\boldsymbol{x}) \ . \tag{1.77}$$

The ensemble average on the other hand, refers to the random process. We assume that the observed density field is just one of an *ensemble* of an infinite number of possible *realisations* that could have resulted from the random process. The random process is governed by the probability distribution, e.g. $\mathcal{P}(\gamma)$ of the quantities γ produced by it. Therefore, the ensemble average of a quantity $f(\gamma)$ is denoted by $\langle f \rangle$ and is defined as

$$\langle f \rangle \equiv \int \mathrm{d}\gamma \mathcal{P}(\gamma) f(\gamma) \ . \tag{1.78}$$

Here f could be (for example) the value of $\rho(\boldsymbol{x})$ at some location $\boldsymbol{x}$. The ensemble average is also known as the *expectation value*. Thus, the ensemble represents a probability distribution, and the properties of the density field (i.e. statistical homogeneity and isotropy, ergodicity etc.) will be properties of this ensemble. Statistical homogeneity means that the expectation value $\langle f(\boldsymbol{x}) \rangle$ must be the same at all $\boldsymbol{x}$ and thus we can just write $\langle f \rangle$. Statistical isotropy means that for quantities which involve a direction, the statistical properties are independent of the direction, i.e. for the vector quantities $\boldsymbol{v}$ all directions must be equally probable, implying $\langle \boldsymbol{v} \rangle = 0$.

How do we compare theory and observation, when we can only observe one realisation but our theory is talking about ensembles? It seems reasonable that the statistics we get by comparing different parts of a large volume should be similar to the statistics of a given part over different realisations, i.e. that they provide a fair sample of the probability distribution. This is called *ergodicity*. Fields that satisfy

$$\bar{f} \to \langle f \rangle \qquad \text{as} \qquad V \to \infty \ , \tag{1.79}$$

are called *ergodic* and we assume that the density field is ergodic. The equality of $\bar{f}$ with $\langle f \rangle$ does not hold for a finite volume V; the difference in these two values is called *sample variance* or *cosmic variance*. This variance is thus inversely proportional to the volume V, and limits how accurately we can compare theory with observations. It is therefore important for galaxy redshift surveys to cover large enough volumes with high enough number densities to reduce cosmic and statistical variance as much as possible.

Chapter 2

The galaxy power spectrum on the past lightcone: deep, wide-angle redshift surveys and the detectability of the turnover scale

2.1 Introduction

The next decade will herald in significant advances in the quantity of high fidelity data for mapping the large-scale distribution of galaxies. This will be facilitated through a series of exciting new wide field observatories, such as the spectroscopic missions DESI[1] [53], 4MOST[2] [54], the ESA Euclid[3] space mission [55] and the NASA mission SPHEREx [56]. These will be complemented by the photometric imaging surveys like LSST[4] [57]. Together these observatories will map the galaxy distribution out to high redshift and over significant fractions of the full-sky, and will thus chart effective volumes that approach the observable size of our Universe out to a given redshift [56]. All of these surveys will be able to make unprecedented measurements of the statistical properties of the spatial distribution of galaxies.

The lowest order spatial statistic of interest is the correlation function, or equivalently its Fourier space dual the power spectrum. The full shape and amplitude of the matter power spectrum carries a great deal of information about the cosmological model and the primordial distribution of the initial density fluctuations [58]. However, the extraction of this information is complicated by a number of effects: first, the initial linear density perturbations become nonlinearly coupled due to gravitational instability [59, 40]. Understanding this process is further complicated by the fact that the matter distribution is built from the weighted densities of baryons, cold dark matter and massive

[1] www.desi.lbl.gov
[2] www.4most.eu/cms/
[3] sci.esa.int/web/euclid
[4] www.lsst.org

neutrinos, each of component of which needs to be propagated into the nonlinear regime through careful modelling [60, 61, 62]. Second, galaxies are a biased set of tracers for the matter distribution, and may in full generality be a nonlinear, time-dependent, non-local, stochastic sampling of the matter, and this connection varies with the types of galaxies that are selected [63, 64, 65, 66, 67, 68, 69]. Third, owing to the fact that galaxy positions are inferred from their measured redshifts there is a distortion in the mapping from observed to true position, which arises due to the fact that galaxies have peculiar velocities relative to the Hubble flow – the so called redshift space distortions [45, 70, 71].

To this standard set one can also add the lightcone effect, which has surfaced in this recent era of precision cosmology – for deep surveys one has to account for the fact that we are correlating galaxy positions on the observer's past lightcone [72, 73]. Furthermore, there are additional corrections that arise due to general relativistic effects and also the magnification effects that all arise due to light propagation in a weakly perturbed spacetime [74, 75]. Another source of error arises from the assumption of a wrong cosmological model, in principle this could be overcome by simply recalculating the statistic of interest for every assumed cosmological model to be tested [76, 77]. Together, these effects can all be thought of as modelling problems and one should forward model the theory to account for them. Besides these 'physical' effects one can add a number of important 'observational' effects that also need to be carefully taken into account: the survey mask; star–galaxy classification; curved sky effects; fibre collision and completeness; accurate flux calibration across the survey; K-corrections.

In this chapter we focus on a subset of these issues. Our goal here is to build up the methodology for forward modelling the theory of the real space, 3D galaxy power spectrum in a survey that is deep and which spans the full sky. This means that we will need to take into account: the lightcone effect, including the unequal-time correlators and work on the curved sky. Our aim is thus to evolve the measurement and analysis methodology to the next level [78, 79, 80, 81, 82]. Regarding the lightcone effect, our work here is most closely inspired by that of [72] and we provide alternate derivations of results from that work. Many authors have explored the formalism of performing a spherical harmonic analysis of a galaxy redshift survey [83, 84, 85, 86, 87, 88, 89, 90, 91, 92], and we take many of our cues from these important works. However, one important distinction is that the main aim here is to retain the full 3D information of the galaxy field and not project out the radial modes, as is usually done in a number of these earlier works.

An additional important science driver for future surveys is the question of: How well can we detect the 'turnover scale' of the matter power spectrum. This length scale denotes the point of maximum amplitude of the matter power spectrum and for the ΛCDM model is a direct imprint of the epoch of matter-radiation equality in the early stages of the Universe. A number of previous works have examined this issue [93, 94, 95]. However, here we now relax some of the simplifying assumptions and use our improved formalism to attempt to address questions on this topic.

The chapter breaks down as follows: In Sections §2.2 and §2.3 we develop the theory of the galaxy power spectrum on the curved-sky, past lightcone. Then in Section §2.4 we describe how

we create mock lightcone catalogues, and detail the process used to estimate the power spectrum from these mocks. In Section §2.5 we discuss the results of these measurements, and how including an optimum weighting scheme effects the power spectrum. We also use our mocks to test the detectability of the turnover scale. Finally, in Section §2.6 we summarise our findings, conclude and discuss future work.

2.2 Theoretical background

We now review some of the key aspects of the background theory necessary for what follows. Note that we will neglect the effects of time delay and photon deviations that are required to describe a full general relativistic treatment of light propagation on the perturbed past lightcone.

2.2.1 The past lightcone

To begin, we assume that the unperturbed background spacetime is a spatially flat, homogeneous and isotropic, spacetime. Hence, in spherical coordinates the differential FLRW line element can be written as:

$$ds^2 = a(\eta)^2 \left[c^2 d\eta^2 - d\chi^2 - \chi^2 d\theta^2 - \chi^2 \sin^2\theta d\phi^2\right] \ , \tag{2.1}$$

where η is the conformal time, $a(\eta)$ is the scale factor, χ is the comoving radial geodesic distance, c is the speed of light and θ and ϕ are the usual polar angles, which we denote collectively as $\boldsymbol{\gamma} \rightarrow (\theta, \phi)$. A light signal emitted at spacetime point $(\eta_1, \chi_1, \boldsymbol{\gamma}_1)$ will be received by an observer located at the origin of our coordinate system at spacetime point $(\eta_2, 0, \mathbf{0})$. From the FLRW line element, we see that points on the past lightcone are required to obey the following relation between the radial comoving distance from the observer and the redshift:

$$r(z) = \left| \int_r^0 d\chi' \right| = \int_{\eta_1}^{\eta_2} c d\eta = \int_0^z \frac{c dz'}{H(z')} \ , \tag{2.2}$$

where the redshift is related to the expansion factor as $z = 1/a(\eta) - 1$ and the Hubble rate is $H(z) \equiv a'/a^2$, with $' = d/d\eta$. This can be calculated from the Friedmann equations, and for the case of flat ΛCDM is given by:

$$H^2(z) = H_0^2 \left[\Omega_{\mathrm{m},0}(1+z)^3 + \Omega_{\Lambda,0}\right] \ , \tag{2.3}$$

where $\Omega_{\mathrm{m},0}$ and $\Omega_{\Lambda,0}$ are the present day matter and Lambda density parameters, respectively. Since we are assuming a flat model here, we also have $\Omega_{\mathrm{m},0} + \Omega_{\Lambda,0} = 1$.

2.2.2 The galaxy overdensity field on the past lightcone

Following [72], let us define the galaxy density field at time η, with radial and angular positions $(\chi, \boldsymbol{\gamma})$, as:

$$n(\eta, \chi, \boldsymbol{\gamma}) = n_0(\eta)\left[1 + \Delta(\eta, \chi, \boldsymbol{\gamma})\right] \ , \tag{2.4}$$

where $n_0(\eta)$ is the mean number density of galaxies at time η and $\Delta(\eta, \chi, \boldsymbol{\gamma})$ is the density contrast of galaxies at the position. Thus on the past lightcone the number density is written:

$$n^{\rm LC}(\mathbf{r}) = \left. n_0(\eta)\left[1 + \Delta(\eta, \chi, \boldsymbol{\gamma})\right]\right|_{\eta\to\eta_0 - r, \chi\to r} \ , \tag{2.5}$$

where $\mathbf{r} \to (r, \boldsymbol{\gamma})$ and where η_0 is the present day conformal time. We can also define another useful quantity:

$$n_0^{\rm LC}(\eta) = \left. n_0(\eta)\right|_{\eta\to\eta_0 - r} \ . \tag{2.6}$$

We now introduce the galaxy survey density field as the quantity:

$$F^{\rm LC}(\mathbf{r}) \equiv A\left[n^{\rm LC}(\mathbf{r}) - \alpha\, n_{\rm s}^{\rm LC}(\mathbf{r})\right] \ , \tag{2.7}$$

where $n_{\rm s}^{\rm LC}(\mathbf{r})$ is a synthetic galaxy catalogue that is $1/\alpha$ times denser than the original galaxy catalogue on the lightcone that replicates all of the selection effects of the true sample, but which contains no intrinsic spatial correlations. A is a constant to be determined. Let us define the overdensity contrast of galaxies on the past lightcone as:

$$\Delta^{\rm LC}(\mathbf{r}) \equiv \Delta(\eta_0 - r, r, \boldsymbol{\gamma}) \equiv \frac{n^{\rm LC}(\mathbf{r}) - n_0^{\rm LC}(r)}{n_0^{\rm LC}(r)} \ . \tag{2.8}$$

In the absence of shot noise, this could also be written in terms of the galaxy survey density field as:

$$\Delta^{\rm LC}(\mathbf{r}) = \frac{F^{\rm LC}(\mathbf{r})}{A\alpha\, n_{\rm s}^{\rm LC}(\mathbf{r})} = \frac{n^{\rm LC}(\mathbf{r}) - \alpha\, n_{\rm s}^{\rm LC}(\mathbf{r})}{\alpha\, n_{\rm s}^{\rm LC}(\mathbf{r})} \ , \tag{2.9}$$

where $\alpha\left\langle n_{\rm s}^{\rm LC}(\mathbf{r})\right\rangle = n_0^{\rm LC}(r)$. Note that at this point we are neglecting the angular mask, redshift space distortions, optimal weighting and relativistic corrections for a perturbed spacetime.

2.2.3 Spherical-Fourier-Bessel (SFB) expansion

For a fundamental observer viewing their past lightcone, homogeneity will be violated, but isotropy is preserved. In addition, the survey mask would be completely angular and evolution and redshift space distortions will be purely radial. It will therefore be useful to decompose the problem into a set of orthogonal spherical and radial modes. To do this we will make use of the Spherical-Fourier-Bessel (SFB) expansion of a scalar field [for a discussion, see 83, 96, 87].

To begin, consider some scalar field $\mathcal{A}(\mathbf{r})$ in space and let us define its forward and backward

Fourier transforms as:

$$\mathcal{A}(\mathbf{r}) = \int \frac{\mathrm{d}^3\mathbf{k}}{(2\pi)^3} \mathcal{A}(\mathbf{k}) e^{-i\mathbf{k}\cdot\mathbf{r}} \Leftrightarrow \mathcal{A}(\mathbf{k}) = \int \mathrm{d}^3\mathbf{r} \mathcal{A}(\mathbf{r}) e^{i\mathbf{k}\cdot\mathbf{r}} \ . \tag{2.10}$$

On following the steps in Appendix §2.A we show that the SFB expansion of $\mathcal{A}(\mathbf{r})$ is given by:

$$\mathcal{A}(\mathbf{r}) = \sum_{\ell=0}^{\infty} \sum_{m=-\ell}^{\ell} Y_{\ell m}(\hat{\mathbf{r}}) \mathcal{A}_{\ell m}(r) \ , \tag{2.11}$$

where the $Y_{\ell m}(\hat{\mathbf{r}})$ are (Laplace) spherical harmonics and the radial harmonic amplitudes are given by:

$$\mathcal{A}_{\ell m}(r) \equiv (-i)^\ell \int \frac{\mathrm{d}^3\mathbf{k}}{(2\pi)^3} j_\ell(kr) Y^*_{\ell m}(\hat{\mathbf{k}}) \mathcal{A}(\mathbf{k}) \ . \tag{2.12}$$

2.3 Spatial statistics on the lightcone

As an initial first step, let us assume that we have a full sky redshift survey that has complete sky coverage and let us neglect the redshift space distortions. While the inclusion of RSD at linear order using the 'distant observer' approximation would be relatively easy to incorporate in the following derivations and has been well studied in the literature (see [70] for a review), for our case where we are dealing with statistics on the full sky a more rigorous treatment of RSD would be required. By working in a spherical basis, we avoid the need to include any 'wide-angle' effects that previous studies [74] have used when extending works like FKP, however, this basis introduces spherical Bessel functions which make calculations more difficult and costly. We will discuss methods in the following chapter that can be used to make the Bessel integrals we will shortly encounter more feasible, after which an inclusion of RSD into the analysis will be more readily achieveable. We refer the reader to the recent study by Grasshorn and Jeong (2020) [97] for a look at the angular power spectrum including RSD in a spherical basis, and note that for our analysis of the turnover scale in section 2.5.3, RSD at the large scales of interest only modify the amplitude, but not the shape, of the power spectrum and thus should not effect the results we obtain.

2.3.1 Two-point correlation function on the past lightcone

Let us now compute the expectation of the product of the density field at two separate locations on the lightcone. Using our Fourier-Bessel harmonic expansion from Eq. (2.11) this can be written as:

$$\begin{aligned} \langle \Delta(\mathbf{r}_1) \Delta(\mathbf{r}_2) \rangle = & \sum_{\ell_1, m_1} \sum_{\ell_2, m_2} Y_{\ell_1 m_1}(\hat{\mathbf{r}}_1) Y^*_{\ell_2 m_2}(\hat{\mathbf{r}}_2) \\ & \times \left\langle \Delta_{\ell_1 m_1}(\eta_1, r_1) \Delta^*_{\ell_2 m_2}(\eta_2, r_2) \right\rangle \ . \end{aligned} \tag{2.13}$$

On substituting in for the harmonic amplitudes given by Eqs (2.12) and (2.97) the above expression becomes:

$$\begin{aligned}\langle\Delta(\mathbf{r}_1)\Delta(\mathbf{r}_2)\rangle = &\sum_{\ell_1,m_1}\sum_{\ell_2,m_2}(-i)^{\ell_1}i^{\ell_2}Y_{\ell_1 m_1}(\hat{\mathbf{r}}_1)Y^*_{\ell_2 m_2}(\hat{\mathbf{r}}_2)\\ &\times\int\frac{\mathrm{d}k_1k_1^2}{2\pi^2}\int\frac{\mathrm{d}k_2k_2^2}{2\pi^2}j_{\ell_1}(k_1r_1)j_{\ell_2}(k_2r_2)\\ &\times\left\langle\Delta_{\ell_1 m_1}(\eta_1,k_1)\Delta^*_{\ell_2 m_2}(\eta_2,k_2)\right\rangle\ . \end{aligned}\tag{2.14}$$

Consider now the expectation factor in the above expression and let us use Eqs (2.92) and (2.93) to rewrite this in the following way:

$$\begin{aligned}\left\langle\Delta_{\ell_1 m_1}(\eta_1,k_1)\Delta^*_{\ell_2 m_2}(\eta_2,k_2)\right\rangle = &\int\mathrm{d}\hat{\mathbf{k}}_1\mathrm{d}\hat{\mathbf{k}}_2\ Y^*_{\ell_1 m_1}(\hat{\mathbf{k}_1})\\ &\times Y_{\ell_2 m_2}(\hat{\mathbf{k}_2})\left\langle\Delta(\eta_1,\mathbf{k}_1)\Delta^*(\eta_2,\mathbf{k}_2)\right\rangle\ . \end{aligned}\tag{2.15}$$

The unequal time correlator $\langle\Delta(\eta_1,\mathbf{k}_1)\Delta^*(\eta_2,\mathbf{k}_2)\rangle$ has the property that:

$$\langle\Delta(\eta_1,\mathbf{k}_1)\Delta^*(\eta_2,\mathbf{k}_2)\rangle = (2\pi)^3\delta^{\mathrm{D}}_{3\mathrm{D}}(\mathbf{k}_1-\mathbf{k}_2)P(\mathbf{k}_1,\eta_1,\eta_2)\ .\tag{2.16}$$

Furthermore, the Dirac delta function can be written in the spherical polar coordinates as:

$$\delta^{\mathrm{D}}_{3\mathrm{D}}(\mathbf{k}_1-\mathbf{k}_2) = \frac{\delta^{\mathrm{D}}_{1\mathrm{D}}(k_1-k_2)}{k_1^2}\delta^{\mathrm{D}}_{2\mathrm{D}}(\hat{\mathbf{k}}_1-\hat{\mathbf{k}}_2)\ .\tag{2.17}$$

On putting all of this together and on integrating over the Dirac delta functions we find Eq. (2.14) becomes:

$$\begin{aligned}\langle\Delta(\mathbf{r}_1)\Delta(\mathbf{r}_2)\rangle = &\frac{(2\pi)^3}{4\pi^4}\sum_{\ell_1,m_1}\sum_{\ell_2,m_2}(-i)^{\ell_1}i^{\ell_2}Y_{\ell_1 m_1}(\hat{\mathbf{r}}_1)Y^*_{\ell_2 m_2}(\hat{\mathbf{r}}_2)\\ &\times\int\mathrm{d}kk^2j_{\ell_1}(kr_1)j_{\ell_2}(kr_2)P(k,\eta_1,\eta_2)\\ &\times\int\mathrm{d}\hat{\mathbf{k}}\ Y^*_{\ell_1 m_1}(\hat{\mathbf{k}})Y_{\ell_2 m_2}(\hat{\mathbf{k}})\ . \end{aligned}\tag{2.18}$$

The last integral on the right-hand-side can be computed owing to the orthogonality of spherical harmonics to give:

$$\int\mathrm{d}\hat{\mathbf{k}}_1\ Y^*_{\ell_1 m_1}(\hat{\mathbf{k}_1})Y_{\ell_2 m_2}(\hat{\mathbf{k}_1}) = \delta^{\mathrm{K}}_{\ell_1,\ell_2}\delta^{\mathrm{K}}_{m_1,m_2}\ ,\tag{2.19}$$

where $\delta^{\rm K}$ is the Kronecker delta symbol. On utilising this fact, Eq. (2.18) becomes:

$$\langle\Delta(\mathbf{r}_1)\Delta(\mathbf{r}_2)\rangle = \frac{2}{\pi}\sum_{\ell,m} Y_{\ell m}(\hat{\mathbf{r}}_1)Y^*_{\ell m}(\hat{\mathbf{r}}_2)\int \mathrm{d}k k^2 j_\ell(kr_1)j_\ell(kr_2) \times P(k,\eta_1,\eta_2)\ . \tag{2.20}$$

The addition theorem of spherical harmonics is:

$$\mathcal{L}_\ell(\cos\theta_{r_1r_2}) = \frac{4\pi}{2\ell+1}\sum_{m=-\ell}^{\ell} Y_{\ell m}(\hat{\mathbf{r}}_1)Y^*_{\ell m}(\hat{\mathbf{r}}_2)\ , \tag{2.21}$$

where $\theta_{r_1r_2}$ is the angle between the two vectors $\hat{\mathbf{r}}_1$ and $\hat{\mathbf{r}}_2$. On using this relation in Eq. (2.20) we find the result:

$$\langle\Delta(\mathbf{r}_1)\Delta(\mathbf{r}_2)\rangle = \sum_\ell (2\ell+1)\mathcal{L}_\ell(\cos\theta_{r_1r_2})\xi_\ell(r_1,r_2)\ , \tag{2.22}$$

where $\mathcal{L}_\ell(x)$ is the Legendre polynomial of order ℓ and where we defined the correlation function multi-pole amplitude as:

$$\xi_\ell(r_1,r_2) \equiv \int \frac{\mathrm{d}^3\mathbf{k}}{(2\pi)^3} j_\ell(kr_1)j_\ell(kr_2)P(k,\eta_1,\eta_2)\ . \tag{2.23}$$

Returning to our observed galaxy density field $F^{\rm LC}(\mathbf{r})$, the above result implies that:

$$\left\langle F^{\rm LC}(\mathbf{r}_1)F^{\rm LC}(\mathbf{r}_2)\right\rangle = A^2 n_0^{\rm LC}(\mathbf{r}_1)n_0^{\rm LC}(\mathbf{r}_2)\sum_\ell (2\ell+1) \times \mathcal{L}_\ell(\cos\theta_{r_1r_2})\xi_\ell(r_1,r_2)\ . \tag{2.24}$$

In order to evaluate the above expression one would need access to a model for the nonlinear unequal time correlator $P(k_1,\eta_1,\eta_2)$.

2.3.2 The power spectrum on the past lightcone

We next turn to the issue of determining the power spectrum of our observed lightcone density field $F^{\rm LC}(\mathbf{r})$. Let us work this out, but starting from:

$$\left\langle F^{\rm LC}(\mathbf{q}_1)\left[F^{\rm LC}(\mathbf{q}_2)\right]^*\right\rangle = \int \mathrm{d}^3\mathbf{r}_1\mathrm{d}^3\mathbf{r}_2 e^{i\mathbf{q}_1\cdot\mathbf{r}_1}e^{-i\mathbf{q}_2\cdot\mathbf{r}_2} \times \left\langle F^{\rm LC}(\mathbf{r}_1)F^{\rm LC}(\mathbf{r}_2)\right\rangle\ . \tag{2.25}$$

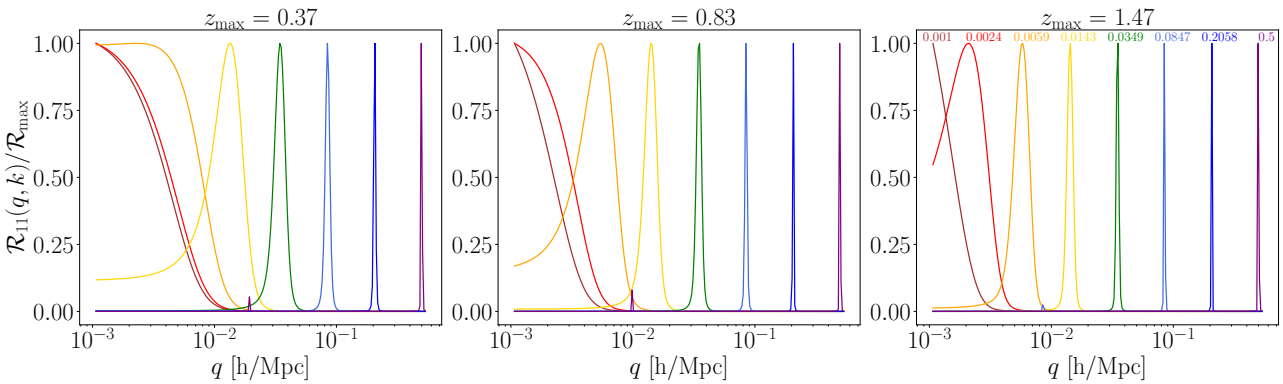

Figure 2.1: The kernel window function $\mathcal{R}_{11}(q,k)$ of Eq. 2.39 as a function of q, for seven values of k selected to lie in the range $k \in \{0.001, 0.5\}\, h\,\mathrm{Mpc}^{-1}$, with the smallest in dark red and the largest in purple (see annotated values in the right-most plot). The panels from left to right show the results for volume limited surveys with maximum redshifts of $z_{\rm max} = \{0.37, 0.83, 1.47\}$, respectively, corresponding to a maximal radial distance of $\{1, 2, 3\}h^{-1}$Gpc in our chosen cosmology. We see that for scales much smaller than the survey volume these window functions do indeed take on Dirac delta function like properties: $\mathcal{R}_{11}(q,k) \approx \delta^D(q-k)$.

If we plug in to this relation Eq. (2.7) we get:

$$\left\langle F^{\rm LC}(\mathbf{q}_1)\left[F^{\rm LC}(\mathbf{q}_2)\right]^*\right\rangle = \int \mathrm{d}^3\mathbf{r}_1\mathrm{d}^3\mathbf{r}_2 A^2 e^{i\mathbf{q}_1\cdot\mathbf{r}_1}e^{-i\mathbf{q}_2\cdot\mathbf{r}_2} \times \left\langle \left[n^{\rm LC}(\mathbf{r}_1) - \alpha\, n_{\rm s}^{\rm LC}(\mathbf{r}_1)\right]\left[n^{\rm LC}(\mathbf{r}_2) - \alpha\, n_{\rm s}^{\rm LC}(\mathbf{r}_2)\right]\right\rangle \ . \tag{2.26}$$

In the absence of shot-noise, the term in angle brackets on the right-hand-side can be written:

$$\left\langle \left[n^{\rm LC}(\mathbf{r}_1) - \alpha\, n_{\rm s}^{\rm LC}(\mathbf{r}_1)\right]\left[n^{\rm LC}(\mathbf{r}_2) - \alpha\, n_{\rm s}^{\rm LC}(\mathbf{r}_2)\right]\right\rangle = n_0^{\rm LC}(r_1) n_0^{\rm LC}(r_2)\left\langle \Delta(\mathbf{r}_1)\Delta(\mathbf{r}_2)\right\rangle \ . \tag{2.27}$$

On inserting the above expression back into Eq. (2.26) and on making use of our derived expression for the matter correlation function given by Eq. (2.20), we can obtain the following relation:

$$\left\langle F^{\rm LC}(\mathbf{q}_1)\left[F^{\rm LC}(\mathbf{q}_2)\right]^*\right\rangle = \int \mathrm{d}^3\mathbf{r}_1\mathrm{d}^3\mathbf{r}_2 A^2 e^{i\mathbf{q}_1\cdot\mathbf{r}_1}e^{-i\mathbf{q}_2\cdot\mathbf{r}_2} \times n_0^{\rm LC}(r_1) n_0^{\rm LC}(r_2) 4\pi \sum_{\ell m} Y_{\ell m}(\hat{\mathbf{r}}_1) Y^*_{\ell m}(\hat{\mathbf{r}}_2)\xi_\ell(r_1, r_2) \ . \tag{2.28}$$

We now make use of the spherical harmonic expansion of the plane waves from Eqs (2.84) and (2.85) and on using these in the above expression we find:

$$\begin{aligned}\left\langle F^{\rm LC}(\mathbf{q}_1)\left[F^{\rm LC}(\mathbf{q}_2)\right]^*\right\rangle &= (4\pi)^3 A^2 \int {\rm d}^3\mathbf{r}_1 {\rm d}^3\mathbf{r}_2 n_0^{\rm LC}(r_1) n_0^{\rm LC}(r_2) \\ &\times \sum_{\ell_1 m_1} i^{\ell_1} j_{\ell_1}(q_1 r_1) Y_{\ell_1 m_1}(\hat{\mathbf{q}}_1) Y^*_{\ell_1 m_1}(\hat{\mathbf{r}}_1) \\ &\times \sum_{\ell_2 m_2} (-i)^{\ell_2} j_{\ell_2}(q_2 r_2) Y^*_{\ell_2 m_2}(\hat{\mathbf{q}}_2) Y_{\ell_2 m_2}(\hat{\mathbf{r}}_2) \\ &\times \sum_{\ell m} Y_{\ell m}(\hat{\mathbf{r}}_1) Y^*_{\ell m}(\hat{\mathbf{r}}_2) \xi_\ell(r_1, r_2) \ , \end{aligned} \tag{2.29}$$

where in rewriting the second plane-wave using the harmonic expansion we have made use of the fact that the complex conjugate can appear on either of the spherical harmonics. The advantage of this is that the volume integrals over r_1 and r_2 can now be broken up into radial and surface integrals. The only terms that depend on $\hat{\mathbf{r}}_1$ and $\hat{\mathbf{r}}_2$ are the spherical harmonics, and so on making repeated use of the orthogonality relation, we have:

$$\begin{aligned}\left\langle F^{\rm LC}(\mathbf{q}_1)\left[F^{\rm LC}(\mathbf{q}_2)\right]^*\right\rangle &= 4\pi A^2 \int {\rm d}^3\mathbf{r}_1 {\rm d}^3\mathbf{r}_2 n_0^{\rm LC}(r_1) n_0^{\rm LC}(r_2) \\ &\times \sum_{\ell m} j_\ell(q_1 r_1) j_\ell(q_2 r_2) Y_{\ell m}(\hat{\mathbf{q}}_1) Y^*_{\ell m}(\hat{\mathbf{q}}_2) \xi_\ell(r_1, r_2). \end{aligned} \tag{2.30}$$

Again, on making use of the addition theorem for spherical harmonics we find that the above expression can be further simplified to:

$$\left\langle F^{\rm LC}(\mathbf{q}_1)\left[F^{\rm LC}(\mathbf{q}_2)\right]^*\right\rangle = \sum_\ell \mathcal{P}_\ell(q_1, q_2) \mathcal{L}_\ell(\cos\theta_{q_1 q_2}) \ , \tag{2.31}$$

where we have defined the $F^{\rm LC}$ power spectrum multipoles:

$$\begin{aligned}\mathcal{P}_\ell(q_1, q_2) \equiv (2\ell+1) A^2 &\int {\rm d}^3\mathbf{r}_1 {\rm d}^3\mathbf{r}_2 n_0^{\rm LC}(r_1) n_0^{\rm LC}(r_2) \\ &\times j_\ell(q_1 r_1) j_\ell(q_2 r_2) \xi_\ell(r_1, r_2). \end{aligned} \tag{2.32}$$

In practice, the above expression for the multipoles is rather cumbersome. A more useful variation can be obtained by substituting our expression for ξ_ℓ from Eq. (2.23) and on rearranging the order of integration, moving the k integral to the front, we get:

$$\begin{aligned}\mathcal{P}_\ell(q_1, q_2) = (2\ell+1) A^2 &\int \frac{{\rm d}^3\mathbf{k}}{(2\pi)^3} \prod_{j=1}^{2} \Big\{ \int {\rm d}^3\mathbf{r}_j n_0^{\rm LC}(r_j) \\ &\times j_\ell(q_j r_j) j_\ell(k r_j) \Big\} P(k, \eta_1, \eta_2) \ . \end{aligned} \tag{2.33}$$

Some interesting points to note are: first, for the case where the unequal time correlator is not a separable function of time, the evaluation of the above expression requires one to compute a 3D-numerical integral. On the other hand if it is, and as we will show in the next section, the integral can be reduced to a set of 2D integrals. Second, the observed lightcone power spectrum, defined $P_{\rm F}(q) \equiv \left\langle \left|F^{\rm LC}(\mathbf{q})\right|^2 \right\rangle$, can be obtained from the above equations by setting $\mathbf{q}_1 = \mathbf{q}_2$, or equivalently $\theta_{q_1 q_2} = 0$, whereupon $\mathcal{L}_\ell(1) = 1$, and we have a sum over all ℓ of $\mathcal{P}_\ell(q_1, q_1)$. It is also interesting to note that, $\left\langle F^{\rm LC}(\mathbf{q}_1) \left[F^{\rm LC}(\mathbf{q}_2)\right]^* \right\rangle$ does not vanish for $\theta_{q_1 q_2} \neq 0$. This arises due to the fact that for the lightcone observer, homogeneity is broken and so there is no Dirac delta function. However, isotropy is not broken. Lastly, for expressions discussing the shell-averages of the observed power spectrum see Appendix 2.C.

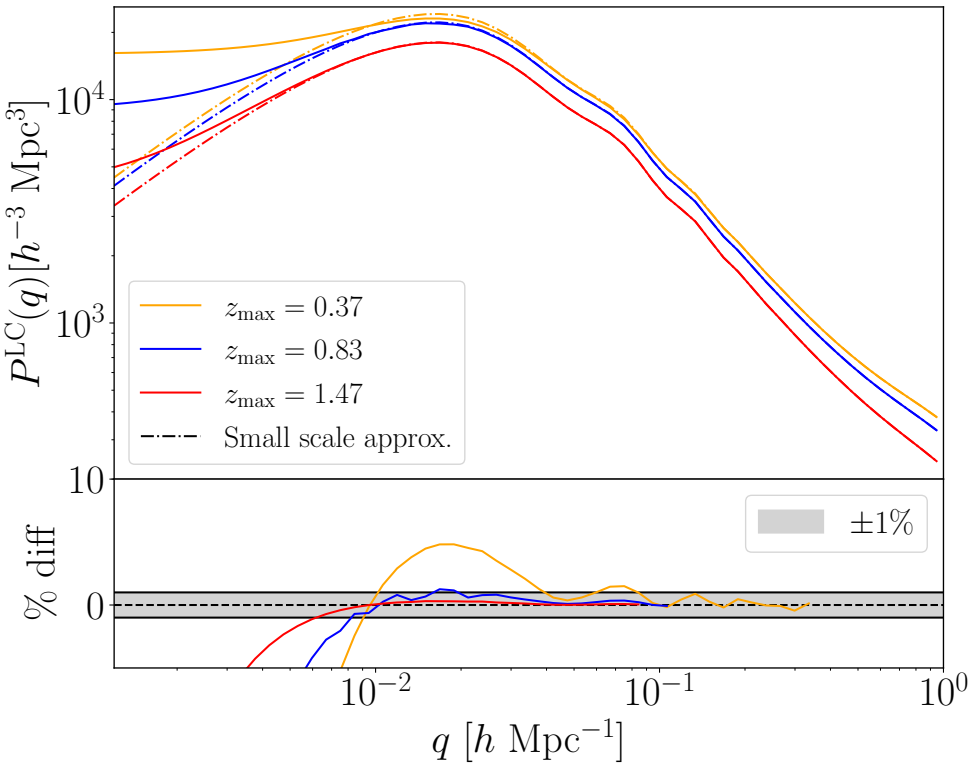

Figure 2.2: Upper: A plot of the window-convolved nonlinear power spectrum on the lightcone for an all sky survey reaching out to increasing redshift depths (corresponding to fainter magnitude cuts). The solid lines show the unequal time model (Eq. (2.38)), while the dot-dashed lines show the small scale approximation (Eq. (2.44)). The lower plot shows the percentage difference between calculating the power spectrum using the full formula versus using the small scale approximation. We see that these two formulas reach convergence to well within 1% on small scales, where the approximate formula is used to reduce computation time.

2.3.3 Approximate forms: the time separable UETC

Let us suppose that the UETC can be written as a separable function of time or more generally as a set of functionals of $P(k, \eta_0)$ each of which has time separable behaviour. Hence, we propose the

ansatz:

$$P(k,\eta_1,\eta_2) = \sum_{a,b} G_a(\eta_1,\eta_0)G_b(\eta_2,\eta_0)\mathcal{F}_{ab}[P](k) \ , \tag{2.34}$$

where the functions $G_a(\eta,\eta_0)$ give the amplification at time η relative to some fiducial time η_0 and the functionals $\mathcal{F}_{ab}$ only involve integrals over the equal time correlator. We note that the above form may be justified on the grounds that the UETC is symmetric in time, i.e. $P(k,\eta_1,\eta_2) = P(k,\eta_2,\eta_1)$ and by the fact that this form will capture a wide range of perturbative expansion schemes. For example, in linear theory Eq. (2.34) has the form:

$$P(k,\eta_1,\eta_2) = D(\eta_1)D(\eta_2)P_{\rm Lin}(k,\eta_0) \ , \tag{2.35}$$

where $G_1(\eta_1,\eta_0) = D(\eta_1)$ are growth factors relative to time η_0 and $\mathcal{F}_{ab}[P](k) = P_{\rm Lin}(k,\eta_0)$ is the linear theory power spectrum at time η_0. In Eulerian perturbation theory the nonlinear power spectrum including the next-to-leading order corrections can also be expressed in the form of Eq. (2.34). In this case $G_a(\eta,\eta_0) = D(\eta)^a$ and $\mathcal{F}_{13} = P_{13}$, $\mathcal{F}_{22} = P_{22}$ and $\mathcal{F}_{12} = \mathcal{F}_{21} = 0$, giving [47]:

$$\begin{aligned} P(k,\eta_1,\eta_2) = {} & D(\eta_1)D(\eta_2)P_{\rm Lin}(k) + D^2(\eta_1)D^2(\eta_2)P_{22}(k) \\ & + \left[D^3(\eta_1)D(\eta_2) + D(\eta_1)D^3(\eta_2)\right] P_{13}(k) \ . \end{aligned} \tag{2.36}$$

Focusing on the general separable form, if we insert Eq. (2.34) into Eq. (2.33) then, for the case of $q_1 = q_2$ we see that:

$$\begin{aligned} \mathcal{P}_\ell(q,q) = {} & (2\ell+1)A^2 \sum_{a,b} \int \frac{{\rm d}^3\mathbf{k}}{(2\pi)^3} \mathcal{F}_{ab}[P(k,\eta_0)](k) \\ & \times \prod_{\alpha=\{a,b\}}^{2} \left\{ \int {\rm d}^3\mathbf{r} n_0^{\rm LC}(r) G_\alpha(\eta,\eta_0) j_\ell(qr) j_\ell(kr) \right\} \ . \end{aligned} \tag{2.37}$$

Notice that the final product of integrals are not dependent upon one another, and this makes the evaluation of the above expression a sum over 2D integrals. With this result in hand, we see that Eq. (2.37) can be written in the compact form:

$$P_{\rm F}(q) = \sum_{a,b} \int \frac{{\rm d}^3\mathbf{k}}{(2\pi)^3} \mathcal{F}_{ab}[P](k) \mathcal{R}_{ab}(q,k) \ , \tag{2.38}$$

where the kernel window function can be written

$$\mathcal{R}_{ab}(q,k) \equiv \sum_\ell (2\ell+1) W_\ell^{(a)}(q,k) W_\ell^{(b)}(q,k) \ , \tag{2.39}$$

where we have defined

$$W_\ell^{(a)}(q,k) \equiv A \int \mathrm{d}^3\mathbf{r} n_0^{\mathrm{LC}}(r) G_a(\eta,\eta_0) j_\ell(qr) j_\ell(kr) \ . \tag{2.40}$$

Figure 2.1 shows the behaviour of the kernel window function of Eq. (2.39), normalised by its maximum value. Here we present the case for the linear theory UETC, and have also made the further simplifying assumption of a volume limited survey with a constant comoving number density of galaxies $n_0^{\mathrm{LC}}(r) = 1$ up to a scale r_{max}, and then a vanishingly small density thereafter. The three panel from left to right show the results for increasing survey volume. We see that on small scales (i.e. when $qr_{\mathrm{max}} \gg 1$ and $kr_{\mathrm{max}} \gg 1$) $\mathcal{R}$ becomes highly spiked and so exhibits delta function like behaviour where $k \approx q$. These plots also demonstrate the need to bound the k integral wisely (i.e. the bounds should be q dependent) to save on computational overheads. Not too unsurprisingly, this mimics the window function $G(k-q)$ described in the FKP method [78].

2.3.4 Approximate forms: small-scale limit: $kr_{\mathrm{max}} \gg 1$

If this behaviour is realised for all of the terms in Eq. (2.34) then Eq. (2.38) can be further approximated. Let us thus consider the case where $\mathcal{R}_{ab}(q,k) \propto \delta^D(k-q)$. If the functions $\mathcal{F}_{ab}[P](k)$ are slowly varying on scale q, then we can write:

$$P_{\mathrm{F}}(q) \approx A^2 \sum_{ab} \mathcal{F}_{ab}[P](q) \int \frac{\mathrm{d}^3\mathbf{k}}{(2\pi)^3} \mathcal{R}_{ab}(q,k) \ , \tag{2.41}$$

where

$$\int \frac{\mathrm{d}^3\mathbf{k}}{(2\pi)^3} \mathcal{R}_{ab}(q,k) = \sum_\ell (2\ell+1) \int \frac{\mathrm{d}^3\mathbf{k}}{(2\pi)^3} \times \prod_{\alpha=\{a,b\}}^{2} \left\{ \int \mathrm{d}^3\mathbf{r} n_0^{\mathrm{LC}}(r) G_\alpha(\eta,\eta_0) j_\ell(qr) j_\ell(kr) \right\} \ . \tag{2.42}$$

On expanding out the square bracket we can reorder the integrals so that we compute the infinite integral over the k dependent terms first. We recognise that this can be computed using the orthogonality of the spherical Bessel functions:

$$\int dk k^2 j_\ell(kr_1) j_\ell(kr_2) = \frac{\pi}{2r_2^2} \delta^D(r_1 - r_2). \tag{2.43}$$

On substituting this equation back into the expanded form of Eq. (2.42) and performing the integral over r_2 we obtain the relation:

$$\begin{aligned} P_{\rm F}(q) &\approx A^2 \sum_{ab} \mathcal{F}_{ab}(q) \int {\rm d}^3\mathbf{r} \left[n_0^{\rm LC}(r)\right]^2 G_a(\eta) G_b(\eta) \\ &\approx A^2 \int {\rm d}^3\mathbf{r} \left[n_0^{\rm LC}(r)\right]^2 P(q,\eta) \ . \end{aligned} \tag{2.44}$$

In order to obtain the above expression we made use of the fact that an infinite sum over the squares of spherical Bessel functions is unity (result 10.1.50 of [98]):

$$\sum_{\ell}^{\infty} (2\ell+1) j_\ell^2(x) = 1 \ , \tag{2.45}$$

and we have made an appropriate choice for A, such that

$$\frac{1}{A^2} \equiv \int {\rm d}^3\mathbf{r} \left[n_0^{\rm LC}(r)\right]^2 \ . \tag{2.46}$$

This tells us that in the limit where the the radial weight functions are very broad and smooth, such that the $W_\ell^{(a)}(q,k)$ are very narrowly peaked, the lightcone power spectrum is approximately given by the equal time correlator weighted by the square of the selection function averaged over the radial extent of the survey.

In Figure 2.2 we plot the window-convolved power spectrum on the past lightcone for an all-sky survey, out to increasing redshift depths, using the full expression of Eq. (2.38) (solid lines). We also plot the small-scale approximation given by Eq. (2.44) with the dash-dotted lines, with the lower panel of the plot showing the percentage difference between the two methods. We see that for the cases considered, for $q > 0.1\,h\,{\rm Mpc}^{-1}$, there is $\lesssim 1\%$ difference between the two formulae, and so in this region we can safely use the approximated formula, which will drastically save on computational time. We also see that the approximation performs worse for shallower survey depths, where one has to calculate the full formula to a higher value of k, relative to a deeper survey, before being able to safely switch over to this approximation.

2.3.5 Approximate forms: the large-scale limit

We also look at the behaviour of the window-convolved power spectrum in the very large scale limit, as $q \to 0$. In this region, the power spectrum and survey window function are highly convolved with one another, and we expect to see significant modifications to the shape of the power. Indeed, we see in Fig. 2.2 that instead of dropping off towards zero as the input spectrum does, we now have that the power converges on some constant value in q.

To determine this value, we use the properly of the spherical Bessel functions:

$$j_\ell(x)\Big|_{x\to 0} = \delta_0^\ell \ , \tag{2.47}$$

and inserting into Eq. (2.38), writing out the terms explicitly at linear order we have

$$P_{\rm F}(q)\Big|_{q\to 0} = \int \frac{{\rm d}^3\mathbf{k}}{(2\pi)^3} P_{\rm Lin}(k)\Big[A\int {\rm d}^3\mathbf{r} G(\eta,\eta_0) j_0(kr)\Big]^2 \ . \tag{2.48}$$

From this we see that on these very large scales, the value of the power spectrum depends purely on the survey depth and form of the radial kernel function $G(\eta,\eta_0)$.

2.3.6 Evaluating theoretical models at an effective time

In many large-scale structure analyses, it is common to find that the theoretical models are evaluated at the mean redshift of the sample, calculated via

$$z_{\rm mean} = \frac{\int {\rm d}z \frac{{\rm d}V}{{\rm d}z}\ z\ n^{\rm LC}_{\rm Eff}(z)}{\int {\rm d}z \frac{{\rm d}V}{{\rm d}z}\ n^{\rm LC}_{\rm Eff}(z)} \ . \tag{2.49}$$

Alternatively, one can instead use an *effective survey-fixed redshift*. On inspection of Eq. (2.38) we see that, for a general nonlinear model, this can not be realised in detail and that the presence of nonlinear terms with different time dependence violates this approximation. To see this let us rewrite Eq. (2.44) in a simplified form and assume that there is an effective time at which we have the following equality:

$$P_{\rm F}(q) \approx \int {\rm d}^3\mathbf{r} w(r) P(q,\eta) \stackrel{?}{\approx} P(q,\eta_{\rm eff}) \ , \tag{2.50}$$

where $w(r) = A^2\left[n^{\rm LC}_0(r)\right]^2$ and a super-script question mark has been used notate that we are asking whether the conjecture is true. On making repeated use of Eq. (2.34) we find:

$$\begin{aligned}\sum_{a,b} G_a(\eta_{\rm eff},\eta_0) G_b(\eta_{\rm eff},\eta_0)\mathcal{F}_{ab}[P](k) \\ \stackrel{?}{\approx} \sum_{a,b}\int {\rm d}^3\mathbf{r} w(r) G_a(\eta,\eta_0) G_b(\eta,\eta_0)\mathcal{F}_{ab}[P](k) \ .\end{aligned} \tag{2.51}$$

For the case of linear theory, where $a=1$, $b=1$, and $\mathcal{F}_{ab}[P](k) = P_{\rm Lin}(k)$, we see that a Linear effective time $\eta^{\rm Lin}_{\rm eff}$ can be found that will satisfy Eq. (2.51) if we can numerically solve the relation:

$$D^2(\eta^{\rm Lin}_{\rm eff}) = \frac{\int {\rm d}^3\mathbf{r}\left[n^{\rm LC}_0(r)\right]^2 D^2(\eta,\eta_0)}{\int {\rm d}^3\mathbf{r}\left[n^{\rm LC}_0(r)\right]^2} \ . \tag{2.52}$$

However, what is also clear, is that as soon as we add in any additional nonlinear terms, there is no effective time for which Eq. (2.51) can be satisfied.

We can get an idea of the error that is incurred by making the unique time approximation by considering the case of standard perturbation theory at the 1-loop level. In this case, if we set $\eta_{\rm eff}$ in accordance with Eq. (2.52), then the first term in the left-hand and right-hand-side expansions of Eq. (2.51) are guaranteed to vanish. The next terms which come from the loop corrections would

thus incur the error:

$$P_{\rm Err}(k,\eta_{\rm eff}^{\rm Lin}) = \left[P_{13}(k,\eta_{\rm eff}^{\rm Lin}) + P_{22}(k,\eta_{\rm eff}^{\rm Lin})\right] \times \left\{1 - \frac{\int {\rm d}^3\mathbf{r}\left[n_0^{\rm LC}(r)\right]^2 \left[D(\eta)/D(\eta_{\rm eff}^{\rm Lin})\right]^4}{\int {\rm d}^3\mathbf{r}\left[n_0^{\rm LC}(r)\right]^2}\right\} . \tag{2.53}$$

If one could guarantee that, on a given scale, a nonlinear correction of a certain order was dominant. Then, one could find a new effective time to evaluate the theory at. For example, if there is a scale where the 1-loop contribution is dominant and the linear and 2-loop corrections are negligible, then one could evaluate the theory at the 1-loop effective time, $\eta_{\rm eff}^{\rm 1-loop}$, defined through solving the relation:

$$D^4(\eta_{\rm eff}^{\rm 1-loop}) = \frac{\int {\rm d}^3\mathbf{r}\left[n_0^{\rm LC}(r)\right]^2 D^4(\eta,\eta_0)}{\int {\rm d}^3\mathbf{r}\left[n_0^{\rm LC}(r)\right]^2} . \tag{2.54}$$

Iterating on this logic, one would thus need a set of effective times for all the scales where the various nonlinear components dominate the clustering signal.

We illustrate the impact of using the different approaches to a fixed-time approximation in Figure 2.3. In both of the plots, we show the unequal-time power spectrum model (solid lines) for increasing survey depth. This is calculated using Eq. (2.38) on large scales, and uses the small-scale approximation of Eq. (2.44) for scales well within the scale of the survey window function. In the left hand plot, we compare this with the mean redshift approximation of Eq. (2.49), and in the right hand plot we instead use the effective redshift (or time) approximation calculated from Eq. (2.52), with both approximations represented by dashed lines[5]. The lower plots in each case show the percentage difference between the full model and the given approximation, with the shaded region showing the $\pm 1\%$ threshold. We see that using the mean redshift approximation results in a k-dependent bias of the power spectrum amplitude, which increases with severity as the survey depth increases. At intermediate scales where there is minimal convolution with the survey window function and non-linear effects are small, this offset is roughly constant due to the fact that the linear power spectrum scales as $D^2(r)$. We notice that the difference grows larger at smaller scales where we pick up non-linear corrections, depending on higher powers of the growth factor. Conversely, from the right hand plot, we see that using the effective time approximation works very well at all but the largest and smallest scales, only deviating from sub-percent level accuracy at these extremities for the deeper survey examples. Therefore, where a fixed time approximation is required to evaluate theory, we strongly advocate the use of Eq. (2.52) to do this.

2.3.7 Extending the theory to the nonlinear regime

Building on the theory from the previous sections, it is straight forward to extend our model for the power spectrum on the lightcone to the non-linear regime, by perturbatively expanding the density

[5]Note that for each of these approximations, the only quantity we are changing when compared to the full UETC model is to evaluate the growth factor at some fixed redshift.

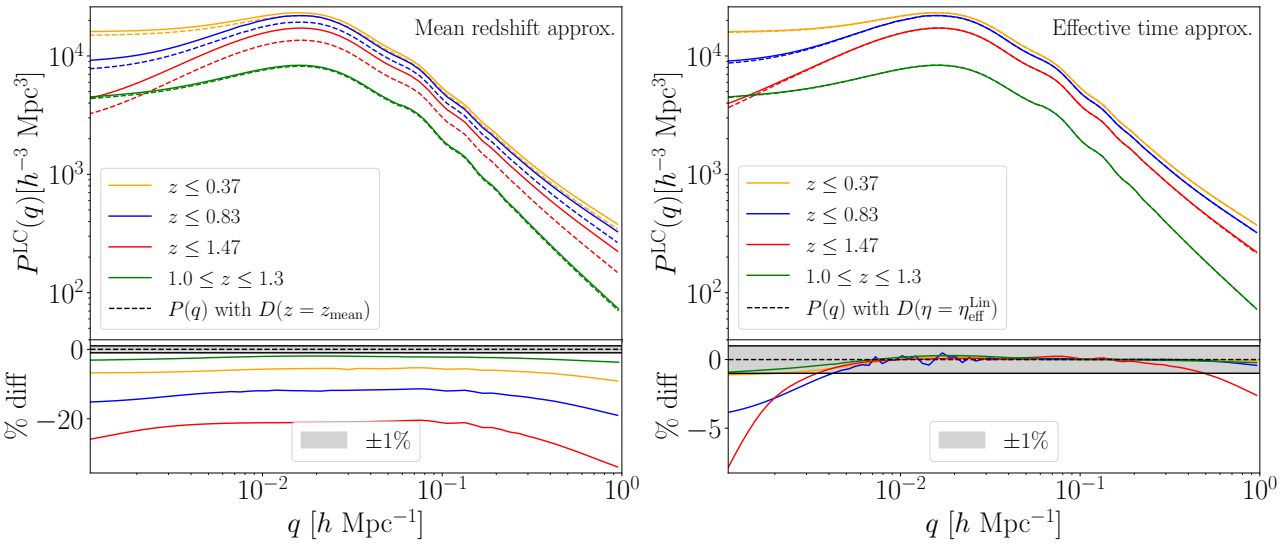

Figure 2.3: Plots showing a comparison between the full unequal-time nonlinear power spectrum model of Eq. (2.38) (solid lines, with colours representing differing survey depths), with various fixed time approximations (dashed lines). In the left hand plot we show the mean redshift approximation of Eq. (2.49), where the power spectrum is evaluated with the growth factor fixed at $D(z = z_{\rm mean})$. The right hand plot instead shows effective time approximation $D(\eta = \eta^{\rm Lin}_{\rm eff})$, calculated from Eq. (2.52). The lower section of each plot shows the percentage difference between the full unequal-time model and the given approximation, with the shaded region showing the $\pm 1\%$ difference. We see that the mean redshift approximation induces a significant scale dependent bias to the power spectrum amplitude, that increases in severity as the redshift depth of the survey increases. The effective time approximation performs much better however, and can achieve sub-percent accuracy over a wide range of scales, only deviating from this at the largest and smallest scales for the deeper surveys (blue and red lines).

field in terms of powers of the growth factor. As we will be in the small-scale limit, we can can use the approximate form of our equation, given by Eq. (2.44), and substitute in the equal-time version of the UETC expansion of the density field, in Eq. (2.36), giving:

$$\begin{aligned} P_{\rm F}(q) &\approx A^2 \int {\rm d}^3\mathbf{r} \left[n_0^{\rm LC}(r)\right]^2 P(q,\eta) \\ &\approx P_{\rm Lin}(q)\mathcal{W}^2 + P_{1-{\rm loop}}(q)\mathcal{W}^4 + P_{2-{\rm loop}}(q)\mathcal{W}^6, \end{aligned} \tag{2.55}$$

where for brevity we have made the definition:

$$\mathcal{W}^i = A^2 \int {\rm d}^3\mathbf{r} \left[n_0^{\rm LC}(r)\right]^2 D^i(r). \tag{2.56}$$

In summary, our final model for the power spectrum on the past lightcone is pieced together using two different models: on large scales, we use the full unequal-time linear model given by Eq. (2.38), and on small scales where the approximation is valid, we use Eq. (2.55). We use `CAMB` to generate the $P_{\rm Lin}$ term, and then use this linear power with FAST-PT [99] to generate the 1-loop term. Finally, as a simple toy model, we take the full `CAMB` non-linear power, and subtract off $P_{\rm Lin}$ and the 1-loop contribution from FAST-PT to get the approximate contribution of the 2-loop term.

These are all generated at $z = 0$ and then scaled as appropriate using powers of the growth factor $D^i(r)$ as indicated above.

2.4 Validation with N-body simulation mock catalogues

We now turn to the issue of validating the derived expressions using galaxy mock catalogues obtained from N-body simulations of the past lightcone. We first detail the N-body data that we use, the process for creating the dark matter lightcone, and then finally the estimator methodology that we use to measure the power spectrum.

2.4.1 Dämmerung Simulation

For construction of the past lightcone we make use of the large-volume simulation from the "Dämmerung Suite" of runs [for full details see 100]. In summary, the cosmological parameters of this run were in accord with the Planck best-fit [101]. The exact cosmological parameter values that were used are: the dark energy equation of state parameters were $w_0 = -1.0$ and $w_a = 0.0$; the dark energy density parameter was $\Omega_{\rm DE} = 0.6914$, which, since the cosmological model was spatially flat, gave a matter density $\Omega_{\rm m} = 0.3086$; the physical densities of cold dark matter and baryons were set to $\omega_c = 0.11889$ and $\omega_b = 0.022161$, respectively; the primordial power spectrum spectral index, amplitude and running were set to $n_{\rm s} = 0.9611$, $A_s = 2.14818 \times 10^{-9}$ and $\alpha = 0.0$, respectively. The linear matter power spectrum was computed using `CAMB` [102], down to $z = 0$. This was rescaled back to the $z = 49$ using the scale-independent matter-only linear growth factor and the initial conditions were lain down using an upgraded version of 2LPT [103].

The N-body simulation was run using the code `Gadget-3` developed for the Millennium-XXL simulation[104, 105]. The large-volume simulation was performed with $N = 2048^3$ dark matter particles, in a comoving box of size $L = 3000\,h^{-1}$Mpc, yielding a mass per particle of $m_{\rm p} = 2.69 \times 10^{11}{\rm h}^{-1}{\rm M}_\odot$. Sixty snapshots were output between $z = 49$ and $z = 0$, with a hybrid linear-logarithmic output spacing that matched the Millennium Run I simulation [51]. The simulation was run on the SuperMUC machine at the Leibniz Rechnum Zentrum in Garching and the full particle data storage was $\sim$20 TB. Haloes and subhaloes were extracted on-the-fly using the built-in `FoF` and `subfind` algorithms. Isolated FoF haloes are identified with at least 15 particles. Thus the smallest dark matter halo in the catalogue has a mass $M_{\rm h}^{\rm min} \approx 4 \times 10^{12}{\rm h}^{-1}{\rm M}_\odot$.

2.4.2 Construction of the past lightcones for dark matter particles

Full details of our method for construction of the past lightcone is described separately in Booth et al. (2021, in preparation). However, the methodology follows in along the same vein as the work of [106], however the precise details differ. Nevertheless, the main steps of the algorithm can be summarised as follows:

- We wish to solve the lightcone crossing equation for each dark matter particle in the N-body

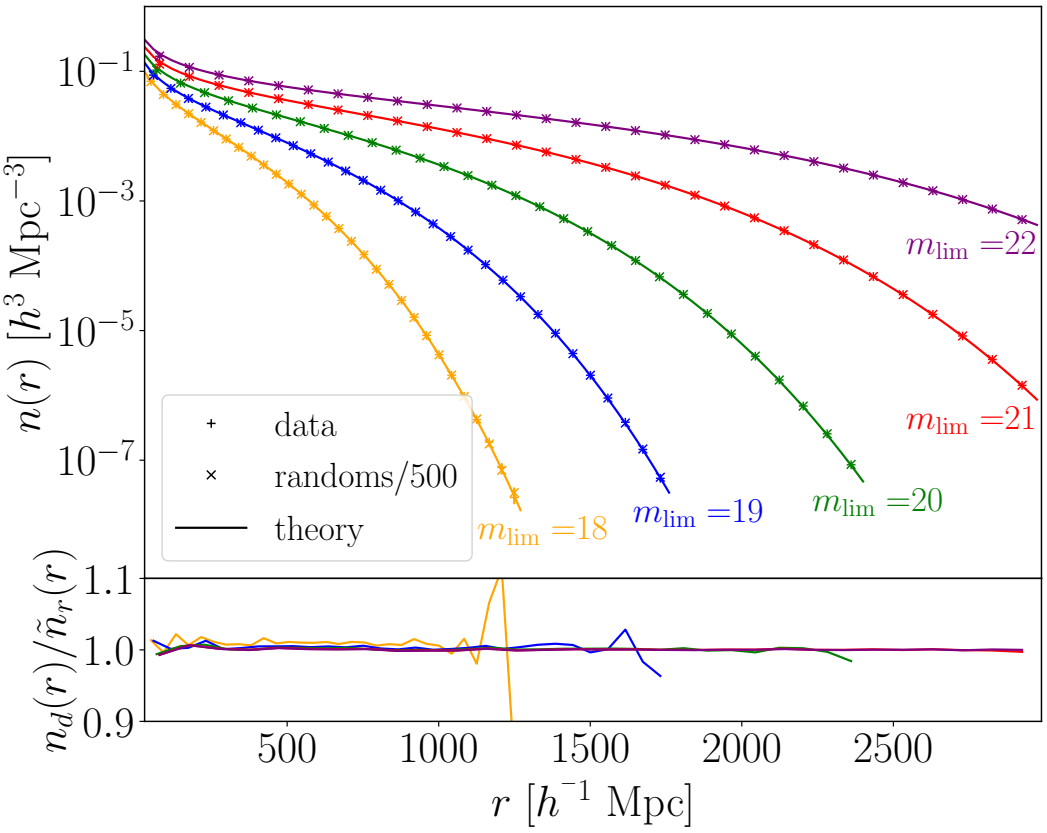

Figure 2.4: Upper: The measured number densities of the data ('+') and random ('x') catalogues from the five magnitude cuts, ranging from 18 in orange to 22 in purple. The theoretical prediction (solid lines) is calculated from the integral of the evolving Schechter function in Eq. (2.99). Lower: The ratio between the data and random $n(r)$ distributions. Note: as there are 500 times as many random points as data points, we have plotted $\tilde{n}_r(r) = n_r(r)/500$ for easier comparison in both plots).

simulation. For the kth particle we want to solve the equation

$$|\mathbf{r}_k(\chi, \theta, \phi, t^{\rm c}) - \mathbf{r}_{\mathcal{O}}| = \int_{t^{\rm c}}^{t_0} \frac{cdt}{a(t)} \,, \tag{2.57}$$

for the time $t^{\rm c}$, which gives the coordinate time when the particle exits the past lightcone. Where $\mathbf{r}_k$ is the world line of the particle and $\mathbf{r}_{\mathcal{O}}$ is the observers location.

- To solve the above equation, we need to reconstruct the full world line of each particle. We do this in a piece wise fashion by using a Taylor expansion up to cubic order in look-back time to interpolate the particle positions and velocities between neighbouring snapshots. The parameters of the Taylor expansion are fixed using the particle positions and velocities at the snapshots. For example, the equation for the Cartesian x component of the particle world

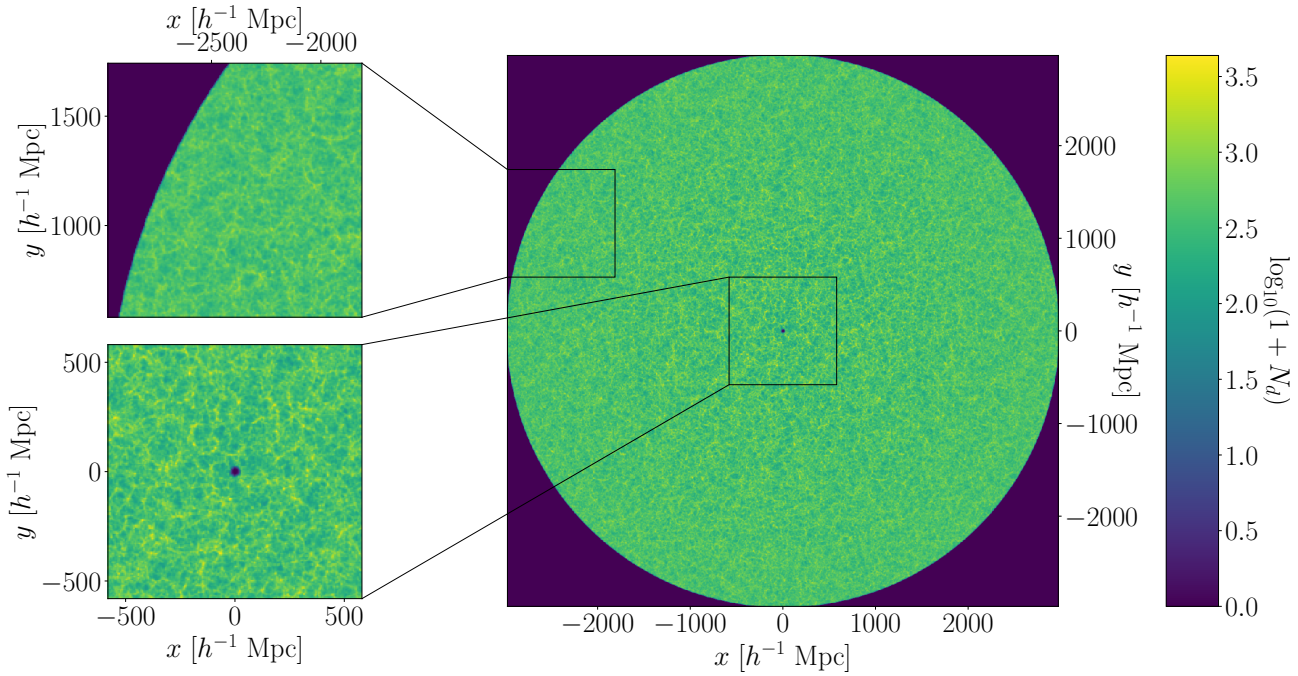

Figure 2.5: A 40 h^{-1} Mpc thick slice through one realisation of the lightcone, including zoom regions near the edge and the centre of the catalogue. The lightcone spans a redshift range of $z = 0$ at the centre to $z \approx 1.45$ at the edge. We can clearly see the difference in structure formation between the two zoom regions, with the lower redshift plot (bottom left) displaying more evolved filaments, clusters and voids.

line is:

$$x(t) \approx \overline{X} - \frac{\Delta V \Delta T}{8} + \frac{\left(3\Delta X - \overline{V}\Delta T\right)}{2}\left(\frac{t-\overline{T}}{\Delta T}\right) + \frac{\Delta V \Delta T}{2}\left(\frac{t-\overline{T}}{\Delta T}\right)^2 - 2\left[\Delta X - \overline{V}\Delta T\right]\left(\frac{t-\overline{T}}{\Delta T}\right)^3 , \tag{2.58}$$

where $\overline{T} \equiv (t_i + t_{i+1})/2$ and where $\delta t = t - \overline{T}_i$ with t_i and t_{i+1} being the lookback times to the neighbouring snapshots, with $t_i < t_{i+1}$. Also we have defined $\overline{X} \equiv (x_i + x_{i+1})/2$, $\Delta X \equiv x_{i+1} - x_i$, $\overline{V} \equiv (v_{i+1} + v_i)/2$, and $\Delta V \equiv v_{i+1} - v_i$, with (x_i, v_i) and (x_{i+1}, v_{i+1}) referring to the particle's position and velocity for the neighbouring snapshots, respectively. In Booth et al. (2021, in prep.) we show that for our simulation we can do this to an accuracy of $r \sim 100\,h^{-1}$kpc, for all particles.

We apply the above algorithm to generate 8 different dark-matter particle lightcones, where we have set the different observer locations to be the vertices of a cubical lattice of side $L/2 = 1500\,h^{-1}$Mpc. The data footprint of each particle lightcone is roughly 2TB. While these lightcones are not fully independent, on scales smaller than $r < L/4$ they have no repeated structures and thus for shallower surveys can be considered independent from one another. The further advantage of doing this for the deeper lightcones is that one averages over similar structures, but at different epochs. Nevertheless, in what follows while we will present the mean statistic averaged over the

8 quasi-independent lightcones, we will compute the errors on the observables using the Gaussian theory estimates.

2.4.3 Constructing the galaxy past lightcone

We would like to be able to explore how well the theory from the previous sections works for a galaxy sample that would be comparable to that for the Bright Galaxy Sample (hereafter BGS-like) from DESI or the 4MOST CRS. However, owing to the fact that the large-volume "Dämmerung run" does not have sufficient resolution to resolve the typical halo masses in these surveys, we have therefore decided to adopt a the simplified strategy of assuming that the BGS-like galaxies are simply a Poisson sampling of the dark matter particles. However, we introduce realistic radial selection functions to emulate the effects of the flux-limits that we adopt.

Our mock galaxy recipe follows the following steps:

1. Adopt a magnitude limit, $m_{\rm lim}$ and set the bounding redshifts $z_{\rm min}$ and $z_{\rm max}$ for the survey.

2. We next assume a functional form for the (evolving) galaxy luminosity function of the survey. The number density of particles in the dark matter past lightcone sets the maximum density of galaxies that we may have in the mock catalogue, such that:

$$\bar{n}_{\rm max}(r_{\rm min}) \leq \int_{\rm L_{min}(r_{min})}^{\infty} \phi(L|r_{\rm min})dL \ . \tag{2.59}$$

   As can be seen this then imposes the minimum luminosity that a galaxy could have and make it into the survey.

3. To each dark matter particle in the lightcone we now sample a luminosity from our desired GLF following the methodology outlined in Appendix 2.B.2.

4. For the specified flux-limit, and for a given particle with redshift z, we then use the minimum luminosity that a galaxy could have at that distance and be contained in the survey, given by

$$\left[L_{\rm min}(\mathbf{r})/h^{-2}L_{\odot}\right] = 10^{-\frac{2}{5}(m_{\rm lim}-25-M_{\odot})}\left[d_{\rm L}(\mathbf{r})/\,h^{-1}{\rm Mpc}\right]^2 \ , \tag{2.60}$$

   where $M_{\odot}$ is the absolute magnitude of the sun. This step is most efficiently done through creating a cubic-spline of this function. We then include or exclude the potential mock galaxy (particle) based on whether it passes the criteria its luminosity should satisfy $L \geq L_{\rm min}(\mathbf{r})$.

5. This process is repeated for all of the flux-limit samples of interest.

We also generate unclustered mock random data sets to go alongside these magnitude-cut catalogues, for use in our power spectrum measurements. These random catalogues are created by distributing points uniform-randomly in a sphere of radius $r_{\rm max} = 3$Gpc, and then sampling magnitudes using the same method as above and making matching apparent magnitude limit cuts

List of simulated catalogues			
$m_{\rm lim}$	Avg. N_d	z range	χ range $[h^{-1}\text{Mpc}]$
None	35.0×10^9	$0.01 \leq z \leq 1.45$	$30 \leq \chi \leq 2974$
18.0	4.6×10^6	$0.01 \leq z \leq 0.36$	$30 \leq \chi \leq 975$
19.0	16.7×10^6	$0.01 \leq z \leq 0.53$	$30 \leq \chi \leq 1390$
20.0	60.0×10^6	$0.01 \leq z \leq 0.81$	$30 \leq \chi \leq 1950$
21.0	212.8×10^6	$0.01 \leq z \leq 1.24$	$30 \leq \chi \leq 2680$
22.0	756.0×10^6	$0.01 \leq z \leq 1.45$	$30 \leq \chi \leq 2974$

Table 2.1: List of the particle count N_d in each of our magnitude cut catalogues, where we have taken the average over the 8 realisations for each cut. We also list the effective ranges of redshift and comoving distance that the catalogues cover, where the upper bounds on these ranges signify where the $n(r)$ drops 4 orders of magnitude below its peak value, if this is less than the maximum range of $2974h^{-1}$Mpc (see Fig. 2.4).

– one small difference though, is that we omit Step ii and use the same $L_{\rm min}(r)$ as the clustered catalogue to sample luminosities with. This process is iterated for each cut, until we have 5 mock random catalogues, which match the overall survey geometry of their data counterparts, but with $N_{\rm rand} \simeq 500 N_{\rm data}$ for each.

In Figure 2.4 we show the resultant number densities of the different apparent magnitude-cut catalogues for both the data and the randoms. Here we also show the expected theoretical prediction given by Eq. (2.99). In Table 2.1, we list some useful properties (averaged over the 8 realisations) of each catalogue.

In Figure 2.5 we show a slice through one of our full-sky dark matter lightcones and several zoom-in regions, which shows how the strength of the large-scale structure drops off as one gets to the outer rim of the sphere.

2.4.4 The power spectrum estimator

We use the FFT method of estimating the power spectrum, based on the work in [78] and [107], which we summarise here. Both data and random catalogues are interpolated onto separate 1024^3 grids using a Triangular-Shaped-Cloud (TSC) mass assignment scheme. To reduce the effects of small scale aliasing caused by finite grid resolution [108] we employ the method of interlacing as covered in [109][6]. In that work, they demonstrate that combining TSC assignment with interlacing is able to measure the power spectrum of N-body simulation data in a periodic box to sub 0.1% accuracies, right up to the Nyquist frequency of the grid. In our case, as we are testing on simulated galaxy data contained in a survey window, we note that it is important to interlace both the data *and* the random catalogues to get the full benefits of interlacing on small scales, while also being able to accurately measure the large scale modes. The offset grids used in interlacing are created by

[6]Grid aliasing is caused by the FFT grid sampling smaller scale modes than are actually supported by the grid, leading to spurious contributions to the FFT-determined Fourier coefficients. This causes an uptick in power for $k \gtrsim k_{\rm Nyq}/2$, and so not correcting for this effect leads to a decrease in the number of k modes that one is effectively able to probe.

taking the original data sets, and displacing each particle by $\{+l_x/2, +l_y/2, +l_z/2\}$ before painting them to a grid, where l_i is the length of an individual grid cell in the x_i Cartesian direction. We thus have 4×1024^3 grids for each measurement: $n_d(\mathbf{x})$, $n_r(\mathbf{x})$, $\hat{n}_d(\mathbf{x})$ and $\hat{n}_r(\mathbf{x})$, where n_d represents our data points, n_r is the random points, and the hat signifies an offset grid for interlacing. For convenience, we normalise our random grids such that $\sum_i n_r(\mathbf{x}_i) = 1$ and make the definition of a survey window grid as $W(\mathbf{x}) = N_d n_r(\mathbf{x})$. Here, N_d is the total number of data particles on the grid. Our process for calculating the power spectrum is as follows:

1. We take the FFT of the galaxy overdensity field and its offset counterpart:

$$\widetilde{F}_{G1}(\mathbf{k}) = A\sum_x w(\mathbf{x})[n_{\rm d}(\mathbf{x}) - W(\mathbf{x})]\exp(i\mathbf{k}\cdot\mathbf{x}), \tag{2.61}$$

$$\widetilde{F}_{G2}(\mathbf{k}) = A\sum_x \hat{w}(\mathbf{x})[\hat{n}_d(\mathbf{x}) - \hat{W}(\mathbf{x})]\exp(i\mathbf{k}\cdot\mathbf{x}). \tag{2.62}$$

   Here, $w(\mathbf{x})$ is the FKP weight function:

$$w(\mathbf{x}) = \frac{1}{1+\bar{n}(\mathbf{x})P_0} = \frac{1}{1+\overline{W(\mathbf{x})}P_0}, \tag{2.63}$$

   designed to maximise the signal to noise[7], and A is the normalisation:

$$A = \Big[\sum_x W^2(\mathbf{x})w^2(\mathbf{x})\Big]^{1/2}. \tag{2.64}$$

2. To perform interlacing, we then take the average of these two fields in Fourier space, while taking into account an additional phase factor[8] for the offset grid:

$$\widetilde{F}_G(\mathbf{k}) = \frac{1}{2}\big[\widetilde{F}_{G1}(\mathbf{k}) + \widetilde{F}_{G2}(\mathbf{k})\exp(-i\mathbf{k}\cdot\Delta\mathbf{x}_{\rm lattice})\big]\ , \tag{2.65}$$

   where $\Delta\mathbf{x}_{\rm lattice} \equiv (l_x\mathbf{i} + l_y\mathbf{j} + l_z\mathbf{k})/2$ in the radial direction. Note that for our case we are setting $l_x = l_y = l_z = L/N_{\rm grid}$.

3. To be able to accurately recover the small scale clustering, the TSC mass assignment window, $W_{\rm TSC}(\mathbf{x})$, needs to be deconvolved from the resultant field. As this is a convolution between the particles and the mass assignment window function in position space, which has then been Fourier transformed, this convolution is thus simply a multiplication in Fourier space, and so a division of the F.T. of the window will correct for this effect. For TSC assignment, this window function in Fourier space is given by [110]:

$$W_{\rm TSC}(\mathbf{k}) = \Big[\frac{\sin(k_{x,\rm N})}{k_{x,\rm N}}\frac{\sin(k_{y,\rm N})}{k_{y,\rm N}}\frac{\sin(k_{z,\rm N})}{k_{z,\rm N}}\Big]^3 \tag{2.66}$$

[7]Note that $\overline{W(\mathbf{x})}$ signifies a spherical average of the window function i.e. the spherically-averaged number density of the synthetic randoms catalogue.

[8]This additional factor comes from the shift theorem of the Fourier transform.

where $k_{i,\mathrm{N}} = \pi k_i / 2k_{\mathrm{Nyq,i}}$. Therefore, we can recover the deconvolved field with the operation:

$$F_G(\mathbf{k}) = \frac{\widetilde{F}_G(\mathbf{k})}{W_{\mathrm{TSC}}(\mathbf{k})}. \tag{2.67}$$

4. The last ingredient of the estimator is to calculate and subtract off the normalised shot noise, given by

$$P_{\mathrm{shot}} = A^{-2} \sum_x W(\mathbf{x}) w^2(\mathbf{x}). \tag{2.68}$$

   We also make sure to model and subtract this off of our theoretical predictions.

5. Finally, we define our estimator of the power spectrum as

$$\hat{P}(\mathbf{k}) = |F_G(\mathbf{k})|^2 - P_{\mathrm{shot}}, \tag{2.69}$$

   which we will measure in logarithmic bins between the fundamental mode and the Nyquist frequency of the grid. This estimate is therefore the shot-noise corrected, survey-window-convolved power spectrum which we can directly compare with our predictions for the convolved power spectrum on the lightcone, as described in §2.3.2.

2.4.5 Statistical fluctuations in the power

For the covariance, we shall simply take Eqn (20) from [107]:

$$\langle \delta P(\mathbf{k}_i) \delta P(\mathbf{k}_j) \rangle = \frac{2A^4 \sum_{\mathbf{k}_i, \mathbf{k}_j} |P_i Q(\mathbf{k}_i - \mathbf{k}_j) + S(\mathbf{k}_i - \mathbf{k}_j)|^2}{N_{\mathbf{k}_i} N_{\mathbf{k}_j}}, \tag{2.70}$$

where $N_{\mathbf{k}_i}$ is the number of modes in a given bin and the equations for $Q(\mathbf{k})$ and $S(\mathbf{k})$ are given by:

$$Q(\mathbf{k}) = \sum W^2(\mathbf{x}) w^2(\mathbf{x}) \exp(i\mathbf{k} \cdot \mathbf{x}) \ , \tag{2.71}$$

$$S(\mathbf{k}) = \sum W(\mathbf{x}) w^2(\mathbf{x}) \exp(i\mathbf{k} \cdot \mathbf{x}) \ . \tag{2.72}$$

It is worth pointing out that Eq. (2.70) assumes that the Fourier coefficients $F_{\mathrm{G}}(k)$ are Gaussian-distributed. While Eq. (2.70) shows that modes in different k-bins *do* become correlated with each other, in the limit that the survey window function is sufficiently compact, centred on each bin, we see that the diagonal covariance approximation will be accurate on scales that lie sufficiently within the survey window. However, for larger scales it will be an under-estimation of the true error. This leads us to the following approximate form of the covariance (FKP Eqn. (2.2.6)):

$$\left\langle \delta P(\mathbf{k}_i)^2 \right\rangle \simeq \frac{2A^4}{N_{\mathbf{k}}} |P(\mathbf{k}_i) Q(\mathbf{k}_i) + S(\mathbf{k}_i)|^2. \tag{2.73}$$

2.4.6 Implementation and Validation of Estimator code

We have implemented our estimator algorithm in Python 3.6[9], making use of `NumPy` [111], `SciPy` [112], `AstroPy` [113], `Numba` [114], and the python wrappers for MPI [115] and FFTW [116]. All code was run on the Cosma7 partition of the Cosma HPC, part of the DiRAC supercomputer facilities hosted at Durham University.

To test the accuracy of the code, we first use it to measure the power spectrum of some of the original Dämmerung Simulation redshift snapshots, where our results can easily be compared to the output of `CAMB` nonlinear power spectra at the specified redshift, as well as the power measured by `GADGET-4` [117]. We perform the measurements in 25 logarithmically spaced bins, where the upper and lower bin edges are set to match the largest and smallest modes supported by the box, giving bin edges such that $0.0021\,h\,\mathrm{Mpc}^{-1} \leq k \leq 1.07\,h\,\mathrm{Mpc}^{-1}$, and bin width $\log_{10}(\Delta k/[\,h\,\mathrm{Mpc}^{-1}]) = 0.108$.

Figure 2.6 presents the results from these tests, where we measure the power spectrum at redshifts $z = 0.0$ and $z = 1.5$, which is the approximate redshift range spanned by our lightcone simulations. We see excellent agreement between our measurements and the nonlinear prediction from `CAMB` and `GADGET` across all scales. Note that the error bars are based on Eq. (2.73) and that we have computed the spectrum all the way to the Nyquist frequency of the Fourier mesh with no resultant boost in power which is characteristic of aliasing effects.

This gives us confidence that the estimator methodology is working as desired, and we now move on to tackle the analysis of the lightcone data.

2.4.7 Measurements of the mock lightcone survey catalogues

We measure the power spectrum for the 8 pseudo-independent realisations of our lightcone catalogue, in the 5 different apparent magnitude limited mock galaxy catalogues that we have created. This gives us a total of 40 sets of measurements. As with our testing on the individual Dämmerung Simulation snapshots, we measure the power in 25 logarithmically spaced bins, but this time in the reduced k-range of $0.0042\,h\,\mathrm{Mpc}^{-1} < k \leq 0.54\,h\,\mathrm{Mpc}^{-1}$. Thus giving a k-bin width of $\log_{10}(\Delta k/[\,h\,\mathrm{Mpc}^{-1}]) = 0.0844$. The range reduction in the nonlinear regime is due to the length of this box being twice the size of the original Dämmerung Simulation box, thus halving the Nyquist frequency of the FFT grid. We set the lowest frequency bin to the fundamental frequency of the base simulation $k_\mathrm{f} = 2\pi/(1500h^{-1}\mathrm{Mpc}) \approx 0.0042\,\mathrm{h\,Mpc}^{-1}$. For wavemodes below this scale the box replication becomes relevant and we would expect repeated structures to appear on the same lightcone, despite existing at different stages of evolution.

2.5 Results and Discussion

The results of our power spectrum measurements, averaged over the 8 realisations for each of the 5 magnitude cuts, is shown in Fig. 2.7 (error bars) as well as our prediction from the theory as out-

[9](Python Software Foundation, https://www.python.org/ .)

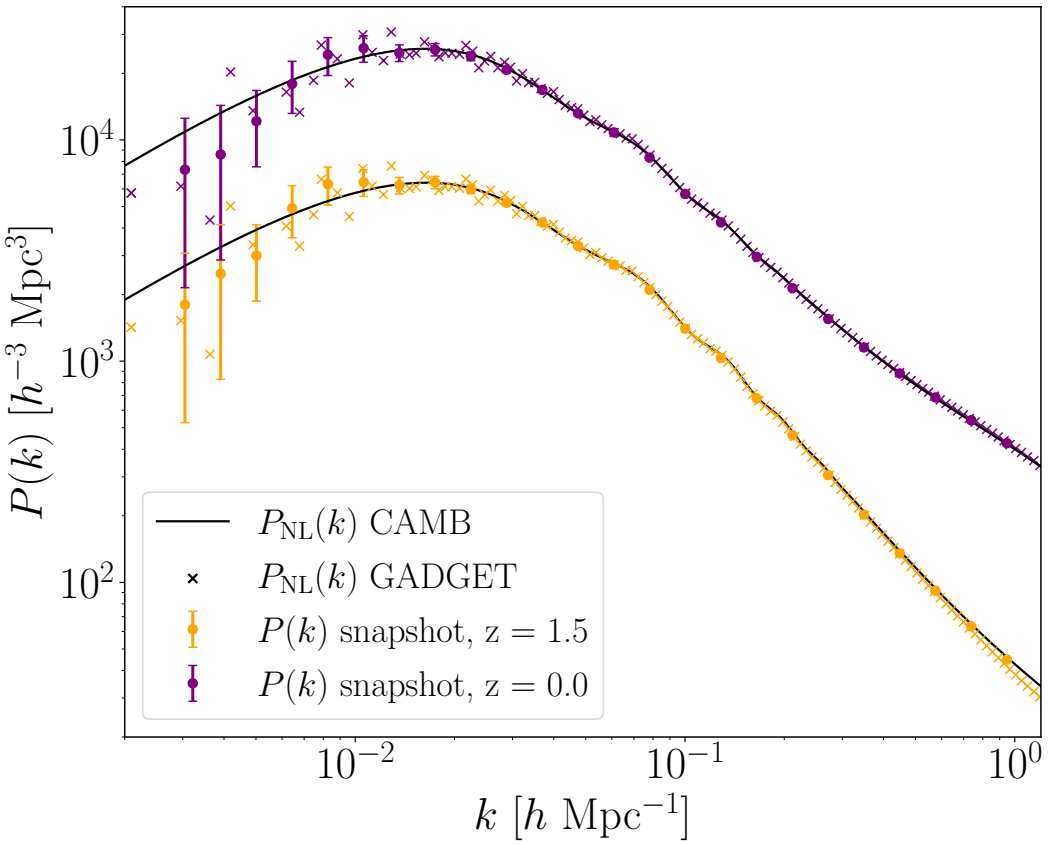

Figure 2.6: Measurements of the power spectrum from individual Dämmerung snapshots at the redshifts of $z = 1.5$ (orange markers) and $z = 0$ (purple markers) using our estimator code, compared with the nonlinear matter $P(k)$ from `CAMB` (solid lines), and measurements from the snapshots performed by `GADGET-4` ('x' markers). Our measurements are in very good agreement with `CAMB` and `GADGET` at all scales, with only some minor deviation around $k \sim 1\ h/\text{Mpc}^{-1}$ for the higher redshift measurement. At large scales just beyond the turnover, we see a slight up-kick in power - the imprint of this cosmic variance can be seen in the lightcone measurements in Fig. 2.7.

lined in §2.3 (solid lines). For this first set of measurements we do not include any optimal weights, equivalent to setting P_0 to zero in Eq. (2.63), so as to form a baseline of measurements for comparison. The bottom right subplot of the figure shows the ratio between the measurements and theory, as shaded regions spanning the width of the measurement error bars, for the $m_{\rm lim} = \{18, 20, 22\}$ catalogues. In this plot we also show the $\pm 5\%$ difference between theory and measurement as the shaded grey horizontal region. For all of the magnitude cuts, we see that the theory lies well within the error bars of the measurements at all scales, right up to the Nyquist frequency of the grid. We do see some slight dipping of the estimated power starting to occur beyond scales of around $k \geq 0.2\ [h\ \text{Mpc}^{-1}]$, most likely due to inaccuracies of our modelling of the 2-loop corrections to the theory as detailed in §2.3.7.

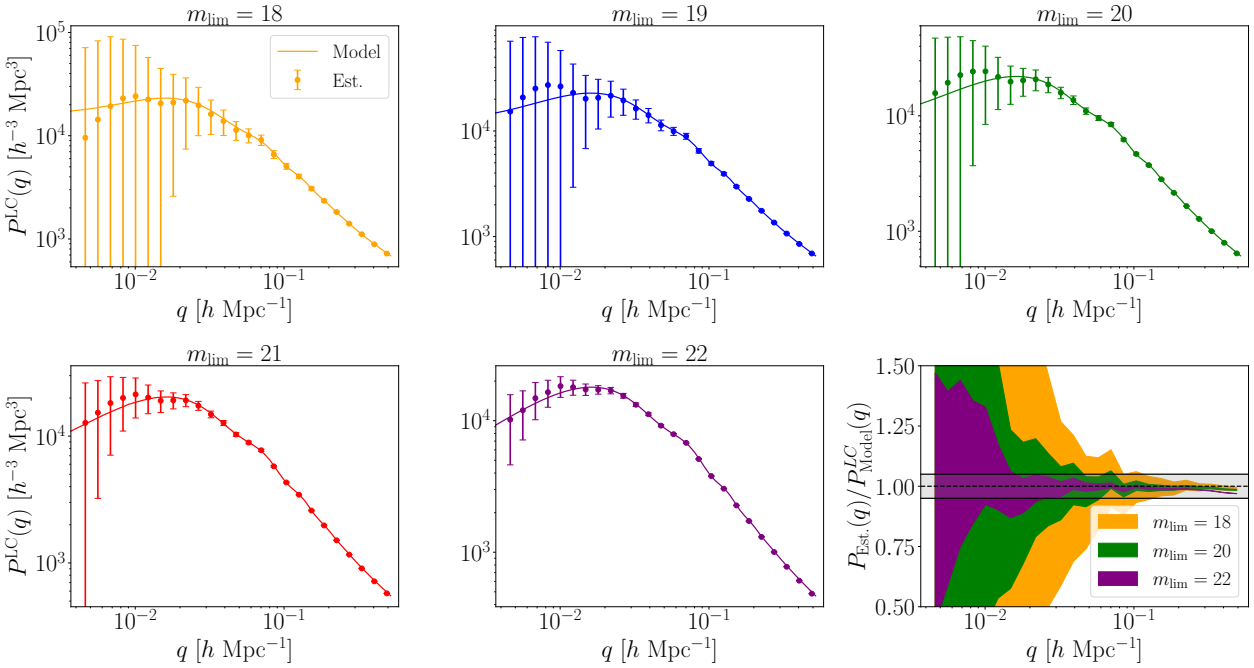

Figure 2.7: Upper and left: Plots of the power spectrum measurements (points with error bars) from the 5 different magnitude cut catalogues, compared with the predictions from the theory (solid line). Bottom right: Ratio plots comparing the measurements to the model for 3 of the catalogues, with 5% difference in the shaded grey region.

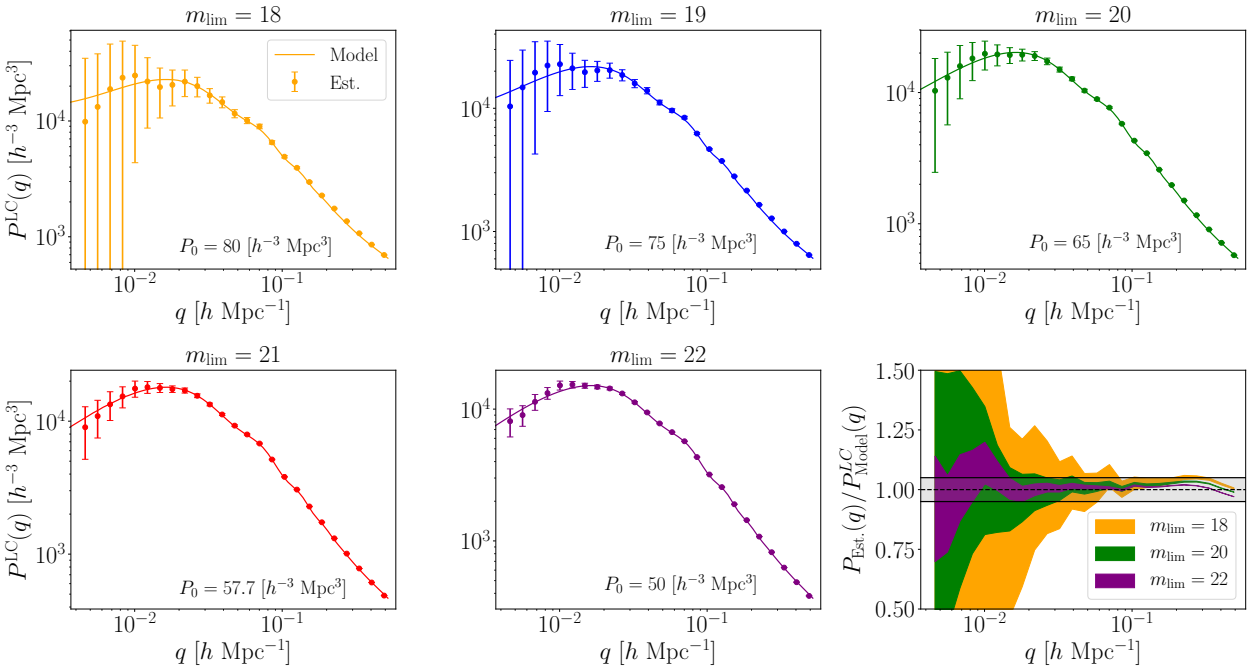

Figure 2.8: Same as Fig. 2.7 but with FKP weights, with the choice of P_0 indicated on each figure.

2.5.1 The effect of optimal weights

The idea of including a weighting scheme in power spectrum analysis was first explored in [78], where they showed that weighting a galaxy in a way that was inversely proportional to the mean number density of the survey at the galaxy's position could improve the signal to noise of the measurement, with a weighing function of the form

$$w_{\rm FKP}(\mathbf{r}) = \frac{1}{1+\bar{n}(\mathbf{r})P_0}. \tag{2.74}$$

The idea behind this weighting scheme is simple: for small r, we have a high number density per unit volume, and so are cosmic variance limited and want to give equal weight to each measurement volume. Conversely at large r where the galaxy field is much more sparsely populated, we are shot noise limited and want to give equal weight per galaxy. This FKP weighting function was derived under the assumptions that the long wavelength Fourier modes are Gaussian distributed, and results in a minimum-variance estimator which tackles both aforementioned issues, and has been used extensively in galaxy survey measurements such as 2dF [118], SDSS [119], 6dF [120], BOSS [121] and WiggleZ [107]. Other, more elaborate weighting schemes have been discussed in the literature, such as those of PVP [81] which depend on position and luminosity, or those of [82, 122] which depend on position and host halo mass.

For our analysis, we opt to use the straight-forward FKP weights[10], and repeat the measurements of the last section, but now using Eq. (2.63) in our estimator and Eq. (2.74) in the modelling of the theory. For each catalogue we chose P_0 such that it matches the total shot noise of the unweighted measurements in Fig. 2.7, as we find at this scale we get a significant gain in the signal to noise of the measurements, without overly affecting the shape of the measured power. The effects of including this optimum weighting scheme are shown in Fig. 2.8, where we see a great reduction in error bars when compared with the unweighted measurements. As with the unweighted case, we do start to see some issues between the theory and measured power at the nonlinear scales, around $k \approx 0.2h\mathrm{Mpc}^{-1}$ and above, where the measured power starts to peak and then fall off, while still remaining in the $\pm 5\%$ region.

We also investigate how the choice of P_0 effects the resulting $P(\mathbf{k})$ estimate, by taking measurements on the smallest and largest catalogues, for various values of P_0, which are shown in Fig. 2.9. In this figure, we plot the shape of the weight function (left), the resulting power spectrum measurement (centre) and the boost gained in signal to noise for including the FKP weight (right), with the upper and lower rows representing different catalogues. The value of P_0 should be chosen so that $w_{\rm FKP}(\mathbf{r})$ slowly but consistently varies over the radial depth of the survey, down weighting those points in high density regions, and up weighting those where the survey is more sparse. If P_0 is set too high, then the majority of particles in the box will be close to zero weighted, except those at the outer edges. In this case (red points in Fig. 2.9), the shape of the power spectrum starts to

[10] We do not resort to these more elaborate weighting schemes in this work due to the fact that we are studying unbiased galaxies in our simulated data sets.

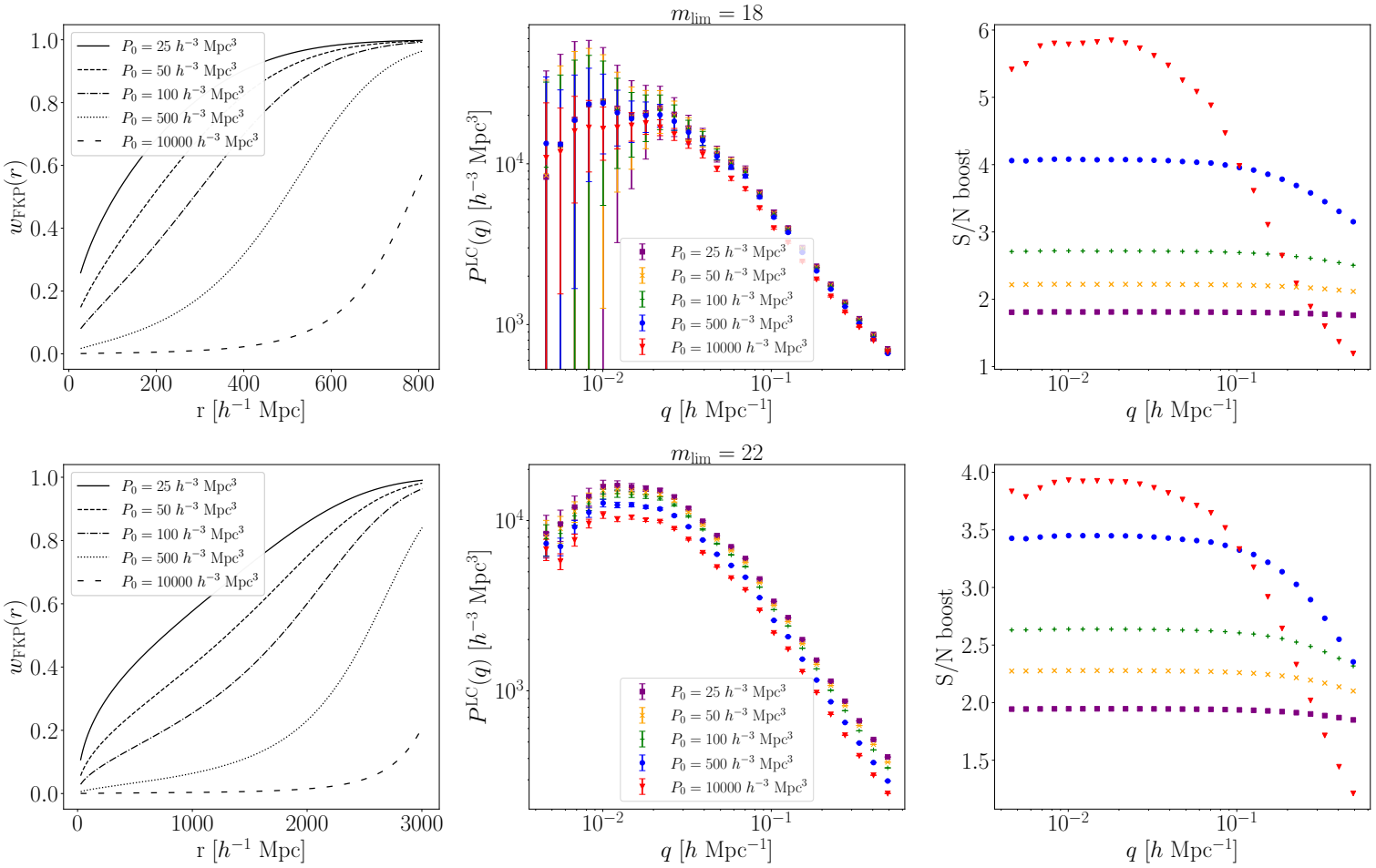

Figure 2.9: Plots demonstrating how varying the P_0 parameter in the FKP weight function in Eq. (2.63) effects the power spectrum analysis. The top (bottom) row relates to the magnitude cut 18 (22) catalogues. Left: A plot of the FKP weight function for various values of P_0. Centre: Measurements of the power spectrum. Right: The boost in the signal to noise of the power spectrum measurement when using these FKP weights. We begin to see diminishing returns in the signal to noise gain as P_0 increases, at the nonlinear scales. In this scenario we also start to see a slight boosting of power at the largest scales.

get mildly distorted (boosted) on large scales, and we also start to see diminishing returns in the signal to noise gain at nonlinear scales. Conversely, if P_0 is set too small then almost all the points have the same weights and provide almost no benefit. We see that in both cases, similar choices of P_0 provide similar gains in the signal to noise. We note that our used values of P_0 are at least an order of magnitude smaller than those used for surveys like BOSS ($P_0 \simeq 10000h^{-3}{\rm Mpc}^3$) [121] or WiggleZ ($P_0 = 2500h^{-3}{\rm Mpc}^3$) [107] due to our number density being significantly higher.

2.5.2 FFT grid resolution tests

Owing to the fact that our full-sky lightcones are non-periodic functions, it is interesting to examine whether there is any impact of grid-resolution, and thus, aliasing effects on the estimated power spectra. We examine this by focusing our attention on the deepest $m_{\rm lim} = 22$ galaxy catalogue and

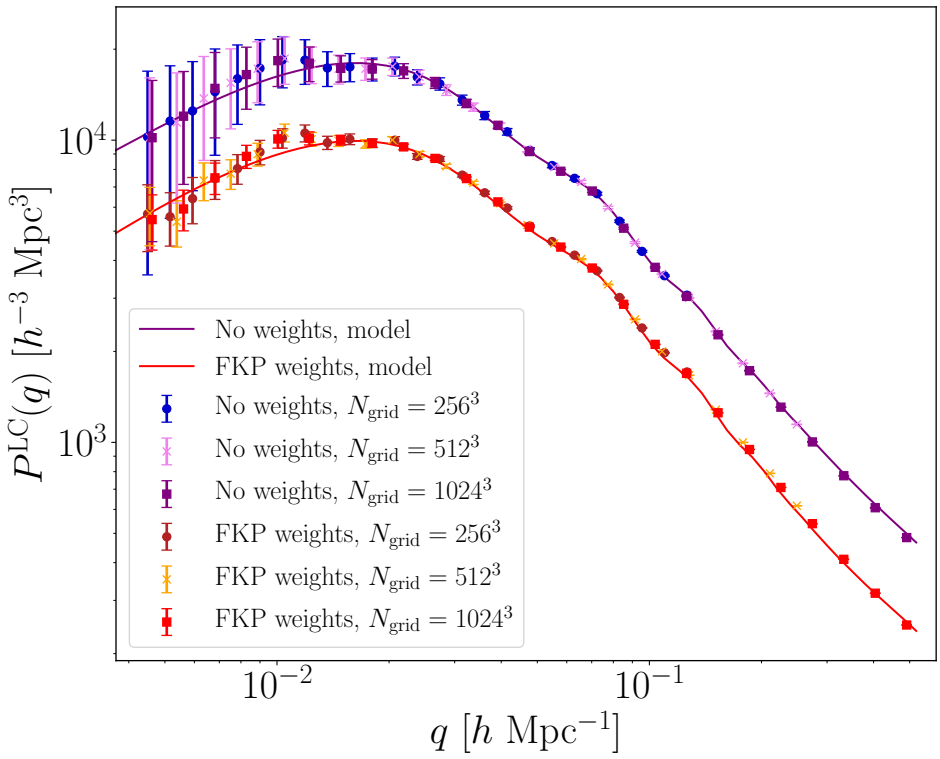

Figure 2.10: Plot showing the effect of varying the grid resolution on the power spectrum measurements. We show estimates from using 256^3, 512^3 and 1024^3 FFT grids, for both unweighted (blue hues) and FKP weighted (red hues) data, using the $m_{\rm lim} = 22$ catalogue, as well as the theoretical predictions (solid lines). Aside from a different available k range of measurements, we see that grid resolution has little effect on the resulting measured power. Note that weighed measurements and model have been offset by a factor of 0.7 in the vertical direction for clarity.

fixing the weighting scheme and varying the FFT grid dimension.

Figure 2.10 shows the results of this exercise for the three grid resolutions $N_{\rm grid} = 256^3$, 512^3 and 1024^3 and for the case of equal weights and FKP weights, with $P_0 = 100h^{-3}{\rm Mpc}^3$. We see that the estimates for the different grid resolutions are in excellent agreement, showing a close grouping for both the weighted and unweighted cases. We also show again our theoretical predictions from §2.3.2 for the case of the equal weight and FKP weighting. These results indicate that the small-scale discrepancies, noted earlier, are most likely caused by issues with the nonlinear modelling, as opposed to any effects from aliasing or the interlacing with the TSC mass assignment.

2.5.3 Measuring the turnover scale

One of the exciting aspects of being able to measure the power spectrum on large scales is it presents us with the opportunity to probe the epoch of matter-radiation equality in the early universe. The imprint of this epoch can be directly linked to the peak power spectrum: the theory

of inflation predicts that the primordial matter power spectrum should possess a simple power-law of the form, $P_{\rm Prim}(k) \propto k^{n_{\rm s}}$. However, as the Universe expands from this hot-dense state, fluctuation growth inside the horizon is suppressed by radiation pressure support and also radiation dominated expansion – the 'Mézáros Effect' (for a detailed treatment see [8]). The consequence of this is that the peak point of the power spectrum, located at k_0, corresponds to the size of the cosmological horizon at the epoch of matter-radiation equality, and its measurement thus allows us to constrain the redshift of this epoch, which in turn is sensitive to both the matter density and Hubble parameters through the combination $\Omega_m h^2$, amongst other parameters.

To explore the detectability of this scale on the past lightcone we shall employ the framework that was developed by [95], and then employed and further refined [123], where they applied the process to the WiggleZ Dark Energy Survey[11] to measure $\{k_0, z_{\rm eq}, \Omega_m h^2\}$. We follow their process for ease of comparison between works, and refer the reader to these papers for full details, but in summary the process is as follows. The power spectrum is modelled as a piecewise power law of the form[12]:

$$\log_{10} P(k) = \begin{cases} \log_{10}\left[P_0(1-\alpha x^2)\right] & \text{if } k < k_0, \\ \log_{10}\left[P_0(1-\beta x^2)\right] & \text{if } k \geq k_0, \end{cases} \tag{2.75}$$

where

$$x \equiv \frac{\ln k - \ln k_0}{\ln k_0}, \tag{2.76}$$

P_0 is the power spectrum amplitude at turnover, and α and β are parameters that define the slope of the power spectrum on either side of the turnover (the point where $k = k_0$). We fit three different sets of power spectra to this model:

- The measured $P(k)$ from our magnitude cut catalogues, as described in §2.4, with no weights (Fig. 2.7).
- The same $P(k)$ but with FKP weights. (Fig. 2.8)
- We also fit directly to the theoretical predictions, given by the solid lines in Fig. 2.8, and using the error bars from the associated measured power (the error bars of the points in the same figure). We use this as a test case to see how easy or difficult it is to measure the turnover scale, if we assume that we can measure the power to a very high degree of accuracy.

The maximum *a posteriori* parameters for the turnover model of Eq. (2.75) are obtained through use of the MCMC algorithm. To do this we make use of the Python package `emcee` [124], which implements an affine-invariant ensemble MCMC sampler. We use 1000 walkers, with an initial

[11] https://wigglez.swin.edu.au/

[12] We chose to model the power in log space as it is a much more slowly varying function in this basis, which will avoid any rapid changes in values for the MCMC walkers.

Parameter	Min	Max
$\log_{10} P_0$	3	5
k_0	5×10^{-3}	0.05
α	-5	10
β	-5	10

Table 2.2: List of allowed ranges for the parameters in the simple power spectrum model listed in equation Eq. (2.75), used to determine the turnover scale. Note, for the no-turnover case, α is set to 0. All ranges are uniform (flat).

burn-in stage of 1000 steps, followed by 10^5 iterations per walker to explore the parameter space giving 10^8 total propositions. We also adopt a Gaussian likelihood model:

$$\ln \mathcal{L} = -\frac{1}{2} \sum_n \frac{(y_n - x_n)^2}{\sigma_n^2} + \ln \sigma_n^2 \ , \tag{2.77}$$

where y_n and σ_n are the measured power spectrum and error bars, and x_n is the fitted power using Eq. (2.75). Note that we actually use 10 raised to the power of these quantities (x_n, y_n, σ_n), as our turnover model is in log base 10. We use flat uninformative priors and Table 2.2 lists the prior ranges for the four fitted parameters. The starting points for our MCMC walkers are distributed in a uniform random way throughout the prior volume. To remove the complexity of modelling non-linear clustering effects and BAO features, we restrict the k-domain of the fit to $k < k_{\rm max} = 0.05\, h\, {\rm Mpc}^{-1}$.

To calculate the probability that a power spectrum turnover has been measured, we perform a likelihood ratio test. We do this for the above turnover model, as well as for the model where α is set to zero, which signifies no turnover. For our adopted Gaussian likelihood models, this ratio can be written as:

$$\mathcal{R}_{\rm rel} = \frac{L_{\rm no-turn}}{L_{\rm turn}} = \exp[-(\chi^2_{\rm no-turn} - \chi^2_{\rm turn})/2] \ , \tag{2.78}$$

where $\chi^2_{\rm no-turn}$ and $\chi^2_{\rm turn}$ are the chi-square distributions:

$$\chi^2_{\rm no-turn} = \sum_i \frac{[P_i - P_{\rm no-turn}(k_i)]^2}{\sigma_i^2} \ ; \tag{2.79}$$

$$\chi^2_{\rm turn} = \sum_i \frac{[P_i - P_{\rm turn}(k_i)]^2}{\sigma_i^2} \ . \tag{2.80}$$

From this information we can now derive the probability that we have detected a turnover[13]. From the constraint that $p_{\rm no-turn} + p_{\rm turn} = 1$, and that the ratio of likelihoods is proportional to the

[13]We note that, strictly speaking, a calculation of the likelihoods would require evaluation of the full covariance matrix, however for our two large catalogues that we are running the current analysis on, the window function is significantly compact at and around the turnover scale as to minimise the effect of our diagonal covariance assumption in Eq. (2.73).

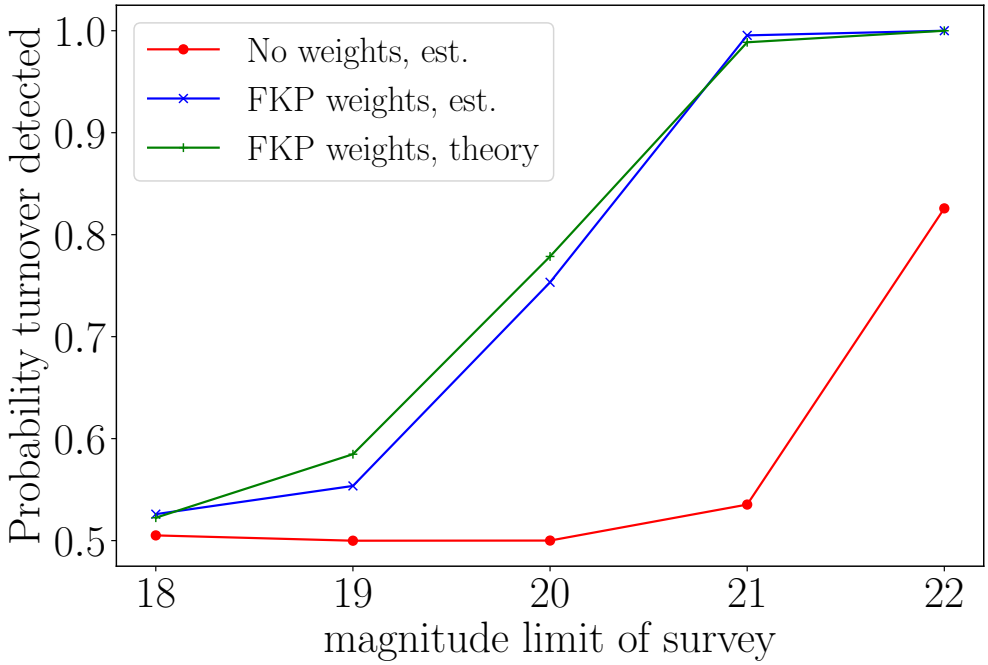

Figure 2.11: The probability that a turnover has been measured, for the 5 different magnitude cut catalogues, and for no weights (red), FKP weights (blue) and FKP weights using the theoretical predictions (green). We see that only the largest two catalogues, using FKP weights, are able to measure a turnover in the power spectrum at the $> 95\%$ CL.

probability ratios $L_{\rm no-turn}/L_{\rm turn} = p_{\rm no-turn}/p_{\rm turn}$, we have:

$$p_{\rm turn} = 1 - p_{\rm no-turn} = \frac{1}{1+\mathcal{R}_{\rm rel}} \ . \tag{2.81}$$

Thus, for each power spectrum measurement, we can calculate the χ^2 value for both models, the relative probability, and then $p_{\rm turn}$.

Figure 2.11 shows the turnover probability as a function of survey limiting magnitude, and for the three different scenarios listed above. We see that the ability to detect a turnover scale with 95% confidence (dashed line) in our magnitude limited catalogues is only achievable for our deepest two mocks ($m_{\rm lim} = 21$ and $m_{\rm lim} = 22$), and only when we employ the FKP weighting scheme. This result is independent of whether we use our actual measurements from the lightcones, or from the theoretical predictions. Conversely, in the absence of an optimal weighting scheme, we find that this simpler approach cannot unambiguously discern the turnover scale.

Figure 2.12 shows the joint 2-D and 1-D posterior distributions for the k_0 and α parameters from the MCMC analysis for the deep $m_{\rm lim} = 22$ catalogue. These are the key parameters that determine whether the data has a turnover or not. The bottom left panel shows the 68% and 95% joint contours as the lighter and darker shaded regions, respectively. The top left and bottom right panels show the 1-D posteriors. We see that the joint constraints from all three scenarios considered find similar

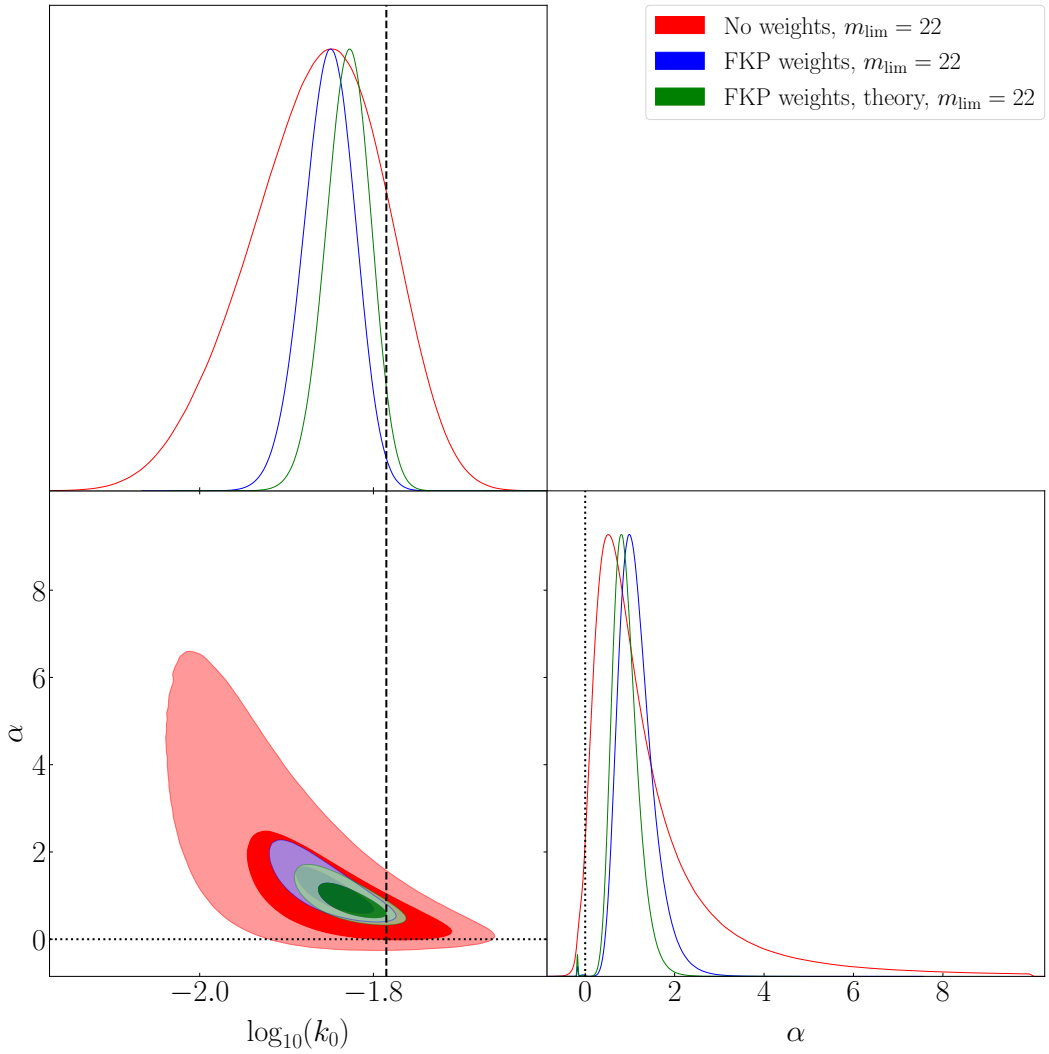

Figure 2.12: Parameter constraints on the turnover scale k_0 and the large scale slope α, for the magnitude cut 22 catalogue, with 68% contours for no weights (red), FKP weights (blue) and the theoretical predictions using FKP weights and error bars from the corresponding measurement (green). For the FKP weighted contours, we see that the value of $\alpha = 0$, corresponding to no turnover (grey dotted lines), is convincingly ruled out. Our range of values of $\log_{10}(k_0)$ lie slightly below the actual value of -1.785 (black dashed line), showing the difficulty of measuring the turnover precisely due to the flattened nature of the peak of the power spectrum, as well as larger error bars around this scale.

values for the turnover scale, with the FKP weighted data giving $k_0 = 0.0141 \pm 0.0015\, h\,\mathrm{Mpc}^{-1}$. This value is within 1.5 sigma of the actual value for the turnover of the underlying linear power spectrum $k = 0.0164\, h\,\mathrm{Mpc}^{-1}$ (denoted as the vertical dashed black line in the plot). We note that the slight bump in the measured power spectra at around $k \simeq 10^{-2}\, h\,\mathrm{Mpc}^{-1}$, which can be seen in Figs. 2.7 and 2.8, has the effect of flattening the top of the power spectrum. This has the effect of dragging the best fit turnover scale towards slightly larger scales. Nevertheless, we also note that the joint constraints for the best-fit turnover slope parameter are, for the FKP weighted data, $\alpha = 1.15^{0.25}_{-0.46}$. Thus the no turnover case corresponding to $\alpha = 0$ can be convincingly rejected for

this sample.

In Figure 2.13 we present again the measured power spectra for the $m_{\rm lim} = 22$ mock catalogue as a function of wavenumber. The lines show the theoretical model predictions using Eq. (2.75), with the best-fit posterior parameters. We also overlay the best-fit values for the turnover scale k_0 for each data set, as coloured dashed vertical lines. The black dash vertical line indicates the true turnover scale as measured from the input linear theory spectrum. One can see that while the model fits well there is a small mismatch between the true k_0 and the one that emerges from the analysis presented here. We will consider improving this modelling in future work.

Up to this point our analysis has focused on an all-sky survey, which is of most relevance to planned missions like `SPHEREx` [56]. However, we now attempt to relate our study to upcoming smaller wide angled deep galaxy redshift surveys. We do this by examining how the probability $p_{\rm turn}$ depends on surveyed sky fraction $f_{\rm sky}$. Recalling Eq. (2.73), we see that the error bars for our $P(k)$ estimates scale as $\sigma(k) \propto 1/\sqrt{N_k}$, where N_k is the number of Fourier modes. This quantity scales as $N_k \propto V_\mu^{\rm max}$, is the survey volume, which in turn is proportional to $f_{\rm sky}$. Thus we expect that $\sigma(k) \propto 1/\sqrt{f_{\rm sky}}$.

Since we were only able to robustly detect the turnover scale for our deeper surveys, we will restrict our attention to the $m_{\rm lim} = 21$ and 22 catalogues. We now repeat the MCMC posterior estimation, but increasing the error bars by a factor of $1/\sqrt{f_{\rm sky}}$ for $f_{\rm sky} \in \{1.0, 0.1\}$ in 0.1 intervals.

Figure 2.14 shows the detection probability for the two deep catalogues as function of the sky fraction $f_{\rm sky}$. We see that the $m_{\rm lim} = 22$ catalogue is able to detect the turnover scale at $\gtrsim 95\%$ CL threshold for sky fractions $\gtrsim 20\%$[14]. For the shallower $m_{\rm lim} = 21$ mock catalogue we see that the sky fraction needs to be $\gtrsim 55\%$ for a similar level of detection.

Before we move on, it is important to note that here we have assumed that the shape of the power spectrum remains constant as the sky fraction is reduced. While this should hold true at smaller scales, depending on how the survey geometry changes, we may lose the ability to probe k-modes at the largest scales, thus decreasing the number of data points past the turnover scale that we have available to constrain the model. Further, the covariance is non-diagonal due to the mask, and so true significance must be determined from recourse to a more advanced analysis.

2.6 Conclusions and discussion

Upcoming measurements of the large-scale structure of the Universe will probe volumes that approach 'effective volumes' for the entire observable Universe [56]. This will enable us to perform cosmological tests to an unprecedented precision. However, in order to extract the information from such data sets, we must ensure that we are also able to model the observable clustering signals with an unprecedented degree of both accuracy and precision. This work contributes to that effort. In this work, we have performed a detailed study of the geometrical lightcone effect on the

[14]For comparison, the DESI footprint has a sky fraction of around 35%, while for the 4MOST cosmology redshift survey its around 18%.

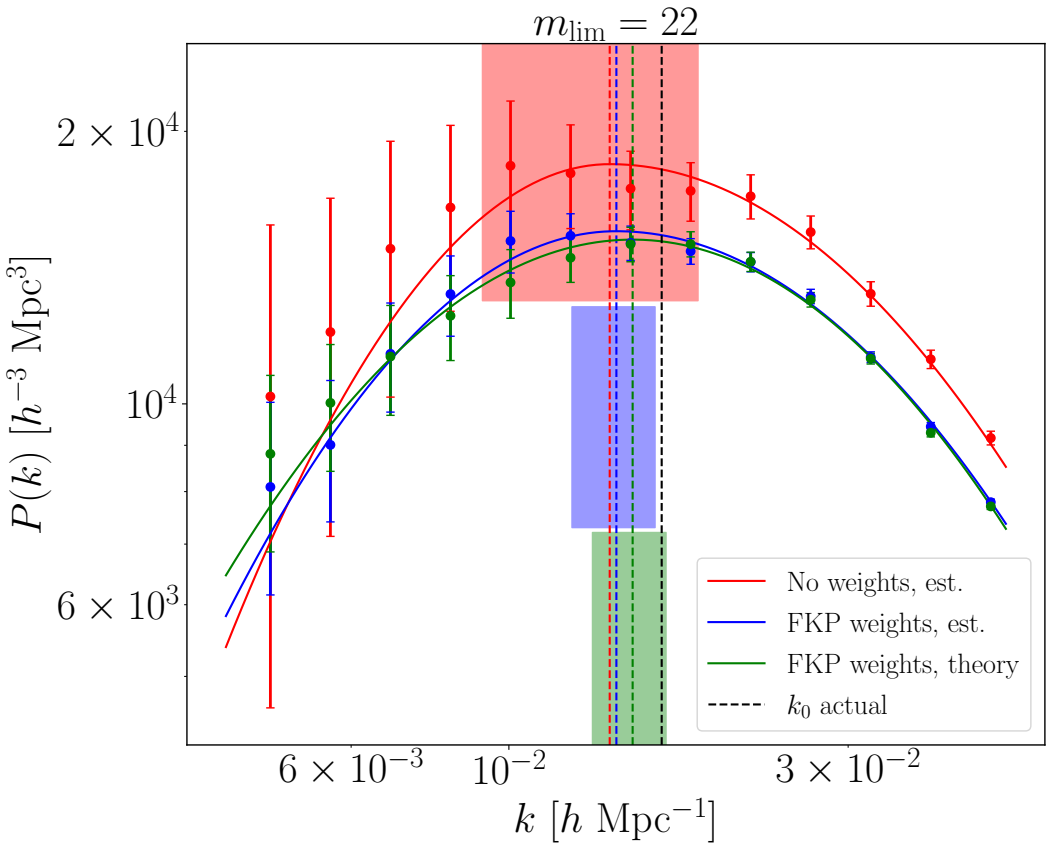

Figure 2.13: Plot showing the turnover model of Eq. (2.75) (solid lines) using the best fitting parameters, fitted to the data points (circles with error bars), corresponding to the contours shown in Fig. 2.12. We plot the derived values of k_0 as dashed vertical lines, with shaded regions (with separate y ranges for clarity) showing the errors. We can see that the large scale fluctuations of the estimated $P(k)$ points (red and blue) drag the measured value of the turnover scale k_0 to larger scales on the left of the plot, compared with using the theoretical prediction $P(k)$ with error bars from the estimate (green). The actual value of k_0 is shown in the dashed vertical black line.

two-point galaxy clustering signal in Fourier space (the power spectrum) for a deep, flux-limited, full-sky survey.

In §2.2 we presented some key background concepts, in particular the observable density field on the past lightcone and the spherical-Fourier-Bessel expansion of the field.

In §2.3 we have derived an expression for the galaxy two-point correlation function of matter fluctuations on the past-lightcone. We also presented the theory for the observable galaxy power spectrum for the case of an evolving luminosity function. We found that the theory required a model for the unequal time correlator (UETC) for galaxies. We also developed a series of approximations to the full analytic expressions that aided evaluation. We explored how the expressions would simplify for time separable models of the UETC. We derived approximations in the large-scale limit, finding that the observed power, unlike the linear theory, asymptoted to a constant value. On small scales, we were able to show that the observed spectrum reduced to a more tractable form. We also examined that the fixed time approximation and showed that provided that the time was

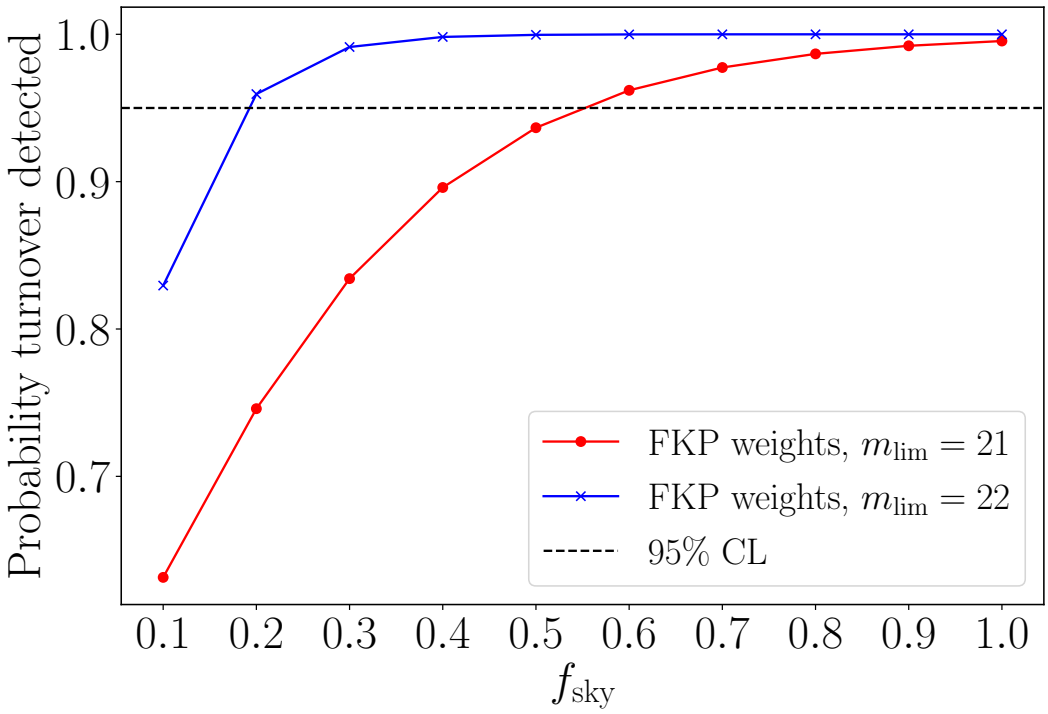

Figure 2.14: We investigate how the sky fraction covered by our simulated data will affect the probability to detect a turnover, using the largest two catalogues with FKP weights. Using the all sky results, we increase the errors bars on the estimate of the power spectrum by a factor of $f_{\rm sky}^{-1/2}$ and re-run the MCMC sampler to fit the turnover model and calculate the detection probability, for $f_{\rm sky} \in \{1.0, 0.1\}$ in 0.1 intervals. We see that a 20% sky coverage is enough to clear the 95% CL threshold for the $m_{\rm lim} = 22$ catalogue, increasing to around a 55% requirement for the $m_{\rm lim} = 21$ catalogue.

carefully chosen, one could minimise the errors on this, but over a restricted range of wavenumbers and that nonlinear evolution would always break this approximation. Here we also discussed how to extend the model into the nonlinear regime.

In §2.4 we turned to validating our model, using N-body simulations. We did this by developing an algorithm to generate full-sky dark matter lightcones by using a quadratic interpolation scheme to interpolate the world lines of all particles in a piecewise fashion between consecutive snapshots. We then used this as the base from which we generated out mock galaxy samples. We also developed a parallel code for estimating the power spectrum from large data sets, making use of an interlacing technique to obtain accurate results all the way up to the Nyquist frequency.

In §2.5 we compared our theoretical predictions to the estimates from our lightcone mocks and found excellent agreement on the scales considered. However, some small discrepancies were found on small scales, which we attributed to the breakdown of the specific form of our nonlinear corrections. We also investigated whether including the FKP weighting scheme would improve the signal-to-noise ratio of our measurements. We found that, provided one makes a careful choice for P_0 and hence $\bar{n}P_0$, we could boost this by a factor of a few. We also found that if values of P_0 were too large, then this would impact the detailed shape of the power on larger scales, but with limited

improvement on the signal-to-noise ratio on scales of $k \lesssim 0.1\,h\,\mathrm{Mpc}^{-1}$.

We also revisited the question of detecting the turnover scale of the power spectrum as a probe for the epoch of matter-radiation equality in the early universe. Following the method outlined in [95] and [123] we used our mock catalogues for various flux-limited surveys to measure a peak scale k_0 and the power-law slope α of the spectrum red-wards of the peak. We did this by performing a standard Bayesian parameter estimation scheme, where we explored the full parameter space using an efficient MCMC sampler. We found that only galaxy catalogues with $m_{\mathrm{lim}} \gtrsim 21$, in conjunction with FKP weighting scheme, had sufficient statistical power to detect the turnover with a probability $P \gtrsim 95\%$. By rescaling the covariance by the inverse of the sky-fraction, $1/f_{\mathrm{sky}}$, we recomputed the posterior distributions and found that the detection level was maintained for surveys with $m_{\mathrm{lim}} = 21$ and $m_{\mathrm{lim}} = 22$ for sky coverages greater than 50% and 20%, respectively.

There are several possible directions in which this work can be extended. First, the model that we have developed is overly simplistic, in that we worked only in real space. In reality, the radial positions are affected by redshift space distortions. However, this is likely not going to change our conclusions concerning the turnover scale, since it is expected that for such large scales these distortions would only modify the amplitude of the signal and not the shape of the peak (the 'Kaiser' effect). Second, we restricted our attention to full-sky surveys only. One should take account of the survey angular mask in the formalism. Third, we neglected galaxy bias and treated all of the particles in our simulation as unbiased galaxies. We were unable to explore this with our simulations, due to resolution issues and the difficulty in interpolating halo positions between snapshots (although see [106] for an example of how this could be done).

All three of these extensions make the model in Eq. (2.38) more complicated, and thus it also becomes necessary to improve the numerical methods used to forward model the theory. Our current method employs a set of adaptive numerical quadrature routines to compute the full Bessel function integrals on large scales. This brute force approach is somewhat slow and prone to convergence issues. A more efficient way of such integrals would be through the FFTLog algorithm of [125]. We will tackle some of these issues in the next chapter.

Another interesting prospect of being able to measure the power spectrum accurately on large scales, particularly past the turnover scale, is the increased ability to constrain signatures of primordial non-Gaussianity. Such measurements remain one of the most promising probes to discriminate between inflationary models, with the most stringent constrains currently coming from measurements of the CMB [13]. However, as we probe out to larger volumes with late-time Universe surveys, measurements of the large-scale structures will be highly complimentary and competitive [56, 126, 127].

Appendices

2.A Spherical-Fourier-Bessel (SFB) expansion

For an observer viewing their past lightcone, homogeneity will be violated, but isotropy is preserved. In addition, the survey mask will be completely angular and redshift space distortions will be radial. It will therefore be useful to decompose the problem into a set of orthogonal spherical and radial modes. To do this we will make use of the Spherical-Fourier-Bessel expansion of a scalar field.

To begin, consider some scalar field $\mathcal{A}(\mathbf{r})$ in space and let us define its forward and backward Fourier transforms as:

$$\mathcal{A}(\mathbf{r}) = \int \frac{\mathrm{d}^3\mathbf{k}}{(2\pi)^3}\mathcal{A}(\mathbf{k})e^{-i\mathbf{k}\cdot\mathbf{r}} \Leftrightarrow \mathcal{A}(\mathbf{k}) = \int \mathrm{d}^3\mathbf{r}\mathcal{A}(\mathbf{r})e^{i\mathbf{k}\cdot\mathbf{r}} \ . \tag{2.82}$$

Let us now consider the overdensity field $\Delta(\eta, \mathbf{r})$ this can be written in Fourier space as:

$$\Delta(\eta, \mathbf{r}) = \int \frac{\mathrm{d}^3\mathbf{k}}{(2\pi)^3}\Delta(\eta, \mathbf{k})e^{-i\mathbf{k}\cdot\mathbf{r}} \ . \tag{2.83}$$

At this point we can expand the plane wave using the Fourier-Bessel expansion, i.e.

$$e^{i\mathbf{k}\cdot\mathbf{r}} = 4\pi\sum_{\ell=0}^{\infty}\sum_{m=-\ell}^{\ell} i^\ell j_\ell(kr)Y_{\ell m}(\hat{\mathbf{k}})Y^*_{\ell m}(\hat{\mathbf{r}}) \ , \tag{2.84}$$

and

$$e^{-i\mathbf{k}\cdot\mathbf{r}} = e^{i(-\mathbf{k})\cdot\mathbf{r}} = 4\pi\sum_{\ell=0}^{\infty}\sum_{m=-\ell}^{\ell} i^\ell j_\ell(kr)Y_{\ell m}(-\hat{\mathbf{k}})Y^*_{\ell m}(\hat{\mathbf{r}}) = 4\pi\sum_{\ell=0}^{\infty}\sum_{m=-\ell}^{\ell} (-i)^\ell j_\ell(kr)Y_{\ell m}(\hat{\mathbf{k}})Y^*_{\ell m}(\hat{\mathbf{r}}) \ , \tag{2.85}$$

where we have used the fact that $Y_{\ell m}(-\hat{\mathbf{k}}) = (-1)^\ell Y_{\ell m}(\hat{\mathbf{k}})$. Thus we have:

$$\Delta(\eta, \mathbf{r}) = \sum_{\ell=0}^{\infty}\sum_{m=-\ell}^{\ell} (-i)^\ell Y^*_{\ell m}(\hat{\mathbf{r}}) \int \frac{\mathrm{d}^3\mathbf{k}}{(2\pi)^3} 4\pi j_\ell(kr)Y_{\ell m}(\hat{\mathbf{k}})\Delta(\eta, \mathbf{k}) \ . \tag{2.86}$$

Consider the integral factor, this can be written as:

$$\int \frac{\mathrm{d}^3\mathbf{k}}{(2\pi)^3} 4\pi j_\ell(kr) Y_{\ell m}(\hat{\mathbf{k}}) \Delta(\eta, \mathbf{k}) = \int \frac{\mathrm{d}k k^2}{(2\pi^2)} j_\ell(kr) \int \mathrm{d}\hat{\mathbf{k}}\ Y_{\ell m}(\hat{\mathbf{k}}) \Delta(\eta, \mathbf{k}) \ . \tag{2.87}$$

Let us focus on the last part of this expression, and we see that it can be written:

$$I_{\ell m}(\eta, k) \equiv \int \mathrm{d}\hat{\mathbf{k}}\ Y_{\ell m}(\hat{\mathbf{k}}) \Delta(\eta, \mathbf{k}) = \left[\int \mathrm{d}\hat{\mathbf{k}}\ Y^*_{\ell m}(\hat{\mathbf{k}}) \Delta^*(\eta, \mathbf{k}) \right]^* \ . \tag{2.88}$$

The condition that the density field is a real quantity means that $\Delta(\eta, \mathbf{k}) = \Delta^*(\eta, -\mathbf{k})$, and using this in the above leads us to:

$$I_{\ell m}(\eta, k) = \left[\int \mathrm{d}\hat{\mathbf{k}}\ Y^*_{\ell m}(\hat{\mathbf{k}}) \Delta(\eta, -\mathbf{k}) \right]^* \ . \tag{2.89}$$

If we now make the change of variables $\mathbf{k}' = -\mathbf{k}$, so $\mathrm{d}\mathbf{k}' = -\mathrm{d}\mathbf{k}$, then the integral becomes:

$$I_{\ell m}(\eta, k) = \left[\int \mathrm{d}\hat{\mathbf{k}}'\ Y^*_{\ell m}(-\hat{\mathbf{k}}') \Delta(\eta, \mathbf{k}') \right]^* \ . \tag{2.90}$$

We now again make use of the fact that $Y_{\ell m}(-\hat{\mathbf{k}}) = (-1)^\ell Y_{\ell m}(\hat{\mathbf{k}})$, to obtain:

$$I_{\ell m}(\eta, k) = (-1)^\ell \left[\int \mathrm{d}\hat{\mathbf{k}}'\ Y^*_{\ell m}(\hat{\mathbf{k}}') \Delta(\eta, \mathbf{k}') \right]^* \ . \tag{2.91}$$

The factor in the brackets is the projection of the function $\Delta(\eta, \mathbf{k}')$ on to the Spherical harmonic basis functions, i.e.

$$\Delta_{\ell m}(\eta, k) \equiv \int \mathrm{d}\hat{\mathbf{k}}\ Y^*_{\ell m}(\hat{\mathbf{k}}) \Delta(\eta, \mathbf{k}) \ , \tag{2.92}$$

$$\Delta^*_{\ell m}(\eta, k) \equiv \int \mathrm{d}\hat{\mathbf{k}}\ Y_{\ell m}(\hat{\mathbf{k}}) \Delta^*(\eta, \mathbf{k}) \ . \tag{2.93}$$

Hence, we find:

$$I_{\ell m}(\eta, k) = (-1)^\ell \Delta^*_{\ell m}(\eta, k) \ . \tag{2.94}$$

On substituting this back into Eq. (2.87) and then in turn substituting this back into Eq. (2.86) gives:

$$\Delta(\eta, \mathbf{r}) = \sum_{\ell=0}^{\infty} \sum_{m=-\ell}^{\ell} Y^*_{\ell m}(\hat{\mathbf{r}}) \Delta^*_{\ell m}(\eta, r) \ , \tag{2.95}$$

$$= \sum_{\ell=0}^{\infty} \sum_{m=-\ell}^{\ell} Y_{\ell m}(\hat{\mathbf{r}}) \Delta_{\ell m}(\eta, r) \ , \tag{2.96}$$

where the second equality follows from the reality of the density field, i.e. $\Delta(\eta, \mathbf{r}) = \Delta^*(\eta, \mathbf{r})$ and

where in the above we have defined the amplitudes of the spherical harmonics as:

$$\Delta^*_{\ell m}(\eta, r) \equiv i^\ell \int \frac{\mathrm{d}^3\mathbf{k}}{(2\pi)^3} j_\ell(kr)\Delta^*_{\ell m}(\eta, k) \ , \tag{2.97}$$

$$\to \Delta_{\ell m}(\eta, r) \equiv (-i)^\ell \int \frac{\mathrm{d}^3\mathbf{k}}{(2\pi)^3} j_\ell(kr)\Delta_{\ell m}(\eta, k) \tag{2.98}$$

2.B Modelling the evolving galaxy luminosity function and generation of mock samples

2.B.1 The evolving luminosity function

In this section, we detail how the number density on the lightcone, $n_0^{\rm LC}(r)$, is calculated. We use the following formula:

$$n_0^{\rm LC}(r) = \int_{M_{\rm lim}(r)}^{-\infty} \phi(M, r)\mathrm{d}M \ , \tag{2.99}$$

where $\phi(M, r)$ is the evolving Schechter luminosity function, given in terms of absolute magnitudes by

$$\begin{aligned}\phi(M, r) &= \frac{2}{5}\phi^*(r)\ln(10)10^{\frac{2}{5}(\alpha+1)[M^*(r)-M]} \\ &\quad \times \exp\big(-10^{\frac{2}{5}[M^*(r)-M]}\big) \ .\end{aligned} \tag{2.100}$$

We let two of the Schechter parameters evolve with survey depth ($M^*(r)$ and $\phi^*(r)$) while keeping the third, α, fixed. We use the evolution parameters and fitted values given in [128], specifically:

$$M^*(z) = M^*(z_0) - Q(z - z_0), \tag{2.101}$$

$$\phi^*(z) = \phi^*(0)10^{0.4Pz}. \tag{2.102}$$

These parameters were fitted to the phase 1 GAMA data using the stepwise maximum likelihood method [129], and we use the combination of blue and red galaxies in the r-band, giving $P = 1.6$, $Q = 0.2$, $\alpha = -1.23$, $M^* - 5\log h = -20.7$ and $\phi^* = 0.94 \times 10^{-2}h^3\mathrm{Mpc}^{-3}$. The fiducial redshift z_0 is the redshift to which the magnitudes were K-corrected, in this case $z_0 = 0.1$. The lower limit on the integral in Eq. (2.99) is the faintest possible object detectable, in terms of its absolute magnitude, at a given comoving radial distance r, and this is calculated as

$$M_{\rm lim}(r) = m_{\rm lim} - 5\log_{10}\Big(\frac{r}{10\mathrm{pc}}\Big). \tag{2.103}$$

Our first use of Eq. (2.99) is in our theoretical modelling of the window-convolved power spectrum on the lightcone Eq. (2.33). Secondly, we use it for sampling magnitudes for our lightcone N-body simulations, so as to make magnitude-cut catalogues to mimic galaxy samples that would

be observed by a real survey. We take 5 magnitude cuts at $m_{\rm lim} = \{18, 19, 20, 21, 22\}$ (see Appendix §2.B.2 for details on sampling). We note that these catalogues are thus not independent realisations from one another, but rather the faintest catalogue, $m_{\rm lim} = 18$, contains a subset of particles from the $m_{\rm lim} = 19$ catalogue, which in itself is a subset of the $m_{\rm lim} = 20$ catalogue, and so on.

2.B.2 Sampling luminosities from the evolving Schechter Function

To be able to sample luminosities from our evolving Schechter function $\phi(L, z)$ covered in Appendix §2.B.1, we want to be able to draw numbers from a random uniform distribution $U(x)$ of variable x, and translate these into a random luminosities L. Using the probability integral transform we have (suppressing the dependency on redshift for neatness)

$$|U(x)\mathrm{d}x| = |P(L)\mathrm{d}L|, \tag{2.104}$$

where $P(L) = \phi(L)/\bar{n}$ with $\phi(L)$ being the Schechter function and $\bar{n}$ the mean number density of the survey. By integrating both sides we require that

$$\int_0^x U(x')\mathrm{d}x' = x = \int_{L_{\rm min}}^{L_{\rm max}} P(L)\mathrm{d}L. \tag{2.105}$$

We chose our luminosities such that $L_{\rm max} = 100L^*$ and the minimum luminosity is determined from the mean number density of our unbiased galaxy sample:

$$\bar{n} = \int_{L_{\rm min}}^{\infty} \phi(M)\mathrm{d}M. \tag{2.106}$$

We can exploit the relationship between integrals of the Schechter function and the incomplete gamma functions, as

$$\begin{aligned}
\int_{L_{\rm min}}^{L_{\rm max}} P(L)\mathrm{d}L &= \frac{\phi^*}{\bar{n}} \int_{L_{\rm min}}^{L_{\rm max}} \Big(\frac{L}{L^*}\Big)^{\alpha} \exp\Big(-\frac{L}{L^*}\Big)\frac{\mathrm{d}L}{L^*}\ , \\
&= \frac{\phi^*}{\bar{n}}\Big[\Gamma\big(\alpha+1, \frac{L_{\rm min}}{L^*}\big) - \Gamma\big(\alpha+1, \frac{L_{\rm max}}{L^*}\big)\Big]\ , \\
&= \Phi(L/L^*) = x.
\end{aligned} \tag{2.107}$$

Therefore, if we invert the above Φ function, we see that by inputting random uniform numbers x, this will generate a distribution of L/L^* that is distributed like a Schechter function:

$$\Phi^{-1}(x) = \frac{L}{L^*}, \qquad\qquad L_{\rm min} \leq L \leq L_{\rm max}\ . \tag{2.108}$$

We implement this by calculating $\Phi(L/L^*)$ for a fixed redshift, over the given range in L/L^* to get the range of x, and then inverse spline the result. We repeat this for a range of redshift values, covering the minimum and maximum redshift of our survey, and create a larger 2D spline of the

overall relationship.

2.C Shell averaged estimates of the power spectrum

When one estimates the observed power spectrum on the past lightcone, it is customary to bin the spectra in a k-space shell of thickness Δk centred on a bin k_i. This needs to be taken into account when comparing the measurements with theory. The bin-averaged spectrum can thus be written:

$$\overline{P_{\rm F}}(k_i) = \frac{1}{V(k_i)} \sum_{\ell} \int_{k_i-\Delta k/2}^{k_i+\Delta k/2} 4\pi q^2 \mathcal{P}_\ell(q,q) {\rm d}q \ , \tag{2.109}$$

where the shell volume is given by:

$$V(k) = \int_{k-\Delta k/2}^{k+\Delta k/2} 4\pi q^2 {\rm d}q = \frac{4}{3}\pi k^3 \left[1 + \frac{1}{12}\left(\frac{\Delta k}{k}\right)^2\right] \ . \tag{2.110}$$

If we substitute Eq. (2.33) into Eq. (2.109) then we find:

$$\begin{aligned}\overline{P_{\rm F}}(k_i) = &\sum_{\ell} (2\ell+1) \frac{4\pi A^2}{V(k_i)} \int_{k_i-\Delta k/2}^{k_i+\Delta k/2} {\rm d}q q^2 \int \frac{{\rm d}^3\mathbf{k}}{(2\pi)^3} \\ &\times \prod_{j=1}^{2} \Big\{ \int {\rm d}^3\mathbf{r}_j n_0^{\rm LC}(r_j) j_\ell(q r_j) j_\ell(k r_j) \Big\} P(k,\eta_1,\eta_2) \ . \end{aligned} \tag{2.111}$$

If we rearrange the integrals so that the q integral is first, we see that we are required to compute an integral of the type (result 5.54.1 [130]):

$$\begin{aligned}\mathcal{J}_\ell(\alpha,\beta,a) &\equiv \int_0^a {\rm d}x x^2 j_\ell(\alpha x) j_\ell(\beta x) \ , \\ &= \frac{a^2}{\alpha^2-\beta^2}\left[\alpha j_{\ell+1}(\alpha a) j_\ell(\beta a) - \beta j_\ell(\alpha a) j_{\ell+1}(\beta a)\right] \ . \end{aligned} \tag{2.112}$$

On using the above relation we see that Eq. (2.111) simplifies to:

$$\begin{aligned}\overline{P_{\rm F}}(k_i) = &\frac{32\pi A^2}{V(k_i)} \sum_{\ell} (2\ell+1) \int {\rm d}k k^2 \int dr_1 r_1^2 \int dr_2 r_2^2 \\ &\times n_0^{\rm LC}(r_1) n_0^{\rm LC}(r_2) j_\ell(k r_1) j_\ell(k r_2) P(k,\eta_1,\eta_2) \\ &\times \left[\mathcal{J}_\ell(r_1,r_2,k_i^+) - \mathcal{J}_\ell(r_1,r_2,k_i^-)\right] \ , \end{aligned} \tag{2.113}$$

where we defined $k_i^+ \equiv k_i + \Delta k/2$ and $k_i^- \equiv k_i - \Delta k/2$.

Contributions

The work in this chapter was has been written up into a paper and submitted to MNRAS, and was primarily carried out in conjunction with my supervisor Dr. Robert Smith, who contributed some derivations to Sections §2.2 and §2.3. The C++ code to evaluate the theoretical model was written entirely by myself. The lightcone catalogues we used to test our model with were provided by Robert Smith and Robin Booth, with some of the descriptions of the Daemmerung simulations and lightcone creation in Section §2.4.1 provided by Robert. The Python pipleline for performing a data reduction on the simulations, creating mock galaxy catalogues and unclustered random catalogues, and measuring the power spectrum from these catalogues was written by myself, with the earliest stages of development overseen by Prof. Chris Blake. Any other authors provided advisory roles only.

Chapter 3

The galaxy power spectrum on the past lightcone II: Galaxy bias and angular masks

3.1 Introduction

In the previous chapter, we focused on developing and testing a model for the full-sky matter power spectrum on the past lightcone, up to two loops in perturbation theory. We now turn our attention to extending this model in order to be more useful for galaxy surveys, including terms for the galaxy bias, as well as modelling an angular survey mask to account for the fact that surveys in general do not observe over the full-sky. We will work under the assumption however that our survey footprint is wide and deep enough such that the standard plane-parallel approximation is not valid, and that we still need to consider the effects of the unequal-time correlator of Eq. (2.16). In addition to this, as the equations encountered will be even more numerically challenging than those of the last chapter (eg. Eq. (2.42)), such that a brute force on the large scales is no longer feasible, we will also review potential methods that can be used to tackle such equations in an accurate and timely manner.

Our work differs from approaches such as those used for the Six-degree Field Galaxy Survey (6dFGS) [120], as in that instance they made the equal-time correlator approximation due to shallow survey depth, and convolved the survey window function with the underlying model power spectrum using 3D grid-based FFT methods. The drawback of such methods is that they can be memory intensive, require numerous FFTs and the k-range available to be probed at small scales is limited by the grid resolution. Additionally, the discretisation of quantities onto 3D grids can introduce aliasing at small k, as discussed in the previous chapter. While our approach is more mathematically complicated, we rely on only 1D FFTs and are less limited in k.

The chapter is laid out as follows: In Section §3.2, we extend the previous model of the full-sky power spectrum on the past lightcone to the generalised case where we now include a survey mask.

We then look at specific scenarios that make the resulting expression more numerically tractable. We also extend the model to the nonlinear regime before briefly discussing calculation of the angular mask term. In Section §3.3 we review and discuss numerical methods for solving the expressions obtained for the masked galaxy power spectrum on the past lightcone, drawing on previous works and adapting to our specific case. Finally, in Section §3.4 we conclude and discuss further work and extensions to the model.

3.2 The masked galaxy power spectrum on the past lightcone

We now look to define the power spectrum on the past lightcone, taking into consideration terms for a survey mask and galaxy bias. We will make use of the forwards and backwards Fourier transform, which we define, for some scalar field $\mathcal{A}(\mathbf{r})$, with the convention

$$\mathcal{A}(\mathbf{r}) = \int \frac{\mathrm{d}^3\mathbf{k}}{(2\pi)^3}\mathcal{A}(\mathbf{k})e^{-i\mathbf{k}\cdot\mathbf{r}} \quad \Leftrightarrow \quad \mathcal{A}(\mathbf{k}) = \int \mathrm{d}^3\mathbf{r}\mathcal{A}(\mathbf{r})e^{i\mathbf{k}\cdot\mathbf{r}} \ . \tag{3.1}$$

We make the assumption that the survey mask is separable into angular and radial components, and as we will be dealing with a wide-angle survey, it is more useful to break down the problem into a set of orthogonal radial and angular modes. For this, we will need the Fourier-Bessel expansion of the plane wave, and its complex conjugate, given by

$$e^{i\mathbf{k}\cdot\mathbf{r}} = 4\pi\sum_{\ell=0}^{\infty}\sum_{m=-\ell}^{\ell} i^\ell j_\ell(kr)Y_{\ell m}(\hat{\mathbf{k}})Y^*_{\ell m}(\hat{\mathbf{r}}) \ , \tag{3.2}$$

$$e^{-i\mathbf{k}\cdot\mathbf{r}} = 4\pi\sum_{\ell=0}^{\infty}\sum_{m=-\ell}^{\ell} (-i)^\ell j_\ell(kr)Y_{\ell m}(\hat{\mathbf{k}})Y^*_{\ell m}(\hat{\mathbf{r}}) \ . \tag{3.3}$$

3.2.1 The generalised case

We start by dealing with the most general case, where we make no assumption about the form of the unequal-time power spectrum, $P(k, \eta_1, \eta_2)$. Following on directly from the arguments in Section §2.2 of the previous chapter, we now define our weighted and masked galaxy survey density field as

$$F^{\mathrm{LC}}(\mathbf{r}) = Aw(\mathbf{r})\Theta(\mathbf{r})\left[n^{\mathrm{LC}}(\mathbf{r}) - \alpha\, n_{\mathrm{s}}^{\mathrm{LC}}(\mathbf{r})\right] \ , \tag{3.4}$$

where A and α are constants to be determined, $w(\mathbf{r})$ is an optimal weighting scheme (e.g. the FKP weights of [78]) and $\Theta(\mathbf{r})$ is the survey mask given by

$$\Theta(\mathbf{r}) = \begin{cases} 1 & \text{Inside the scope of the survey} \ , \\ 0 & \text{elsewhere} \ . \end{cases} \tag{3.5}$$

The quantities $n^{\rm LC}(\mathbf{r})$ and $n_{\rm s}^{\rm LC}(\mathbf{r})$ represent the number densities on the lightcone of galaxy and unclustered synthetic catalogues, respectively, and relate back to the the true overdensity of galaxies via

$$\Delta(\eta_0 - r, r, \boldsymbol{\gamma}) = \frac{n^{\rm LC}(\mathbf{r}) - \alpha\, n_{\rm s}^{\rm LC}(\mathbf{r})}{\alpha\, n_{\rm s}^{\rm LC}(\mathbf{r})} = \frac{n^{\rm LC}(\mathbf{r}) - n_0^{\rm LC}(r)}{n_0^{\rm LC}(r)} \ , \tag{3.6}$$

where the second equality follows from the assumption that $\alpha \left\langle n_{\rm s}^{\rm LC}(\mathbf{r}) \right\rangle = n_0^{\rm LC}(r)$.

Taking the Fourier transform of our $F^{\rm LC}(\mathbf{r})$ field and looking at the correlation of a product of two of these, we have:

$$\begin{aligned}\left\langle F^{\rm LC}(\mathbf{q}_1) \left[F^{\rm LC}(\mathbf{q}_2)\right]^* \right\rangle = A^2 \int {\rm d}^3\mathbf{r}_1 {\rm d}^3\mathbf{r}_2 e^{i\mathbf{q}_1\cdot\mathbf{r}_1} e^{-i\mathbf{q}_2\cdot\mathbf{r}_2} w(r_1) w(r_2) \Theta(\mathbf{r}_1)\Theta(\mathbf{r}_2) \\ \times \left\langle \left[n^{\rm LC}(\mathbf{r}_1) - \alpha\, n_{\rm s}^{\rm LC}(\mathbf{r}_1)\right] \left[n^{\rm LC}(\mathbf{r}_2) - \alpha\, n_{\rm s}^{\rm LC}(\mathbf{r}_2)\right] \right\rangle \ .\end{aligned} \tag{3.7}$$

Using the expression for the overdensity of galaxies in Eq. (3.6), we can reduce this to

$$\begin{aligned}\left\langle F^{\rm LC}(\mathbf{q}_1) \left[F^{\rm LC}(\mathbf{q}_2)\right]^* \right\rangle = A^2 \int {\rm d}^3\mathbf{r}_1 {\rm d}^3\mathbf{r}_2 e^{i\mathbf{q}_1\cdot\mathbf{r}_1} e^{-i\mathbf{q}_2\cdot\mathbf{r}_2} w(r_1) w(r_2) \Theta(\mathbf{r}_1)\Theta(\mathbf{r}_2) \\ \times n_0^{\rm LC}(r_1) n_0^{\rm LC}(r_2) \left\langle \Delta(\mathbf{r}_1)\Delta(\mathbf{r}_2) \right\rangle + P_{\rm shot}(\mathbf{q}_1, \mathbf{q}_2) \ .\end{aligned} \tag{3.8}$$

We calculate the shot noise term $P_{\rm shot}(\mathbf{q}_1, \mathbf{q}_2)$ in Appendix §3.A, and omit it for brevity in the following calculations, only adding it on to key results at the end of derivations. The ensemble average brackets term on the RHS of the equation is the real space unequal-time correlator (UETC). We derived an expression for this in Section §2.3.1 in the previous chapter:

$$\langle \Delta(\mathbf{r}_1)\Delta(\mathbf{r}_2) \rangle \ = \tfrac{2}{\pi} \textstyle\sum_{\ell,m} Y_{\ell m}(\hat{\mathbf{r}}_1) Y^*_{\ell m}(\hat{\mathbf{r}}_2) \int {\rm d}k k^2 j_\ell(kr_1) j_\ell(kr_2) P(k, \eta_1, \eta_2) \ , \tag{3.9}$$

where $P(k, \eta_1, \eta_2)$ is the unequal time power spectrum, $Y_{\ell m}(\hat{\mathbf{r}})$ are spherical harmonics and the $j_\ell(r)$ are spherical Bessels. Inserting this into our equation we have[1]

$$\begin{aligned}\left\langle F^{\rm LC}(\mathbf{q}_1) \left[F^{\rm LC}(\mathbf{q}_2)\right]^* \right\rangle \ = A^2 \textstyle\int {\rm d}^3\mathbf{r}_1 {\rm d}^3\mathbf{r}_2 e^{i\mathbf{q}_1\cdot\mathbf{r}_1} e^{-i\mathbf{q}_2\cdot\mathbf{r}_2} w(r_1) w(r_2) \Theta(\mathbf{r}_1)\Theta(\mathbf{r}_2) n_0^{\rm LC}(r_1) n_0^{\rm LC}(r_2) \\ \times \textstyle\sum_{\ell,m} Y_{\ell m}(\hat{\mathbf{r}}_1) Y^*_{\ell m}(\hat{\mathbf{r}}_2) \int {\rm d}k k^2 j_\ell(kr_1) j_\ell(kr_2) P(k, \eta_1, \eta_2) \ .\end{aligned} \tag{3.10}$$

Next, using the spherical Fourier-Bessel expansion of the plane wave given by Eq. (3.2) and Eq. (3.3) to expand the two exponential terms, separating out the survey mask so that $\Theta(\mathbf{r}) = \Theta(r)\Theta(\hat{\mathbf{r}})$ and

[1] Whenever we obtain any constant factors in the following derivations we will automatically absorb them into the normalisation constant term A, and define this quantity later on.

defining a radial kernel function $Z(r) \equiv w(r)\Theta(r)n_0^{\rm LC}(r)$, we obtain

$$\begin{aligned}\left\langle F^{\rm LC}(\mathbf{q}_1)\left[F^{\rm LC}(\mathbf{q}_2)\right]^*\right\rangle &= A^2\int \mathrm{d}^3\mathbf{r}_1\mathrm{d}^3\mathbf{r}_2 Z(r_1)Z(r_2)\Theta(\hat{\mathbf{r}}_1)\Theta(\hat{\mathbf{r}}_2)\sum_{\ell,m}Y_{\ell m}(\hat{\mathbf{r}}_1)Y^*_{\ell m}(\hat{\mathbf{r}}_2)\\ &\times\int \mathrm{d}k k^2 j_\ell(kr_1)j_\ell(kr_2)P(k,\eta_1,\eta_2)\sum_{\ell_1,m_1} i^{\ell_1}j_{\ell_1}(q_1r_1)Y_{\ell_1m_1}(\hat{\mathbf{q}}_1)Y^*_{\ell_1m_1}(\hat{\mathbf{r}_1})\\ &\times\sum_{\ell_2,m_2}(-i)^{\ell_2}j_{\ell_2}(q_2r_2)Y_{\ell_2m_2}(\hat{\mathbf{q}}_2)Y^*_{\ell_2m_2}(\hat{\mathbf{r}_2})\ . \end{aligned} \tag{3.11}$$

We can also expand the angular components of the mask in terms of spherical harmonics:

$$\Theta(\hat{\mathbf{r}}_1) = \sum_{\ell_3,m_3}\Theta_{\ell_3m_3}Y_{\ell_3m_3}(\hat{\mathbf{r}}_1)\ , \tag{3.12}$$

$$\Theta(\hat{\mathbf{r}}_2) = \sum_{\ell_4,m_4}\Theta^*_{\ell_4m_4}Y^*_{\ell_4m_4}(\hat{\mathbf{r}}_2)\ , \tag{3.13}$$

where for the second expression we have used the fact that the $\Theta(\hat{\mathbf{r}})$ function is real. If we shift the conjugate from the $Y^*_{\ell_1m_1}(\hat{\mathbf{r}_1})$ term to the $Y_{\ell_1m_1}(\hat{\mathbf{q}}_1)$ term, using that

$$\begin{aligned}\sum_{m=-\ell_1}^{\ell_1}Y_{\ell_1m_1}(\hat{\mathbf{q}}_1)Y^*_{\ell_1m_1}(\hat{\mathbf{r}}_1) &= \sum_{m=-\ell_1}^{\ell_1}(-1)^{m_1}Y^*_{\ell_1,-m_1}(\hat{\mathbf{q}}_1)(-1)^{m_1}Y_{\ell_1,-m_1}(\hat{\mathbf{r}}_1)\ ,\\ &= \sum_{m=-\ell_1}^{\ell_1}Y^*_{\ell_1,-m_1}(\hat{\mathbf{q}}_1)Y_{\ell_1,-m_1}(\hat{\mathbf{r}}_1)\ ,\\ &= \sum_{m=-\ell_1}^{\ell_1}Y^*_{\ell_1,m_1}(\hat{\mathbf{q}}_1)Y_{\ell_1,m_1}(\hat{\mathbf{r}}_1)\ , \end{aligned} \tag{3.14}$$

we are then free to perform the angular integrals $\mathrm{d}\hat{\mathbf{r}}_1$ and $\mathrm{d}\hat{\mathbf{r}}_2$:

$$\int \mathrm{d}\hat{\mathbf{r}}_1 Y_{\ell m}(\hat{\mathbf{r}}_1)Y_{\ell_1m_1}(\hat{\mathbf{r}}_1)Y_{\ell_3m_3}(\hat{\mathbf{r}}_1) = \mathcal{G}^{\ell\ell_1\ell_3}_{mm_1m_3}\ , \tag{3.15}$$

$$\int \mathrm{d}\hat{\mathbf{r}}_2 Y^*_{\ell m}(\hat{\mathbf{r}}_2)Y^*_{\ell_2m_2}(\hat{\mathbf{r}}_2)Y^*_{\ell_4m_4}(\hat{\mathbf{r}}_2) = \mathcal{G}^{\ell\ell_2\ell_4}_{mm_2m_4}\ . \tag{3.16}$$

where $\mathcal{G}$ is the Gaunt symbol, which we cover in Appendix §3.B. Putting this all together, we are left with the following expression:

$$\begin{aligned}\left\langle F^{\rm LC}(\mathbf{q}_1)\left[F^{\rm LC}(\mathbf{q}_2)\right]^*\right\rangle &= A^2\sum_{\ell,m}\sum_{\ell_1,m_1}\sum_{\ell_2,m_2}\sum_{\ell_3,m_3}\sum_{\ell_4,m_4} i^{\ell_1}(-i)^{\ell_2}\mathcal{G}^{\ell\ell_1\ell_3}_{mm_1m_3}\mathcal{G}^{\ell\ell_2\ell_4}_{mm_2m_4}\Theta_{\ell_3m_3}\Theta^*_{\ell_4m_4}Y^*_{\ell_1m_1}(\hat{\mathbf{q}}_1)\\ &\times\ Y_{\ell_2m_2}(\hat{\mathbf{q}}_2)\int \mathrm{d}k k^2\prod_{i=1}^{2}\Big\{\int \mathrm{d}r_i r_i^2 j_\ell(kr_i)j_{\ell_i}(q_ir_i)Z(r_i)\Big\}P(k,\eta_1,\eta_2)\ . \end{aligned} \tag{3.17}$$

Numerical evaluation of such an expression will be a tricky task: the unequal-time power spectrum

couples the two r integrals, such that we would have to evaluate a 3D integral over products of highly oscillatory Bessel functions, all while performing multiple order sums. In addition to this, integration would need to be done to calculate the angular mask expansion coefficients $\Theta_{\ell_3 m_3}\Theta^*_{\ell_4 m_4}$ in advance.

Luckily, we are interested in calculating the observed power spectrum on the lightcone, which will simplify this expression. Using that while homogeneity is broken on the lightcone (the above expression does not vanish for $\mathbf{q}_1 \neq \mathbf{q}_2$), isotropy must be maintained, we require that $P_{\rm F}(q) \equiv \int \mathrm{d}\hat{\mathbf{q}} \left\langle \left| F^{\rm LC}(\mathbf{q}) \right|^2 \right\rangle$. Thus, restricting ourselves to the case where $\mathbf{q}_1 = \mathbf{q}_2$ and performing the angular integral over $\hat{\mathbf{q}}$, we can make this expression more tractable. Using the orthogonality of the spherical harmonics,

$$\int \mathrm{d}\hat{\mathbf{q}} Y^*_{\ell_1 m_1}(\hat{\mathbf{q}}) Y_{\ell_2 m_2}(\hat{\mathbf{q}}) = \delta_{\ell_1 \ell_2}\delta_{m_1 m_2} \ , \tag{3.18}$$

we can reduce Eq. (3.17) to

$$\begin{aligned} P_{\rm F}(q) \ &= A^2 \textstyle\sum_{\ell,m} \sum_{\ell_1,m_1} \sum_{\ell_3,m_3} \sum_{\ell_4,m_4} \mathcal{G}^{\ell\ell_1\ell_3}_{mm_1m_3} \mathcal{G}^{\ell\ell_1\ell_4}_{mm_1m_4} \Theta_{\ell_3 m_3}\Theta^*_{\ell_4 m_4} \\ &\quad \times \int \mathrm{d}k k^2 \textstyle\prod_{i=1}^2 \left\{ \int \mathrm{d}r_i r_i^2 j_\ell(kr_i) j_{\ell_1}(q_i r_i) Z(r_i) \right\} P(k,\eta_1,\eta_2) \ . \end{aligned} \tag{3.19}$$

Following from this, summing over the product of two Gaunt symbols where the first two columns of indices are the same can be written as:

$$\sum_m \sum_{m_1} \mathcal{G}^{\ell\ell_1\ell_3}_{mm_1m_3} \mathcal{G}^{\ell\ell_1\ell_4}_{mm_1m_4} = \frac{(2l+1)(2l_1+1)}{4\pi} \delta_{l_3 l_4}\delta_{m_3 m_4} \begin{pmatrix} \ell & \ell_1 & \ell_3 \\ 0 & 0 & 0 \end{pmatrix}^2 \{l \ l_1 \ l_3\} \ , \tag{3.20}$$

where $\{l \ l_1 \ l_3\}$ is the triangular delta (see Appendix §3.B for necessary derivations and definitions), imposing additional restrictions on the sums which will speed up any calculations. Our expression for the power spectrum is now[2]

$$\begin{aligned} P_{\rm F}(q) \ &= \ A^2 \sum_{\ell_1} \sum_{\ell_2} \sum_{\ell_3,m_3} |\Theta_{\ell_3 m_3}|^2 (2\ell_1+1)(2\ell_2+1) \begin{pmatrix} \ell_1 & \ell_2 & \ell_3 \\ 0 & 0 & 0 \end{pmatrix}^2 \{l_1 \ l_2 \ l_3\} \\ &\quad \times \ \int \mathrm{d}k k^2 \prod_{i=1}^2 \left\{ \int r_i r_i^2 j_{\ell_1}(kr_i) j_{\ell_2}(q_i r_i) Z(r_i) \right\} P(k,\eta_1,\eta_2) \ . \end{aligned} \tag{3.21}$$

We can write this in a more succinct form:

$$P_{\rm F}(q) = \hat{\sum_{\ell_1\ell_2\ell_3}} C_{\ell_3} \int \mathrm{d}k k^2 \prod_{i=1}^2 \left\{ \mathcal{T}^{(i)}_{\ell_1\ell_2}(q,k) \right\} P(k,\eta_1,\eta_2) + P_{\rm shot} \ , \tag{3.22}$$

[2]Note that we have renamed the indices $\ell_1 \to \ell_2$ and $\ell \to \ell_1$.

where we now include the shot noise term, and have made the definitions:

$$\hat{\sum_{\ell_1\ell_2\ell_3}} \equiv \sum_{\ell_1}\sum_{\ell_2}\sum_{\ell_3}(2\ell_1+1)(2\ell_2+1)\begin{pmatrix}\ell_1 & \ell_2 & \ell_3\\ 0 & 0 & 0\end{pmatrix}^2\{l_1\ l_2\ l_3\}\ , \tag{3.23}$$

$$\mathcal{C}_{\ell_3} \equiv \sum_{m_3}|\Theta_{\ell_3 m_3}|^2\ , \tag{3.24}$$

$$\mathcal{T}^{(i)}_{\ell_1\ell_2}(q,k) \equiv A\int \mathrm{d}r_i r_i^2 Z(r_i) j_{\ell_1}(kr_i) j_{\ell_2}(qr_i)\ . \tag{3.25}$$

To check that the above result of Eq. (3.22) is sensible, we require that in the limit our survey mask becomes constant everywhere, we can recover the full-sky result of Eq. (2.33) in Chapter §2. We address this in Appendix §3.C.

At this point, it is worth noting the similarities between Eq. (3.22) and the result of FKP [78]: our survey power spectrum is the convolution of the underlying power spectrum with a survey window function $\prod_{i=1}^{2}\left\{\mathcal{T}^{(i)}_{\ell_1\ell_2}(q,k)\right\}$, which is the analogue of the $|G(\mathbf{k}-\mathbf{k}')|^2$ function in FKP equation (2.1.6), plus a shot noise term. Introducing the survey mask, wide-angle effects and an unequal-time power spectrum has added in some new elements in terms of having to perform infinite (but converging) sums, as well as the coupling of the k integral with the r integrals. As with Eq. (3.17), we are still faced with a complicated numerical 3D integral, however we now turn our attention to some specific cases that can make this expression more manageable.

3.2.2 The time separable UETC at linear order

In a similar fashion to our workings in Section §2.3.3 of the previous chapter, we now look to make the ansatz that the unequal-time power spectrum is time-separable. Starting with the simplest case [72], we make the assumption that the relationship between the galaxy field with the underlying matter field is described by a linear bias parameter which may evolve in time, but is independent of scale:

$$\Delta(\eta,k) = b_1(\eta)\delta(\eta,k)\ , \tag{3.26}$$

and that we have linear growth of density fluctuations:

$$\delta(\eta,k) = D(\eta)\delta(\eta_0,k)\ . \tag{3.27}$$

Using this, the unequal-time galaxy power spectrum at linear order is thus given by

$$P^{\mathrm{G}}_{\mathrm{Lin}}(k,\eta_1,\eta_2) = D(\eta_1)D(\eta_2)b_1(\eta_1)b_1(\eta_2)P_{\mathrm{Lin}}(k,\eta_0)\ . \tag{3.28}$$

where $D(\eta)$ is the linear growth factor, normalised against some time η_0, $b_1(\eta)$ is the evolving linear galaxy bias, and $P_{\mathrm{Lin}}(k,\eta_0)$ is the equal-time linear matter power spectrum. Substituting this into

Eq. (3.22), we have

$$\begin{aligned} P_{\rm F,Lin}(q) &= \hat{\sum_{\ell_1\ell_2\ell_3}} \mathcal{C}_{\ell_3} \int {\rm d}k k^2 \prod_{i=1}^{2} \left\{ \mathcal{T}^{(i)}_{\ell_1\ell_2}(q,k) \right\} D(\eta_1) D(\eta_2) b_1(\eta_1) b_1(\eta_2) P_{\rm Lin}(k,\eta_0) + P_{\rm shot}(q,q) \ , \\ &= \hat{\sum_{\ell_1\ell_2\ell_3}} \sum_{m_3} (2\ell_1+1)(2\ell_2+1) |\Theta_{\ell_3 m_3}|^2 \int {\rm d}k k^2 P_{\rm Lin}(k,\eta_0) \\ &\quad \times \Big[A \int {\rm d}r r^2 D(\eta) b_1(\eta) Z(r) j_{\ell_1}(kr) j_{\ell_2}(qr) \Big]^2 + P_{\rm shot} \ . \end{aligned} \tag{3.29}$$

We see immediately that in assuming time separability, we have decoupled the r integrals and reduced the overall dimensionality of integration from 3D down to 2D. Moreover, we have halved the number of spherical Bessel functions that need to be integrated. The two problem areas that remain in terms of numerical evaluation are the multiple sums and the remaining Bessel integral. The former is not as challenging as it seems on the surface, as the triangular delta imposes conditions coupling ℓ_1, ℓ_2 and ℓ_3, such that in practice it is only a double sum (see the end of Appendix §3.B for these conditions). Additionally, the angular mask coefficients $\Theta_{\ell_3 m_3}$ are the only quantities depending on m_3, and these can be computed and the sum over m_3 done in advance and stored, as we will show in Section §3.2.6. The integral can be tackled in two different ways: on large scales, we can use the FFTLog algorithm on the radial kernel functions, after which the whole integration over the r domain can be done analytically. We will cover this method in Section §3.3.1. On smaller scales we can use an approximation owing to the shape of the window function which we discuss in the next section.

Before moving on, it is worth noting that one of the interesting prospects of being able to measure the power spectrum on the largest scales is the ability to test for signatures of primordial non-Gaussianity (PNG): any deviation from the assumption that the primordial fluctuations laid down by inflation are Gaussian in nature. While single-field slow-roll inflation predicts that any non-Gaussian contribution will be small [35], it has yet to be decisively ruled out by experiment [36, 131]. A significant detection of PNG would therefore lead to a breakthrough in terms of our understanding of inflationary models and provide invaluable information about the nature of physical processes in the early universe. Including PNG in a model for the power spectrum effects the linear bias term by adding in a correction [132, 133, 134, 135]:

$$b_1(\eta) \to b_1(\eta) + \Delta b(k,\eta) \ , \tag{3.30}$$

where this new term is inversely proportional to k^2. We see that including this in our model for the power spectrum does not break time-separability:

$$P^{\rm G}_{\rm Lin}(k,\eta_1,\eta_2) = D(\eta_1)D(\eta_2)[b_1(\eta_1)+\Delta b(k,\eta_1)][b_1(\eta_2)+\Delta b(k,\eta_2)]P_{\rm Lin}(k,\eta_0) \ , \tag{3.31}$$

but will introduce additional terms to calculate at these large scales where the effect is important.

3.2.3 The small-scale limit and normalisation

We now turn our attention to any approximations that can be made to Eq. (3.29), to improve the prospects of numerical evaluation, without introducing significant systematics to the results. In the previous chapter we showed that, on small scales, i.e. where $q \gg 1/L$ with L^3 being the volume of our survey box, the survey window function becomes very compact and sharply peaks around the point where $q = k$, such that it acts like a Dirac delta function $\delta^D(q-k)$. We found this approximation to differ from the full result by $\ll 1\%$ in the appropriate q range (lower right plot of Fig. 2.2). While in that scenario we were working on the full sky, introducing a survey mask will not affect this property of the window function, so long as we only apply the approximation to scales much smaller than the characteristic scale of the survey volume.

Taking Eq. (3.29), and using that the function $P(k,\eta_0)$ is smooth and slowly varying in k, we have in the small-scale limit ($q > q_{\rm lim}$) that the Linear order term can be approximated as

$$\begin{aligned}
P_{\rm F,Lin}(q>q_{\rm lim}) &\approx \hat{\sum_{\ell_1\ell_2\ell_3}}\sum_{m_3}(2\ell_1+1)(2\ell_2+1)|\Theta_{\ell_3 m_3}|^2 P_{\rm Lin}(q,\eta_0) \\
&\quad\times\int {\rm d}k k^2\Big[A\int {\rm d}r r^2 D(\eta)b_1(\eta)Z(r)j_{\ell_1}(kr)j_{\ell_2}(qr)\Big]^2 \,, \\
&\approx \hat{\sum_{\ell_1\ell_2\ell_3}}\sum_{m_3}(2\ell_1+1)(2\ell_2+1)|\Theta_{\ell_3 m_3}|^2 P_{\rm Lin}(q,\eta_0)\Big[A\int {\rm d}r r^2 D(\eta)b_1(\eta)Z(r)j_{\ell_2}(qr)\Big]^2 \\
&\quad\times\int {\rm d}k k^2 j_{\ell_1}(kr_1)j_{\ell_1}(kr_2) \,, \\
&\approx \hat{\sum_{\ell_1\ell_2\ell_3}}\sum_{m_3}(2\ell_1+1)(2\ell_2+1)|\Theta_{\ell_3 m_3}|^2 P_{\rm Lin}(q,\eta_0)A^2 \\
&\quad\times\int {\rm d}r r^2 D^2(\eta)b_1^2(\eta)Z^2(r)j_{\ell_2}^2(qr) \,,
\end{aligned} \tag{3.32}$$

where in the last line we have used the orthogonality the spherical Bessel function:

$$\int dk k^2 j_\ell(kr_1)j_\ell(kr_2) = \frac{\pi}{2r_2^2}\delta^D(r_1-r_2) \,. \tag{3.33}$$

As the power spectrum has effectively decoupled from survey window function in this small-scale limit, the estimated power should be the same as in the full sky case: only the covariance will be different between the two scenarios, as that is related to the survey volume. Thus, by setting our survey mask equal to 1 in this limit, we can use Eq. (3.98) from Appendix §3.C, further reducing our approximate result to

$$P_{\rm F,Lin}(q>q_{\rm lim}) \approx \sum_{\ell_1}(2\ell_1+1)P_{\rm Lin}(q,\eta_0)A^2\int {\rm d}r r^2 D^2(\eta)b_1^2(\eta)[n_0^{\rm LC}(r)]^2 w^2(r) j_{\ell_1}^2(qr) \,. \tag{3.34}$$

The final step is to use the completeness relation of the spherical Bessel functions

$$\sum_{\ell}(2\ell+1)j_{\ell}^{2}(x)=1\ , \tag{3.35}$$

which leaves us with

$$P_{\rm F,Lin}(q>q_{\rm lim})\approx P_{\rm Lin}(q,\eta_0)A^2\int {\rm d}r r^2 D^2(\eta)b_1^2(\eta)[n_0^{\rm LC}(r)]^2w^2(r)+P_{\rm shot}\ . \tag{3.36}$$

There are several important points to note here. Firstly, the small scale limit has allowed us to reduce a multi-sum, 2D numerical integration problem, containing oscillating functions, down to a simple 1D integral over smooth functions. This means that we only have to compute the full expression on the largest of scales, where q is small, and then switch over to this very fast approximate form once the value of q reaches a certain limit, which can be obtained numerically. Secondly, if we chose our normalisation constant to be

$$A=\Big[\int {\rm d}r r^2[n_0^{\rm LC}(r)]^2w^2(r)\Big]^{-1/2}\ , \tag{3.37}$$

we see that our observed power spectrum on these scales will just be the true underlying power spectrum, with the amplitude modulated by a constant factor determined by the survey depth:

$$P_{\rm F,Lin}(q>q_{\rm lim})\approx \alpha_0\ P_{\rm Lin}(q,\eta_0)+P_{\rm shot}\ , \tag{3.38}$$

where the α_0 factor is given by

$$\alpha_0=\frac{\int {\rm d}r r^2 D^2(\eta)b_1^2(\eta)[n_0^{\rm LC}(r)]^2w^2(r)}{\int {\rm d}r r^2[n_0^{\rm LC}(r)]^2w^2(r)}\ . \tag{3.39}$$

The result of Eq. (3.38) is analogous to Eq. (2.1.8) of FKP and Eq. (16) of Yamamoto [72].

3.2.4 The large-scale limit

Turning our attention to the largest scales, we now investigate the expected shape of the power spectrum as $q\to 0$. Starting from Eq. (3.29) and including the bias term for PNG:

$$\begin{aligned}P_{\rm F,Lin}(q) \ &= \ \hat{\sum_{\ell_1\ell_2\ell_3}}\sum_{m_3}(2\ell_1+1)(2\ell_2+1)|\Theta_{\ell_3 m_3}|^2\int {\rm d}k k^2 P_{\rm Lin}(k,\eta_0)\\ &\quad\times\Big[A\int {\rm d}r r^2 D(\eta)[b_1(\eta)+\Delta b(k,\eta)]Z(r)j_{\ell_1}(kr)j_{\ell_2}(qr)\Big]^2\ ,\end{aligned} \tag{3.40}$$

we exploit a property of the spherical Bessel function:

$$j_{\ell}(x)\Big|_{x\to 0}=\delta_0^{\ell}\ . \tag{3.41}$$

Using this eliminates any q dependence from the equation:

$$P_{\rm F,Lin}(q)\Big|_{q\to 0} = \hat{\sum_{\ell_1\ell_3}}\sum_{m_3}(2\ell_1+1)|\Theta_{\ell_3 m_3}|^2\int {\rm d}k k^2 P_{\rm Lin}(k,\eta_0) \times\Big[A\int {\rm d}r r^2 D(\eta)[b_1(\eta)+\Delta b(k,\eta)]Z(r)j_{\ell_1}(kr)\Big]^2 + P_{\rm shot}\ , \tag{3.42}$$

and we see the power will converge to a constant value on these scales, similar to our findings in Section §2.3.5.

3.2.5 Extension to the nonlinear regime

We now generalise the result of a time-separable power spectrum beyond the linear order, and make an ansatz that the unequal time power spectrum of can be expanded in the following way:

$$P(k,\eta_1,\eta_2) = \sum_{a,b} G_a(\eta_1,\eta_0)G_b(\eta_2,\eta_0)b_a(\eta_1,k)b_b(\eta_2,k)\mathcal{F}_{ab}[P](k)\ , \tag{3.43}$$

where the functions $G_a(\eta,\eta_0)$ give the amplification at time η relative to some fiducial time η_0, $b_a(\eta_1,k)$ are generalised evolving bias functions which may be scale dependent, and the functionals $\mathcal{F}_{ab}$ only involve integrals over the equal time correlator. Note that we make no assumptions about the form of the bias functions, except that they must be smoothly varying in k, and include them here in a general way as an example (we discuss this more at the end of the section). Assuming this power-series form allows us to encompass a range of models, such as that of Kitching & Heavens [47]. Listing terms up to first order, we have

$$\begin{aligned} P(k,\eta_1,\eta_2) &= D(\eta_1)D(\eta_2)b_1(\eta_1,k)b_1(\eta_2,k)P_{\rm Lin}(k,\eta_0) \\ &\quad + D^2(\eta_1)D^2(\eta_2)b_2(\eta_1,k)b_2(\eta_2,k)\mathcal{F}_{22}[P](k) \\ &\quad + \big[D(\eta_1)D^3(\eta_2)b_1(\eta_1,k)b_3(\eta_2,k) + D^3(\eta_1)D(\eta_2)b_3(\eta_1,k)b_1(\eta_2,k)\big]\mathcal{F}_{13}[P](k) \\ &\quad + \ldots\ . \end{aligned} \tag{3.44}$$

Substituting this into Eq. (3.22) will give three terms, which we refer to as linear, '2-2' and '1-3' terms. The linear term can be solved in two regimes: on large scales where, we have the expression given by Eq. (3.29) and can use the FFTLog algorithm, which we cover in Section §3.3.1, to avoid having to numerically compute the double Bessel integral. For the rest of the q domain, we can use the small scale approximation of Eq. (3.36).

Turning our attention next to the first order corrections, we start with the '2-2' term, substi-

tuting line 2 of Eq. (3.44) into Eq. (3.22):

$$\begin{aligned} P_{\rm F,22}(q) &= \hat{\sum_{\ell_1\ell_2\ell_3}} \mathcal{C}_{\ell_3} \int {\rm d}k k^2 \prod_{i=1}^{2} \left\{ \mathcal{T}^{(i)}_{\ell_1\ell_2}(q,k) \right\} D^2(\eta_1) D^2(\eta_2) b_2(\eta_1,k) b_2(\eta_2,k) \mathcal{F}_{22}[P](k) \ , \\ &= \hat{\sum_{\ell_1\ell_2\ell_3}} \sum_{m_3} (2\ell_1+1)(2\ell_2+1)|\Theta_{\ell_3 m_3}|^2 \int {\rm d}k k^2 \mathcal{F}_{22}[P](k) \\ &\quad \times \Big[A \int {\rm d}r r^2 D^2(\eta) b_2(\eta,k) Z(r) j_{\ell_1}(kr) j_{\ell_2}(qr) \Big]^2 \ , \end{aligned} \tag{3.45}$$

where as before we have been able to decouple the radial integrals do reduce the overall dimensionality of integration. As this term is only significant in the nonlinear regime were q is small, and as we expect our bias functions to be smooth and slowly varying in k, we are again free to use the small-scale approximation. This will reduce thus reduce down to

$$P_{\rm F,22}(q > q_{\rm lim}) \approx \alpha_1(q) \ \mathcal{F}_{22}[P](q) \ , \tag{3.46}$$

where

$$\alpha_1(q) = \frac{\int {\rm d}r r^2 D^4(\eta) b_2^2(\eta,q) [n_0^{\rm LC}(r)]^2 w^2(r)}{\int {\rm d}r r^2 [n_0^{\rm LC}(r)]^2 w^2(r)} \ . \tag{3.47}$$

For the '1-3' term, we have

$$\begin{aligned} P_{\rm F,13}(q) &= \hat{\sum_{\ell_1\ell_2\ell_3}} \mathcal{C}_{\ell_3} \int {\rm d}k k^2 \prod_{i=1}^{2} \left\{ \mathcal{T}^{(i)}_{\ell_1\ell_2}(q,k) \right\} \Big[D(\eta_1) D^3(\eta_2) b_1(\eta_1,k) b_3(\eta_2,k) \\ &\quad + D^3(\eta_1) D(\eta_2) b_3(\eta_1,k) b_1(\eta_2,k) \Big] \mathcal{F}_{13}[P](k) \ , \\ &= \hat{\sum_{\ell_1\ell_2\ell_3}} \sum_{m_3} (2\ell_1+1)(2\ell_2+1)|\Theta_{\ell_3 m_3}|^2 \int {\rm d}k k^2 \mathcal{F}_{213}[P](k) \\ &\quad \times A^2 \Big[\int {\rm d}r_1 r_1^2 D(\eta_1) b_1(\eta_1,k) Z(r_1) j_{\ell_1}(kr_1) j_{\ell_2}(qr_1) \\ &\quad \times \int {\rm d}r_2 r_2^2 D^3(\eta_2) b_3(\eta_2,k) Z(r_2) j_{\ell_1}(kr_2) j_{\ell_2}(qr_2) + \int {\rm d}r_1 r_1^2 D^3(\eta_1) b_3(\eta_1,k) Z(r_1) j_{\ell_1}(kr_1) j_{\ell_2}(qr_1) \\ &\quad \times \int {\rm d}r_2 r_2^2 D(\eta_2) b_1(\eta_2,k) Z(r_2) j_{\ell_1}(kr_2) j_{\ell_2}(qr_2) \Big] \ , \end{aligned} \tag{3.48}$$

which in the small-scale approximation reduces down to

$$P_{\rm F,13}(q > q_{\rm lim}) \approx \alpha_2(q) \ \mathcal{F}_{13}[P](q) \ , \tag{3.49}$$

with

$$\alpha_2(q) = \frac{2 \int {\rm d}r r^2 D^4(\eta) b_1(\eta) b_3(\eta,q) [n_0^{\rm LC}(r)]^2 w^2(r)}{\int {\rm d}r r^2 [n_0^{\rm LC}(r)]^2 w^2(r)} \ . \tag{3.50}$$

Putting all this together, we have a piecewise expression for evaluating our masked galaxy power spectrum on the lightcone, up to first order:

$$P_{\rm F}(q) \simeq \begin{cases} \hat{\sum}_{\ell_1\ell_2\ell_3} \mathcal{C}_{\ell_3} \int {\rm d}k k^2 P_{\rm Lin}(k,\eta_0) \Big[A \int {\rm d}r r^2 D(\eta) b_1(\eta) Z(r) j_{\ell_1}(kr) j_{\ell_2}(qr) \Big]^2 + P_{\rm shot} & \text{for } q \leq q_{\rm lim} \ , \\ \alpha_0 \ P_{\rm Lin}(q,\eta_0) + \alpha_1(q) \ \mathcal{F}_{22}[P](q) + \alpha_2(q) \ \mathcal{F}_{13}[P](q) + P_{\rm shot} & \text{for } q > q_{\rm lim} \ , \end{cases} \tag{3.51}$$

where for the case $q \leq q_{\rm lim}$ we work at large scales and so neglect nonlinear corrections, and for the case $q > q_{\rm lim}$ we use the small-scale approximation and consider terms up to 1-loop in perturbation theory. We see that for each term of our generalised expansion of the unequal time power spectrum, assuming time separability allows us to reduce the complexity of the problem on large scales, and combining this with the small-scale approximation significantly simplifies the problem at smaller scales, as in this region we always obtain 1D integrals over smooth functions.

Applying this model in a real-world scenario can be difficult however, as the value of the bias parameters are not directly predicted by theory, and will vary with tracer type. These parameters will also depend on time: in the early universe, the first galaxies to form will be those situated in the largest over-densities of the matter distribution, and so galaxy bias will be higher at these times than in the late-time universe where the distribution of galaxies more evenly represents the distribution of matter. A significant amount of work in the literature over the past few decades has been dedicated to the topic of tracer bias ([136] for a comprehensive review), with the approaches broadly fall into two categories: the first is where one does not try to tackle the complicated process of galaxy formation, and instead starts off with a model of bias once the galaxy has formed and thus evolves under the force of gravity. An example of this, for modelling the evolution of the linear bias parameter, was proposed in [137] and given a more general form in [138]:

$$b_1(\eta) = c + \frac{b_0 - c}{D^\gamma(\eta)} \ , \tag{3.52}$$

where b_0 is the constant linear bias term, $D(\eta)$ is the usual linear growth factor, and c and γ are constants to be determined empirically by fitting to data or simulations. We see that this term is a smoothly varying function in time and thus will not introduce any numerical complications on large scales. We can also include the PNG term from Eq. (3.30) here, which has the form [135]

$$\Delta b(k,\eta) = \frac{3(b_1(\eta) - 1) f_{\rm NL} \Omega_{m,0} H_0^2 \delta_c}{D(\eta) k^2 T(k)} \ , \tag{3.53}$$

where $\Omega_{m,0}$ and H_0 are the matter density and Hubble parameters today, $T(k)$ is the transfer function, $\delta_c \simeq 1.68$ is the threshold linear density contrast for a spherical collapse of an overdensity region, and $f_{\rm NL}$ paramterises the amount of PNG. The effect of this term modifies the power on large scales in a smooth manner (see eg. Fig. 7 in [132]), based on the value of $f_{\rm NL}$, and therefore, similar to $b_1(\eta)$, this term will be easy to handle from a numerical perspective.

The other approach to tackling bias is based on the knowledge that the large-scale structure

we see today was seeded by small fluctuations in the underlying matter-density field in the early universe. Thus, one can take the approach of perturbation theory, modelling the galaxy density field as a series expansion of an unknown function of the matter-density field, with the coefficients of the series expansion being the bias parameters, for example in the case of SPT we have

$$\delta_g(\mathbf{r}) = f(\delta_m(\mathbf{r})) = \sum_n \frac{b_n}{n!}\delta_m^n(\mathbf{r}) \ . \tag{3.54}$$

However, the bias parameters in this approach must be renormalised in order to obtain sensible results that can match observables [139], whereby one can obtain an expression for the power spectrum that is similar in form to Eq. (3.44). While the specific details of this are not in-scope for the current work, the important point is that as long as time separability holds, the problem can always be reduced to one that is more numerically feasible.

3.2.6 Calculating the angular mask

Before moving on to numerical methods for tackling our model of galaxy power spectrum on the lightcone, we turn our attention to computation of the angular mask term $\mathcal{C}_{\ell_3}^{\Theta} \equiv \sum_{m_3} |\Theta_{\ell_3 m_3}|^2$, effectively the power spectrum of the angular mask. As this is the only quantity in our main result of Eq. (3.22) than has an index of m_3, for a specific survey mask, the array of $\mathcal{C}_{\ell_3}^{\Theta}$'s can be pre-computed up to some large value of $\ell_{\max}$ and stored.

We start by giving an example where our survey has a simple geometry: the spherical cap mask. This could be used to approximate the angular component for any survey over a single, continuous field with geometry that roughly approximates a circle. Recall from equations (3.12) and (3.13) that we performed a spherical harmonic expansion of the angular component of the survey mask:

$$\Theta(\hat{\mathbf{r}}) = \Theta(\theta, \phi) = \sum_{\ell,m} \Theta_{\ell m} Y_{\ell m}(\theta, \phi) \ . \tag{3.55}$$

The coefficients of such an expansion can be recovered by integrating the original angular function against the complex conjugate of the spherical harmonic,

$$\Theta_{\ell m} \quad = \quad \int_0^{2\pi} \mathrm{d}\phi \int_0^{\pi} d\theta \sin(\theta) Y^*_{\ell m}(\theta, \phi)\Theta(\theta, \phi) \ , \tag{3.56}$$

and recalling that the spherical harmonics are related to the associated Legendre polynomials via

$$Y^*_{\ell m}(\theta, \phi) \quad = \quad (-1)^m \sqrt{\frac{(2\ell+1)}{4\pi}\frac{(\ell-m)!}{(\ell+m)!}} \mathcal{P}_{\ell m}(\cos\theta) e^{-im\phi} \ , \tag{3.57}$$

allows us to separate the integration variables θ and ϕ:

$$\Theta_{\ell m} = (-1)^m \sqrt{\frac{(2\ell)}{4\pi}\frac{(\ell-m)!}{(\ell+m)!}} \int_0^{2\pi} \mathrm{d}\phi \ e^{-im\phi} \int_0^{\pi} \mathrm{d}\theta \sin(\theta) \mathcal{P}_{\ell m}(\cos\theta). \tag{3.58}$$

For a spherical cap mask, we have that $\Theta(\theta, \phi)$ is 1 in the regions $0 \leq \phi \leq 2\pi$ and $0 \leq \theta \leq \mu$, where μ is some arbitrary angle in declination, and zero elsewhere:

$$\begin{aligned}\Theta_{\ell m} &= \int_0^{2\pi} \mathrm{d}\phi\, e^{-im\phi} \int_0^{\mu} \mathrm{d}\theta \sin(\theta)(-1)^m \sqrt{\frac{(2\ell+1)}{4\pi}\frac{(\ell-m)!}{(\ell+m)!}}\mathcal{P}_{\ell m}(\cos\theta)\ , \\ &= 2\pi\delta_0^m \int_0^{\mu} \mathrm{d}\theta \sin(\theta)(-1)^m \sqrt{\frac{(2\ell+1)}{4\pi}\frac{(\ell-m)!}{(\ell+m)!}}\mathcal{P}_{\ell m}(\cos\theta)\ , \\ &= \sqrt{\pi(2\ell+1)} \int_0^{\mu} \mathrm{d}\theta \sin(\theta)\mathcal{P}_{\ell}(\cos\theta)\ . \end{aligned} \tag{3.59}$$

If we then make the substitution $y = \cos(\theta)$ and take the modulus-square, we obtain the expression for C_ℓ^Θ in this case:

$$C_\ell^\Theta = \pi(2\ell+1)\Big| \int_1^{\cos(\mu)} \mathcal{P}_\ell(y)\mathrm{d}y\Big|^2. \tag{3.60}$$

By assuming this geometry of the mask, we have removed the sum over m and the problem reduces to simple integration over standard Legendre polynomials.

For a more generalised case, where we have a complicated survey mask that may also contain multiple regions, we can compute the C_ℓ^Θ's numerically with software like `HEALPix`[3] [140]. As an example, in Fig. 3.1 we plot the angular footprint of the upcoming 4MOST Cosmology Redshift Survey [54], as well as the resulting C_ℓ^Θ's, and compare this to the simple case of the spherical cap mask with declination angle $\mu = 25°$. While both of these cases produce mask coefficients that are oscillatory in nature, as we are only summing over them and not integrating, this task is numerically fast. In addition to this, we see a general trend that the value of the mask power spectrum drops off exponentially as ℓ increases, which will speed up convergence of the double sum in Eq. (3.29).

3.3 Numerical methods for evaluating the wide-angle masked power spectrum

Having now established our theoretical model for the masked galaxy power spectrum on the light-cone, we now review some numerical methods that can be used to tackle the double-Bessel integrals encountered in §3.2 such as Eq. (3.29), which contains an integral of the form

$$R_{\ell_1\ell_2}(q,k) = \int \mathrm{d}r\ r^2\chi(r) j_{\ell_1}(kr) j_{\ell_2}(qr)\ , \tag{3.61}$$

where $\chi(r)$ is some smooth radial kernel function. These integrals can be challenging in nature to solve and prone to numerical instability, due to the oscillatory nature of the Bessel functions,

[3]See for example the 'healpy.sphtfunc.anafast' routine in the python implementation of HEALPix - https://healpy.readthedocs.io/

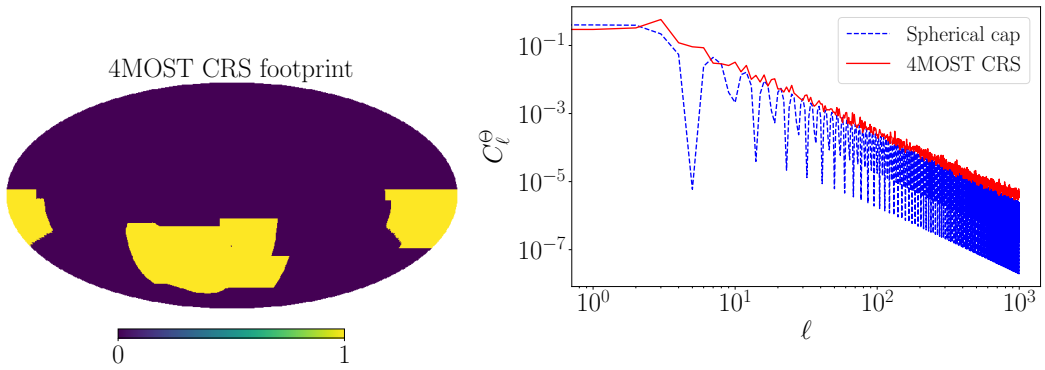

Figure 3.1: Left: A `HEALPix` map showing the angular mask of the 4MOST Cosmology Redshift Survey. Right: The corresponding C_ℓ^Θ's up to $\ell_{\rm max} = 1000$ for the 4MOST survey mask (red solid line), calculated using `healpy`, the python implementation of `HEALPix`. We also plot the result for the spherical cap mask presented in Eq. (3.60) with $\mu = 25°$ (blue dashed line), calculated directly from the equation.

particularly as ℓ or the argument grow larger. This is compounded by the fact that as we go to smaller scales, a growing number of $\{\ell_1, \ell_2\}$ terms need to be calculated before the sums converge to a specified precision. In Chapter §2 we encountered a similar expression, but where $\ell_1 = \ell_2$, and only one sum over ℓ was required (see Eq. (3.100)). In that scenario, it was sufficient to brute force the equation on large scales ($q > q_{\rm lim}$), after which we could use the small-scale approximation outlined in §3.2.3. By introducing an angular mask, we now have a product of Bessel functions of differing ℓ order, and a conditional double sum over $\{\ell_1, \ell_2 \ell_3\}$, therefore it is appropriate to look for analytical solutions that will be more numerically feasible.

The double-Bessel integral of Eq. (3.61) is a challenge being encountered more frequently in the field of cosmology as surveys have grown in size and the required modelling of observables has necessarily become more sophisticated. One of the most commonly used techniques to solve the problem involves performing a complex power-law expansion on the kernel function via the FFTLog method, after which an analytic solution to the integral can be employed. In doing this, we reduce a difficult integral over r to a finite sum over a smooth function in q and k.

The FFTLog algorithm takes the fast Fourier (or Hankel) transform of a periodic sequence of logarithmically spaced points - it is the logarithmic analogue of the standard transforms that work in a linear spacing. An early example of this method being applied to the field of cosmology was in Hamilton [125], allowing for fast transforms between the power spectrum and two point correlation function. More recent developments have seen this method applied to Bessel integrals, particularly when dealing with perturbation theory calculations [99], angular and projected power spectra [141, 142, 143, 144], as well as higher order statistics [145, 146]. The majority of this literature has been focused on solving integrals over the Power spectrum multiplied by one or two Bessel functions

(with common index ℓ), of the form:

$$I_\ell(r) = \int \mathrm{d}k k^2 P(k) j_\ell(kr) \ , \tag{3.62}$$

$$I_\ell(r_1, r_2) = \int \mathrm{d}k k^2 P(k) j_\ell(kr_1) j_\ell(kr_2) \ , \tag{3.63}$$

with the focus being performing a power-law expansion of the power spectrum. For our scenario in Eq. (3.29), this approach is sub optimal, as if we look to tackle the k integral first it would re-couple the r integrals, turning the overall expression back into a 3D integral, and we would still be left with integrals over Bessel functions. In this work we apply the method to the radial integral instead, where the Bessels have differing index ℓ.

3.3.1 FFTLog of the radial integral

We now apply the FFTLog method to our radial kernel function $r^2\chi(r)$, following the convention of McEwen et al. [99]. We look to approximate the function, sampled evenly in logspace over N_r points, as a complex series expansion of the form

$$\chi(r_n) = \sum_{m=-N_r/2}^{N_r/2} c_m r_n^{\beta + i\eta_m} \quad \Leftrightarrow \quad c_m = W_m \sum_{n=0}^{N_r-1} \chi(r_n) r_n^{-\beta} e^{-2\pi i m n/N} \ , \tag{3.64}$$

where c_m are the Fourier coefficients, $\eta_m = 2\pi m/N_r\Delta$ with Δ the linear spacing i.e. $r_n = r_0 \exp(n\Delta)$, $m = -N_r/2, -N_r/2+1, \ldots, N_r/2-1, N_r/2$, and W_m is a window function designed to reduce ringing that can be induced by the transform (we use a window function given by equation (C.1) in McEwen). We bias the transform by a factor of r_n^β, with beta chosen such that it causes the function $r_n^{\beta+2}\chi(r_n)$ to be approximately periodic over the interval of interest, which can improve the convergence of the FFTLog method [141]. As an example, in Fig. 3.2 we demonstrate the FFTLog of a radial kernel

$$r^2\chi(r) = r^2 n_0^{\mathrm{LC}}(r) b_1(\eta) D(\eta) \ , \tag{3.65}$$

where for $n_0^{\mathrm{LC}}(r)$ we use the evolving Schechter function described in Appendix §2.B, and $b_1(\eta)$ is given by the linear evolving bias model of Eq. (3.52) with parameters $\{c = 0.57, b_0 = 0.79, \gamma = 2.23\}$ [138]. We sample the radial kernel over $N_r = 65$ points and chose a bias value of $\beta = 0.48$. The exact function is represented as the black dashed line in the figure, with the FFTLog approximation shown by the blue solid line. In the lower half of the plot we show the percentage difference between these two lines, where we see that the FFTLog approximates the function to much less than 1% error over the whole range, with some small amount of ringing at either end. We also plot the exact function multiplied by r^β to demonstrate the effect this has: the bias effectively 'tilts' the original function, such that it becomes very close to being periodic over the interval.

One of the advantages of this FFTLog method is that the c_m coefficients can be computed in

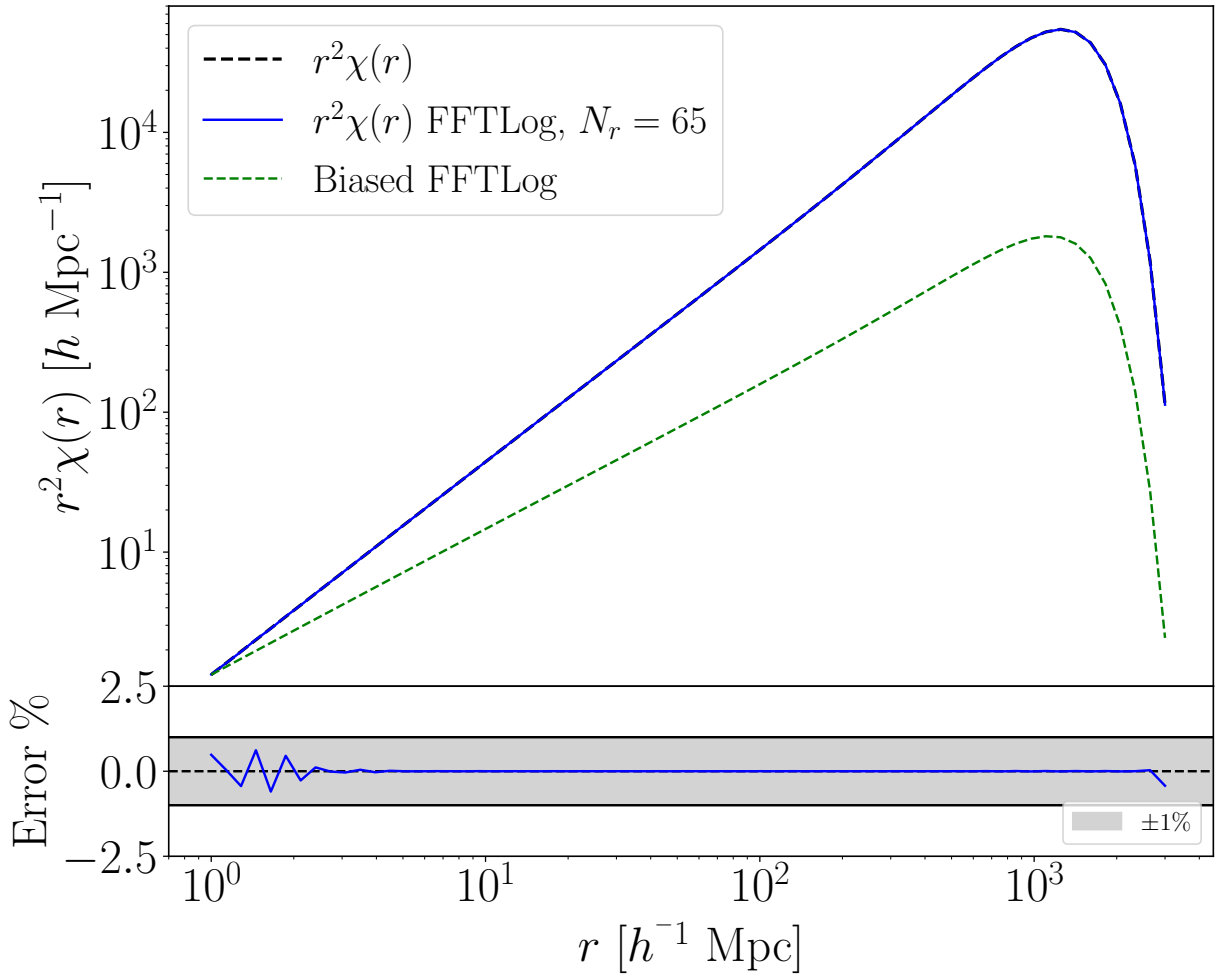

Figure 3.2: Figure showing the radial kernel function $r^2\chi(r)$ of Eq. (3.65) (black dashed line), and its approximation using the FFTLog method of Eq. (3.64) (blue solid line) using $N_r = 65$ sampling points and a bias factor of $\beta = 0.48$. The lower sub plot shows the percentage error between these two lines, with the solid black lines bounding the shaded grey region representing the $\pm 1\%$ error. We see that the FFTLog method with our choice of N and β provides an excellent approximation to the original function. The green dashed line in the upper plot is the radial kernel function multiplied by r^β: we see that this has the effect of 'tilting' the original function, making it very close to being periodic over the interval.

advance of any calculation, and only ever need to be calculated once for a given $\chi(r)$ and then stored. We chose $N_r = 65$ sampling points as this was the lowest possible value for our example $\chi(r)$ that still gave accurate results. In practice, one wants to minimize N as much as possible for two reasons: firstly, it reduces the number of terms that are required to be summed, which increases the speed of any further calculation steps that rely on this method. Secondly, it reduces the size of the arguments being fed into the hypergeometric functions that we will encounter in the next section, which is important for both speed and numerical stability.

The FFTLog method is still applicable if a scale-dependent bias term is included in the radial

kernel function such that $\chi(r) \to \chi(r,k)$. In this case, the function should be sampled as a 2D array, with the additional dimension coming from a sampling in the k range by N_k points, where for each k_n we have a specific bias value β_k. While this will slightly increase the up-front computational cost, it is not prohibitive as the process is already fast and only needs to be performed once. Care must be chosen to pick a value of N_r that is suitable for all values of k_n, but employing a method like a least-squares fitting to quickly determine the β_k values could be used to automate this process.

3.3.2 The analytic Bessel integrals

Once the complex power law decomposition of the radial function has been employed, our radial integral becomes

$$\begin{aligned} R_{\ell_1\ell_2}(q,k) &= \int \mathrm{d}r\ r^2 \chi(r) j_{\ell_1}(kr) j_{\ell_2}(qr)\ , \\ &= \sum_{m=-N/2}^{N/2} c_m \int \mathrm{d}r\ r^{\beta+i\eta_m} j_{\ell_1}(kr) j_{\ell_2}(qr)\ . \end{aligned} \tag{3.66}$$

We now look for analytic solutions to this equation, based on the values of k and q. In the region where $k \leq q$, we make the substitutions $\tau = k/q$, $qr = x$ and $\beta + i\eta_m = -\nu$, leading to

$$\begin{aligned} R_{\ell_1\ell_2}(q,k) &= \sum_{m=-N/2}^{N/2} c_m q^{\nu_m - 1} \int \mathrm{d}x\ x^{-\nu_m} j_{\ell_1}(\tau x) j_{\ell_2}(x)\ , \\ &= \sum_{m=-N/2}^{N/2} c_m q^{\nu_m - 1} I_{\ell_1\ell_2}(\nu_m, \tau)\ , \end{aligned} \tag{3.67}$$

where we have defined the quantity

$$I_{\ell_1\ell_2}(\nu_m,\tau) \equiv \int \mathrm{d}x\ x^{-\nu_m} j_{\ell_1}(\tau x) j_{\ell_2}(x)\ . \tag{3.68}$$

In Appendix §3.D we briefly derive the transforms of this equation using [130], and for $0 < \tau < 1$ we have from Eq. (3.104):

$$\begin{aligned} I_{\ell_1\ell_2}(\nu_m,\tau) &= \frac{\pi \tau^{\ell_1} \Gamma\Big(\frac{\ell_1+\ell_2-\nu_m+1}{2}\Big)}{2^{\nu_m+2}\Gamma\Big(\frac{-\ell_1+\ell_2+\nu_m+2}{2}\Big)\Gamma\Big(\ell_1+\frac{3}{2}\Big)} \\ &\quad \times {}_2F_1\Big(\frac{\ell_1+\ell_2-\nu_m+1}{2}, \frac{\ell_1-\ell_2-\nu_m}{2}, \ell_1+\frac{3}{2}, \tau^2\Big)\ , \\ &\quad \mathrm{Re}[\ell_1+\ell_2-\nu_m+1] > 0\ ,\ \mathrm{Re}[\nu_m] > -2\ ,\ 0<\tau<1\ , \end{aligned} \tag{3.69}$$

where $\Gamma(x)$ is the usual Gamma function and ${}_2F_1(a,b,c;z)$ is know as the Gauss Hypergeometric function, which has a series representation of

$$ {}_2F_1(a,b,c,z) = \sum_{n=0}^{\infty} \frac{(a)_n (b)_n}{(c)_n} \frac{z^n}{n!} \ . \tag{3.70} $$

Here, $(x)_n$ is the (rising) Pochhammer symbol:

$$ (x)_n \equiv \frac{\Gamma(x+n)}{\Gamma(x)} \ , \tag{3.71} $$

and the ${}_2F_1(a,b,c;z)$ series converges if c is not a negative integer, for $|z|<1$, and on the unit circle $|z|=1$ for $\mathrm{Re}[c-a-b]>0$. In the instance where $\tau = 1$, the hypergeometric function can be expressed purely in terms of gamma functions, and we can use the transform of Eq. (3.105):

$$ I_{\ell_1\ell_2}(\nu_m,1) = \frac{\pi\Gamma\big(\nu+1\big)\Gamma\Big(\frac{\ell_1+\ell_2-\nu_m+1}{2}\Big)}{2^{\nu_m+2}\Gamma\Big(\frac{-\ell_1+\ell_2+\nu_m+2}{2}\Big)\Gamma\Big(\frac{\ell_1+\ell_2+\nu_m+3}{2}\Big)\Gamma\Big(\frac{\ell_1-\ell_2+\nu_m+2}{2}\Big)} \ , \tag{3.72} $$
$$ \mathrm{Re}[\ell_1+\ell_2+2] > \mathrm{Re}[\nu_m+1] > 0 \ . $$

In the region where $k>q$, we instead make the substitutions[4] $\tau' = q/k$ and $kr = x$ and $\beta + i\eta_m = -\nu_m$, giving

$$ \begin{aligned} R_{\ell_1\ell_2}(q,k) &= \sum_{m=-N/2}^{N/2} c_m k^{\nu_m - 1} \int \mathrm{d}x \ x^{-\nu_m} j_{\ell_1}(x) j_{\ell_2}(\tau' x) \ , \\ &= \sum_{m=-N/2}^{N/2} c_m k^{\nu_m - 1} M_{\ell_1\ell_2}(\nu_m, \tau') \ , \end{aligned} \tag{3.73} $$

where we have defined the quantity

$$ M_{\ell_1\ell_2}(\nu_m,\tau') \equiv \int \mathrm{d}x \ x^{-\nu_m} j_{\ell_1}(x) j_{\ell_2}(\tau' x) \ . \tag{3.74} $$

[4]The usual method in the literature to solve Eq. (3.68) for the region where $\tau > 1$ is to make a substitution of integration variables, where it can then easily be shown that $I_{\ell_1\ell_2}(\nu_m,\tau) = \tau^{-\nu_m} I_{\ell_1\ell_2}(\nu_m, 1/\tau)$, which will bring the 4th argument of the Gauss Hypergeometric function back into the domain of validity. However, this trick only works when $\ell_1 = \ell_2$: we can see from [130] equation (6.574.1) that the RHS is not symmetric on swapping the arguments and orders of the two Bessel functions when $\ell_1 \neq \ell_2$.

For this, we use Eq. (3.108):

$$
\begin{aligned}
M_{\ell_1\ell_2}(\nu_m,\tau') &= \frac{\pi\tau'^{\ell_1}\Gamma\Big(\frac{\ell_1+\ell_2-\nu_m+1}{2}\Big)}{2^{\nu_m+2}\Gamma\Big(\frac{\ell_1-\ell_2+\nu_m+2}{2}\Big)\Gamma\Big(\ell_1+\frac{3}{2}\Big)} \\
&\quad\times {}_2F_1\Big(\frac{\ell_1+\ell_2-\nu_m+1}{2},\frac{-\ell_1+\ell_2-\nu_m}{2},\ell_2+\frac{3}{2},\tau'^2\Big)\ , \\
&\quad \mathrm{Re}[\ell_1+\ell_2-\nu_m+1]>0\ ,\ \mathrm{Re}[\nu_m]>-2\ ,\ 0<\tau'<1\ .
\end{aligned}
\tag{3.75}
$$

Despite being integrals over rapidly oscillating Bessel functions, the analytic transforms $I_{\ell_1\ell_2}(\nu_m,\tau)$ and $M_{\ell_1\ell_2}(\nu_m,\tau')$ are actually smooth in τ and Λ, and thus performing these transforms has turned a challenging numerical integral into a finite sum of terms of smooth functions. To summarise, we have the following piecewise expression for solving our radial integral analytically:

$$
R_{\ell_1\ell_2}(q,k)=\begin{cases}\sum_m c_m q^{\nu_m-1} I_{\ell_1\ell_2}(\nu_m,\tau) & \text{when } k<q, \text{ see Eq. (3.69)}\ ,\\ \sum_m c_m q^{\nu_m-1} I_{\ell_1\ell_2}(\nu_m,1) & \text{when } k=q, \text{ see Eq. (3.72)}\ ,\\ \sum_m c_m q^{\nu_m-1} M_{\ell_1\ell_2}(\nu_m,\tau') & \text{when } k>q, \text{ see Eq. (3.75)}\ ,\end{cases}
\tag{3.76}
$$

and our full expression for the power spectrum on large scales is now

$$
P_F(q)=A^2\hat{\sum}_{\ell_1\ell_2\ell_3}\mathcal{C}_{\ell_3}\int \mathrm{d}k k^2 P_{\mathrm{Lin}}(k,\eta_0)[R_{\ell_1\ell_2}(q,k)]^2+P_{\mathrm{shot}}\ .
\tag{3.77}
$$

The task therefore boils down to efficient evaluation of the hypergeometric function contained in $I_{\ell_1\ell_2}(\nu_m,\tau)$ and $M_{\ell_1\ell_2}(\nu_m,\tau')$, over the region $0<\tau<1$. This has already been studied in the literature [141, 143, 142], where the general method involves performing transforms on the the ${}_2F_1(a,b,c;\tau^2)$ function to reduce the size of the arguments into domains of increased numerical speed and stability[5]. In particular, care must be taken when either a, b or c grow large, especially if they are complex as a and b are in our case, as in these regions numerical instability will occur [147]. Additionally, as $\tau\to 1$, computation of the hypergeometric function is slower as more terms are needed to reach convergence, and so it is useful to find a value τ^* (numerically) such that whenever $\tau^*<\tau<1$, a transform is performed on this argument to bring it back below $\tau*$ (examples in Appendix A and B of [141]).

3.3.3 A practical algorithm

We now bring together all the steps of the previous sections to outline a practical algorithm for evaluating the masked power spectrum $P_F(q)$ on the lightcone, assuming the underlying unequal time power spectrum $P(k,\eta_1,\eta_2)$ is time separable. We outline the process as follows:

1. Several quantities can be precomputed and saved in advance of the calculation:

[5] See https://mathworld.wolfram.com/EulersHypergeometricTransformations.html for the Euler's hypergeometric transforms or Abramowitz and Stegun p.555 [98].

(a) The power of the angular mask $C_{\ell_3}^{\Theta}$ outlined in Section §3.2.6, up to some $\ell_{\rm max}$. This can be be done quickly using existing software packages like `HEALPix`, and only has to be calculated once for a specified angular mask.

(b) Perform the FFTLog decomposition of the radial kernel function, as outlined in Section §3.3.1 to obtain the Fourier coefficients c_m given by Eq. (3.64), which only have to be calculated once for a given radial kernel function $r^2\chi(r)$. An appropriate number of sampling points N_r and value for the bias parameter β should be chosen, to ensure accuracy and fast convergence of the series.

(c) The the allowed combinations of ℓ_1, ℓ_2 and ℓ_3 using the triangular rules outlined at the end of Appendix §3.B: determine all of the valid pairs of ℓ_1 and ℓ_2 for a given ℓ_3, for $0 \leq \ell_3 \leq \ell_{\rm max}$. This is independent of cosmology and survey geometry and so can be calculated and stored as a 2D array for all future calculations.

(d) The shot noise contribution $P_{\rm shot}$ derived in Appendix §3.A and the normalisation constant A given by Eq. (3.37), with the former depending on the survey mask and radial kernel, and the latter dependent only on the number density $n_0^{\rm LC}(r)$ and choice of optimal weighting scheme $w(r)$.

2. With these pre-calculations complete, we can then compute $P_{\rm F}(q)$ over the full range of q using the small-scale approximation, given by the lower line of Eq. (3.51). While this will only give you the correct power on small scales ($q > q_{\rm lim}$), it is very fast to compute as you are only having to evaluate smooth 1D integrals, and having this evaluated over the full range of q can be useful as a reference.

3. We now need to perform the full calculation of $P_{\rm F,Lin}(q)$ given by the upper line of Eq. (3.51), between the ranges $q_{\rm min} < q < q_{\rm lim}$. For a given q, starting from $\ell_3 = 0$, sum over the allowed pairs of ℓ_1 and ℓ_2:

   (a) Calculate the square of the radial integral $R_{\ell_1\ell_2}(\tau)$ using Eq. (3.76), following the analytic methods described in Section §3.3.2, for the given q, ℓ_1 and ℓ_2, over an array of N_k points of k values between $k_{\rm min}$ and $k_{\rm max}$, choosing N_k to be large enough to accurately sample the function, and then create a spline of this function in k.

   (b) Use this to calculate the full expression for the power given by Eq. (3.77), by performing the integral over k of this spline multiplied by $k^2 P_{\rm Lin}(k)$, and then multiply this by the power of the angular mask and any other constant terms, including the normalisation, and subtract off the shot noise

   (c) Once convergence over the ℓ_1 ℓ_2 sum pair has been reached, iterate over ℓ_3 and repeat the above two steps, until convergence over the ℓ_3 sum has been achieved.

   (d) Then step to the next value of q and repeat the above three steps, until the power has been evaluated for all desired values of q.

If the FFTLog method is deployed optimally, then the calculation of $P_{\rm F,Lin}(q)$ will be fast ($\sim$ seconds) for a given $\{q, \ell_1, \ell_2, \ell_3\}$ combination [143], and is easily parallelisable. One potential source of difficulty in the above process is ensuring that the ℓ sums have fully converged, as the overall expression is not necessarily a decreasing function as the combinations of the ℓs increases: this can potentially be countered by always calculating a few more ℓ terms than we may think is necessary, which will not overly effect the total computation time.

3.4 Conclusions and extensions

In this chapter, we extended the modelling of the previous chapter of the survey window-convolved power spectrum on the lightcone $P_F(q)$, by including terms for galaxy bias and a survey mask that includes both angular and radial components. We also gave a generalised case for the extension of the model into the nonlinear regime, assuming that the unequal-time power spectrum remains time separable. As the obtained expression for the power spectrum when including an angular survey mask is significantly more numerically challenging than in the full-sky regime, we detailed several methods that can be used for calculation. Similarly to the method used in Section §2.3.4, for $q \gg q_{\rm lim}$ we can use the small-scale approximation, which reduces the multi-dimensional integration over a pair of spherical Bessel functions down to a simple 1D integration over a smooth radial kernel function. On large scales however, where this approximation is not valid, we detailed how the use of the FFTLog algorithm, in combination with analytic transforms of the double-Bessel integrals, can be used to make the problem numerically tractable. We also laid out the steps required for implementing this procedure, and highlighted potential problem regions where parameters can cause this method to encounter numerical instability or run at sub-optimal speeds. Due to the challenging nature of the implementation, we leave this to future work, however once in place, we can then look to test this extended model against large-scale N-body lightcone simulations, similarly to the methods used in the previous chapter.

Being able to accurately model the power spectrum on large scales will be important for upcoming and future galaxy redshift surveys, which will enable cosmologists to probe as-of-yet measured features of the power spectrum, such as the turnover scale or if there is any scale-dependent bias caused by primordial non-Gaussianity. To be useful for such surveys, the most pressing extension to the modelling in this chapter is to look at how the effects of working in redshift-space modify our obtained expressions. There have been numerous works already into wide-angle redshift-space distortions [148, 87, 149, 70, 150, 151] which can be drawn on to integrate with the current model. In Raccanelli et al. (2010) [152], they showed that using a local plane-parallel approximation, which greatly simplifies the mathematics of RSD, can lead to a non-negligible error induced in the clustering amplitude even for small galaxy-pair separations, highlighting the importance of the need to model this effect correctly for future surveys.

A further area of modelling that we have yet to discuss is the covariance of the power spectrum on the past lightcone when working in a spherical geometry. As this will depend on the Fourier

transform of products of four of our $F^{\rm LC}(r)$ fields, it is important to develop robust numerical methods to evaluate the power spectrum before approaching this even more challenging task.

Appendices

3.A The shot noise term

In this appendix we detail the calculation of the shot noise term. Starting from equation Eq. (3.7), we had

$$\left\langle F^{\rm LC}(\mathbf{q}_1)\left[F^{\rm LC}(\mathbf{q}_2)\right]^*\right\rangle = \int {\rm d}^3\mathbf{r}_1{\rm d}^3\mathbf{r}_2 A^2 e^{i\mathbf{q}_1\cdot\mathbf{r}_1}e^{-i\mathbf{q}_2\cdot\mathbf{r}_2}w(r_1)w(r_2)\Theta(\mathbf{r}_1)\Theta(\mathbf{r}_2) \times\left\langle \left[n^{\rm LC}(\mathbf{r}_1)-\alpha\, n_{\rm s}^{\rm LC}(\mathbf{r}_1)\right]\left[n^{\rm LC}(\mathbf{r}_2)-\alpha\, n_{\rm s}^{\rm LC}(\mathbf{r}_2)\right]\right\rangle . \tag{3.78}$$

If we now expand out the angular brackets but do not neglect the shot noise then we need to work out the following three terms:

$$\left\langle n^{\rm LC}(\mathbf{r}_1)\, n^{\rm LC}(\mathbf{r}_2)\right\rangle ,$$
$$\left\langle n_{\rm s}^{\rm LC}(\mathbf{r}_1)\, n_{\rm s}^{\rm LC}(\mathbf{r}_2)\right\rangle ,$$
$$\left\langle n^{\rm LC}(\mathbf{r}_1)\, n_{\rm s}^{\rm LC}(\mathbf{r}_2)\right\rangle ,$$

which can be achieved by following the lines of the FKP method. For the first, we have

$$\begin{aligned}\left\langle n^{\rm LC}(\mathbf{r}_1)\, n^{\rm LC}(\mathbf{r}_2)\right\rangle &= \left\langle n_0^{\rm LC}(r_1)n_0^{\rm LC}(r_2)\left[1+\Delta(\eta_1,\mathbf{r}_1)\right]\left[1+\Delta(\eta_2,\mathbf{r}_2)\right]\right\rangle + \frac{N}{V}\delta(\mathbf{r}_1-\mathbf{r}_2) ,\\ &= n_0^{\rm LC}(r_1)n_0^{\rm LC}(r_2)\left\langle\left[1+\Delta(\eta_1,\mathbf{r}_1)+\Delta(\eta_2,\mathbf{r}_2)+\Delta(\eta_1,\mathbf{r}_1)\Delta(\eta_2,\mathbf{r}_2)\right]\right\rangle \\ &\quad +n_0^{\rm LC}(r_1)\delta(\mathbf{r}_1-\mathbf{r}_2) ,\\ &= n_0^{\rm LC}(r_1)n_0^{\rm LC}(r_2)\left[1+\left\langle\Delta(\eta_1,\mathbf{r}_1)\Delta(\eta_2,\mathbf{r}_2)\right\rangle\right]+n_0^{\rm LC}(r_1)\delta(\mathbf{r}_1-\mathbf{r}_2) .\end{aligned} \tag{3.79}$$

The second term is as above but with the correlation function set to zero and with factors of α, such that

$$\left\langle n_{\rm s}^{\rm LC}(\mathbf{r}_1)\, n_{\rm s}^{\rm LC}(\mathbf{r}_2)\right\rangle = \alpha^{-2}n_0^{\rm LC}(r_1)n_0^{\rm LC}(r_2)+\alpha^{-1}n_0^{\rm LC}(r_1)\delta(\mathbf{r}_1-\mathbf{r}_2) . \tag{3.80}$$

The third term is simpler still, giving just

$$\left\langle n^{\rm LC}(\mathbf{r}_1)\, n_{\rm s}^{\rm LC}(\mathbf{r}_2)\right\rangle = \alpha^{-1}n_0^{\rm LC}(r_1)n_0^{\rm LC}(r_2) . \tag{3.81}$$

Substituting back in for these terms with appropriate factors of α, we obtain

$$\begin{aligned}\left\langle F^{\rm LC}(\mathbf{q}_1)\left[F^{\rm LC}(\mathbf{q}_2)\right]^*\right\rangle &= \int \mathrm{d}^3\mathbf{r}_1\mathrm{d}^3\mathbf{r}_2 A^2 e^{i\mathbf{q}_1\cdot\mathbf{r}_1}e^{-i\mathbf{q}_2\cdot\mathbf{r}_2}w(r_1)w(r_2)\Theta(\mathbf{r}_1)\Theta(\mathbf{r}_2)\\ &\quad\times\Big\langle\left[n^{\rm LC}(\mathbf{r}_1)-\alpha\, n_{\rm s}^{\rm LC}(\mathbf{r}_1)\right]\left[n^{\rm LC}(\mathbf{r}_2)-\alpha\, n_{\rm s}^{\rm LC}(\mathbf{r}_2)\right]\Big\rangle\,,\\ &= \int \mathrm{d}^3\mathbf{r}_1\mathrm{d}^3\mathbf{r}_2 A^2 e^{i\mathbf{q}_1\cdot\mathbf{r}_1}e^{-i\mathbf{q}_2\cdot\mathbf{r}_2}w(r_1)w(r_2)\Theta(\mathbf{r}_1)\Theta(\mathbf{r}_2)\\ &\quad\times\Big[n_0^{\rm LC}(r_1)n_0^{\rm LC}(r_2)\langle\Delta(\eta_1,\mathbf{r}_1)\Delta(\eta_2,\mathbf{r}_2)\rangle\\ &\quad+(1+\alpha)n_0^{\rm LC}(r_1)\delta(\mathbf{r}_1-\mathbf{r}_2)\Big]\,, \end{aligned} \tag{3.82}$$

where in the last line, the second term with the delta function is our new shot noise term. Thus,

$$\begin{aligned}P_{\rm shot}(\mathbf{q}_1,\mathbf{q}_2) &= (1+\alpha)A^2\int \mathrm{d}^3\mathbf{r}_1\mathrm{d}^3\mathbf{r}_2 e^{i\mathbf{q}_1\cdot\mathbf{r}_1}e^{-i\mathbf{q}_2\cdot\mathbf{r}_2}w(r_1)w(r_2)\Theta(\mathbf{r}_1)\Theta(\mathbf{r}_2)n_0^{\rm LC}(r_1)\delta(\mathbf{r}_1-\mathbf{r}_2)\,,\\ &= (1+\alpha)A^2\int \mathrm{d}^3\mathbf{r}\, e^{i\mathbf{r}\cdot(\mathbf{q}_1-\mathbf{q}_2)}w^2(r)\Theta^2(\mathbf{r})n_0^{\rm LC}(r), \end{aligned} \tag{3.83}$$

and at this stage our shot noise term only differs from the FKP result by the inclusion of the survey mask $\Theta(\mathbf{r})$. We now look at the case where $\mathbf{q}_1=\mathbf{q}_2$ and, similar to the derivation in Section §3.2, separate out the survey mask into a radial and an angular component, the latter of which we expand in terms of spherical harmonics using Eq. (3.12) and Eq. (3.13), giving

$$\begin{aligned}P_{\rm shot} &= (1+\alpha)A^2\int \mathrm{d}^3\mathbf{r}\, w^2(r)\Theta^2(r)n_0^{\rm LC}(r)\Theta^2(\hat{\mathbf{r}})\,,\\ &= (1+\alpha)A^2\int \mathrm{d}^3\mathbf{r}\, w^2(r)\Theta^2(r)n_0^{\rm LC}(r)\sum_{\ell_3m_3}\sum_{\ell_4m_4}Y_{\ell_3m_3}(\hat{\mathbf{r}})Y^*_{\ell_4m_4}(\hat{\mathbf{r}})\Theta_{\ell_3m_3}\Theta^*_{\ell_4m_4}\,, \end{aligned} \tag{3.84}$$

where we have used the shorthand $P_{\rm shot}(\mathbf{q}_1,\mathbf{q}_1)=P_{\rm shot}$. Using the orthogonality relation of spherical harmonics (Eq. (3.18)) we perform the angular $\mathrm{d}\hat{\mathbf{r}}$ integral, killing off the spherical harmonic terms and causing $\ell_4m_4\to\ell_3m_3$, resulting in

$$P_{\rm shot} = (1+\alpha)A^2\sum_{\ell_3m_3}|\Theta_{\ell_3m_3}|^2\int \mathrm{d}r\, r^2w^2(r)\Theta^2(r)n_0^{\rm LC}(r)\,. \tag{3.85}$$

We see that the effect of including a survey mask only adds the complication of having to precompute and sum over some expansion coefficients $\Theta_{\ell m}$, the same coefficients that appear in the main expression for our power spectrum on the lightcone, Eq. (3.22). We cover the computation of such coefficients in Section §3.2.6 for the general case, as well as a simplified case where we assume the mask has some spherical symmetry.

3.B Properties of the Gaunt symbol

We now cover some useful properties of the Gaunt symbol, used in our derivations in Section §3.2. The symbol is defined by the integral over a product of three spherical harmonics $Y_{\ell m}(\hat{\mathbf{x}})$ which have a common argument $\hat{\mathbf{x}}$ but can have differing subscripts ℓ and m:

$$\mathcal{G}^{\ell_1\ell_2\ell_3}_{m_1m_2m_3} \equiv \int \mathrm{d}\hat{\mathbf{r}}_1 Y_{\ell_1 m_1}(\hat{\mathbf{r}}_1) Y_{\ell_2 m_2}(\hat{\mathbf{r}}_1) Y_{\ell_3 m_3}(\hat{\mathbf{r}}_1) \ . \tag{3.86}$$

The Gaunt symbol itself can be described in terms of the Wigner 3-j symbol:

$$\mathcal{G}^{\ell_1\ell_2\ell_3}_{m_1m_2m_3} = \sqrt{\frac{(2\ell_1+1)(2\ell_2+1)(2\ell_3+1)}{4\pi}} \begin{pmatrix} \ell_1 & \ell_2 & \ell_3 \\ 0 & 0 & 0 \end{pmatrix} \begin{pmatrix} \ell_1 & \ell_2 & \ell_3 \\ m_1 & m_2 & m_3 \end{pmatrix} \ . \tag{3.87}$$

As the Wigner 3-j symbol returns real values, we see that the Gaunt symbol is a real function. Subsequently, it must be true that the Gaunt symbol can also be defined by the integral over a product of three complex conjugate spherical harmonic functions:

$$\mathcal{G}^{\ell_1\ell_2\ell_3}_{m_1m_2m_3} \stackrel{?}{\equiv} \int \mathrm{d}\hat{\mathbf{r}}_1 Y^*_{\ell_1 m_1}(\hat{\mathbf{r}}_1) Y^*_{\ell_2 m_2}(\hat{\mathbf{r}}_1) Y^*_{\ell_3 m_3}(\hat{\mathbf{r}}_1) \ . \tag{3.88}$$

We can show this relatively easily using the relationship between a spherical harmonic and its complex conjugate, which is given by $Y^*_{\ell_1 m_1} = (-1)^m Y^*_{\ell_1 -m}$. Substituting this in we have

$$\begin{aligned}
\int \mathrm{d}\hat{\mathbf{r}}_1 Y^*_{\ell_1 m_1}(\hat{\mathbf{r}}_1) Y^*_{\ell_2 m_2}(\hat{\mathbf{r}}_1) Y^*_{\ell_3 m_3}(\hat{\mathbf{r}}_1) &= (-1)^{m_1+m_2+m_3} \int \mathrm{d}\hat{\mathbf{r}}_1 Y_{\ell_1 -m_1}(\hat{\mathbf{r}}_1) Y_{\ell_2 -m_2}(\hat{\mathbf{r}}_1) Y_{\ell_3 -m_3}(\hat{\mathbf{r}}_1) \ , \\
&= (-1)^{m_1+m_2+m_3} \mathcal{G}^{\ell_1\ell_2\ell_3}_{-m_1-m_2-m_3} \ , \\
&= (-1)^{m_1+m_2+m_3} \sqrt{\frac{(2\ell_1+1)(2\ell_2+1)(2\ell_3+1)}{4\pi}} \begin{pmatrix} \ell_1 & \ell_2 & \ell_3 \\ 0 & 0 & 0 \end{pmatrix} \\
&\quad \times \begin{pmatrix} \ell_1 & \ell_2 & \ell_3 \\ -m_1 & -m_2 & -m_3 \end{pmatrix} \ , \\
&= \sqrt{\frac{(2\ell_1+1)(2\ell_2+1)(2\ell_3+1)}{4\pi}} \begin{pmatrix} \ell_1 & \ell_2 & \ell_3 \\ 0 & 0 & 0 \end{pmatrix} \begin{pmatrix} \ell_1 & \ell_2 & \ell_3 \\ m_1 & m_2 & m_3 \end{pmatrix} \ , \\
&= \mathcal{G}^{\ell_1\ell_2\ell_3}_{m_1m_2m_3} \ ,
\end{aligned} \tag{3.89}$$

as required. Note that in moving from the 3rd to the 4th line we used the property of the 3-j symbol:

$$(-1)^{m_1+m_2+m_3} \begin{pmatrix} \ell_1 & \ell_2 & \ell_3 \\ -m_1 & -m_2 & -m_3 \end{pmatrix} = \begin{pmatrix} \ell_1 & \ell_2 & \ell_3 \\ m_1 & m_2 & m_3 \end{pmatrix} \ . \tag{3.90}$$

In the main text we also encountered the product of two Gaunt symbols, sharing identical indices on the first and second columns:

$$\begin{aligned}\mathcal{G}^{\ell_1\ell_2\ell_3}_{m_1m_2m_3}\mathcal{G}^{\ell_1\ell_2\ell_4}_{m_1m_2m_4} &= \sqrt{\frac{(2\ell_1+1)(2\ell_2+1)(2\ell_3+1)}{4\pi}}\sqrt{\frac{(2\ell_1+1)(2\ell_2+1)(2\ell_4+1)}{4\pi}} \\ &\times \begin{pmatrix} \ell_1 & \ell_2 & \ell_3 \\ 0 & 0 & 0 \end{pmatrix}\begin{pmatrix} \ell_1 & \ell_2 & \ell_3 \\ m_1 & m_2 & m_3 \end{pmatrix} \\ &\times \begin{pmatrix} \ell_1 & \ell_2 & \ell_4 \\ 0 & 0 & 0 \end{pmatrix}\begin{pmatrix} \ell_1 & \ell_2 & \ell_4 \\ m_1 & m_2 & m_4 \end{pmatrix}. \end{aligned} \tag{3.91}$$

Next we can employ the orthogonality relation of the Wigner 3-j symbol, given by

$$\sum_{m_1m_2}\begin{pmatrix} \ell_1 & \ell_2 & \ell_3 \\ m_1 & m_2 & m_3 \end{pmatrix}\begin{pmatrix} \ell_1 & \ell_2 & \ell_4 \\ m_1 & m_2 & m_4 \end{pmatrix} = \frac{\delta_{\ell_3\ell_4}\delta_{m_3m_4}}{(2\ell_3+1)}\{\ell_1\ \ \ell_2\ \ \ell_3\}\ , \tag{3.92}$$

where the triangular delta $\{\ell_1\ \ \ell_2\ \ \ell_3\}$ is equal to 1 when the triad (ℓ_1,ℓ_2,ℓ_3) satisfies the triangle condition (see bullet point 3 below), and zero otherwise. Note that the 3-j symbol and triangular delta are invariant under cyclic permutations of their columns, and pick up a factor of $(-1)^{\ell_1+\ell_2+\ell_3}$ for non-cyclic permutations. Combining the above two equations gives

$$\begin{aligned}\sum_{m_1m_2}\mathcal{G}^{\ell_1\ell_2\ell_3}_{m_1m_2m_3}\mathcal{G}^{\ell_1\ell_2\ell_4}_{m_1m_2m_4} &= \sqrt{\frac{(2\ell_1+1)(2\ell_2+1)(2\ell_3+1)}{4\pi}}\sqrt{\frac{(2\ell_1+1)(2\ell_2+1)(2\ell_4+1)}{4\pi}} \\ &\times \begin{pmatrix} \ell_1 & \ell_2 & \ell_3 \\ 0 & 0 & 0 \end{pmatrix}\begin{pmatrix} \ell_1 & \ell_2 & \ell_4 \\ 0 & 0 & 0 \end{pmatrix}\frac{\delta_{\ell_3\ell_4}\delta_{m_3m_4}}{(2\ell_3+1)}\{\ell_1\ \ \ell_2\ \ \ell_3\}\ , \\ &= \frac{(2\ell_1+1)(2\ell_2+1)}{4\pi}\begin{pmatrix} \ell_1 & \ell_2 & \ell_3 \\ 0 & 0 & 0 \end{pmatrix}^2\delta_{\ell_3\ell_4}\delta_{m_3m_4}\{\ell_1\ \ \ell_2\ \ \ell_3\}\ . \end{aligned} \tag{3.93}$$

It is also worth noting at this point the that the 3-j symbol and the triangular delta are zero unless the following conditions on the values of ℓ_{123} and m_{123} are met:

- $m_i \in \{-|\ell_i|,...,|\ell_i|\}$, $(i=1,2,3)$,
- $m_1+m_2+m_3=0$,
- $|\ell_1-\ell_2| \leq \ell_3 \leq \ell_1+\ell_2$,
- $\ell_1+\ell_2+\ell_3$ is an integer (and, moreover, an even integer if $m_1=m_2=m_3=0$) .

For all the scenarios in consideration here, we always end up with Wigner 3-j symbols in our final results that have all zeros on the bottom row, and as we are always summing the ℓ's from zero upwards, we only need to pay attention to the 3rd condition as the other three are satisfied by default.

3.C Recovery of the full sky result

We now check that in limit where our survey mask becomes equal to unity everywhere, we can recover the full sky result of the previous chapter. Aside from simply setting the radial component $\Theta(r) = 1$, we need to establish the value of the angular coefficients $\Theta_{\ell m}$ in this limit. For an angular function expanded in terms of spherical harmonics $\Theta(\mathbf{r}) = \sum_{\ell m} \Theta_{\ell m} Y_{\ell m}(\hat{\mathbf{r}})$, we can recover these coefficients via

$$\Theta_{\ell m} = \int_0^{2\pi} \mathrm{d}\phi \int_0^{\pi} \mathrm{d}\theta \sin(\theta) Y^*_{\ell m}(\theta, \phi) \Theta(\theta, \phi) \ . \tag{3.94}$$

Setting the term $\Theta(\theta, \phi) = 1$, we thus need to perform the integral over all angles of the spherical harmonic function. To do this, we note that as $\sqrt{4\pi} Y^0_0(\theta, \phi) = 1$, and then can substitute this in, exploiting the orthogonality relation of the spherical harmonics:

$$\begin{aligned} \Theta_{\ell m}\Big|_{\Theta(\mathbf{r})\to 1} &= \int_0^{2\pi} \mathrm{d}\phi \int_0^{\pi} \mathrm{d}\theta \sin(\theta) Y^*_{\ell m}(\theta, \phi) * 1 \ , \\ &= \sqrt{4\pi} \int_0^{2\pi} \mathrm{d}\phi \int_0^{\pi} \mathrm{d}\theta \sin(\theta) Y^*_{\ell m}(\theta, \phi) Y^0_0(\theta, \phi) \ , \\ &= \sqrt{4\pi} \delta^l_0 \delta^m_0 \ . \end{aligned} \tag{3.95}$$

We note that the same result will hold true for the complex conjugate $\Theta^*_{\ell m}$ in this limit. In the case of our main result of the masked power spectrum on the lightcone, given by Eq. (3.22), these angular mask coefficients have subscript $\ell_3 m_3$, and so writing out only terms from this equation that contain these subscripts, we have

$$\begin{aligned} \sum_{\ell_3} \sum_{m_3} |\Theta_{\ell_3 m_3}|^2 \begin{pmatrix} \ell_1 & \ell_2 & \ell_3 \\ 0 & 0 & 0 \end{pmatrix}^2 \{\ell_1 \ \ell_2 \ \ell_3\} &= 4\pi \sum_{\ell_3} \sum_{m_3} \delta^{\ell_3}_0 \delta^{m_3}_0 \begin{pmatrix} \ell_1 & \ell_2 & \ell_3 \\ 0 & 0 & 0 \end{pmatrix}^2 \{\ell_1 \ \ell_2 \ \ell_3\} \ , \\ &= 4\pi \begin{pmatrix} \ell_1 & \ell_2 & 0 \\ 0 & 0 & 0 \end{pmatrix}^2 \{\ell_1 \ \ell_2 \ 0\} \ , \\ &= 4\pi \begin{pmatrix} \ell_1 & \ell_1 & 0 \\ 0 & 0 & 0 \end{pmatrix}^2 \delta^{\ell_1}_{\ell_2} \ , \end{aligned} \tag{3.96}$$

where the last line follows from the third condition of the Wigner 3-j rules at the end of Appendix §3.B. From here, we can use a special case of the 3-j symbol:

$$\begin{pmatrix} \ell_1 & \ell_1 & 0 \\ 0 & 0 & 0 \end{pmatrix} = \frac{(-1)^{\ell_1}}{\sqrt{2\ell_1 + 1}} \to \begin{pmatrix} \ell_1 & \ell_1 & 0 \\ 0 & 0 & 0 \end{pmatrix}^2 = \frac{1}{2\ell_1 + 1} \ . \tag{3.97}$$

Combining these to previous results, we therefore have that:

$$\sum_{\ell_3}\sum_{m_3}|\Theta_{\ell_3 m_3}|^2\begin{pmatrix}\ell_1 & \ell_2 & \ell_3\\ 0 & 0 & 0\end{pmatrix}^2\{\ell_1\ \ell_2\ \ell_3\}=\frac{4\pi}{2\ell_1+1}\delta^{\ell_1}_{\ell_2}\ . \tag{3.98}$$

Remembering our main result of Eq. (3.22):

$$\begin{aligned}P_{\rm F}(q) &= \hat{\sum_{\ell_1\ell_2\ell_3}}\mathcal{C}_{\ell_3}\int{\rm d}k k^2\prod_{i=1}^{2}\Big\{\mathcal{T}^{(i)}_{\ell_1\ell_2}(q,k)\Big\}P(k,\eta_1,\eta_2)\ ,\\ &= A^2\sum_{\ell_1}\sum_{\ell_2}\sum_{\ell_3,m_3}|\Theta_{\ell_3 m_3}|^2(2\ell_1+1)(2\ell_2+1)\begin{pmatrix}\ell_1 & \ell_2 & \ell_3\\ 0 & 0 & 0\end{pmatrix}^2\{l_1\ l_2\ l_3\}\\ &\quad\times\int{\rm d}k k^2\prod_{i=1}^{2}\Big\{\int{\rm d}r_i r_i^2 j_{\ell_1}(kr_i)j_{\ell_2}(q_i r_i)Z(r_i)\Big\}P(k,\eta_1,\eta_2)\ ,\end{aligned} \tag{3.99}$$

we then substitute in Eq. (3.98) and set $\Theta(r)=1$, giving:

$$\begin{aligned}P_{\rm F}(q)\Big|_{\Theta(\mathbf{r})\to 1} &= A^2\sum_{\ell_1}\sum_{\ell_2}(2\ell_1+1)(2\ell_2+1)\frac{4\pi}{2\ell_1+1}\delta^{\ell_1}_{\ell_2}\\ &\quad\times\int{\rm d}k k^2\prod_{i=1}^{2}\Big\{\int{\rm d}r_i r_i^2 n_0^{\rm LC}(r)w(r)j_{\ell_1}(kr_i)j_{\ell_2}(q_i r_i)\Big\}P(k,\eta_1,\eta_2)\ ,\\ &= A^2\sum_{\ell_1}(2\ell_1+1)\int{\rm d}k k^2\prod_{i=1}^{2}\Big\{\int{\rm d}r_i r_i^2 n_0^{\rm LC}(r)w(r)j_{\ell_1}(kr_i)j_{\ell_1}(q_i r_i)\Big\}\\ &\quad\times P(k,\eta_1,\eta_2)\ ,\end{aligned} \tag{3.100}$$

where we see that this last line matches the result obtained in Section (§2.3.2) of Chapter §2.

3.D Derivations of the Bessel integral transforms

Here we derive the integral transforms $I_{\ell_1\ell_2}(\nu,\tau)$ and $M_{\ell_1\ell_2}(\nu,\Lambda)$ for a double spherical Bessel integral of differing orders, with a power law. Starting with Eq. (3.68) for the case where $k\leq q$, with $\tau=k/q$,

$$I_{\ell_1\ell_2}(\nu,\tau)\equiv\int{\rm d}x\ x^{-\nu}j_{\ell_1}(\tau x)j_{\ell_2}(x)\ , \tag{3.101}$$

and substituting in the relationship between the Bessel function and its spherical counterpart:

$$j_\ell(x)=\sqrt{\frac{\pi}{2x}}J_{\ell+1/2}(x), \tag{3.102}$$

gives

$$I_{\ell_1\ell_2}(\nu,\tau) = \frac{\pi}{2}\tau^{-1/2}\int \mathrm{d}x\ x^{-\nu-1}J_{\ell_1+1/2}(\tau x)J_{\ell_2+1/2}(x)\ . \tag{3.103}$$

We can now use Gradshteyn [130] Eq. (6.574) to find analytic solutions for this, for different values of τ. In the case where $\tau < 1$, we have (from 6.574.1):

$$I_{\ell_1\ell_2}(\nu,\tau) = \frac{\pi\tau^{\ell_1}\Gamma\Big(\frac{\ell_1+\ell_2-\nu+1}{2}\Big)}{2^{\nu+2}\Gamma\Big(\frac{-\ell_1+\ell_2+\nu+2}{2}\Big)\Gamma\Big(\ell_1+\frac{3}{2}\Big)}{}_2F_1\Big(\frac{\ell_1+\ell_2-\nu+1}{2},\frac{\ell_1-\ell_2-\nu}{2},\ell_1+\frac{3}{2},\tau^2\Big)\ , \tag{3.104}$$
$$\mathrm{Re}[\ell_1+\ell_2-\nu+1]>0\ ,\ \mathrm{Re}[\nu]>-2\ ,\ 0<\tau<1\ .$$

The RHS of this equation is not analytic where $\tau = 1$, and so for this case we instead use Gradshteyn Eq. (6.574.2):

$$I_{\ell_1\ell_2}(\nu,1) = \frac{\pi\Gamma\big(\nu+1\big)\Gamma\Big(\frac{\ell_1+\ell_2-\nu+1}{2}\Big)}{2^{\nu+2}\Gamma\Big(\frac{-\ell_1+\ell_2+\nu+2}{2}\Big)\Gamma\Big(\frac{\ell_1+\ell_2+\nu+3}{2}\Big)\Gamma\Big(\frac{\ell_1-\ell_2+\nu+2}{2}\Big)}\ , \tag{3.105}$$
$$\mathrm{Re}[\ell_1+\ell_2+2]>\mathrm{Re}[\nu+1]>0\ .$$

Next we consider Eq. (3.74) for the case where $q < k$ and we make the substitution $\tau' = q/k$:

$$M_{\ell_1\ell_2}(\nu,\tau') \equiv \int \mathrm{d}x\ x^{-\nu}j_{\ell_1}(x)j_{\ell_2}(\tau' x)\ . \tag{3.106}$$

Substituting out the spherical Bessel functions for the regular Bessels as before, gives

$$M_{\ell_1\ell_2}(\nu,\tau') = \frac{\pi}{2}\tau'^{-1/2}\int \mathrm{d}x\ x^{-\nu-1}J_{\ell_1+1/2}(x)J_{\ell_2+1/2}(\tau' x)\ , \tag{3.107}$$

and to solve we use Gradshteyn Eq. (6.574.3), resulting in:

$$\begin{aligned} M_{\ell_1\ell_2}(\nu,\tau') \ &= \ \frac{\pi\tau'^{\ell_1}\Gamma\Big(\frac{\ell_1+\ell_2-\nu+1}{2}\Big)}{2^{\nu+2}\Gamma\Big(\frac{\ell_1-\ell_2+\nu+2}{2}\Big)\Gamma\Big(\ell_1+\frac{3}{2}\Big)} \\ &\quad \times {}_2F_1\Big(\frac{\ell_1+\ell_2-\nu+1}{2},\frac{-\ell_1+\ell_2-\nu}{2},\ell_2+\frac{3}{2},\tau'^2\Big)\ , \\ &\quad \mathrm{Re}[\ell_1+\ell_2-\nu+1]>0\ ,\ \mathrm{Re}[\nu]>-2\ ,\ 0<\tau'<1\ . \end{aligned} \tag{3.108}$$

Contributions

All of the work in this chapter was performed by myself, with input, feedback and guidance from my supervisor Dr. Robert Smith.

Chapter 4

Clustering of the 4MOST simulations

The 4MOST[1] (4-metre Multi-Object Spectroscopic Telescope) Cosmology Redshift Survey (CRS) is an upcoming large-volume spectroscopic survey in the southern hemisphere. With the aim of obtaining approximately four million accurate redshifts for multiple types of dark-matter tracers, they key science goal of the survey is to help better understand the nature of dark energy and the expansion rate of the universe. In advance of the survey launching in 2023, the 4MOST Facility Simulator (4FS) team has been producing simulated data catalogues of the expected observations from 4MOST, for use in forecasting and survey design optimisation. The aim of this current work is to develop a clustering pipeline to analyse the simulated galaxy catalogues produced by the 4FS, focusing on calculating two-point clustering statistics in both configuration and Fourier space. The chapter breaks down as follows: in Section §4.1 and §4.2, we give an overview of the 4MOST project and the CRS, outlining the survey specifications and main science aims. In Section §4.3 we give a brief overview of the clustering estimators used by the pipeline software to calculate the statistics, before then reviewing some of the results produced by the pipeline when run on the latest 4FS catalogues in Section §4.4. We provide links to the relevant software libraries used in Appendix §4.A, and a more detailed guide of each stage of the pipeline in Appendix §4.B.

4.1 The 4MOST project

The 4MOST instrument is an upcoming fibre-fed spectrograph being fitted to the existing Visible and Infrared Survey Telescope for Astronomy (VISTA) facility in Chile. Forming part of the European Southern Observatory's (ESO) array of telescopes in the region, the new instrument is being overseen and managed by the 4MOST consortium, with operations planned to start in Q3 2023, and an initial run time of five years.

The 4MOST project [153] consists of ten surveys being run in parallel[2], with five of these dedicated to studying the Milky Way galaxy, and the remaining five, which includes the CRS,

[1] https://www.4most.eu/cms/

[2] The 4MOST consortium surveys will be assigned 70% of the fibre hours with the rest going to community surveys.

Name	z	Selected (AB) magnitude range	R-band (magnitude [AB])	Sky area (deg^2)	Density (deg^2)	Colour selection	Redshift completeness	Number of targets (10^6)
BG	0.15–0.4	$16 < J < 18$	20.2 ± 0.4	7500	250	*J–Ks, J–W1*	95%	1.88
LRG	0.4–0.7	$18.0 < J < 19.5$	21.8 ± 0.7	7500	400	*J–Ks, J–W1*	75%	3.00
QSO	0.9–2.2	$g < 22.5$	22.2 ± 0.7	7500	190	*g–i,i–W1,W1–W2*	65%	1.43
QSO-Lyα	2.2–3.5	$r < 22.7$	22.2 ± 0.7	7500	50	*g–i,i–W1,W1–W2*	90%	0.38

Figure 4.1: Table showing the expected survey parameters for the four different galaxy targets of the 4MOST Cosmology Redshift survey, from [54].

being extra-galactic in nature. The key aim of the galactic surveys is to complement the Gaia[3] space observatory in understanding the formation and evolution of the Milky Way. By recording 18 million spectra from a variety of stellar populations, these surveys will provide a dense and deep map of the stellar properties in the Milky Way and the Magellanic Clouds. The primary science goals of the extra-galactic consortium surveys are to study the growth rate of structure in the universe, test theories for the nature of dark energy and dark matter, constrain the cosmological equation of state, as well as investigate the formation and evolution of the first stars, black holes, galaxies. They will also look to study supermassive black holes and how they influence their surroundings and host galaxies. These goals will be achieved by obtaining a total of 13 million low-resolution spectra for galaxies, active galactic nuclei and quasars; and around 100,000 transient sources such as supernovae, out to a redshift of 6.

The 4MOST instrument has a viewing plane of 4.2 square degrees, and the ability to observe up to 2400 targets simultaneously through robotically controlled fibre-fed high and low resolution spectrographs, with a target collision radius of $15''$. The telescopes will observe targets over an area of $20,000$ square degrees in the southern hemisphere, in the visible to near-infrared wavelengths ($370\text{nm} < \lambda < 950\text{nm}$), and a limiting AB magnitude of $\sim 20.2(15.8)$ for the low(high) resolution spectrographs, from 6×20 minute exposures. Due to the complicated nature of conducting a large number of different surveys in parallel, specific tiling patterns and fibre assignment algorithms have been developed [154, 155], to maximise fibre efficiency while meeting the required goals of each survey.

4.2 The 4MOST Cosmology Redshift Survey

The 4MOST Cosmology Redshift Survey [54] will measure spectroscopic redshifts for four distinct galaxy types: Bright Galaxies (BG), Luminous Red Galaxies (LRG), Quasars (QSO) and Quasar Lyman Alpha's (Lyα), shown in the table in Fig. 4.1, covering an area 7500 square degrees and a redshift range of $0.15 < z < 3.5$. The key science aim of the CRS is to help understand the nature of dark energy, and more accurately constrain the expansion rate of the universe. Providing a high number density of targets over a wide redshift range, the CRS will enable the measurement of the growth rate of structure and baryon acoustic oscillations (BAO) in many fine-binned redshift intervals, offering improved constraints over more data points. Additionally, there is currently no

[3] https://sci.esa.int/web/gaia/

existing large-scale southern hemisphere redshift survey beyond the local Universe, a gap in the data that 4MOST will fill.

Many of the key science aims of the CRS will be achieved through cross-correlations with overlapping surveys, some of which are shown in shown in Fig. 4.2. In particular, utilising weak lensing data from surveys such as KiDS[4], LSST[5] and DES[6] will enable a '3x2' point analysis of combined probes: using galaxy-galaxy clustering measurements with galaxy-galaxy lensing (seeing how foreground lens galaxies distort the shape of background source galaxies) and cosmic shear (correlating shape distortions on background galaxies). This can be used to break the degeneracy of galaxy bias with the growth factor - a vital step for recovery of underlying cosmological parameters. Having accurate spectroscopic redshifts for source galaxies, which 4MOST will provide, will also help to reduce systematics in the measurements from existing weak lensing data sets.

Being the only large-scale spectroscopic redshift survey in the southern hemisphere, the CRS is also uniquely positioned to provide cross correlations with ongoing and upcoming CMB surveys such as the South Pole Telescope[7] (SPT), the Atacama Cosmology Telescope[8] (ACT), CMB-S4[9] and Simons Observatory[10] (SO) which will map the CMB to unprecedented resolution and accuracy. Much like galaxy-galaxy lensing, CMB photons are gravitationally deflected by the large-scale distribution of matter in the Universe which leaves subtle imprints in the CMB temperature and polarization anisotropies. These can be used to create a reconstructed map of the lensing potential, indicating how matter is distributed, from which cosmological information can be extracted.

In advance of 4MOST launching, mock data catalogues are produced by the 4MOST Facility Simulator (4FS), software designed to simulate what 4MOST will be able to observe over the initial five year run period. This is a vital tool for examining how particular survey design specifications are likely to affect survey outcomes, and is able to model the local operating environment, such as long-term atmospheric and environmental conditions at the Paranal site in Chile. The software runs on the latest algorithms for determining fibre-to-target assignment, survey strategy and tiling, as well as survey balancing and feedback mechanisms, and so can be used to improve all of these methods. To aid in the analysis of the catalogues produced by 4FS, we have created a clustering pipeline in Python, detailed in Appendix §4.B, to perform two-point statistics on the mock CRS data, and tested this on the latest available catalogues.

[4]http://kids.strw.leidenuniv.nl/
[5]https://www.lsst.org/
[6]https://www.darkenergysurvey.org/
[7]https://pole.uchicago.edu/public/Home.html
[8]https://act.princeton.edu/
[9]https://cmb-s4.org/
[10]https://simonsobservatory.org/

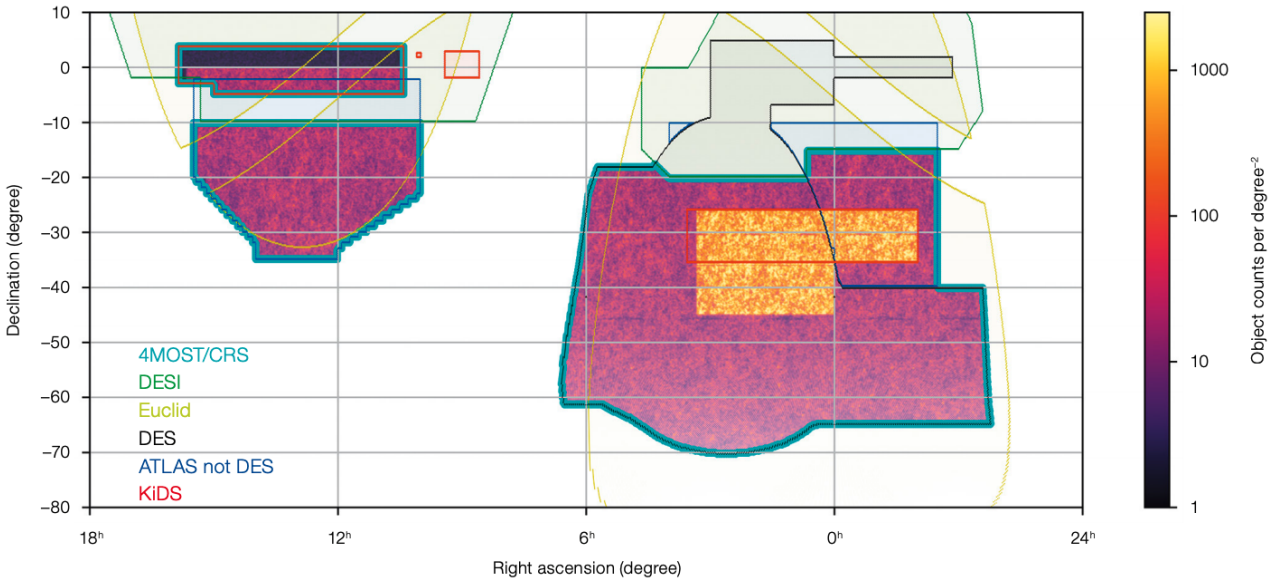

Figure 4.2: Footprint of the 4MOST CRS shown in the shaded regions outlined in turquoise, and we refer to the larger 4MOST footprint on the right as 'field 1' and the smaller on the left as 'field 2'. Also overlaid are footprints from some overlapping surveys which 4MOST will synergise with. Fig from [54]. Note that the light coloured, higher density region in field 1 on the right denotes Emission Line Galaxy (ELG) tracers that have since been removed from the scope of the CRS.

4.3 The two-point clustering estimators

4.3.1 In configuration space

To measure two-point clustering statistics in configuration space, our pipeline uses the `TreeCorr` [156] and `CorrFunc` [157] Python libraries. The clustering algorithms employed by these libraries use the Landy & Szalay (LS) [158] estimator, which has been shown [159] to outperform other types of estimators on large scales while matching performance at small scales. The binned $w(\theta_n)$ and $\xi(r_n)$ correlation functions are calculated in `TreeCorr`, and given by:

$$\mathcal{S}_{\rm LS}(x_n) = \frac{DD(x_n) - 2DR(x_n) + RR(x_n)}{RR(x_n)} \ . \tag{4.1}$$

Here, $\mathcal{S}$ is the type of correlation function (e.g. ξ or w), measured in bins x_n, and the quantities DD, DR and RR correspond to normalised data-data, random-random, and data-random pair counts, respectively. These are defined as

$$DD(r_n) = \frac{dd(r_n)}{N_d(N_d-1)/2} \ , \tag{4.2}$$

$$RR(r_n) = \frac{rr(r_n)}{N_r(N_r-1)/2} \ , \tag{4.3}$$

$$DR(r_n) = \frac{dr(r_n)}{N_d N_r} \ , \tag{4.4}$$

where N_d and N_r are the number of data and random points in the sample, respectively, and $xx(r_n)$ are the pair counts in bin r_n. The $N(N-1)/2$ factors are to avoid overestimating the number of pairs from double counting or self counting.

The projected correlation function $w_p(r_p)$, performed using `CorrFunc`, can be calculated by first breaking up the 3D correlation function into separations perpendicular to (r_p) and parallel to (π) the line of sight, before integrating along the line of sight. Specifically,

$$w_p(r_p) = \int_{-\infty}^{\infty} \xi(r_p, \pi) d\pi \ , \tag{4.5}$$

$$\approx 2 \int_{0}^{\pi_{\max}} \xi(r_p, \pi) d\pi \ , \tag{4.6}$$

where the second line follows from assuming (large-scale) isotropy and imposing some finite upper limit on the integral. This is a particularly useful measure when considering RSD, as these contaminate any radial positional data such that we cannot truly tell where the galaxy is. We can try to negate this complication by performing a line of sight integral, providing the region of integration is wide enough to make the approximation valid. Typically, $\pi_{\max}$ is set somewhere between 40 and 80 h^{-1} Mpc [160], with the default value in our implementation set to 50 h^{-1} Mpc. If set too small then the amplitude may be under estimated, but if set too large then calculation can become very slow and may be dominated by noise. The details of the implementation in `CorrFunc` can be found in [157], and it uses the LS estimator as described above.

Covariance matrix calculations are performed using the 'jackknife' resampling method [161], which consists of splitting the data into N sub-regions, the performing N clustering measurements by omitting an individual region at a time for each measurement. The volume of one of these individual measurements is then $(N-1)/N$ of the original full volume, and the covariance is given by

$$C_{jk}(x_i, x_j) = \frac{N-1}{N} \sum_{k=1}^{N} (x_i^k - \bar{x}_i)(x_j^k - \bar{x}_j) \ , \tag{4.7}$$

where x_i is the ith measure of the statistic of interest (out of N total measures), and the mean is given by $\bar{x}_i = \sum_{k=1}^{N} x_i^k / N$. The jackknife method reduces the bias on an estimate, and in our implementation, we divide our regions into equal slices in right-ascension for the calculation. Due to the irregular survey geometry of 4MOST, this means the areas will be uneven in size for this covariance estimate, an area of potential improvement for the code. The correlation matrices $\hat{C}$ are calculated from the covariance matrices:

$$\hat{C}_{x_i x_j} = \frac{C(x_i, x_j)}{\sigma_i \sigma_j} \ , \tag{4.8}$$

where σ_i^2 is the variance of the ith variable.

We also implement a simple fibre-collision correction on the $w(\theta)$ measurement of the output

catalogues. Fibre collisions can occur where the physical size of the spectroscopic fibre prevents observations of targets that are too close to each other on the sky [162]. This effect can thus hinder observations in high target density regions such as those found in galaxy clusters, and will cause a loss in observed clustering signal. The effect can partly be mitigated by an observing strategy that involves repeated measurements of the same areas, so that close galaxy pairs can be measured individually on separate visits, but is expensive in terms of fibre hours to completely eliminate. The correction scheme [163] applied to $w(\theta_n)$ of the output catalogues involves multiplying the results by an up-weighting factor $w_{fc}(\theta_n)$, based on the expected clustering signal from the parent catalogue (in this case, the input catalogues):

$$w_{fc}(\theta_n) = \frac{1 + w_{\rm in}(\theta_n)}{1 + w_{\rm out}(\theta_n)} \ . \tag{4.9}$$

Accounting for the fibre-collision effect for 3D clustering statistics is a more complicated process. Various 'nearest-neighbour' approaches have been used, whereby one assigns a redshift to an unobserved galaxy based on the redshift of the closest observed neighbour [164], or assigns the weight of the unobserved galaxy to this observed neighbour [165]. The problems with these methods is they do not properly account for the correlation between the observed and unobserved pairs, and can also introduce systematics due to intrinsic alignments of galaxies. An alternate method, more recently put forward in Bianchi & Percival [166], proposed a 'pair-inverse-probability' (PIP) weighting scheme. This involves calculating the selection probability of a pair of galaxies by averaging over many mock simulations, designed to accurately represent the survey in consideration, and then using this to up-weight galaxy pairs by the inverse of the probability. Due to the current lack of multiple realisations of 4FS simulations, as well as the complicated fibre-to-target algorithms used by 4MOST to manage the demands of many different surveys simultaneously, we leave correcting this effect for 3D statistics to future work. We note that a good starting point may be to test out the methodology put forward in Smith et al. (2019) [167], where they combined the PIP method with an angular upweighting scheme to a DESI-like Bright Galaxy mock sample to achieve an unbiased correction to galaxy clustering measurements.

The results of the real space clustering measurements are calculated individually for each of the two observing fields of the CRS (pictured in Fig. 4.2) and then averaged using an inverse variance weighting. These results are stored in the 'full_4FS_results' class, the attributes of which are listed in Table 4.6.

4.3.2 In Fourier space

The pipeline uses the `nbodykit` [168] Python library to perform power spectrum measurements, which we chose over our own implementation of an estimator detailed in Chapter §2, due to it being well documented as well as having ongoing support. The library has an implementation of a FFT-based anisotropic power spectrum estimator, with multipole decomposition. The details of this are covered in [169], which is based on the Yamamoto estimator [170], and we give a brief

review here.

Similar to derivations found in Chapters §2 & §3, we start by defining the weighted galaxy density field:

$$F(\mathbf{r}) = \frac{w_{\rm FKP}(\mathbf{r})[n_g(\mathbf{r}) - \alpha n_s(\mathbf{r})]}{A} \ , \tag{4.10}$$

where $n_g(\mathbf{r})$ and $n_s(\mathbf{r})$ are the number densities of the data and random catalogues respectively, and the α factor renormalises the density of the randoms if the catalogues have a differing total number of objects N: $\alpha = N_g/N_s$. The $w_{\rm FKP}$ term is the optimal weighting (see Eq. (2.63)) of Feldman, Kaiser and Peacock [78], and normalisation A is:

$$A = \Big[\int \mathrm{d}^3\mathbf{r}\ w_{\rm FKP}^2(\mathbf{r}) \bar{n}^2(\mathbf{r}) \Big]^{1/2} \ , \tag{4.11}$$

with $\bar{n}(\mathbf{r})$ the mean number of objects at position $\mathbf{r}$. The estimator for the multipole moments of the power spectrum is then given by

$$P_\ell(k) = \frac{2\ell+1}{A^2} \int \frac{d\Omega_k}{4\pi} \Big[\int \mathrm{d}^3\mathbf{r}_1 \int \mathrm{d}^3\mathbf{r}_2\ F(\mathbf{r}_1) F(\mathbf{r}_2) e^{i\mathbf{k}\cdot(\mathbf{r}_1-\mathbf{r}_2)} \mathcal{L}_\ell(\hat{\mathbf{k}}\cdot\hat{\mathbf{r}}_h) - P_\ell^{\rm noise}(\mathbf{k}) \Big] \ , \tag{4.12}$$

where $\mathbf{r}_h \equiv (\mathbf{r}_1 + \mathbf{r}_2)/2$ is the line-of-sight to the mid-point of the two objects, $\mathcal{L}_\ell(\mathbf{x})$ are Legendre polynomials and $P_\ell^{\rm noise}(\mathbf{k})$ is the shot noise term:

$$P_\ell^{\rm noise}(\mathbf{k}) = (1+\alpha) \int \mathrm{d}^3\mathbf{r}\ \bar{n}(\mathbf{r}) w_{\rm FKP}^2(\mathbf{r}) \mathcal{L}_\ell(\hat{\mathbf{k}}\cdot\hat{\mathbf{r}}) \ . \tag{4.13}$$

By defining the Fourier transformed galaxy density field multipoles as

$$\begin{aligned} F_\ell(\mathbf{k}) &\equiv \int \mathrm{d}\mathbf{r} F(\mathbf{r}) e^{i\mathbf{k}\cdot\mathbf{r}} \mathcal{L}_\ell(\hat{\mathbf{k}}\cdot\hat{\mathbf{r}}) \ , \\ &= \frac{4\pi}{2\ell+1} \sum_{m=-\ell}^{\ell} Y_{\ell m}(\mathbf{k}) \int \mathrm{d}\mathbf{r} F(\mathbf{r}) Y_{\ell m}^*(\mathbf{r}) e^{i\mathbf{k}\cdot\mathbf{r}} \ , \end{aligned} \tag{4.14}$$

where we have made use of the addition theorem of the spherical harmonic functions $Y_{\ell m}(\hat{\mathbf{x}})$, the expression for the power spectrum multipoles simplifies to

$$P_\ell(k) = \frac{2\ell+1}{A^2} \int \frac{\mathrm{d}\Omega_k}{4\pi} F_0(\mathbf{k}) F_\ell(-\mathbf{k}) \ . \tag{4.15}$$

This estimator is implemented in `nbodykit` by painting the data and random points onto a combined 3D mesh, with the integrals turning into sums over the grid. The sum over m has $2\ell+1$ terms and so each calculation of $P_\ell(k)$ only requires this many FFT operations.

The discretisation of particles onto a grid causes some amount of aliasing, caused by spurious contribution to high-k modes, corresponding to small-scale modes not supported by the grid that masquerade as modes of the frequency range we are interested in. To reduce the effects of this

aliasing as k approaches the Nyquist frequency of the grid ($k_{\rm Nyq}$, the maximum k mode the grid can support), we opt to use Triangular-Shaped Cloud (TSC) interpolation on to the grid with the interlacing technique, outlined in [109]. Simply put, this technique involves the averaging of two grids that are offset by half a cell width in each direction, which causes the aliasing contributions to destructively interfere. This technique, in combination with TSC, is able to achieve at least sub-percent accuracy on $P(k)$ measurements right up to the Nyquist frequency. We also have window compensation turned on as default, to deconvolve the mass-assignment window-kernel function (see equation (18-21) in [108], and the specific `nbodykit` page[11] for more information).

As `nbodykit` does not include any in-built functionality for covariance matrix calculation, a rough estimate for the error on the power spectrum is calculated by the pipeline as

$$\sigma_{P_\ell(k_n)} = \sqrt{\frac{2}{N_k}}\Big[P_\ell(k_n) + \frac{1}{\bar{n}}\Big] \ , \tag{4.16}$$

where N_k is the number of modes in the k_nth bin, and the second term in the square brackets is the contribution from the shot noise. Here we have used the Gaussian approximation that the covariance matrix is diagonal, and the selection function is constant everywhere [107]. We will implement the more robust but time consuming jackknife covariance technique via MPI in a future update, to be in line with how the covariance is calculated for the configuration-space measurements.

4.4 Clustering in the 4MOST OpSim Output

We use the latest input and output catalogues from the 4FS simulation data to test the pipeline, for all of the four tracers that will be targeted by the CRS. The input data was generated by the 4FS team from the `UNIT`[12] simulations, which runs on the `GADGET-2` [104] N-body simulation code. This is then run through the 4FS OpSim simulation code to generate the output data. The input file is from the '**cat-20210525**' batch, while the outputs come from the file '**iwg2_20210610_run03fix4newtiling'**. Table 4.1 lists some key properties of these catalogues by tracer type, including number of targets in each as well as the completeness and sky densities of the output catalogues. The sky coverage of the total footprint for the CRS is approximately 7500 deg^2, with field 1 contributing $\sim 65\%$ to this and and the remaining $\sim 35\%$ covered by field 2.

For all of our configuration-space clustering measurements, we chose to measure in 20 log-spaced bins, with ranges of $0.01 < \theta < 10$ [deg], $0.1 < r < 50$ [h^{-1} Mpc] and $0.1 < r_p < 50$ [h^{-1} Mpc] for the $w(\theta)$, $\xi(r)$ and $w_p(r_p)$ measurements, respectively. We also set a default value of $\pi_{\rm max} = 50$ [h^{-1} Mpc] for the projected clustering, and calculate the covariance using 20 jackknife regions.

The results of the real-space $w(\theta)$ measurement are shown in Fig. 4.3, where each of the subplots represents a tracer type, with the upper part of the plot showing the measurements and the lower part showing the fibre-collision correction w_{fc} applied to the displayed output data points using

[11] https://nbodykit.readthedocs.io/en/latest/mesh/creating.html
[12] https://unitsims.ft.uam.es/index.php/simulations

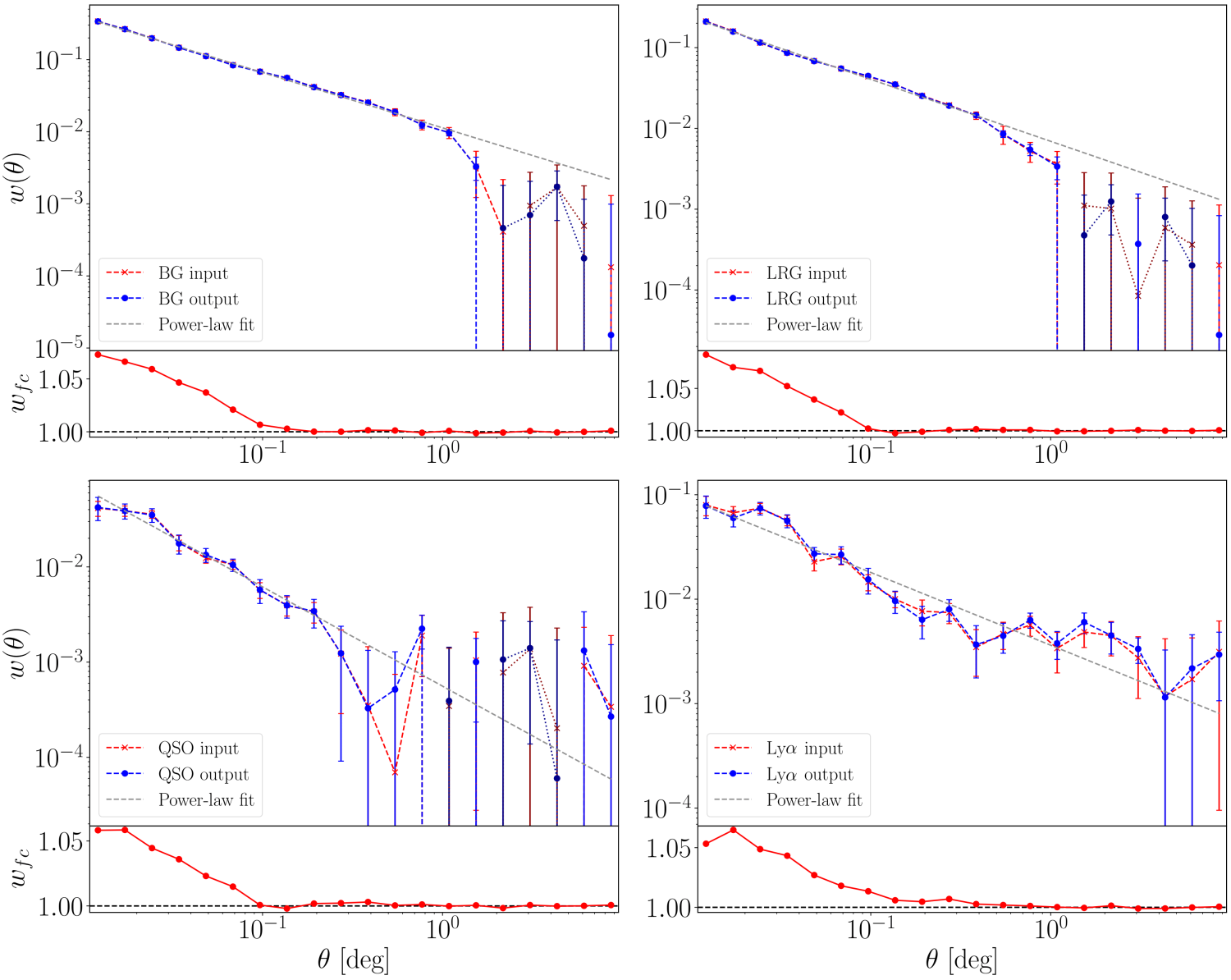

Figure 4.3: Figure showing the results of the angular clustering measurement $w(\theta)$, for all tracers and both input and output catalogues. Each plot has a subplot showing the correction for fibre collisions, which has been applied to the output results, and is more dominant at smaller scales. The lighter blue and red points joined by dashed lines show positive values, while the darker red and blue points joined by dotted lines show the modulus of negative values. We also fit a power-law model to the data, using the positive values only, which is shown by the grey dashed lines with the fitted parameters given in Table 4.2.

Tracer	$N_{\rm in}$	$N_{\rm out}$	$\bar{n}_{\rm out}$ [deg^{-2}]	Redshift range	Completeness
BG	1.89×10^6	1.42×10^6	189	$0.02 \leq z \leq 0.62$	74.8%
LRG	3.02×10^6	1.95×10^6	260	$0.01 \leq z \leq 1.13$	64.6%
QSO	1.06×10^6	7.87×10^5	105	$0.90 \leq z \leq 2.20$	74.4%
Lyα	3.75×10^5	3.01×10^5	40	$2.20 \leq z \leq 6.00$	80.1%

Table 4.1: Table showing the number of objects in the input and output catalogues used to test the pipeline, by tracer type. Also included is the angular number density of targets in the output catalogue $\bar{n}_{\rm out}$, the redshift range spanned by the data and the completeness: $(N_{\rm output}/N_{\rm input})\%$.

Tracer	A_ω	γ
BG	$(1.13 \pm 0.05) \times 10^{-2}$	1.77 ± 0.01
LRG	$(6.93 \pm 0.36) \times 10^{-3}$	1.77 ± 0.02
QSO	$(5.59 \pm 1.23) \times 10^{-4}$	2.04 ± 0.07
Lyα	$(3.62 \pm 0.62) \times 10^{-4}$	1.70 ± 0.06

Table 4.2: Table showing the obtained parameters of the power law, given by Eq. (4.17), when fitted to the angular clustering measurements of the output catalogue data.

Eq. (4.9). The results from the input(output) catalogues are plotted with red(blue) lines for all of the following configuration-space measurements. At larger scales where there is more noise and some points become negative, we have plotted the modulus, represented by the darker colour markers and joined by dotted instead of dashed lines. We also perform a power-law fit to the output measurements for reference:

$$w(\theta) = A_\omega \theta^{1-\gamma} \ , \tag{4.17}$$

represented by the grey dashed lines, where we only use positive values in the fit, with the resulting parameter values A_ω and γ given in Table 4.2. Both the BG and LRG tracers are well represented by a power law up to scales of about one degree, before this relationship begins to break down. We find a slope parameter of $\gamma \sim 1.75$ for the power-law fits to the BG, LRG and Lyα samples, with a value similar to that found by 2dFGRS and SDSS ($\gamma \simeq 1.7$ [171], $\gamma \simeq 1.72$ [172], $\gamma_{\rm LRG} = 1.67 \pm 0.07$ [173]), with the QSO slope parameter being slightly higher than expected. The QSO and Lyα tracers, being sparser in number density, follow the power-law relationship much more loosely, with the QSO angular clustering showing signs of break-down at around 0.4 degrees. While the fibre-collision correction by design forces the output measurements to exactly match those of the input, this matching has been mildly broken in some cases by the inverse variance weighting when averaging the results from the two survey fields. The associated correlation matrix, calculated from the covariance matrix, is shown for the output catalogue measurements in Fig. 4.4.

The real-space 3D and projected clustering measurements are shown in Fig. 4.5 and Fig. 4.6 for all tracers. We also plot the redshift-space $\xi(r)$ measurements for the BG and LRG samples from the input(output) catalogues with orange(green) lines, as this information is also available in

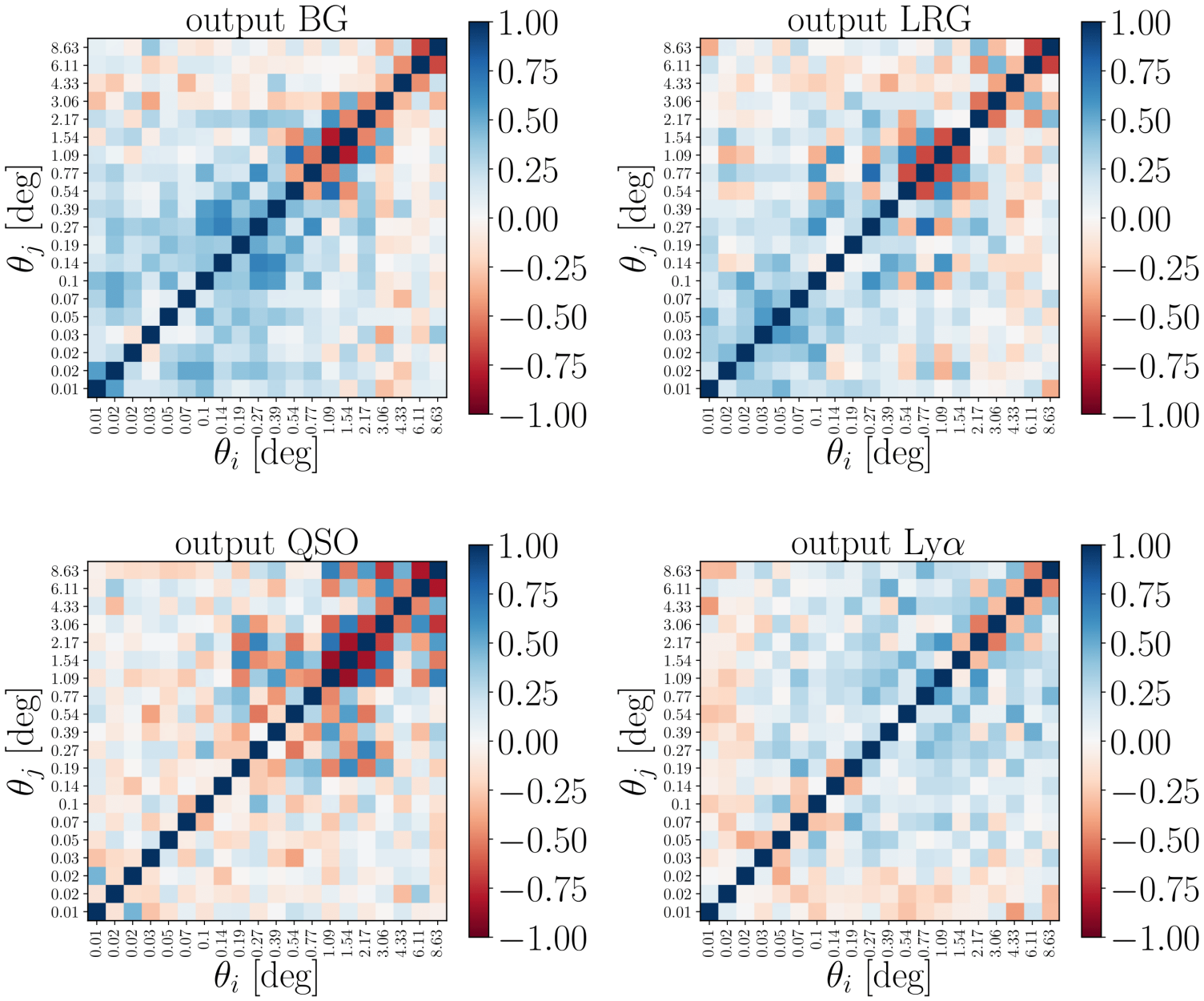

Figure 4.4: The correlation matrices for the output samples of the $w(\theta)$ measurements in Fig. 4.3.

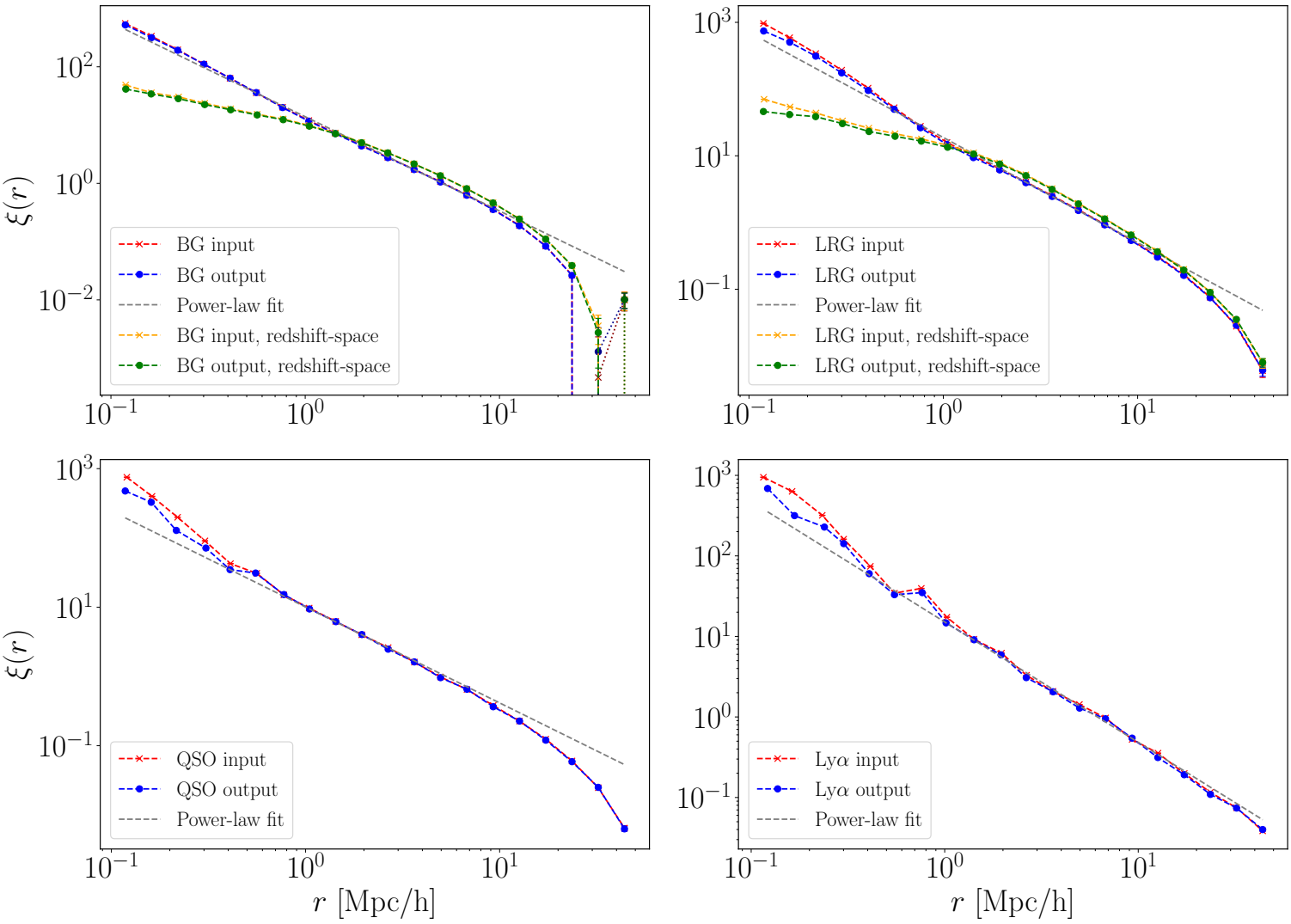

Figure 4.5: Figure showing the results of the real-space 3D clustering measurement $\xi(r)$, for all tracers and both input and output catalogues. We also plot the redshift-space measurements for the BG and LRG tracers. We perform a power-law fit to the data, represented by a dashed grey line, with the best-fit parameters given in Table 4.3.

the 4FS raw data. For these redshift-space measurements, the linear Kaiser effect can be seen by a boost in amplitude at larger scales, with the Fingers-of-God effect causing damping at smaller scales. We fit power laws of the form [174]

$$\xi(r) = \left(\frac{r_0}{r}\right)^{\gamma}, \tag{4.18}$$

$$\frac{w_p(r_p)}{r_p} = \left(\frac{r_0}{r_p}\right)^{\gamma}\left[\frac{\Gamma\left(\frac{1}{2}\right)\Gamma\left(\frac{\gamma-1}{2}\right)}{\Gamma\left(\frac{\gamma}{2}\right)}\right] = \left(\frac{r_0}{r_p}\right)^{\gamma} A(\gamma), \tag{4.19}$$

to the real-space output results, where in the second line $A(\gamma)$ represents the term in the square brackets, and $\Gamma(x)$ is the gamma function. As with the angular measurements, we only fit to

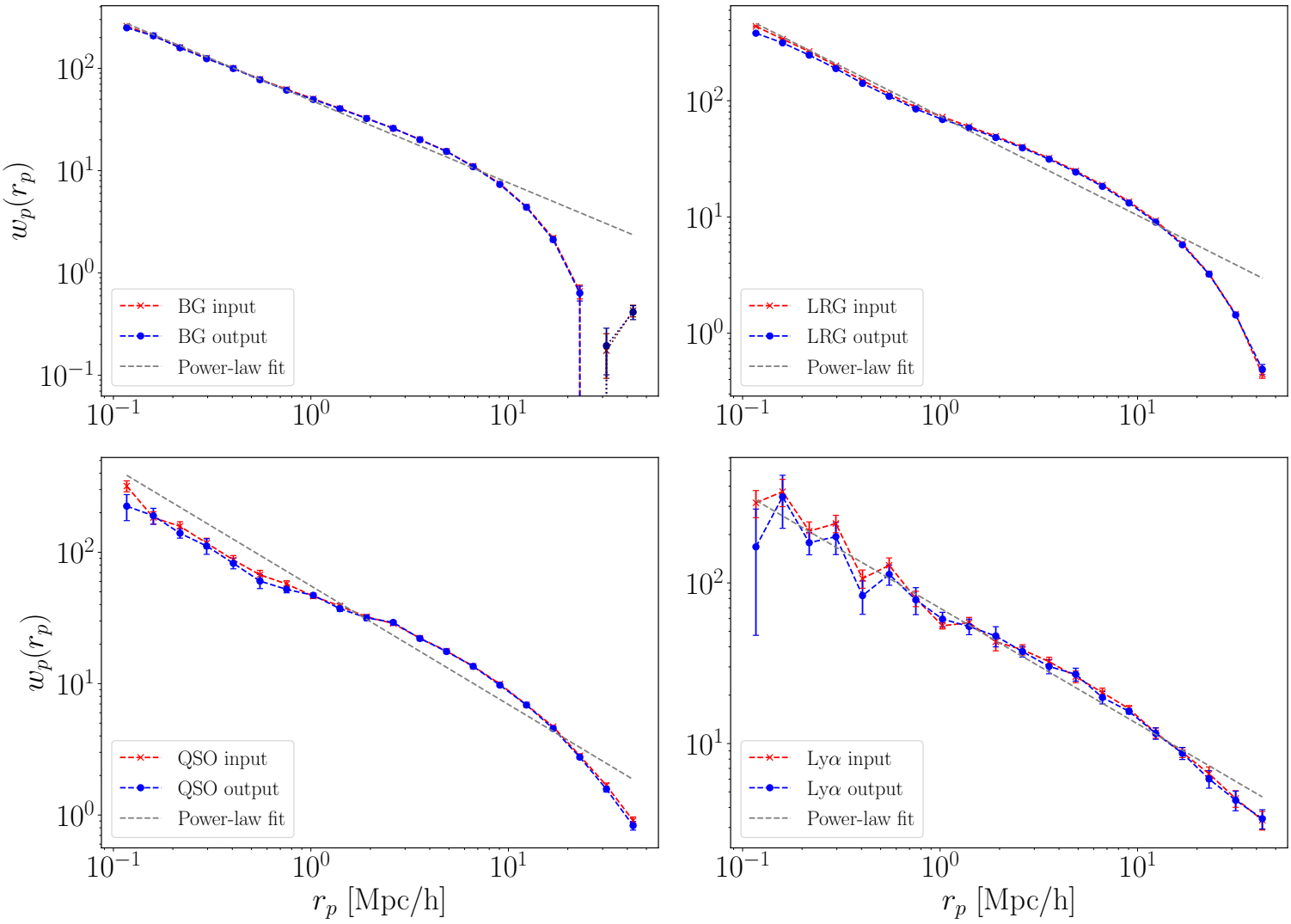

Figure 4.6: Figure showing the results of the real-space projected clustering measurement $w_p(r_p)$, for all tracers and both input and output catalogues, with $\pi_{\max} = 50$ [h^{-1} Mpc]. We perform a power-law fit to the data, represented by a dashed grey line, with the best-fit parameters given in Table 4.3.

positive values, and for $\xi(r)$ fit in the regions $r > 3$ Mpc h^{-1} for BG and LRG, and $r > 1$ Mpc h^{-1} for QSO and Lyα, to reduce the effects of non-linear clustering. We display the fitted parameters in Table 4.3. For $\xi(r)$, we find a fitted power-law slope parameter γ, for all of the tracers, to be within a few error bars of measurements from 2dFGRS ($\gamma_{\rm LRG} \sim 1.72 \pm 0.06$ [173]) and SDSS ($\gamma_{\rm QSO} = 1.55 \pm 0.3$ [175]). The BG, LRG and QSO samples start to deviate from the power-law form on larger scales at around 20 h^{-1}Mpc, with the BGs showing a break down at approximately 35 h^{-1}Mpc. Similarly, the fit to the projected clustering results gives a slope parameter within a few error bars of 2dFGRS and SDSS ($\gamma_{\rm LRG} = 1.83 \pm 0.05$ [173], $\gamma_{\rm QSO} = 1.86 \pm 0.23$ [175]). The fits perform visibly worse in this case, due to the characteristic inflections in $w_p(r_p)$ at around $r_p \sim 1-2$ h^{-1}Mpc, caused by the transition between the small-scale one halo regime to the large-scale two halo regime, as predicted by Halo Occupation Distribution (HOD) models [176, 177]. For both of

Tracer	$\xi(r)$: r_0	$\xi(r)$: γ	$w_p(r_p)$: r_0	$w_p(r_p)$: γ
BG	5.09 ± 0.02	1.62 ± 0.02	4.19 ± 0.08	1.81 ± 0.02
LRG	6.43 ± 0.02	1.58 ± 0.01	5.17 ± 0.12	1.85 ± 0.03
QSO	5.30 ± 0.07	1.39 ± 0.01	4.36 ± 0.19	1.90 ± 0.05
Lyα	6.15 ± 0.21	1.49 ± 0.03	5.28 ± 0.13	1.72 ± 0.03

Table 4.3: Table showing the obtained parameters of the power laws, given by Eq. (4.18) & (4.19), when fitted to the 3D and projected measurements of the real-space output catalogue data.

these statistics, we see small scale drops in the output catalogues compared to the inputs, most likely due to the fibre-collision effect. This is more pronounced in the lower target density QSO and Lyα catalogues.

We show measurements of the real-space monopole power spectrum in Fig. 4.7, additionally including the redshift-space measurements for the BG and LRG samples, using the same colour scheme as in the previous plots. The catalogues are painted to a 1024^3 mesh, minimising the effects of high-k aliasing by using the Triangular-Shaped Cloud mass assignment scheme with the interlacing technique (described in Chapter §2 and Section §4.3.2). The measurements are taken in linearly-spaced bins[13] between $0.01 < k < k_{\rm Nyq}$, with the bin width varying by tracer type to ensure an appropriate number of measurements are obtained for each sample. We use FKP weights with $P_{\rm fid} = 10^4\ h^{-3}\ {\rm Mpc}^3$, and also plot the theoretical prediction from CAMB [102] for the matter power spectrum at $z = 0$ for reference. We see good agreement between input and output catalogues at larger scales, with a visible drop in power for the BG and LRG output catalogues at the more non-linear scales, most likely due to the fibre-collision effect. For these two tracers, the Kaiser and Fingers-of-God effects caused by RSD can be clearly seen with the yellow and green lines, similar to the configuration-space measurements.

In Fig. 4.8 we show an example of the redshift-binned power spectrum measurements for the output LRG and QSO catalogues, plotting only a few of the bins for clarity. The pipeline is able to perform this binned measurement for any number of redshift bins and across all catalogues, in both real and redshift-space (where available), which can be used to test how parameters like the growth rate evolve as a function of cosmological time.

4.5 Pipeline summary and future work

In its first five years of operation, the upcoming 4MOST Cosmology Redshift Survey will obtain accurate spectroscopic redshifts for roughly four million galaxies over a significant portion of the southern hemisphere and spanning a wide redshift range. Such a large catalogue will enable tighter constraints on cosmological models and help in the task of understanding the nature of dark energy, via measurements of galaxy clustering and cross-correlations with weak lensing and CMB surveys.

[13]Currently, `nbodykit` is unable to measure in log-space bins, which are useful for measuring the power on large-scales. This feature has been requested.

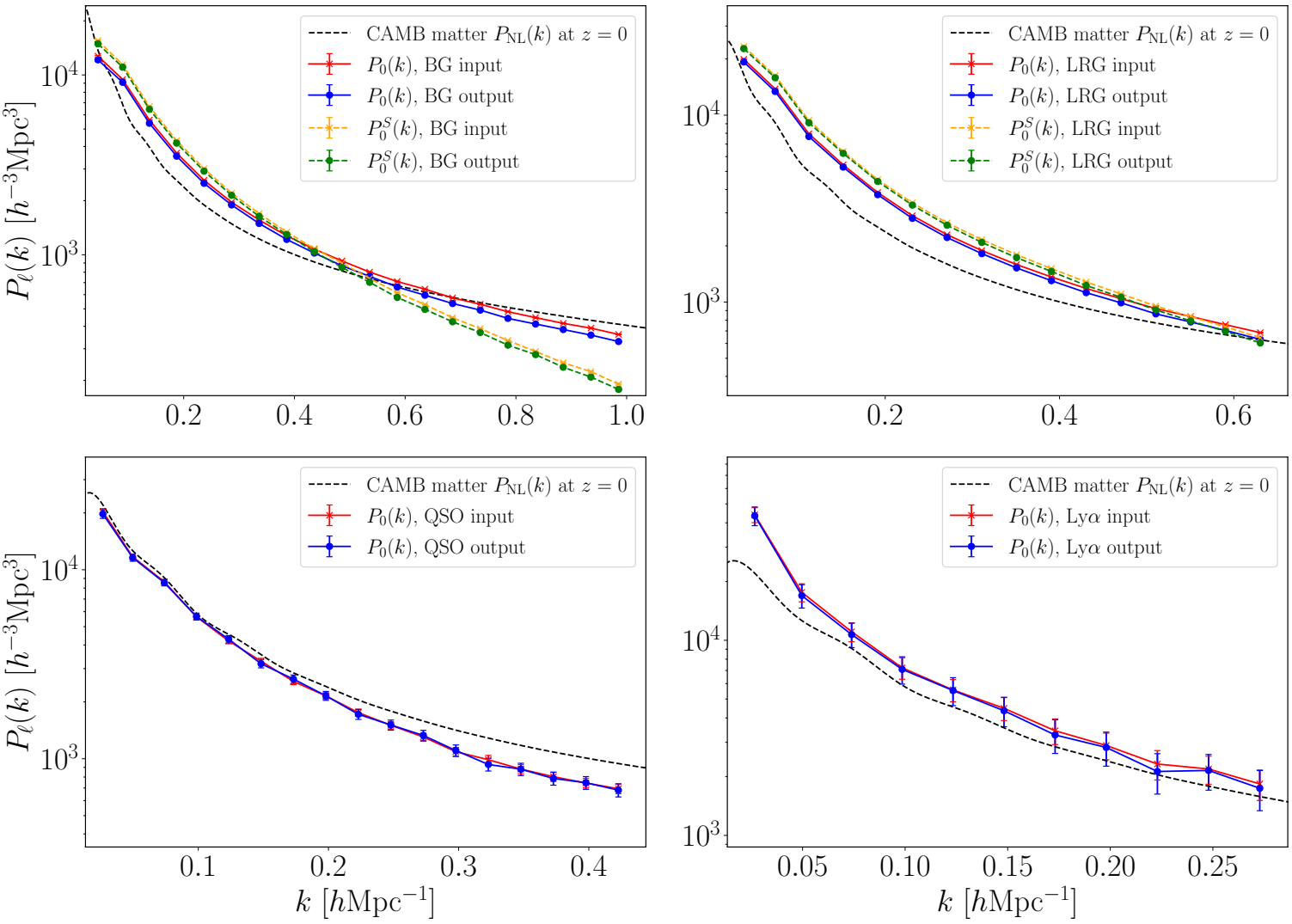

Figure 4.7: Measurements of the real-space monopole power spectrum for the four tracers for both input (red line) and output (blue line) catalogues. We also show the redshift-space measurements where available in green and yellow-dashed lines. The theoretical prediction for the matter power spectrum from CAMB at $z = 0$ is plotted as a dashed black line for reference.

In advance of the CRS going live, it is imperative to run simulations of the expected performance of the instrument, particularly as the 4MOST project is a complex multi-survey operation. To aid in the analysis of the simulation outputs for the CRS, we have developed a clustering pipeline, focusing on data validation, creation of mock-random catalogues and two-point clustering statistics in both configuration and Fourier space. While these stages are all performing as intended, there are several areas where improvements can be made, which we summarise as following:

- Currently, the output files generated by the 4MOST OpSim do not have any radial positional data (redshifts), and so the most labour intensive stage of the pipeline is having to use the `TOPCAT` [178] software to perform a merge on the input and output raw data files to pull this information through. This merge then also produces duplicate columns that have to be

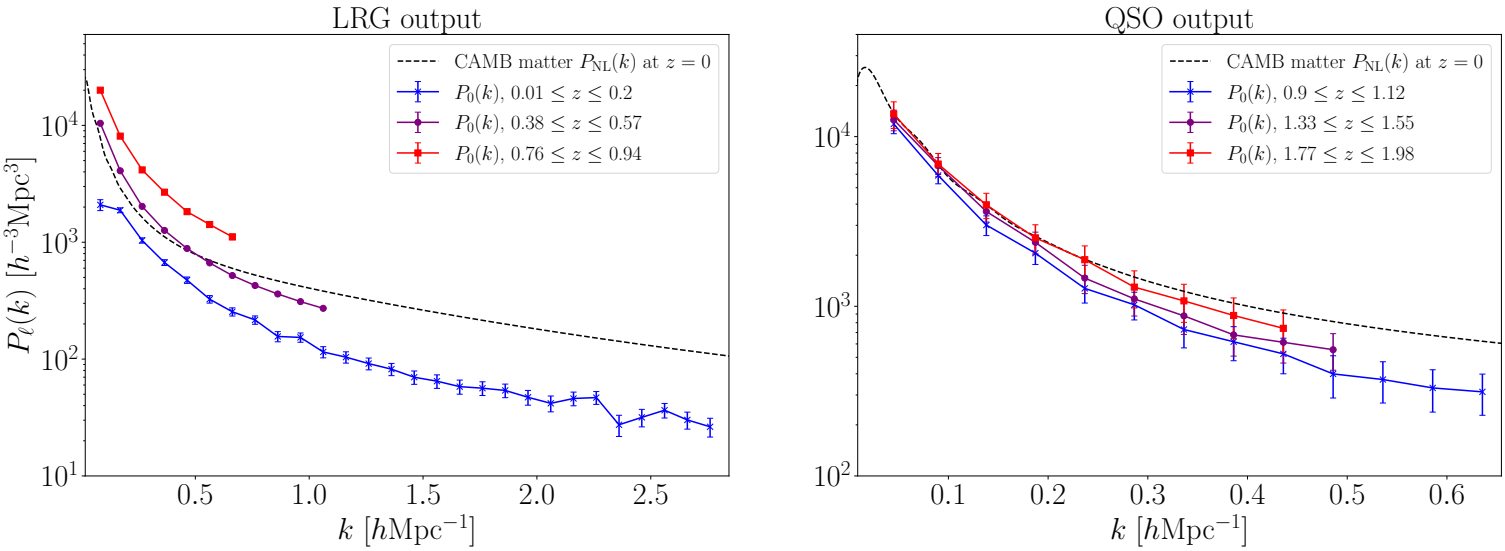

Figure 4.8: Measurements of the real-space monopole power spectrum in redshift bins for the LRG and QSO tracers. The theoretical prediction for the matter power spectrum from CAMB at $z = 0$ is plotted as a dashed black line for reference.

removed. In future versions of the OpSim where the full 3D information is generated, this entire data cleaning and reduction stage of the pipeline can easily be automated in Python, significantly reducing the amount of manual work that has to be done up front.

- The jackknife covariance matrix calculation on the real space clustering statistics is one of the main bottlenecks in terms of speed at present. This is performed by each task looping over the jackknife region and calculating the correlation functions in a sequential manner, but could be adapted so that each task on a node is given a region to calculate via MPI, with the root task then collating the results to calculate the covariance matrix. However, an even more efficient algorithm could be employed, whereby instead of repeating the pair counts for every jackknife region, the pair counts could just be performed once for the entire region, and then one could use a weighting scheme for the individual pair counts at the binning stage. Using this method, the pair weights would be equal to 1 if the galaxy pair is in scope for this region, and 0 if one or both of the galaxies of the pair are out of scope. This would drastically speed up computation time such that it would remain roughly the same as for a single calculation, regardless of how many jackknife regions are chosen, but requires a more sophisticated algorithm in terms of weights at the binning stage.

- The error calculation on the Power spectrum (Eq. (4.16)) currently assumes a diagonal covariance matrix and constant survey selection function, but should be upgraded to use the jackknife technique (or equivalent) to give more robust results. It is also worth drawing attention to the very recent work of Mohammad & Percival (2021) [179] on Jackknife methods for 2-point correlation functions, where they compare different Jackknife methods and demonstrate correction terms that can be used to obtain unbiased results.

- We currently only employ the fibre-collision correction on the angular clustering statistic $w(\theta)$ for the output catalogue, via the simple method of comparison with the expected signal from the input catalogue, but this should be extended to all of the statistics to account for missing pairs that particularly effect the smaller scales. This will be a challenging tasks for the 4MOST survey and outside the scope of the current work, due to the complicated and stochastic nature of the fibre assignment process when dealing with targeting many different tracers for multiple surveys simultaneously.

- As the 4FS OpSim catalogues provide data on reddening caused by dust in the interstellar medium, this information could be used to weight the clustering statistics to improve results.

- The next major stage of the pipeline will be to use the output measurements for forecasting on parameter constraints, which will require accurate and fast modelling of the theoretical predictions for each of the statistics. While we have demonstrated a model with accompanying code to forward-model the full-sky window-convolved power spectrum in Chapter §2, extending this to improve speed and include angular survey masks and galaxy bias (described in Chapter §3) remains a challenging prospect.

Appendices

4.A Clustering pipeline software and links

The three main pieces of software required for the pipeline are Python3.6, `TOPCAT`[14], and Jupyter Notebooks. Links for the pipeline, including download locations of the code and of the data files, is provided in Table 4.4. In Table 4.5 we list the Python libraries required for the clustering pipeline to run, as well as the versions used to write the code.

Item	Link
Clustering pipeline code	`https://github.com/danpryer/4FS_clustering_pipeline`
Input and Output data catalogues	`https://4most.mpe.mpg.de/IWG2/`
Survey mask files[15]	`https://gitlab.mpcdf.mpg.de/joco/lss_mock_dev/`
UNIT simulations	`https://unitsims.ft.uam.es/index.php/simulations`

Table 4.4: Links to key files needed to run the clustering pipeline.

4.B The clustering pipeline

We now give a more detailed overview of the clustering pipeline. In terms of data that is most relevant to the CRS, the 4FS takes a large target input catalogue of positional galaxy data, and then produces an output catalogue of the measurements, including data on the probability that each target was observed. We can then use this data to make any relevant redshift and magnitude cuts, while keeping only observed targets, and then feed this into the clustering pipeline for further analysis. Radial redshift data is provided in both real and redshift space, with the latter, enabling the measurement of redshift-space distortions (RSD), only provided for the BG and LRG tracers.

The clustering pipeline is broken up into several stages, with an initial data cleaning stage performed using `TOPCAT` [178], to separate the full output catalogue down into separate tracer catalogues specific to the CRS (for the BG, LRG, QSO and Lyα targets). The remaining stages of the pipeline are coded in Python3.6, with any visualisation steps performed in Jupyter Notebooks. The pipeline generates mock random un-clustered catalogues to go alongside the simulated data

[14] http://www.star.bris.ac.uk/ mbt/topcat/

[15] Navigate to the data → masks folder and download the atlasngc, atlasngcnotdes, des, kidsn and kidss polygon files.

Library	Version	Link
NumPy	1.19.5	https://numpy.org/doc/
Matplotlib	2.2.2	https://matplotlib.org/
Numba	0.51.2	https://numba.pydata.org/
Jupyter	1.0.0	https://jupyter.org/
Pandas	0.22.0	https://pandas.pydata.org/
Mpi4Py	3.0.0	https://mpi4py.readthedocs.io/en/stable/
AstroPy	4.1	https://www.astropy.org/
SciPy	1.5.4	https://scipy.org/
HealPy	1.12.0	https://healpy.readthedocs.io/en/latest/
PyMangle	0.9.2	https://github.com/esheldon/pymangle
Fitsio	0.9.11	https://pypi.org/project/fitsio/
nbodykit	0.3.7	https://nbodykit.readthedocs.io/en/latest/
TreeCorr	4.1.7	https://rmjarvis.github.io/TreeCorr/
CorrFunc	2.2.0	https://corrfunc.readthedocs.io/en/master/
CAMB	1.3.2	https://camb.readthedocs.io/en/latest/

Table 4.5: List of Python libraries used by the pipeline, including versions used in development, and links to main document pages.

catalogues, for use in the two-point clustering statistics. We use the `TreeCorr` library to perform both 3D $\xi(r)$ and and angular $w(\theta)$ correlation function measurements, and the `CorrFunc` library to produce projected clustering measurements, $w_p(r_p)$. For Fourier-space clustering, we use the `nbodykit` library, which provides measurement of the power spectrum multipoles $P_\ell(k)$, which are particularly useful when studying the effects of redshift space distortions.

The pipeline is designed to be run on a HPC, and uses parallelisation via the Python implementation of MPI (`mpi4py` [115]). In addition to this, the `TreeCorr` and `CorrFunc` libraries use `OpenMP`[16] under the hood to speed up pair counting operations. The `nbodykit` library can be configured to run data I/O and Fast Fourier Transforms (FFTs) in parallel however we have not currently implemented this due to the relatively small data sets from 4FS, as well as a good baseline speed from the library without these features.

In the following sub-sections, we give a more detailed outline of each stage of the pipeline (also pictured in Fig. 4.9), listing any parameter configurations that are required at each stage, as well as any relevant background equations for the statistical tools used. The pipeline is designed to be as 'hands-off' as possible, aside from the initial data cleaning stage performed in `TOPCAT`. Links to relevant websites for the pipeline code data catalogues and survey mask files, as well as the list of software requirements, are covered in Appendix §4.A.

4.B.1 Stage 1 - Folder preparation (Python)

The first stage of the pipeline involves setting up the relevant folder structure on the machine that the pipeline is to be run on, as well as defining some key properties relating to the catalogues being

[16] https://www.openmp.org/

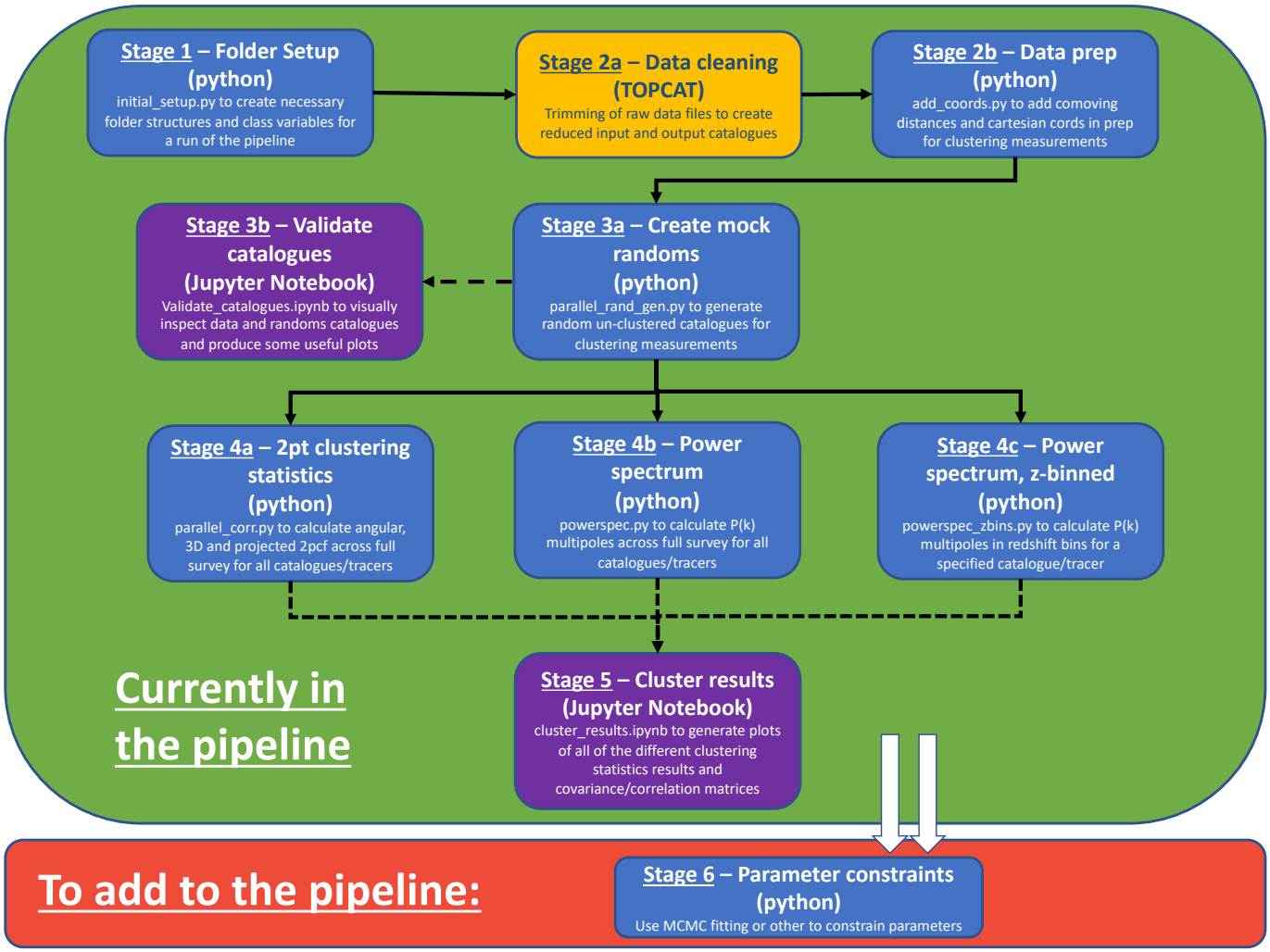

Figure 4.9: Flow diagram of the clustering pipeline in its current form.

processed. The user can modify the variables in the '**initial_setup.py**' program, specifying the main file path for where the data and results are to be stored, and then once run, the program will create the hierarchy of folders required for the rest of the pipeline, as well as saving the relevant catalogue variables for a given run to a pickle file to be read by the latter stages of the code. The user will also provide the cosmological parameters from the initial N-Body simulation that was used to create the input simulation data. The created folder structure is shown in Fig. 4.10.

Once the folder structure is set up, the raw input and output data catalogues, as well as the survey mask files, should be downloaded and placed into the relevant folders as indicated in the folder structure diagram.

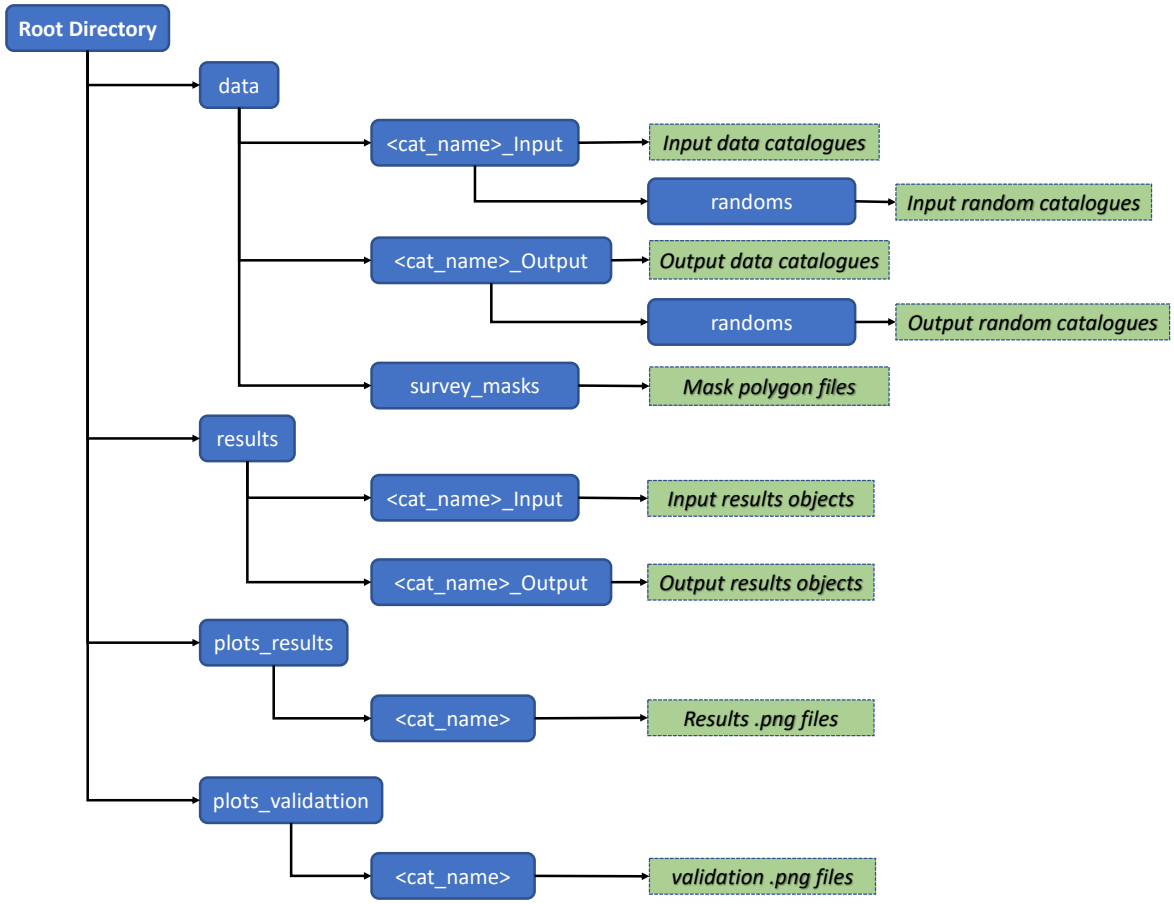

Figure 4.10: The folder structure created for the data being fed into, and created by, the pipeline, as well as the results that it produces. Each run of the pipeline will have a specified catalogue name, ⟨cat_name⟩, and stage 1 generates run-specific folders for any of the blue boxes in the diagram that have this variable in the name.

4.B.2 Stage 2a - Data cleaning (TOPCAT)

The second stage of the pipeline involves some cleaning of the input and output data files from 4FS, which can contain many columns of data, a lot of which are redundant for our clustering work. The aim of this stage is to create reduced catalogues which contain only the necessary columns, which are the angular and radial data columns, as well as any magnitude and colour information which can be used to make data cuts where necessary. If the raw output files do not contain any radial or magnitude/colour information, then a merge can be performed in `TOPCAT` on the input files to pull this information through. Resulting reduced catalogues should be saved as FITS files to the relevant Input and Output data folders as specified in Stage 1, with the minimum columns needed for the rest of the pipeline to run being 'RA', 'DEC' and 'REDSHIFT_ESTIMATE' (case sensitive). The BG and LRG tracers will also have a 'redshift_S' column (redshift-space redshift measurement), which can be included for RSD measurements if desired. As the QSO and Lyα

samples are at a much higher redshift, the peculiar velocity component of their observed recession velocity will be much less than the Hubble flow velocity, so only one redshift is given. The files should be named as 'input_reduced_⟨tracer⟩.fits' and 'output_reduced_⟨tracer⟩.fits', with ⟨tracer⟩ ∈ {BG, LRG, QSO, Ly-α}. The raw output files will also contain a 'fobs' column, detailing if the specified target has been observed or not, and suitable filter should be put on this column before saving (e.g. only rows where fobs ≥ 1). Additionally, at this stage one could choose to make any redshift or magnitude cuts to the data before proceeding.

4.B.3 Stage 2b - Data preparation (Python)

The next step involves adding Cartesian coordinates and comoving distances to the eight reduced catalogues. This is done by running the file '**add_cords.py**', which uses the 'comoving_distance' function from the 'FLRW' class of the `Astropy` cosmology class, as well as the 'spherical_to_cartesian' function from the `Astropy` coordinates class. This stage will overwrite the reduced catalogues, now containing four additional columns: 'comov_dist', 'xpos', 'ypos' and 'zpos'. For the LRG and BG samples, redshift-space Cartesian coordinates will aso be added ('comov_dist_S', 'xpos_S', 'ypos_S' and 'zpos_S') if the 'redshift_S' column was included in the previous stage.

4.B.4 Stage 3a - Creating mock random catalogues (Python)

Mock random (un-clustered) catalogues are then generated by running the '**parallel_rand_gen.py**' file. As this is parallel code using MPI, it should be submitted to a job queue on a HPC, and is designed to run on $N_{\rm cat} \times N_{\rm tracer}$ tasks. for example if we have two sets of catalogues (input and output) and four tracer types, this will run on eight tasks producing eight random catalogues. The resultant catalogues will have $N_{\rm data} \times R_{\rm multi} = N_{\rm rand}$ points, where the random multiplier $R_{\rm multi}$ variable is set in the catalogue variables class in stage 1. An example submission script for how to run this on an HPC using the `Slurm`[17] workload manager is provided in '**submit_rand_gen.sh**'.

To create the random catalogues, the data catalogues are first broken up into their separate fields (where field 1 is the larger field on the right of figure 4.2, and field 2 the smaller on the left) for speed purposes[18], with a square in angular space placed around each field, and random points generated uniformly in RA and sin(DEC) within each square. The program then uses the polygon survey footprint files, together with functions in the '**surv_footprint.py**' file, to see if the generated points are in scope, discarding any that are not. For the input catalogues, this process is repeated until we have the desired number of points $N_{\rm rand}$ in scope for each field. For the output catalogues, we generate more random points than are required, based on the completeness of the sample. We then use a `Healpix` map to down weight the randoms on a pixel by pixel basis, to match the varying angular completeness, such that we end up with the correct $N_{\rm rand}$) points overall.

[17] https://slurm.schedmd.com/documentation.html

[18] Note that this splitting into fields may artificially suppress any Poisson fluctuations between fields, if present, and so this should only be done when the target densities are equivalent for the fields (as is the case in our mock catalogues used in our tests.)

The `Healpix` nside parameter, which determines how many pixels a `Healpix` map will contain and is given by

$$\text{nside} = 12 \times 2^{\text{n}} \ , \tag{4.20}$$

is set with $n = 2$, giving a pixel area of ~ 1.5 square degrees, to match the 4MOST viewing plane as closely as possible.

To obtain random redshifts, the program will take R_{multi} randomly shuffled copies of the 'REDSHIFT_ESTIMATE' column from the data catalogue. Finally, the program will then calculate and add the comoving distance and Cartesian coordinates for these random points, and save the resulting catalogues to FITS files in the respective randoms folders, as shown in Fig. 4.10.

4.B.5 Stage 3b - Data and Randoms validation (Jupyter Notebook)

Before running the clustering measurements, the data and random catalogues can be inspected in the '**validate_catalogues.ipynb**' Jupyter notebook. A multi-grid plot is produced for each of the tracers, showing `Healpix` maps of the data and randoms for both input and output catalogues, as well as a radial profile of the number density $n(z)$, and completeness of the outputs. The plots are saved for each tracer into the relevant 'plots_validation' folder, and an example for the Bright Galaxy (BG) sample is shown in Fig. 4.11. This notebook is intended to serve as an easy visual tool to check that the random catalogues have been created in the correct survey footprint, as well as checking that there are no problem areas in terms of completeness of the output sample. It can also be used to check if there are any irregularities of the radial selection function via the $n(z)$ plot.

4.B.6 Stage 4a - Real-space clustering (Python)

Once the data catalogues have been cleaned and the associated random catalogue generated, we can run the file '**parallel_corr.py**', which will use the functions in '**twopointcorr.py**' to calculate the real-space two-point clustering statistics $w(\theta)$, $\xi(r)$ and $w_p(r_p)$. As with stage 3, this step is also designed to run on a HPC for speed, and, following the previous example, will run on eight tasks using MPI (one for each task and catalogue combination). The `TreeCorr` and `CorrFunc` programs used to calculate the statistics run `OpenMP` under the hood for parallelisation, and so it is recommended that each task has its own full node to run on, with all the CPUs on the node given over to the `OpenMP` parallelisation. An example `Slurm` script for this can be found in '**submit_parallel_corr.sh**', showing the specific task and CPU configurations.

Before running the program, variables can be configured at the top of the Python file, to specify the number of bins and bin ranges for each of the statistics to be calculated. The user can also specify the number of `OpenMP` threads to use, and the number of jackknife regions to split the data into for covariance matrix calculation. Finally, one can specify which of the three statistics to calculate via the 'statistics' variable array, and also add a custom string onto the naming of the results files, if one wants to take measurements with different parameter configurations and save

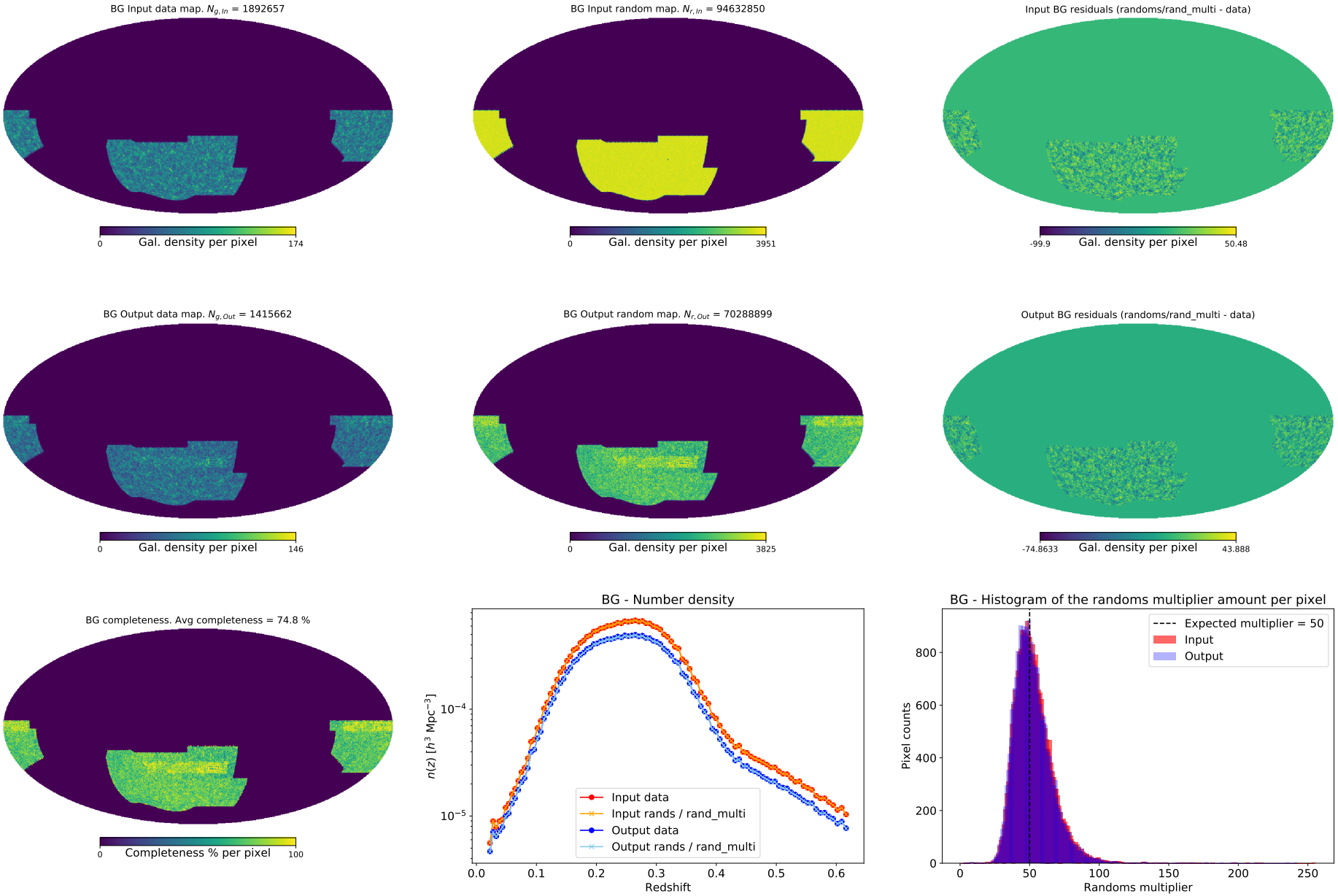

Figure 4.11: Plot showing the output from the validation Jupyter Notebook, for the BG sample, showing data for both the input and output catalogues as well as their randoms counterparts.

these all to separate files.

The `TreeCorr` and `CorrFunc` libraries use the Landy-Szalay estimator to calculate the correlation functions, which we discussed in section §4.3.1, along with the jackknife method for calculating the covariance matrices, and a simple fibre-collision correction is performed on the angular $w(\theta)$ measurements. Calculations are done individually on each of the two footprint fields, and then averaged using an inverse variance weighting scheme[19]. The results are saved in a results class object ('**full_4FS_results**' - see Table 4.6 for a list of attributes) in the associated input and output results folders.

4.B.7 Stage 4b - Fourier-space clustering (Python)

To perform measurements of the Fourier-space clustering of the 4FS data, we employ the widely used Python library `nbodykit`[20]. This code implements an FFT-based anisotropic estimator of the power spectrum and its multipoles, detailed in [169] and which we briefly covered in Section §4.3.2. The library computes the survey-window convolved power spectrum, with optional functionality for a choice of custom weighting and mesh interpolation schemes, anti-aliasing, parallelisation and more. We opt to use this code over our own implementation, discussed in Chapter §2, due to it being well documented and will have ongoing support and updates.

We use this library in our program '**powerspec.py**', which is designed to be run as an array job on a HPC (included example run script '**submit_powerspec.sh**'), with each job calculating a specific catalogue and tracer combination. Some variables for each run can be configured at the top of the program, such as bin parameters, FFT mesh resolutions and interpolation schemes, as well as anti-aliasing options. As a default, the program computes the $\ell = [0, 2, 4]$ multipoles of the power but this can be set to any combination of any ℓ's the user needs: `nbodykit` and the pipeline can calculate and store up to arbitrary order. The calculation is performed over the whole survey region (both fields at once), with the main run parameters stored in a parent class, and the specific power spectrum measurements stored in a child class which then gets attributed to the parent[21] and saved to the relevant output folders.

4.B.8 Stage 4c - Fourier-space clustering in redshift bins (Python)

Measurement of the power spectrum multipoles can also be calculated over a range of redshift bins, using the '**powerspec_zbins.py**' program, which functions similar to '**powerspec.py**' except for a few differences. In this instance, the program only calculates for one tracer and catalogue combination at a time, with the majority of the run parameters specified as command line arguments[22]. A sample `Slurm` script for this program is included in '**submit_powerspec_zbins.sh**'. The results are stored in the same class structure as the full survey volume results, where we have a parent

[19] Note the covariance matrices are averaged using a simple average, $C_{\rm avg} = (C_1 + C_2)/2$.

[20] https://nbodykit.readthedocs.io/en/latest/index.html .

[21] The '**results_powerspec**' class is the parent and the '**powerspec_measurement**' class is the child, see Tables 4.7 & 4.8 at the botto of this Appendix for details.

[22] To enable the user to quickly submit multiple jobs to a HPC queue.

List of attributes of the real-space correlation function results class		
Attribute	Type	Description
bin_mid	1D array	Mid point of the measurement bin.
res_1	1D array	Clustering result from field 1 .
res_2	1D array	As above for field 2.
res_avg	1D array	Average of the results from field 1 and 2.
err_1	1D array	Error on the calculation for field 1 .
err_2	1D array	As above for field 2
err_avg	1D array	Average of the errors from field 1 and 2.
cov_1	2D array	Covariance matrix for field 1 calc.
cov_2	2D array	As above for field 2.
cov_avg	2D array	Average of the covariances from field 1 and 2.
DD1	1D array	
DD2	1D array	
RR1	1D array	Pair counts for the fields.
RR2	1D array	
DR1	1D array	
DR2	1D array	
res_1_uncorr	1D array	$w(\theta)$ only. Result without fibre-collision correction, field 1
res_2_uncorr	1D array	$w(\theta)$ only. Result without fibre-collision correction, field 2
fibre_1_corr	1D array	$w(\theta)$ only. Fibre-collision correction factor, field 1
fibre_2_corr	1D array	$w(\theta)$ only. Fibre-collision correction factor, field 2

Table 4.6: Description of the attributes stored in the '**full_4FS_results**' class, generated by the three real-space clustering statistics, $\xi(r)$, $w(\theta)$ and $w_p(r_p)$.

class for the overall run parameters, then an instance of a child class for each set of measurements in a given redshift bin.

4.B.9 Stage 5 - Clustering Results (Jupyter Notebook)

A Jupyter Notebook '**cluster_results.ipynb**' is provided for accessing and plotting the results from the clustering measurements. Example plotting routines are provided for all statistics, including the covariance and correlation matrices, and the resulting plots are saved in the relevant 'plots_results' folder. We discuss some of the plots generated by this notebook in Section §4.4

Contributions

All of the work in this chapter, including the development of the clustering pipeline, was undertaken by myself, with feedback, suggestions and guidance from my supervisor Dr. Jon Loveday. The pipeline uses several key Python libraries, particularly for performing clustering statistics, and I have indicated as necessary where this is the case.

List of attributes of the $P_\ell(k)$ parent class		
Attribute	Type	Description
tracer	string	Which tracer the calculation is for.
catalogue	string	'input' or 'output' catalogue.
Nmesh	Int	Mesh resolution of the FFT grid.
window	String	Mass assignment scheme used.
interlaced	Boolean	If interlacing was used.
compensated	Boolean	If compensating for the mass window was used.
Ndata	Int	Number of data points in the full volume.
Nrand	Int	Number of random points in the full volume.
Nbins_Z	Int	Number of redshift bins if doing a binned measurement.
Z_edges	1D double array	Edges of the redshift bins.
Z_bins_mid	1D double array	Mid points of the redshift bins.

Table 4.7: Description of the attributes stored in the '**results_powerspec**' class, generated by the power spectrum calculation using `nbodykit`. This is the parent class for the overall run, and will also store an instance of the '**powerspec_measurement**' class in Table 4.8 for each redshift bin measurement that is performed. These child classes will be named ['bin0', 'bin1', 'bin2', ..., 'bin$n$'].

List of attributes of the $P_\ell(k)$ child class		
Attribute	Type	Description
bin_mid	1D double array	Mid point of the measurement k bin.
multipoles	1D int array	Array of ℓ modes to be measured.
Pk0	1D double array	Monopole $P_0(k)$ measurement.
Pk2	1D double array	Quadrupole $P_2(k)$ measurement.
...	...	...
Pkn	1D double array	nth pole measurement of the power spectrum.
Pk0_err	1D double array	Error on the monopole power.
Pk2_err	1D double array	Error on the quadrupolepole power.
...	...	...
Pkn_err	1D double array	Error on the nth pole measurement.
Nmodes	1D int array	Number of modes in each k bin.
Ndata	Int	Number of data points in the binned calculation.
Nrand	Int	Number of random points in the binned calculation.
dk	Double	Linear bin width.
kmin	Double	Lowest edge of first k bin measured.
Nbins	Int	Number of k bins.
Pk_fid	Double	Fiducial $P(k)$ used for the FKP weights.
Z_min	Double	Lower edge of redshift bin for this measurement.
Z_max	Double	Upper edge of redshift bin for this measurement.
Z_mid	Double	Mid points of the redshift edges.

Table 4.8: Description of the attributes stored in the '**powerspec_measurement**' child class, generated by the power spectrum calculation using `nbodykit`. An instance of this class will be created for each redshift bin measurement and added to the parent '**results_powerspec**' class in Table 4.7. The power spectrum measurements $P_\ell(k)$, and their errors, get dynamically added to the class to allow for arbitrary order of ℓ to be calculated and saved.

Chapter 5

Conclusions

Cosmology redshift surveys are a powerful tool for extracting cosmological information from the large-scale structure of the late-time universe. With a whole host of such surveys launching over the next decade, the universe is set to be probed to greater precision and over larger volumes than previously observed. The power spectrum is one of the most useful statistics for analysing data from cosmology redshift surveys, being able to constrain cosmological models in multiple different ways. In particular, the measurement of redshift space distortions and baryon acoustic oscillations, which leave imprints in the shape and amplitude of the power spectrum, provide powerful means to constrain the growth rate of structure and expansion history of the universe.

As statistical measurement errors shrink due to the growing size of survey data, careful consideration must be given to the modelling of observables like the power spectrum, to minimise any systematics that can be introduced by not properly accounting for certain effects. In this work, we focused on a forward-modelling approach of the power spectrum on the past lightcone, when convolved with a survey window function, taking into consideration large-survey effects.

5.1 The power spectrum on the past lightcone

In Chapter 2, we began by reviewing the current model of the past lightcone power spectrum for deep-redshift surveys on the full-sky. In this regime, working in spherical coordinates is preferable due to the curved nature of the survey volume, and the large survey depth requires the use of unequal-time correlators, to properly account for pair counting objects that exist at significantly different redshifts. We provided an alternative derivation of the key result as well as a generalised expression to extend the model into the non-linear regime (Sec. §2.3.7). As the model contains numerically challenging multi-dimensional integrals of spherical Bessel functions, we investigated approximations that can be employed in the small-scale regime, where the Bessel functions are more difficult to integrate due to their highly oscillatory nature. We developed C++ code to numerically evaluate the model up to two-loops in perturbation theory, making use of a small-scale approximation (Sec. §2.3.4) under the assumption of time-separability of the unequal-time correlator. We found this approximation dramatically reduced calculation time while maintaining

accuracy. We used this code to test the mean-redshift approximation that is commonly used in place of the unequal-time correlator when dealing with shallow survey depths, finding that this approximation significantly biases the amplitude of the power spectrum (see left plot in Fig. 2.3), particularly as survey depth increases. We go on to show that an 'effective fixed-time' redshift can be easily calculated (Sec. §2.3.6), giving a more accurate approximation to the unequal-time correlator than the mean-redshift approximation (right plot in Fig. 2.3).

We then put our model to the test by comparing it to power spectra measured from lightcone mock catalogues, constructed from large-volume N-body simulations. We developed a Python pipeline to perform a data reduction on these very large data sets, creating magnitude-limited unbiased galaxy catalogues, with associated random unclustered mocks, as well as code to measure the power spectrum from the resulting data cubes (Sec. §2.4). We found excellent agreement between our measurements and the theory, to within $\pm 5\%$, over a range of magnitude limits and for the scales $4 \times 10^{-3} \leq k \leq 0.5$ [h Mpc^{-1}] (Fig. 2.7). We also tested how well the commonly used FKP weights effected the measurements, for various values of fiducial power P_0 and over the range of magnitude-limited samples, finding they could boost the signal-to-noise by factors of a few (Fig. 2.9). We closed the chapter by using the lightcone mocks to test how well we could measure the turnover scale in the power spectrum, an important feature which allows us to probe the epoch of matter-radiation equality in the early universe. We found that a turnover was detectable with a probability of $P \geq 95\%$ in an all-sky catalogue, limited to an apparent magnitude of $m_{\rm lim} \sim 21$, with this probability remaining high for surveys with $m_{\rm lim} \sim 22$ at 20% sky coverage.

In Chapter 3 we extended the previous model of the power spectrum on the past lightcone, now including terms for galaxy bias and an angular survey mask that is not necessarily isotropic. As the obtained expression for the power spectrum when including these additional components is significantly more numerically challenging than in the full-sky regime, we detailed several methods that can be used for calculation of the model. Similarly to the method used in the previous chapter, on small scales we showed that as long as time-separability of the unequal-time power spectrum holds, an approximation can be used that dramatically simplifies the mathematics. On large scales however, where this approximation is not valid, we detailed how the use of the FFTLog algorithm (Sec. §3.3), in combination with analytic transforms of the double-Bessel integrals, can be used to make the problem numerically tractable. We also laid out the steps required for implementing this procedure, and highlighted potential problem regions where parameters can cause this method to encounter numerical instability or run at sub-optimal speeds.

There are several different ways in which this work can be extended. On the modelling side, the most pressing issue for advancing our model of the power spectrum on the past lightcone is to include the effect of wide-angle redshift-space distortions [148, 87, 149, 70, 150, 151]. While these have not been accounted for in the model so far, we do not believe that their inclusion will effect our findings for measuring the turnover scale, as at these scales RSD is expected to only modify the amplitude of the power spectrum peak, and not its shape. Additionally, being able to accurately

model and measure the power spectrum past this turnover scale increases the ability to test for signatures of primordial non-Gaussianity. Such measurements can provide vital information about the physics of the universe at very early times, and would help to discriminate between different inflationary models. As these signatures of PNG would manifest as a scale-dependent bias term, modifying the shape of the power spectrum on the largest scales, it is of key importance to be able to accurately model the theory in this regime.

From a numerical perspective, work needs to be done in order to speed up calculation times of the model. While we were able to develop C++ code to effectively evaluate the lightcone power spectrum in the case where we have an all-sky survey, this code still has a run time on the order of tens of minutes when running in parallel on a single HPC node, and was unsuitable for the model including an angular mask. These run times make the code prohibitive for use in a likelihood analysis in its current form, however, deployment of the FFTLog algorithm and analytic Bessel transforms, as covered in Chapter §3, are expected to speed up evaluation dramatically while also allowing for inclusion of the angular-mask term. These methods could be used in conjunction with interpolation techniques to allow for a wide range of parameter space to be covered while minimising the required amount of full evaluations of the model. Additionally, the development of efficient routines to calculate the challenging expressions encountered when working in spherical coordinates will make the prospect of calculating the covariance matrix, as well as higher order correlation functions like the Bispectrum and Trispectrum, more feasible. Some work has already been done in this area (for example in [145] they address the angular Trispectra), but would require adapting to our specific case. On the near horizon, there are plans to include fast and efficient code for solving double-Bessel integrals using the analytic methods as described in 3 in the Core Cosmology Library[1] (CCL) [180]. The team behind this software recently hosted a hackathon challenge to to address these types of numerical problems, and so once the winning code has been tested and implemented, this would provide an easy pathway to extend the lightcone work to include non-isotropic survey geometry, redshift-space distortions, covariance matrix calculations and parameter estimation.

5.2 Clustering of the 4MOST simulations

The 4MOST Cosmology Redshift Survey is an upcoming spectroscopic southern-hemisphere survey, which will obtain accurate redshifts for approximately four million dark-matter tracers over an initial run period of five years. The main aim of the survey is to help uncover the nature of dark energy and measure the expansion rate of the universe, via measurements of large-scale structure clustering as well as through cross-correlations with other surveys and CMB experiments. In advance of the survey going live, the 4MOST Facility Simulator (4FS) team have been running simulations to produce expected output data sets for the survey. This data is vital for cosmological parameter forecasting and survey design optimisation.

[1] https://ccl.readthedocs.io/en/latest/

In Chapter 4, we gave an overview of the clustering pipeline that we have developed to analyse this 4FS data. The pipeline currently has three key roles: to generate mock random unclustered catalogues that mimic the survey data for use in clustering statistics, to provide validation of both data and mock-random catalogues for identification of issues with the underlying data, and finally to measure two-point clustering statistics in both configuration and Fourier space. In Section §4.4 we reviewed the clustering results produced by the pipeline when run on the latest available input and output data sets for the 4MOST CRS. For the configuration-space measurements, we fitted power law models to the output data catalogues, finding derived parameters for the power-law slope of these models to be in close agreement to measurements from surveys such as 2dF and SDSS. We observed some drop off in clustering signal in the output catalogues across all of the statistics at small-scales, most probably caused by the fibre-collision effect, and found we were able to eliminate this effect via way of a simple correction factor for the angular clustering measurements.

There are several key areas of development for the clustering pipeline, the most pressing of which is the modelling and correction of the fibre-collision effect for the 3D and projected clustering statistics. Due to the complicated nature of 4MOST observing thousands of targets simultaneously for multiple different surveys, work should be undertaken to see if previous methods like the pair-inverse-probability weighting of [166] can be employed, or if a new approach is required. In addition to this, the pipeline should be optimised through further parallelisation to increase speed, particularly for the covariance matrix calculations that rely on the jackknife technique. With these improvements in place, the clustering statistics of the pipeline could be used to make forecasts for cosmological parameters through a Fisher matrix analysis. This will require accurate modelling of theoretical predictions for the two-point statistics, taking into consideration the effects of the survey window. As the 4MOST survey volume covers a wide angle across two separate fields, and spans a large redshift range, methods outlined in Chapters 2 & 3 could be utilised for this modelling.

Bibliography

[1] Edwin Hubble. "A Relation between Distance and Radial Velocity among Extra-Galactic Nebulae". In: *Proceedings of the National Academy of Science* 15.3 (Mar. 1929), pp. 168–173. DOI: 10.1073/pnas.15.3.168.

[2] F. Zwicky. "Die Rotverschiebung von extragalaktischen Nebeln". In: *Helvetica Physica Acta* 6 (Jan. 1933), pp. 110–127.

[3] Jaan Einasto, Ants Kaasik, and Enn Saar. "Dynamic evidence on massive coronas of galaxies". In: *Nature* 250.5464 (July 1974), pp. 309–310. DOI: 10.1038/250309a0.

[4] V. C. Rubin. "The Rotation of Spiral Galaxies". In: *Science* 220.4604 (June 1983), pp. 1339–1344. DOI: 10.1126/science.220.4604.1339.

[5] A. A. Penzias and R. W. Wilson. "A Measurement of Excess Antenna Temperature at 4080 Mc/s." In: *ApJ* 142 (July 1965), pp. 419–421. DOI: 10.1086/148307.

[6] A. G. Riess et al. "Observational Evidence from Supernovae for an Accelerating Universe and a Cosmological Constant". In: AJ 116 (Sept. 1998), pp. 1009–1038. DOI: 10.1086/300499. eprint: arXiv:astro-ph/9805201.

[7] S. Perlmutter et al. "Measurements of Omega and Lambda from 42 High-Redshift Supernovae". In: *ApJ* 517 (June 1999), pp. 565–586. DOI: 10.1086/307221. eprint: arXiv:astro-ph/9812133.

[8] S. Dodelson. *Modern cosmology*. Modern cosmology / Scott Dodelson. Amsterdam (Netherlands): Academic Press. ISBN 0-12-219141-2, 2003, XIII + 440 p., 2003.

[9] G. F. Smoot et al. "Structure in the COBE differential microwave radiometer first-year maps". In: *ApJL* 396 (Sept. 1992), pp. L1–L5. DOI: 10.1086/186504.

[10] D. N. Spergel and The WMAP Team. "First-Year Wilkinson Microwave Anisotropy Probe (WMAP) Observations: Determination of Cosmological Parameters". In: *ApJS* 148 (Sept. 2003), pp. 175–194. DOI: 10.1086/377226. eprint: astro-ph/0302209.

[11] Planck Collaboration et al. "Planck 2013 results. XVI. Cosmological parameters". In: *A&A* 571, A16 (Nov. 2014), A16. DOI: 10.1051/0004-6361/201321591. arXiv: 1303.5076 [astro-ph.CO].

[12] Planck Collaboration et al. "Planck 2015 results. XIII. Cosmological parameters". In: *A&A* 594, A13 (Sept. 2016), A13. DOI: 10.1051/0004-6361/201525830. arXiv: 1502.01589 [astro-ph.CO].

[13] Planck Collaboration et al. "Planck 2018 results. VI. Cosmological parameters". In: *A&A* 641, A6 (Sept. 2020), A6. DOI: 10.1051/0004-6361/201833910. arXiv: 1807.06209 [astro-ph.CO].

[14] Matthew Colless et al. "The 2dF Galaxy Redshift Survey: spectra and redshifts". In: *MNRAS* 328.4 (Dec. 2001), pp. 1039–1063. DOI: 10.1046/j.1365-8711.2001.04902.x. arXiv: astro-ph/0106498 [astro-ph].

[15] K. N. Abazajian et al. "The Seventh Data Release of the Sloan Digital Sky Survey". In: *ApJS* 182 (June 2009), pp. 543–558. DOI: 10.1088/0067-0049/182/2/543. arXiv: 0812.0649.

[16] DES Collaboration et al. "Dark Energy Survey Year 1 Results: Cosmological Constraints from Galaxy Clustering and Weak Lensing". In: *ArXiv e-prints* (Aug. 2017). arXiv: 1708.01530.

[17] E. Komatsu et al. "Five-Year Wilkinson Microwave Anisotropy Probe Observations: Cosmological Interpretation". In: *ApJS* 180 (Feb. 2009), pp. 330–376. DOI: 10.1088/0067-0049/180/2/330. arXiv: 0803.0547.

[18] D. J. Fixsen. "The Temperature of the Cosmic Microwave Background". In: *ApJ* 707.2 (Dec. 2009), pp. 916–920. DOI: 10.1088/0004-637X/707/2/916. arXiv: 0911.1955 [astro-ph.CO].

[19] E. Aprile et al. "Dark Matter Results from 100 Live Days of XENON100 Data". In: *PRL* 107.13, 131302 (Sept. 2011), p. 131302. DOI: 10.1103/PhysRevLett.107.131302. arXiv: 1104.2549 [astro-ph.CO].

[20] D. S. Akerib et al. "Results from a Search for Dark Matter in the Complete LUX Exposure". In: *PRL* 118.2, 021303 (Jan. 2017), p. 021303. DOI: 10.1103/PhysRevLett.118.021303. arXiv: 1608.07648 [astro-ph.CO].

[21] E. Polisensky and M. Ricotti. "Constraints on the Dark Matter Particle Mass from the Number of Milky Way Satellites". In: *ArXiv e-prints* (Apr. 2010). arXiv: 1004.1459 [astro-ph.CO].

[22] M. Ackermann et al. "Searching for Dark Matter Annihilation from Milky Way Dwarf Spheroidal Galaxies with Six Years of Fermi Large Area Telescope Data". In: *PRL* 115.23, 231301 (Dec. 2015), p. 231301. DOI: 10.1103/PhysRevLett.115.231301. arXiv: 1503.02641 [astro-ph.HE].

[23] S. Weinberg. "The cosmological constant problem". In: *Reviews of Modern Physics* 61 (Jan. 1989), pp. 1–23. DOI: 10.1103/RevModPhys.61.1.

[24] Adam G. Riess et al. "A 2.4% Determination of the Local Value of the Hubble Constant". In: *ApJ* 826.1, 56 (July 2016), p. 56. DOI: 10.3847/0004-637X/826/1/56. arXiv: 1604.01424 [astro-ph.CO].

[25] Shadab Alam et al. "Completed SDSS-IV extended Baryon Oscillation Spectroscopic Survey: Cosmological implications from two decades of spectroscopic surveys at the Apache Point Observatory". In: *PRD* 103.8, 083533 (Apr. 2021), p. 083533. DOI: 10.1103/PhysRevD.103.083533. arXiv: 2007.08991 [astro-ph.CO].

[26] Levon Pogosian, Gong-Bo Zhao, and Karsten Jedamzik. "Recombination-independent Determination of the Sound Horizon and the Hubble Constant from BAO". In: *ApJL* 904.2, L17 (Dec. 2020), p. L17. DOI: 10.3847/2041-8213/abc6a8. arXiv: 2009.08455 [astro-ph.CO].

[27] Michel Chevallier and David Polarski. "Accelerating Universes with Scaling Dark Matter". In: *International Journal of Modern Physics D* 10.2 (Jan. 2001), pp. 213–223. DOI: 10.1142/S0218271801000822. arXiv: gr-qc/0009008 [gr-qc].

[28] E. V. Linder. "Exploring the Expansion History of the Universe". In: *Physical Review Letters* 90.9 (Mar. 2003), pp. 091301–+. DOI: 10.1103/PhysRevLett.90.091301. eprint: arXiv:astro-ph/0208512.

[29] Timothy Clifton et al. "Modified gravity and cosmology". In: *Phys. Rep.* 513.1 (Mar. 2012), pp. 1–189. DOI: 10.1016/j.physrep.2012.01.001. arXiv: 1106.2476 [astro-ph.CO].

[30] B. P. Abbott et al. "Observation of Gravitational Waves from a Binary Black Hole Merger". In: *PRL* 116.6, 061102 (Feb. 2016), p. 061102. DOI: 10.1103/PhysRevLett.116.061102. arXiv: 1602.03837 [gr-qc].

[31] Alan H. Guth. "Inflationary universe: A possible solution to the horizon and flatness problems". In: *PRD* 23.2 (Jan. 1981), pp. 347–356. DOI: 10.1103/PhysRevD.23.347.

[32] A. D. Linde. "A new inflationary universe scenario: A possible solution of the horizon, flatness, homogeneity, isotropy and primordial monopole problems". In: *Physics Letters B* 108.6 (Feb. 1982), pp. 389–393. DOI: 10.1016/0370-2693(82)91219-9.

[33] A. A. Starobinsky. "Dynamics of phase transition in the new inflationary universe scenario and generation of perturbations". In: *Physics Letters B* 117.3-4 (Nov. 1982), pp. 175–178. DOI: 10.1016/0370-2693(82)90541-X.

[34] D. Baumann. "TASI Lectures on Inflation". In: *ArXiv e-prints* (July 2009). arXiv: 0907.5424 [hep-th].

[35] David Wands et al. "New approach to the evolution of cosmological perturbations on large scales". In: *PRD* 62.4, 043527 (Aug. 2000), p. 043527. DOI: 10.1103/PhysRevD.62.043527. arXiv: astro-ph/0003278 [astro-ph].

[36] Planck Collaboration et al. "Planck 2018 results. IX. Constraints on primordial non-Gaussianity". In: *A&A* 641, A9 (Sept. 2020), A9. DOI: 10.1051/0004-6361/201935891. arXiv: 1905.05697 [astro-ph.CO].

[37] Antony Lewis, Anthony Challinor, and Anthony Lasenby. "Efficient Computation of CMB anisotropies in closed FRW models". In: *Astrophys. J.* 538 (2000), pp. 473–476. eprint: astro-ph/9911177.

[38] J. Lesgourgues. "The Cosmic Linear Anisotropy Solving System (CLASS) I: Overview". In: *ArXiv e-prints* (Apr. 2011). arXiv: 1104.2932 [astro-ph.IM].

[39] J. A. Peacock. *Cosmological Physics*. Cambridge, UK: Cambridge University Press, 1999., Jan. 1999.

[40] F. Bernardeau et al. "Large-scale structure of the Universe and cosmological perturbation theory". In: *Phys. Rep.* 367 (Sept. 2002), pp. 1–3. eprint: arXiv:astro-ph/0112551.

[41] F. R. Bouchet et al. "Perturbative Lagrangian approach to gravitational instability." In: *A&A* 296 (Apr. 1995), pp. 575–+. eprint: arXiv:astro-ph/9406013.

[42] Hugo Martel and Wolfram Freudling. "Second-Order Perturbation Theory in Omega not = 1 Friedmann Models". In: *ApJ* 371 (Apr. 1991), p. 1. DOI: 10.1086/169864.

[43] R. Scoccimarro et al. "Nonlinear Evolution of the Bispectrum of Cosmological Perturbations". In: *ApJ* 496 (Mar. 1998), pp. 586–+. DOI: 10.1086/305399. eprint: arXiv:astro-ph/9704075.

[44] Eric V. Linder and Robert N. Cahn. "Parameterized beyond-Einstein growth". In: *Astroparticle Physics* 28.4-5 (Dec. 2007), pp. 481–488. DOI: 10.1016/j.astropartphys.2007.09.003. arXiv: astro-ph/0701317 [astro-ph].

[45] Nick Kaiser. "Clustering in real space and in redshift space". In: *MNRAS* 227 (July 1987), pp. 1–21. DOI: 10.1093/mnras/227.1.1.

[46] Lucia F. de la Bella, Nicolas Tessore, and Sarah Bridle. "The unequal-time matter power spectrum: impact on weak lensing observables". In: *Journal of Cosmology and Astro-Particle Physics* 2021.8, 001 (Aug. 2021), p. 001. DOI: 10.1088/1475-7516/2021/08/001. arXiv: 2011.06185 [astro-ph.CO].

[47] T. D. Kitching and A. F. Heavens. "Unequal-time correlators for cosmology". In: *PRD* 95.6, 063522 (Mar. 2017), p. 063522. DOI: 10.1103/PhysRevD.95.063522. arXiv: 1612.00770 [astro-ph.CO].

[48] Solène Chabanier, Marius Millea, and Nathalie Palanque-Delabrouille. "Matter power spectrum: from Ly α forest to CMB scales". In: *MNRAS* 489.2 (Oct. 2019), pp. 2247–2253. DOI: 10.1093/mnras/stz2310. arXiv: 1905.08103 [astro-ph.CO].

[49] M. J. Geller and J. P. Huchra. "Groups of galaxies. III. THe CfA survey." In: *ApJS* 52 (June 1983), pp. 61–87. DOI: 10.1086/190859.

[50] Margaret J. Geller and John P. Huchra. "Mapping the Universe". In: *Science* 246.4932 (Nov. 1989), pp. 897–903. DOI: 10.1126/science.246.4932.897.

[51] V. Springel et al. "Simulations of the formation, evolution and clustering of galaxies and quasars". In: *Nature* 435 (June 2005), pp. 629–636. DOI: 10.1038/nature03597. eprint: astro-ph/0504097.

[52] Volker Springel, Carlos S. Frenk, and Simon D. M. White. "The large-scale structure of the Universe". In: *Nature* 440.7088 (Apr. 2006), pp. 1137–1144. DOI: 10.1038/nature04805. arXiv: astro-ph/0604561 [astro-ph].

[53] DESI Collaboration et al. "The DESI Experiment Part I: Science,Targeting, and Survey Design". In: *arXiv e-prints*, arXiv:1611.00036 (Oct. 2016), arXiv:1611.00036. arXiv: 1611.00036 [astro-ph.IM].

[54] J. Richard et al. "4MOST Consortium Survey 8: Cosmology Redshift Survey (CRS)". In: *The Messenger* 175 (Mar. 2019), pp. 50–53. DOI: 10.18727/0722-6691/5127. arXiv: 1903.02474 [astro-ph.CO].

[55] R. Laureijs et al. "Euclid Definition Study Report". In: *ArXiv e-prints* (Oct. 2011). arXiv: 1110.3193 [astro-ph.CO].

[56] Olivier Doré et al. "Cosmology with the SPHEREX All-Sky Spectral Survey". In: *arXiv e-prints*, arXiv:1412.4872 (Dec. 2014), arXiv:1412.4872. arXiv: 1412.4872 [astro-ph.CO].

[57] LSST. "LSST Science Book, Version 2.0". In: *ArXiv e-prints* (Dec. 2009). arXiv: 0912.0201 [astro-ph.IM].

[58] M. Tegmark. "Measuring Cosmological Parameters with Galaxy Surveys". In: *Physical Review Letters* 79 (Nov. 1997), pp. 3806–3809. eprint: arXiv:astro-ph/9706198.

[59] P. J. E. Peebles. *The large-scale structure of the universe*. Research supported by the National Science Foundation. Princeton, N.J., Princeton University Press, 1980. 435 p., 1980.

[60] Y. P. Jing et al. "The Influence of Baryons on the Clustering of Matter and Weak-Lensing Surveys". In: *ApJL* 640.2 (Apr. 2006), pp. L119–L122. DOI: 10.1086/503547. arXiv: astro-ph/0512426 [astro-ph].

[61] G. Somogyi and R. E. Smith. "Cosmological perturbation theory for baryons and dark matter: One-loop corrections in the renormalized perturbation theory framework". In: *PRD* 81.2 (Jan. 2010), pp. 023524–+. DOI: 10.1103/PhysRevD.81.023524. arXiv: 0910.5220.

[62] Ian G. McCarthy et al. "The BAHAMAS project: the CMB-large-scale structure tension and the roles of massive neutrinos and galaxy formation". In: *MNRAS* 476.3 (May 2018), pp. 2999–3030. DOI: 10.1093/mnras/sty377. arXiv: 1712.02411 [astro-ph.CO].

[63] N. Kaiser. "On the spatial correlations of Abell clusters". In: *ApJL* 284 (Sept. 1984), pp. L9–L12. DOI: 10.1086/184341.

[64] J. N. Fry and E. Gaztanaga. "Biasing and hierarchical statistics in large-scale structure". In: *ApJ* 413 (Aug. 1993), pp. 447–452. DOI: 10.1086/173015. eprint: arXiv:astro-ph/9302009.

[65] P. Coles. "Galaxy formation with a local bias". In: *MNRAS* 262 (June 1993), pp. 1065–1075.

[66] A. Dekel and O. Lahav. "Stochastic Nonlinear Galaxy Biasing". In: *ApJ* 520 (July 1999), pp. 24–34. DOI: 10.1086/307428. eprint: arXiv:astro-ph/9806193.

[67] Tobias Baldauf et al. "Evidence for quadratic tidal tensor bias from the halo bispectrum". In: *PRD* 86.8, 083540 (Oct. 2012), p. 083540. DOI: 10.1103/PhysRevD.86.083540. arXiv: 1201.4827 [astro-ph.CO].

[68] Kwan Chuen Chan, Román Scoccimarro, and Ravi K. Sheth. "Gravity and large-scale nonlocal bias". In: *PRD* 85.8, 083509 (Apr. 2012), p. 083509. DOI: 10.1103/PhysRevD.85.083509. arXiv: 1201.3614 [astro-ph.CO].

[69] Alexander Eggemeier et al. "Testing one-loop galaxy bias: Joint analysis of power spectrum and bispectrum". In: *PRD* 103.12, 123550 (June 2021), p. 123550. DOI: 10.1103/PhysRevD.103.123550. arXiv: 2102.06902 [astro-ph.CO].

[70] A. J. S. Hamilton. "Linear Redshift Distortions: a Review". In: *The Evolving Universe*. Ed. by D. Hamilton. Vol. 231. Astrophysics and Space Science Library. 1998, pp. 185–+.

[71] R. Scoccimarro. "Redshift-space distortions, pairwise velocities, and nonlinearities". In: *PRD* 70.8 (Oct. 2004), pp. 083007–+. DOI: 10.1103/PhysRevD.70.083007. eprint: arXiv:astro-ph/0407214.

[72] Kazuhiro Yamamoto, Hiroaki Nishioka, and Yasushi Suto. "The Cosmological Light-Cone Effect on the Power Spectrum of Galaxies and Quasars in Wide-Field Redshift Surveys". In: *ApJ* 527.2 (Dec. 1999), pp. 488–497. DOI: 10.1086/308126. arXiv: astro-ph/9908006 [astro-ph].

[73] Takahiko Matsubara. "The Correlation Function in Redshift Space: General Formula with Wide-Angle Effects and Cosmological Distortions". In: *ApJ* 535.1 (May 2000), pp. 1–23. DOI: 10.1086/308827. arXiv: astro-ph/9908056 [astro-ph].

[74] Jaiyul Yoo and Uroš Seljak. "Wide-angle effects in future galaxy surveys". In: *MNRAS* 447.2 (Feb. 2015), pp. 1789–1805. DOI: 10.1093/mnras/stu2491. arXiv: 1308.1093 [astro-ph.CO].

[75] Daniele Bertacca et al. "Relativistic wide-angle galaxy bispectrum on the light cone". In: *PRD* 97.2, 023531 (Jan. 2018), p. 023531. DOI: 10.1103/PhysRevD.97.023531. arXiv: 1705.09306 [astro-ph.CO].

[76] C. Alcock and B. Paczynski. "An evolution free test for non-zero cosmological constant". In: *Nature* 281 (Oct. 1979), p. 358. DOI: 10.1038/281358a0.

[77] W. E. Ballinger, J. A. Peacock, and A. F. Heavens. "Measuring the cosmological constant with redshift surveys". In: *MNRAS* 282 (Oct. 1996), p. 877. DOI: 10.1093/mnras/282.3.877. arXiv: astro-ph/9605017 [astro-ph].

[78] H. A. Feldman, N. Kaiser, and J. A. Peacock. "Power-spectrum analysis of three-dimensional redshift surveys". In: *ApJ* 426 (May 1994), pp. 23–37. DOI: 10.1086/174036. eprint: arXiv:astro-ph/9304022.

[79] M. Tegmark. "Measuring Cosmological Parameters with Galaxy Surveys". In: *Physical Review Letters* 79 (Nov. 1997), pp. 3806–3809. eprint: arXiv:astro-ph/9706198.

[80] Kazuhiro Yamamoto. "Optimal Weighting Scheme in Redshift-Space Power Spectrum Analysis and a Prospect for Measuring the Cosmic Equation of State". In: *ApJ* 595.2 (Oct. 2003), pp. 577–588. DOI: 10.1086/377488. arXiv: astro-ph/0208139 [astro-ph].

[81] W. J. Percival, L. Verde, and J. A. Peacock. "Fourier analysis of luminosity-dependent galaxy clustering". In: *MNRAS* 347 (Jan. 2004), pp. 645–653. DOI: 10.1111/j.1365-2966.2004.07245.x. eprint: arXiv:astro-ph/0306511.

[82] Robert E. Smith and Laura Marian. "Towards optimal estimation of the galaxy power spectrum". In: *MNRAS* 454.2 (Dec. 2015), pp. 1266–1289. DOI: 10.1093/mnras/stv2042. arXiv: 1503.06830 [astro-ph.CO].

[83] P. J. E. Peebles. "Statistical Analysis of Catalogs of Extragalactic Objects. I. Theory". In: *ApJ* 185 (Oct. 1973), pp. 413–440. DOI: 10.1086/152431.

[84] Caleb Scharf et al. "Spherical harmonic analysis of IRAS galaxies : implications for the GreatAttractor and cold dark matter." In: *MNRAS* 256 (May 1992), pp. 229–237. DOI: 10.1093/mnras/256.2.229.

[85] C. A. Scharf and O. Lahav. "Spherical Harmonic Analysis of the 2-JANSKY IRAS Galaxy Redshift Survey". In: *MNRAS* 264 (Sept. 1993), p. 439. DOI: 10.1093/mnras/264.2.439.

[86] K. B. Fisher et al. "Wiener reconstruction of density, velocity and potential fields from all-sky galaxy redshift surveys". In: *MNRAS* 272.4 (Feb. 1995), pp. 885–908. DOI: 10.1093/mnras/272.4.885. arXiv: astro-ph/9406009 [astro-ph].

[87] A. F. Heavens and A. N. Taylor. "A spherical harmonic analysis of redshift space". In: *MNRAS* 275.2 (July 1995), pp. 483–497. DOI: 10.1093/mnras/275.2.483. arXiv: astro-ph/9409027 [astro-ph].

[88] H. Tadros et al. "Spherical harmonic analysis of the PSCz galaxy catalogue: redshift distortions and the real-space power spectrum". In: *MNRAS* 305.3 (May 1999), pp. 527–546. DOI: 10.1046/j.1365-8711.1999.02409.x. arXiv: astro-ph/9901351 [astro-ph].

[89] W. J. Percival et al. "The 2dF Galaxy Redshift Survey: spherical harmonics analysis of fluctuations in the final catalogue". In: *MNRAS* 353 (Oct. 2004), pp. 1201–1218. DOI: 10.1111/j.1365-2966.2004.08146.x. eprint: arXiv:astro-ph/0406513.

[90] Andrina Nicola et al. "Three-dimensional spherical analyses of cosmological spectroscopic surveys". In: *PRD* 90.6, 063515 (Sept. 2014), p. 063515. DOI: 10.1103/PhysRevD.90.063515. arXiv: 1405.3660 [astro-ph.CO].

[91] F. Lanusse, A. Rassat, and J. -L. Starck. "3D galaxy clustering with future wide-field surveys: Advantages of a spherical Fourier-Bessel analysis". In: *A&A* 578, A10 (June 2015), A10. DOI: 10.1051/0004-6361/201424456. arXiv: 1406.5989 [astro-ph.CO].

[92] Maresuke Shiraishi et al. "Minimum Variance Estimation of Galaxy Power Spectrum in Redshift Space". In: *MNRAS* (July 2020). DOI: 10.1093/mnrasl/slaa132. arXiv: 2005.03438 [astro-ph.CO].

[93] Chris Blake and Karl Glazebrook. "Probing Dark Energy Using Baryonic Oscillations in the Galaxy Power Spectrum as a Cosmological Ruler". In: *ApJ* 594.2 (Sept. 2003), pp. 665–673. DOI: 10.1086/376983. arXiv: astro-ph/0301632 [astro-ph].

[94] H.-J. Seo and D. J. Eisenstein. "Probing Dark Energy with Baryonic Acoustic Oscillations from Future Large Galaxy Redshift Surveys". In: *ApJ* 598 (Dec. 2003), pp. 720–740. DOI: 10.1086/379122. eprint: arXiv:astro-ph/0307460.

[95] Chris Blake and Sarah Bridle. "Cosmology with photometric redshift surveys". In: *MNRAS* 363.4 (Nov. 2005), pp. 1329–1348. DOI: 10.1111/j.1365-2966.2005.09526.x. arXiv: astro-ph/0411713 [astro-ph].

[96] James Binney and Thomas Quinn. "Gaussian random fields in spherical coordinates". In: *MNRAS* 249 (Apr. 1991), pp. 678–683. DOI: 10.1093/mnras/249.4.678.

[97] Henry S. Grasshorn Gebhardt and Donghui Jeong. "Nonlinear redshift-space distortions in the harmonic-space galaxy power spectrum". In: *PRD* 102.8, 083521 (Oct. 2020), p. 083521. DOI: 10.1103/PhysRevD.102.083521. arXiv: 2008.08706 [astro-ph.CO].

[98] Milton Abramowitz and Irene A. Stegun. *Handbook of mathematical functions : with formulas, graphs, and mathematical tables*. Dover, 1970.

[99] Joseph E. McEwen et al. "FAST-PT: a novel algorithm to calculate convolution integrals in cosmological perturbation theory". In: *Journal of Cosmology and Astro-Particle Physics* 2016.9, 015 (Sept. 2016), p. 015. DOI: 10.1088/1475-7516/2016/09/015. arXiv: 1603.04826 [astro-ph.CO].

[100] Robert E. Smith and Raul E. Angulo. "Precision modelling of the matter power spectrum in a Planck-like Universe". In: *MNRAS* 486.1 (June 2019), pp. 1448–1479. DOI: 10.1093/mnras/stz890. arXiv: 1807.00040 [astro-ph.CO].

[101] Planck Collaboration et al. "Planck 2013 results. XVI. Cosmological parameters". In: *A&A* 571, A16 (Nov. 2014), A16. DOI: 10.1051/0004-6361/201321591. arXiv: 1303.5076.

[102] Antony Lewis, Anthony Challinor, and Anthony Lasenby. "Efficient Computation of Cosmic Microwave Background Anisotropies in Closed Friedmann-Robertson-Walker Models". In: *ApJ* 538.2 (Aug. 2000), pp. 473–476. DOI: 10.1086/309179. arXiv: astro-ph/9911177 [astro-ph].

[103] M. Crocce, S. Pueblas, and R. Scoccimarro. "Transients from initial conditions in cosmological simulations". In: *MNRAS* 373 (Nov. 2006), pp. 369–381. DOI: 10.1111/j.1365-2966.2006.11040.x. eprint: arXiv:astro-ph/0606505.

[104] V. Springel. "The cosmological simulation code GADGET-2". In: *MNRAS* 364 (Dec. 2005), pp. 1105–1134. DOI: 10.1111/j.1365-2966.2005.09655.x. eprint: astro-ph/0505010.

[105] R. E. Angulo et al. "Scaling relations for galaxy clusters in the Millennium-XXL simulation". In: *MNRAS* 426 (Nov. 2012), pp. 2046–2062. DOI: 10.1111/j.1365-2966.2012.21830.x. arXiv: 1203.3216.

[106] Alexander I. Merson et al. "Lightcone mock catalogues from semi-analytic models of galaxy formation - I. Construction and application to the BzK colour selection". In: *MNRAS* 429.1 (Feb. 2013), pp. 556–578. DOI: 10.1093/mnras/sts355. arXiv: 1206.4049 [astro-ph.CO].

[107] Chris Blake et al. "The WiggleZ Dark Energy Survey: the selection function and z = 0.6 galaxy power spectrum". In: *MNRAS* 406.2 (Aug. 2010), pp. 803–821. DOI: 10.1111/j.1365-2966.2010.16747.x. arXiv: 1003.5721 [astro-ph.CO].

[108] Y. P. Jing. "Correcting for the Alias Effect When Measuring the Power Spectrum Using a Fast Fourier Transform". In: *ApJ* 620 (Feb. 2005), pp. 559–563. DOI: 10.1086/427087. eprint: arXiv:astro-ph/0409240.

[109] E. Sefusatti et al. "Accurate estimators of correlation functions in Fourier space". In: *MNRAS* 460.4 (Aug. 2016), pp. 3624–3636. DOI: 10.1093/mnras/stw1229. arXiv: 1512.07295 [astro-ph.CO].

[110] R. W. Hockney and J. W. Eastwood. *Computer Simulation Using Particles*. CRC Press, 1981.

[111] Charles R. Harris et al. "Array programming with NumPy". In: *Nature* 585.7825 (Sept. 2020), pp. 357–362. DOI: 10.1038/s41586-020-2649-2. arXiv: 2006.10256 [cs.MS].

[112] Pauli Virtanen et al. *scipy/scipy: SciPy 1.2.1*. Version v1.2.1. Feb. 2019. DOI: 10.5281/zenodo.2560881.

[113] Astropy Collaboration et al. "Astropy: A community Python package for astronomy". In: *A&A* 558, A33 (Oct. 2013), A33. DOI: 10.1051/0004-6361/201322068. arXiv: 1307.6212 [astro-ph.IM].

[114] Siu Kwan Lam, Antoine Pitrou, and Stanley Seibert. "Numba: A LLVM-Based Python JIT Compiler". In: *Proceedings of the Second Workshop on the LLVM Compiler Infrastructure in HPC*. LLVM '15. Austin, Texas: Association for Computing Machinery, 2015. ISBN: 9781450340052. DOI: 10.1145/2833157.2833162. URL: https://doi.org/10.1145/2833157.2833162.

[115] Lisandro D. Dalcin et al. "Parallel distributed computing using Python". In: *Advances in Water Resources* 34.9 (Sept. 2011), pp. 1124–1139. DOI: 10.1016/j.advwatres.2011.04.013.

[116] Henry Gomersall. *Pyfftw*. June 2016. DOI: 10.5281/zenodo.59508.

[117] Volker Springel et al. "Simulating cosmic structure formation with the GADGET-4 code". In: *MNRAS* 506.2 (Sept. 2021), pp. 2871–2949. DOI: 10.1093/mnras/stab1855. arXiv: 2010.03567 [astro-ph.IM].

[118] S. Cole et al. "The 2dF Galaxy Redshift Survey: power-spectrum analysis of the final data set and cosmological implications". In: *MNRAS* 362 (Sept. 2005), pp. 505–534. DOI: 10.1111/j.1365-2966.2005.09318.x. eprint: arXiv:astro-ph/0501174.

[119] M. Tegmark et al. "The Three-Dimensional Power Spectrum of Galaxies from the Sloan Digital Sky Survey". In: *ApJ* 606 (May 2004), pp. 702–740. DOI: 10.1086/382125. eprint: arXiv:astro-ph/0310725.

[120] Chris Blake, Paul Carter, and Jun Koda. "Power spectrum multipoles on the curved sky: an application to the 6-degree Field Galaxy Survey". In: *MNRAS* 479.4 (Oct. 2018), pp. 5168–5183. DOI: 10.1093/mnras/sty1814. arXiv: 1801.04969 [astro-ph.CO].

[121] Héctor Gil-Marin et al. "The power spectrum and bispectrum of SDSS DR11 BOSS galaxies - I. Bias and gravity". In: *MNRAS* 451.1 (July 2015), pp. 539–580. DOI: 10.1093/mnras/stv961. arXiv: 1407.5668 [astro-ph.CO].

[122] Robert E. Smith and Laura Marian. "What is the optimal way to measure the galaxy power spectrum?" In: *Mon. Not. Roy. Astron. Soc.* 457.4 (2016), pp. 4285–4290. DOI: 10.1093/mnras/stw282. arXiv: 1507.04365 [astro-ph.CO].

[123] Gregory B. Poole et al. "The WiggleZ Dark Energy Survey: probing the epoch of radiation domination using large-scale structure". In: *MNRAS* 429.3 (Mar. 2013), pp. 1902–1912. DOI: 10.1093/mnras/sts431. arXiv: 1211.5605 [astro-ph.CO].

[124] D. Foreman-Mackey et al. "emcee: The MCMC Hammer". In: *PASP* 125.925 (Mar. 2013), pp. 306–320. DOI: 10.1086/670067. arXiv: 1202.3665 [astro-ph.IM].

[125] A. J. S. Hamilton. "Uncorrelated modes of the non-linear power spectrum". In: *MNRAS* 312 (Feb. 2000), pp. 257–284. eprint: arXiv:astro-ph/9905191.

[126] Eva-Maria Mueller, Will J. Percival, and Rossana Ruggeri. "Optimizing primordial non-Gaussianity measurements from galaxy surveys". In: *MNRAS* 485.3 (May 2019), pp. 4160–4166. DOI: 10.1093/mnras/sty3150. arXiv: 1702.05088 [astro-ph.CO].

[127] Eva-Maria Mueller et al. "The clustering of galaxies in the completed SDSS-IV extended Baryon Oscillation Spectroscopic Survey: Primordial non-Gaussianity in Fourier Space". In: *arXiv e-prints*, arXiv:2106.13725 (June 2021), arXiv:2106.13725. arXiv: 2106.13725 [astro-ph.CO].

[128] J. Loveday et al. "Galaxy and Mass Assembly (GAMA): ugriz galaxy luminosity functions". In: *MNRAS* 420.2 (Feb. 2012), pp. 1239–1262. DOI: 10.1111/j.1365-2966.2011.20111.x. arXiv: 1111.0166 [astro-ph.CO].

[129] G. Efstathiou, R. S. Ellis, and B. A. Peterson. "Analysis of a complete galaxy redshift survey. II - The field-galaxy luminosity function". In: *MNRAS* 232 (May 1988), pp. 431–461.

[130] I. S. Gradshteyn et al. *Table of Integrals, Series, and Products*. Acaemic Press, 2007.

[131] Emanuele Castorina et al. "Redshift-weighted constraints on primordial non-Gaussianity from the clustering of the eBOSS DR14 quasars in Fourier space". In: *Journal of Cosmology and Astro-Particle Physics* 2019.9, 010 (Sept. 2019), p. 010. DOI: 10.1088/1475-7516/2019/09/010. arXiv: 1904.08859 [astro-ph.CO].

[132] N. Dalal et al. "Imprints of primordial non-Gaussianities on large-scale structure: Scale-dependent bias and abundance of virialized objects". In: *PRD* 77.12 (June 2008), pp. 123514–+. DOI: 10.1103/PhysRevD.77.123514. eprint: arXiv:0710.4560.

[133] S. Matarrese and L. Verde. "The Effect of Primordial Non-Gaussianity on Halo Bias". In: *ApJL* 677 (Apr. 2008), pp. L77–L80. DOI: 10.1086/587840. arXiv: 0801.4826.

[134] A. Slosar et al. "Constraints on local primordial non-Gaussianity from large scale structure". In: *Journal of Cosmology and Astro-Particle Physics* 8 (Aug. 2008), pp. 31–+. DOI: 10.1088/1475-7516/2008/08/031. arXiv: 0805.3580.

[135] Donghui Jeong and Eiichiro Komatsu. "Primordial Non-Gaussianity, Scale-dependent Bias, and the Bispectrum of Galaxies". In: *ApJ* 703.2 (Oct. 2009), pp. 1230–1248. DOI: 10.1088/0004-637X/703/2/1230. arXiv: 0904.0497 [astro-ph.CO].

[136] Vincent Desjacques, Donghui Jeong, and Fabian Schmidt. "Large-scale galaxy bias". In: *Phys. Rep.* 733 (Feb. 2018), pp. 1–193. DOI: 10.1016/j.physrep.2017.12.002. arXiv: 1611.09787 [astro-ph.CO].

[137] J. N. Fry. "The Evolution of Bias". In: *ApJL* 461 (Apr. 1996), pp. L65+. DOI: 10.1086/310006.

[138] L. Clerkin et al. "A prescription for galaxy biasing evolution as a nuisance parameter". In: *MNRAS* 448.2 (Apr. 2015), pp. 1389–1401. DOI: 10.1093/mnras/stu2754. arXiv: 1405.5521 [astro-ph.CO].

[139] P. McDonald. "Erratum: Clustering of dark matter tracers: Renormalizing the bias parameters [Phys. Rev. D 74, 103512 (2006)]". In: *PRD* 74.12 (Dec. 2006), pp. 129901–+. DOI: 10.1103/PhysRevD.74.129901.

[140] K. M. Górski et al. "HEALPix: A Framework for High-Resolution Discretization and Fast Analysis of Data Distributed on the Sphere". In: *ApJ* 622 (Apr. 2005), pp. 759–771. DOI: 10.1086/427976. eprint: arXiv:astro-ph/0409513.

[141] Valentin Assassi, Marko Simonović, and Matias Zaldarriaga. "Efficient evaluation of angular power spectra and bispectra". In: *Journal of Cosmology and Astro-Particle Physics* 2017.11, 054 (Nov. 2017), p. 054. DOI: 10.1088/1475-7516/2017/11/054. arXiv: 1705.05022 [astro-ph.CO].

[142] Henry S. Grasshorn Gebhardt and Donghui Jeong. "Fast and accurate computation of projected two-point functions". In: *PRD* 97.2, 023504 (Jan. 2018), p. 023504. DOI: 10.1103/PhysRevD.97.023504. arXiv: 1709.02401 [astro-ph.CO].

[143] Nils Schöneberg et al. "Beyond the traditional line-of-sight approach of cosmological angular statistics". In: *Journal of Cosmology and Astro-Particle Physics* 2018.10, 047 (Oct. 2018), p. 047. DOI: 10.1088/1475-7516/2018/10/047. arXiv: 1807.09540 [astro-ph.CO].

[144] Xiao Fang et al. "Beyond Limber: efficient computation of angular power spectra for galaxy clustering and weak lensing". In: *Journal of Cosmology and Astro-Particle Physics* 2020.5, 010 (May 2020), p. 010. DOI: 10.1088/1475-7516/2020/05/010. arXiv: 1911.11947 [astro-ph.CO].

[145] Hayden Lee and Cora Dvorkin. "Cosmological angular trispectra and non-Gaussian covariance". In: *Journal of Cosmology and Astro-Particle Physics* 2020.5, 044 (May 2020), p. 044. DOI: 10.1088/1475-7516/2020/05/044. arXiv: 2001.00584 [astro-ph.CO].

[146] Shu-Fan Chen, Hayden Lee, and Cora Dvorkin. "Precise and accurate cosmology with CMB×LSS power spectra and bispectra". In: *Journal of Cosmology and Astro-Particle Physics* 2021.5, 030 (May 2021), p. 030. DOI: 10.1088/1475-7516/2021/05/030. arXiv: 2103.01229 [astro-ph.CO].

[147] Nico Temme. "Numerical aspects of special functions". In: *Acta Numerica* 16 (May 2007), pp. 379–478. DOI: 10.1017/S0962492906330012.

[148] Karl B. Fisher, Caleb A. Scharf, and Ofer Lahav. "A spherical harmonic approach to redshift distortion and a measurement of Omega(0) from the 1.2-Jy IRAS Redshift Survey". In: *MNRAS* 266 (Jan. 1994), p. 219. DOI: 10.1093/mnras/266.1.219. arXiv: astro-ph/9309027 [astro-ph].

[149] Alexander S. Szalay, Takahiko Matsubara, and Stephen D. Landy. "Redshift-Space Distortions of the Correlation Function in Wide-Angle Galaxy Surveys". In: *ApJL* 498.1 (May 1998), pp. L1–L4. DOI: 10.1086/311293. arXiv: astro-ph/9712007 [astro-ph].

[150] István Szapudi. "Wide-Angle Redshift Distortions Revisited". In: *ApJ* 614.1 (Oct. 2004), pp. 51–55. DOI: 10.1086/423168. arXiv: astro-ph/0404477 [astro-ph].

[151] Péter Pápai and István Szapudi. "Non-perturbative effects of geometry in wide-angle redshift distortions". In: *MNRAS* 389.1 (Sept. 2008), pp. 292–296. DOI: 10.1111/j.1365-2966.2008.13572.x. arXiv: 0802.2940 [astro-ph].

[152] Alvise Raccanelli, Lado Samushia, and Will J. Percival. "Simulating redshift-space distortions for galaxy pairs with wide angular separation". In: *MNRAS* 409.4 (Dec. 2010), pp. 1525–1533. DOI: 10.1111/j.1365-2966.2010.17388.x. arXiv: 1006.1652 [astro-ph.CO].

[153] R. S. de Jong et al. "4MOST: Project overview and information for the First Call for Proposals". In: *The Messenger* 175 (Mar. 2019), pp. 3–11. DOI: 10.18727/0722-6691/5117. arXiv: 1903.02464 [astro-ph.IM].

[154] E. Tempel et al. "Probabilistic fibre-to-target assignment algorithm for multi-object spectroscopic surveys". In: *A&A* 635, A101 (Mar. 2020), A101. DOI: 10.1051/0004-6361/201937228. arXiv: 2001.09348 [astro-ph.IM].

[155] E. Tempel et al. "An optimized tiling pattern for multiobject spectroscopic surveys: application to the 4MOST survey". In: *MNRAS* 497.4 (Oct. 2020), pp. 4626–4643. DOI: 10.1093/mnras/staa2285. arXiv: 2007.03307 [astro-ph.IM].

[156] M. Jarvis, G. Bernstein, and B. Jain. "The skewness of the aperture mass statistic". In: *MNRAS* 352 (July 2004), pp. 338–352. DOI: 10.1111/j.1365-2966.2004.07926.x. eprint: arXiv:astro-ph/0307393.

[157] Manodeep Sinha and Lehman H. Garrison. "CORRFUNC - a suite of blazing fast correlation functions on the CPU". In: *MNRAS* 491.2 (Jan. 2020), pp. 3022–3041. DOI: 10.1093/mnras/stz3157. arXiv: 1911.03545 [astro-ph.CO].

[158] S. D. Landy and A. S. Szalay. "Bias and variance of angular correlation functions". In: *ApJ* 412 (July 1993), pp. 64–71. DOI: 10.1086/172900.

[159] Martin Kerscher, István Szapudi, and Alexander S. Szalay. "A Comparison of Estimators for the Two-Point Correlation Function". In: *ApJL* 535.1 (May 2000), pp. L13–L16. DOI: 10.1086/312702. arXiv: astro-ph/9912088 [astro-ph].

[160] Frank C. van den Bosch et al. "Cosmological constraints from a combination of galaxy clustering and lensing - I. Theoretical framework". In: *MNRAS* 430.2 (Apr. 2013), pp. 725–746. DOI: 10.1093/mnras/sts006. arXiv: 1206.6890 [astro-ph.CO].

[161] Jun Shao. "Discussion: Jackknife, Bootstrap and Other Resampling Methods in Regression Analysis". In: *The Annals of Statistics* 14.4 (1986), pp. 1322–1326. DOI: 10.1214/aos/1176350154. URL: https://doi.org/10.1214/aos/1176350154.

[162] Y. P. Jing, H. J. Mo, and G. Börner. "Spatial Correlation Function and Pairwise Velocity Dispersion of Galaxies: Cold Dark Matter Models versus the Las Campanas Survey". In: *ApJ* 494.1 (Feb. 1998), pp. 1–12. DOI: 10.1086/305209. arXiv: astro-ph/9707106 [astro-ph].

[163] Ed Hawkins et al. "The 2dF Galaxy Redshift Survey: correlation functions, peculiar velocities and the matter density of the Universe". In: *MNRAS* 346.1 (Nov. 2003), pp. 78–96. DOI: 10.1046/j.1365-2966.2003.07063.x. arXiv: astro-ph/0212375 [astro-ph].

[164] I. Zehavi et al. "Galaxy Clustering in Early Sloan Digital Sky Survey Redshift Data". In: *ApJ* 571 (May 2002), pp. 172–190. DOI: 10.1086/339893. eprint: astro-ph/0106476.

[165] Beth Reid et al. "SDSS-III Baryon Oscillation Spectroscopic Survey Data Release 12: galaxy target selection and large-scale structure catalogues". In: *MNRAS* 455.2 (Jan. 2016), pp. 1553–1573. DOI: 10.1093/mnras/stv2382. arXiv: 1509.06529 [astro-ph.CO].

[166] Davide Bianchi and Will J. Percival. "Unbiased clustering estimation in the presence of missing observations". In: *MNRAS* 472.1 (Nov. 2017), pp. 1106–1118. DOI: 10.1093/mnras/stx2053. arXiv: 1703.02070 [astro-ph.CO].

[167] Alex Smith et al. "Correcting for fibre assignment incompleteness in the DESI Bright Galaxy Survey". In: *MNRAS* 484.1 (Mar. 2019), pp. 1285–1300. DOI: 10.1093/mnras/stz059. arXiv: 1809.07355 [astro-ph.CO].

[168] Nick Hand et al. "nbodykit: An Open-source, Massively Parallel Toolkit for Large-scale Structure". In: AJ 156.4, 160 (Oct. 2018), p. 160. DOI: 10.3847/1538-3881/aadae0. arXiv: 1712.05834 [astro-ph.IM].

[169] Nick Hand et al. "An optimal FFT-based anisotropic power spectrum estimator". In: *Journal of Cosmology and Astro-Particle Physics* 2017.7, 002 (July 2017), p. 002. DOI: 10.1088/1475-7516/2017/07/002. arXiv: 1704.02357 [astro-ph.CO].

[170] Kazuhiro Yamamoto et al. "A Measurement of the Quadrupole Power Spectrum in the Clustering of the 2dF QSO Survey". In: *Publications of the ASJ* 58 (Feb. 2006), pp. 93–102. DOI: 10.1093/pasj/58.1.93. arXiv: astro-ph/0505115 [astro-ph].

[171] Andrew J. Connolly et al. "The Angular Correlation Function of Galaxies from Early Sloan Digital Sky Survey Data". In: *ApJ* 579.1 (Nov. 2002), pp. 42–47. DOI: 10.1086/342787. arXiv: astro-ph/0107417 [astro-ph].

[172] Y. Wang, R. J. Brunner, and J. C. Dolence. "The SDSS galaxy angular two-point correlation function". In: *MNRAS* 432.3 (July 2013), pp. 1961–1979. DOI: 10.1093/mnras/stt450. arXiv: 1303.2432 [astro-ph.CO].

[173] N. P. Ross et al. "The 2dF-SDSS LRG and QSO Survey: the LRG 2-point correlation function and redshift-space distortions". In: *MNRAS* 381 (Oct. 2007), pp. 573–588. DOI: 10.1111/j.1365-2966.2007.12289.x. eprint: arXiv:astro-ph/0612400.

[174] M. Davis and P. J. E. Peebles. "A survey of galaxy redshifts. V - The two-point position and velocity correlations". In: *ApJ* 267 (Apr. 1983), pp. 465–482. DOI: 10.1086/160884.

[175] G. Mountrichas et al. "QSO-LRG two-point cross-correlation function and redshift-space distortions". In: *MNRAS* 394.4 (Apr. 2009), pp. 2050–2064. DOI: 10.1111/j.1365-2966.2009.14456.x. arXiv: 0801.1816 [astro-ph].

[176] Idit Zehavi et al. "The Luminosity and Color Dependence of the Galaxy Correlation Function". In: *ApJ* 630.1 (Sept. 2005), pp. 1–27. DOI: 10.1086/431891. arXiv: astro-ph/0408569 [astro-ph].

[177] Z. Zheng et al. "Halo Occupation Distribution Modeling of Clustering of Luminous Red Galaxies". In: *ArXiv e-prints* (Sept. 2008). arXiv: 0809.1868.

[178] M. B. Taylor. "TOPCAT & STIL: Starlink Table/VOTable Processing Software". In: *Astronomical Data Analysis Software and Systems XIV*. Ed. by P. Shopbell, M. Britton, and R. Ebert. Vol. 347. Astronomical Society of the Pacific Conference Series. Dec. 2005, p. 29.

[179] Faizan G. Mohammad and Will J. Percival. "Creating Jackknife and Bootstrap estimates of the covariance matrix for the two-point correlation function". In: *arXiv e-prints*, arXiv:2109.07071 (Sept. 2021), arXiv:2109.07071. arXiv: 2109.07071 [astro-ph.CO].

[180] Nora Elisa Chisari et al. "Core Cosmology Library: Precision Cosmological Predictions for LSST". In: *ApJS* 242.1, 2 (May 2019), p. 2. DOI: 10.3847/1538-4365/ab1658. arXiv: 1812.05995 [astro-ph.CO].